Numerical Modeling of High-energy Transients from Black Holes and Neutron Stars

Thesis by
Yoonsoo Kim

In Partial Fulfillment of the Requirements for the
degree of
Doctor of Philosophy

CALIFORNIA INSTITUTE OF TECHNOLOGY
Pasadena, California

2025
Defended Apr 8 2025

Yoonsoo Kim
ORCID: 0000-0002-4305-6026

ACKNOWLEDGEMENTS

I would like to thank my advisors Elias Most and Saul Teukolsky for their guidance and support throughout my PhD studies. Elias was always willing to offer unstinting help ranging from elementary physics questions to practical research skills, and I am taking a leaf out of his book for an untiring enthusiasm towards newly emerging science. I have also greatly benefited from Saul's concise but always incisive comments and advice for many years. One of the most valuable lessons from Saul was the easiest way to be an expert: to fail in every possible way. I cannot overstate how fortunate and grateful I have been for having Elias and Saul, passionate scholars and considerate mentors, as my doctoral advisors.

My early years in grad school were enriched by the mentorship from Nils Deppe, who taught me how to rigorously assess numerical methodologies and properly apply them to problems in computational physics. I would also like to express my gratitude to Mark Scheel, who instructed me how to split a long-term technical project into smaller logical units that can be tested and tackled individually. Thank you Nils and Mark.

My special thanks go to JoAnn Boyd, the world's best admin, for her help, support, and generosity in office candies, matched only by her satiric humor.

It was my genuine pleasure to share spacetime trajectories at Caltech with Sarah Habib, Isaac Legred, Kyle Nelli, Nicholas Rui, Kiran Shila, and Rhiannon Udall, not only as colleagues at the workplace but also as friends who have livened up my personal life in Pasadena. To our postdocs Mike Pajkos and Nils Vu, thank you for all your help, encouraging words, and office companionship; I wish you all the best. I also thank the members of Caltech TAPIR and the SXS Collaboration for helpful discussions, collaborative efforts, and, most of all, supportive atmosphere.

To my family, this could not have been done without your unconditional support and encouragement. Thank you.

Lastly, I would like to thank everyone—within which this margin is too narrow to contain—who made my years at Caltech happy and memorable.

Y.K. acknowledges support from National Science Foundation, Sherman Fairchild Foundation, and Korea Foundation for Advanced Studies.

Figures in this article were produced using `matplotlib` (The Matplotlib Development Team, 2025), `numpy` (Harris et al., 2020), and `scipy` (Virtanen et al., 2020) packages.

ABSTRACT

Along with recent breakthroughs in relativistic astrophysics and multi-messenger astronomy, theoretical studies on compact objects and the dynamics of relativistic matter surrounding them have a growing significance. General relativistic approaches are required to properly describe astrophysical phenomena taking place in a strong gravity regime, yet the high complexity and nonlinearity of the equations governing those systems compel numerical approaches. In this thesis, we develop a computational method for and present global numerical simulations of relativistic plasma around compact objects, particularly focusing on high-energy electromagnetic transients originating from black holes and neutron stars. Our works include a new hybrid numerical scheme for modeling force-free magnetospheres of compact objects, large-scale simulations of a spinning black hole immersed in a magnetized wind, and magnetospheric transients from a merging black hole–neutron star binary.

PUBLISHED CONTENT AND CONTRIBUTIONS

Kim, Yoonsoo, Elias R. Most, William Throwe, et al. (2024). "General relativistic force-free electrodynamics with a discontinuous Galerkin-finite difference hybrid method". In: *Physical Review D* 109.12, p. 123019. DOI: 10.1103/PhysRevD.109.123019. arXiv: 2404.01531. URL: https://journals.aps.org/prd/abstract/10.1103/PhysRevD.109.123019.
Y.K. is a lead developer of the code module, ran test problems, and wrote the majority of the manuscript.

Kim, Yoonsoo and Elias R. Most (2025). "General relativistic magnetized Bondi-Hoyle-Lyttleton accretion with a spin-field misalignment: Jet nutation, polarity reversals, and Magnus drag". In: *Physical Review D* 111 (8), p. 083025. DOI: 10.1103/PhysRevD.111.083025. URL: https://link.aps.org/doi/10.1103/PhysRevD.111.083025.
Y.K. developed several code functionalities required for the study, performed simulations, analyzed the data, and wrote the majority of the manuscript.

Kim, Yoonsoo, Elias R. Most, Andrei M. Beloborodov, et al. (2024). "Black Hole Pulsars and Monster Shocks as Outcomes of Black Hole–Neutron Star Mergers". In: *Astrophysical Journal Letters* 982.2, p. L54. DOI: 10.3847/2041-8213/adbff9. URL: https://iopscience.iop.org/article/10.3847/2041-8213/adbff9.
Y.K. performed simulations, analyzed the data, and wrote the majority of the manuscript.

Deppe, Nils et al. (Mar. 2025). *SpECTRE v2025.03.17*. Version 2025.03.17. DOI: 10.5281/zenodo.15040490. URL: https://spectre-code.org.
Y.K. has been a developer of the code since 2021.

TABLE OF CONTENTS

LIST OF ILLUSTRATIONS

LIST OF TABLES

Chapter 1

PROLOGUE: ASTROPHYSICAL PLASMAS IN STRONG GRAVITY

Compact objects such as black holes and neutron stars can harbor the strongest magnetic field in the Universe. When a compact object interacts with astrophysical plasma surrounding it, this extreme magnetic field can trigger a variety of observable electromagnetic bursts. Deciphering these electromagnetic transient signals provide a unique window for probing an unknown realm of physics in strong gravity and of dense matter, which cannot be reproduced in any terrestrial laboratories.

Following the first detection of gravitational waves from a merging binary black hole (B. P. Abbott et al., 2016), the past decade has witnessed unprecedented advances in relativistic astrophysics, including the first multi-messenger observation of a binary neutron star merger (B. P. Abbott et al., 2017) and the first direct imaging of a black hole (Akiyama et al., 2019). However, many aspects of the high-energy astrophysical phenomena, such as fast radio bursts and gamma ray bursts, which are thought to be associated with compact objects and their interactions with the surrounding plasma via hydrodynamic or magnetic processes, still remain unclear.

As we expect a larger number of and more precise observations of such electromagnetic bursts from upcoming next-generation detectors and space missions, improved theoretical models are required in order to properly interpret the observed features and to understand physical properties of compact objects and their host environment. Since the physics underlying these systems — general relativity, electromagnetism, hydrodynamics — are described with highly complex and nonlinear governing equations, numerical simulations on supercomputers are often drawn to study a particular scenario of our interest. Numerical relativity and computational relativistic astrophysics, products of scientific efforts to accurately and efficiently immitate those physical systems on computers, provides an ideal set of toolkits for this purpose.

This thesis collects three independent studies on numerical modeling of astrophysical plasmas around compact objects. We develop a new computational method for and present two global, large-scale numerical simulations particularly focusing on high-energy electromagnetic transients originating from black holes and neutron stars.

In Chapter 2, we present a new numerical method for relativistic electrodynamics.

The key idea is hybridizing the discontinuous Galerkin method with the shock-capturing finite difference method to selectively combine the merits of each approaches. This hybrid method achieves spectral convergence in smooth regions while robustly resolving sharp dissipative features such as current sheets and reconnection points. Our new approach can perform two to three times better efficiently than conventional simulation techniques, potentially up to ten times in an ideal setting.

A black hole flying through a magnetized medium can be related to many astrophysical contexts, including common envelope phase, wind-fed X-ray binaries, or a recoiled remnant of a binary black hole merger in a gaseous environment. In Chapter 3, we present 3D general relativistic magnetohydrodynamics simulations of the Bondi-Hoyle-Lyttleton accretion onto a spinning black hole when the magnetic field of the incoming wind is inclined relative to the spin of the black hole. This study brings a detailed 3D picture of an accreting black hole in a magnetized wind, and sheds light on electromagnetic transients from compact binary merger remnants in a gaseous environment.

When a compressive mode is excited within a compact object magnetosphere, the resulting outgoing waves can evolve into strongly radiative shockwaves. This particular mechanism is thought to produce *monster shocks*, the strongest shockwaves in the Universe, which can power electromagnetic bursts in various wavelengths. In Chapter 4, we show that strong disturbances in the circumbinary magnetosphere during a neutron star–black hole merger develop into monster shocks within milliseconds following the merger. The remnant black hole dissipates the post-merger magnetosphere via magnetic reconnection and launches a magnetized wind resembling that of pulsars. This study is the first self-contained demonstration of the monster shock formation as well as the emergence of a transient ‘black hole pulsar’ state from a compact binary merger, unveiling a novel type of shock-powered and reconnection-driven transient associated with merging compact objects.

Chapter 2

A HYBRID NUMERICAL METHOD FOR GENERAL RELATIVISTIC FORCE-FREE ELECTRODYNAMICS

Kim, Yoonsoo et al. (2024). "General relativistic force-free electrodynamics with a discontinuous Galerkin-finite difference hybrid method". In: *Physical Review D* 109.12, p. 123019. DOI: 10.1103/PhysRevD.109.123019. arXiv: 2404.01531. URL: https://journals.aps.org/prd/abstract/10.1103/PhysRevD.109.123019.

Relativistic plasmas around compact objects can sometimes be approximated as being force-free. In this limit, the plasma inertia is negligible and the overall dynamics is governed by global electric currents. We present a novel numerical approach for simulating such force-free plasmas, which allows for high accuracy in smooth regions as well as capturing dissipation in current sheets. Using a high-order accurate discontinuous Galerkin method augmented with a conservative finite-difference method, we demonstrate efficient global simulations of black hole and neutron star magnetospheres. In addition to a series of challenging test problems, we show that our approach can — depending on the physical properties of the system and the numerical implementation — be up to 10× more efficient than conventional simulations, with a speedup of 2–3× for most problems we consider in practice.

2.1 Introduction

Compact objects such as neutron stars and black holes can feature some of the strongest magnetic fields in the universe. Under these conditions, the environments surrounding them can be filled with a highly conducting plasma. The plasma dynamics of these magnetospheres are thought to be responsible for several observable transients in the radio (Bochenek et al., 2020; Lyubarsky, 2020; Mahlmann, Philippov, Levinson, et al., 2022) and X-ray (Thompson and Duncan, 1995; Kaspi et al., 2003; Beloborodov, 2013; Archibald et al., 2017; Tavani et al., 2021) bands. While the description of emission processes fundamentally necessitates modeling the relevant kinetic scales (Philippov, Cerutti, et al., 2015; A. Y. Chen and Beloborodov, 2017), the available energy budget as well as the presence of any dissipative or emitting region inside the magnetosphere is a result of the bulk dynamics. It is this latter aspect that our present work aims to advance. Since these scenarios are highly nonlinear, their effective description requires numerical approaches.

The global dynamics of the plasma is usually modeled under several simplifying assumptions. In a very strongly magnetized magnetosphere, the inertia of the plasma can approximately be neglected (Uchida, 1997; Gruzinov, 1999). In this force-free electrodynamics (FFE) state, the evolution of the system is governed largely by bulk currents, obtained via an effective closure of the Maxwell equations. It is important to point out that the main assumption—neglecting plasma inertia—can break down, e.g., during shock formation, as well as the absence of physically meaningful dissipation in reconnection regions. In this regime, the closest extension of force-free electrodynamics is magnetohydrodynamical (MHD) models, retaining a single-component plasma rest-mass density. MHD studies of relativistic magnetospheres are not commonly employed.[1] Instead, most studies adopt an FFE approach.

Recent examples include applications to magnetar quakes (Bransgrove, Beloborodov, and Y. Levin, 2020), nonlinear steepening of Alfvén waves (Yuan, Beloborodov, A. Y. Chen, and Y. Levin, 2020; Yuan, Beloborodov, A. Y. Chen, Y. Levin, et al., 2022), magnetar giant flares (Parfrey, Beloborodov, and Hui, 2013; Mahlmann, Akgün, et al., 2019; Carrasco, Viganò, et al., 2019; Mahlmann, Philippov, Mewes, et al., 2023), outbursts from gravitational collapse of a neutron star (Lehner et al., 2012),[2] and black hole and neutron star magnetospheres (Komissarov, 2004a; Spitkovsky, 2006; McKinney, 2006b; A. Y. Chen, Yuan, and Vasilopoulos, 2020; Carrasco and Shibata, 2020). Apart from isolated compact objects, force-free electrodynamics has also been employed in the context of jets from massive black hole mergers (Palenzuela, Garrett, et al., 2010; Palenzuela, Lehner, and Liebling, 2010) and potential electromagnetic precursor to gravitational wave events involving merger of compact objects (Alic et al., 2012; Palenzuela, Lehner, and Yoshida, 2010; Carrasco, Shibata, and Reula, 2021; Most and Philippov, 2020; Most and Philippov, 2022; Most and Philippov, 2023a; Most and Philippov, 2023b).

Several approaches have been adopted in the literature for numerically solving the FFE equations. Most commonly, either unlimited finite-difference (Spitkovsky, 2006; Kalapotharakos and Contopoulos, 2009; Palenzuela, Garrett, et al., 2010;

[1] See, e.g. Tchekhovskoy and Spitkovsky (2013) for a notable exception in neutron star magnetospheres.

[2] See also Nathanail, Most, and Rezzolla (2017) and Most, Nathanail, and Rezzolla (2018) for related studies in electrovacuum.

A. Y. Chen, Yuan, and Vasilopoulos, 2020; Carrasco and Reula, 2017) or conservative finite-volume schemes (Komissarov, 2002; Cho, 2005; Asano, Uchida, and Matsumoto, 2005; McKinney, 2006a; Yu, 2011; Etienne, Wan, et al., 2017; Most and Philippov, 2020; Mahlmann, Aloy, et al., 2021a) have been employed. These methods are robust, can easily capture strong gradients inside the magnetosphere, and work well with commonly employed mesh refinement techniques (Dubey et al., 2014). However, they come with a major drawback. Properly capturing wave solutions over long integration times, e.g., Alfvén waves (Yuan, Beloborodov, A. Y. Chen, and Y. Levin, 2020), requires a large number of grid points, especially when less accurate versions of finite-difference/volume schemes are being used. This prohibitively increases computational costs, especially for applications such as compact binary magnetospheres in which scale separations can span two orders of magnitude.

On the other hand, spectral-type methods such as the pseudospectral method offer exponential convergence for smooth solutions, providing a maximum in accuracy over computational cost. Several studies have made use of spectral schemes to solve the FFE equations (Parfrey, Beloborodov, and Hui, 2012; Petri, 2012; Cao, L. Zhang, and Sun, 2016). One serious limitation of spectral methods is the appearance of unphysical oscillations (Gibbs phenomenon) near a discontinuity or a large gradient e.g. current sheets, which are naturally present in compact object magnetospheres. Remedying these numerical instabilities requires special treatments such as filtering or a limiting procedure (Hesthaven and Warburton, 2007). In addition, globally spectral methods are not easily parallelizable, making it difficult to simulate physical scenarios with large scale separations.

To counteract this shortcoming, popular approaches in the literature focus on spectral element methods in which the computational domain is divided into non-overlapping spectral elements, communicating only with the directly neighboring elements through the element boundaries. This approach allows for highly parallelizable implementations while retaining the exponential convergence property for smooth solutions. A concrete example of this approach, a discontinuous Galerkin (DG) method, is gaining its popularity in computational fluid dynamics and astrophysics (e.g. Bugner et al., 2016; Zanotti, Fambri, Dumbser, and Hidalgo, 2015; Zanotti, Fambri, and Dumbser, 2015; Fambri et al., 2018; Reinarz et al., 2020; Deppe et al., 2022; Tichy et al., 2023; Dumbser, Zanotti, Gaburro, et al., 2024; Cernetic et al., 2024), as well as in FFE (Petri, 2015; Petri, 2016).

While a DG scheme naturally permits a discontinuity at the element boundary, without special care to suppress unphysical oscillations, it suffers from the same fate as globally spectral methods described above. Several strategies have been proposed in the DG literature, which are frequently referred to as *limiters*. Common types of DG limiters are implemented as direct manipulations on spectral coefficients, addition of artificial viscosity, or a flattening correction of the solution with respect to its average value within an element. We refer the reader to Zanotti, Fambri, Dumbser, and Hidalgo (2015) and Deppe, Hébert, et al. (2022) and references therein for the available types of DG limiters and related discussions.

DG limiters currently are not particularly accurate or reliable compared with corresponding finite-volume or finite-difference techniques, especially for curved meshes or relativistic applications (Deppe, Hébert, et al., 2022). A recently developed alternative strategy is to supplement the DG evolution with a more robust sub-element discretization, which has been mostly chosen to be finite volume (e.g. Dumbser, Zanotti, Loubère, et al., 2014; Zanotti, Fambri, Dumbser, and Hidalgo, 2015; Zanotti, Fambri, and Dumbser, 2015; Fambri et al., 2018; Vilar, 2019; Núñez-de la Rosa and Munz, 2018; Rueda-Ramírez, Pazner, and Gassner, 2022; Maltsev et al., 2023). Motivated by the idea of the a posteriori finite-volume limiting approach of Dumbser, Zanotti, Loubère, et al. (2014), the discontinuous Galerkin-finite difference (DG-FD) hybrid method was introduced by Deppe, Hébert, et al. (2022); see also Deppe et al. (2022) and Legred et al. (2023) for applications to relativistic fluid dynamics simulations.

Here we present a new numerical scheme and code for general-relativistic FFE simulations based on a discontinuous Galerkin discretization. Our motivation is twofold. First, we explore the suitability of the DG-FD hybrid approach to enable large-scale, parallel yet accurate numerical simulations, especially of compact binary magnetospheres. Second, since FFE on physical grounds has very localized regions of non-smoothness such as current sheets, these simulations serve as an ideal testbed to calibrate and assess the usefulness of the DG-FD hybrid approach. Our hybrid scheme also incorporates previously developed implicit-explicit time integration schemes by Pareschi and Russo (2005), which allows us to enforce a set of algebraic constraints present in the FFE system. This joint approach achieves high-order convergence in smooth regions while capturing discontinuous features such as magnetic reconnection points and current sheets.

This chapter is organized as follows. In Sec. 2.2, we briefly review Maxwell's equations in general relativity and introduce the formulation we adopt in this work.

We also discuss our strategy for maintaining the force-free conditions in simulations. In Sec. 2.3, we describe the numerical implementation of spatial discretization, time stepping, and the discontinuous Galerkin-finite difference hybrid solver. We present results from a set of test problems in Sec. 2.4, and conclude with a discussion of result in Sec. 2.5.

In this chapter, we adopt geometrized ($c = G = 1$) Heaviside-Lorentz units, where electric and magnetic fields have been rescaled by $1/\sqrt{4\pi}$ compared to Gaussian units. We use the abstract index notation using latin indices $(a, b, \cdots)$ for spacetime tensors, but reserve $\{i, j, k, \ldots\}$ for spatial tensors. We follow the sign convention of the Levi-Civita tensor from Misner, Thorne, and Wheeler (1973),

$$\varepsilon_{abcd} = \sqrt{-g}\,[abcd]\,, \tag{2.1}$$

where g is the determinant of spacetime metric and $[abcd] = \pm 1$ with $[0123] = +1$ is the flat-space antisymmetric symbol.[3]

2.2 General relativistic force-free electrodynamics

We begin by outlining the mathematical description used to numerically study magnetospheric dynamics. This includes a general relativistic formulation of electrodynamics in a curved spacetime, which is then specialized to the force-free case: general relativistic force-free electrodynamics (GRFFE).

2.2.1 Electrodynamics

The dynamics of electric and magnetic fields is governed by the Maxwell equations. In covariant form, they are given by

$$\nabla_b F^{ab} = \mathcal{J}^a \tag{2.2}$$

$$\nabla_b\, {}^*F^{ab} = 0 \tag{2.3}$$

where F^{ab} and ${}^*F^{ab} = \varepsilon^{abcd}F_{cd}/2$ are the electromagnetic field tensor and its dual, and $\mathcal{J}^a$ is the electric 4-current density.

For the standard 3+1 decomposition of the spacetime metric

$$ds^2 = -\alpha^2 dt^2 + \gamma_{ij}(dx^i + \beta^i dt)(dx^j + \beta^j dt), \tag{2.4}$$

where α is lapse, β^i is the shift vector, and γ_{ij} is the spatial metric, the normal to spatial hypersurfaces is given by

$$n^a = (1/\alpha, -\beta^i/\alpha), \quad n_a = (-\alpha, 0). \tag{2.5}$$

[3] Note that an opposite sign convention is sometimes adopted in the literature (e.g. Palenzuela, Lehner, and Yoshida, 2010; Palenzuela, 2013)

In terms of the normal vector n^a, electromagnetic field tensor F^{ab} and its dual ${}^*F^{ab}$ can be decomposed as

$$F^{ab} = n^a E^b - n^b E^a - \varepsilon^{abcd} B_c n_d, \tag{2.6}$$
$${}^*F^{ab} = -n^a B^b + n^b B^a - \varepsilon^{abcd} E_c n_d, \tag{2.7}$$

where

$$n_a E^a = n_a B^a = 0. \tag{2.8}$$

$E^a = (0, E^i)$ and $B^a = (0, B^i)$ are electric and magnetic fields in the frame of an Eulerian observer. One can read off E^a and B^a from F^{ab} using the following relations

$$E^a = F^{ab} n_b, \tag{2.9}$$
$$B^a = -\frac{1}{2}\varepsilon^{abcd} n_b F_{cd} = -{}^*F^{ab} n_b\,. \tag{2.10}$$

While analytically complete, Maxwell equations cannot be directly evolved numerically, as any violation of the divergence constraints (Eqs. (2.2) and (2.3) with $a = 0$) will break strong hyperbolicity of the system (Schoepe, Hilditch, and Bugner, 2018; Hilditch and Schoepe, 2019). This can be avoided by either using constrained transport approaches (Evans and J. F. Hawley, 1988) or extending the system using effective Lagrange multipliers (Dedner et al., 2002). We here adopt the latter approach. The extended (or augmented) Maxwell equations (Komissarov, 2007; Palenzuela, 2013) are

$$\nabla_a (F^{ab} + g^{ab}\psi) = -\mathcal{J}^b + \kappa_\psi n^b \psi \tag{2.11}$$

$$\nabla_a ({}^*F^{ab} + g^{ab}\phi) = \kappa_\phi n^b \phi \tag{2.12}$$

$$\nabla_a \mathcal{J}^a = 0 \tag{2.13}$$

where auxiliary scalar fields ψ and ϕ propagate divergence constraint violations of electric field and magnetic field. κ_ψ and κ_ϕ are damping constants, leading to an exponential damping of the constraints in the characteristic timescales $\kappa^{-1}_{\psi,\phi}$.

Performing a standard 3+1 decomposition of the extended Maxwell's equations (2.11)–(2.13) using the normal vector n^a and the spatial projection operator $h^a{}_b \equiv \delta^a{}_b + n^a n_b$, we get

$$(\partial_t - \mathcal{L}_\beta) E^i - \varepsilon^{ijk}_{(3)} D_j (\alpha B_k) + \alpha \gamma^{ij} D_j \psi = -\alpha J^i + \alpha K E^i, \tag{2.14a}$$

$$(\partial_t - \mathcal{L}_\beta)B^i + \varepsilon_{(3)}^{ijk} D_j(\alpha E_k) + \alpha\gamma^{ij} D_j\phi = \alpha K B^i, \tag{2.14b}$$

$$(\partial_t - \mathcal{L}_\beta)\psi + \alpha D_i E^i = -\alpha\kappa_\psi\psi + \alpha q, \tag{2.14c}$$

$$(\partial_t - \mathcal{L}_\beta)\phi + \alpha D_i B^i = -\alpha\kappa_\phi\phi, \tag{2.14d}$$

$$(\partial_t - \mathcal{L}_\beta)q + D_i(\alpha J^i) = \alpha q K, \tag{2.14e}$$

where $D_i = h^a{}_i \nabla_a$ is the spatial covariant derivative, K is the trace of extrinsic curvature, $q = -n_\mu \mathcal{J}^\mu$ is the electric charge density measured by an Eulerian observer, and $J^i = h^i{}_a \mathcal{J}^a$ is the spatial electric current density. Here we also defined the spatial Levi-Civita tensor associated with the spatial metric as

$$\varepsilon_{(3)}^{abc} \equiv n_d \varepsilon^{dabc} \,. \tag{2.15}$$

The Lie derivative along the shift vector applied to a spatial vector E^i is

$$\mathcal{L}_\beta E^i = \beta^j \partial_j E^i - E^j \partial_j \beta^i,$$

and same for B^i on the left hand side of Eq. (2.14), while it is simply a directional derivative (e.g. $\mathcal{L}_\beta(q) = \beta^i \partial_i q$) when applied to a scalar variable.

Evolution equations (2.14) can be cast into conservative form

$$\partial_t \mathbf{U} + \partial_j \mathbf{F}^j = \mathbf{S}, \tag{2.16}$$

with evolved variables

$$\mathbf{U} = \sqrt{\gamma} \begin{bmatrix} E^i \\ B^i \\ \psi \\ \phi \\ q \end{bmatrix} \equiv \begin{bmatrix} \tilde{E}^i \\ \tilde{B}^i \\ \tilde{\psi} \\ \tilde{\phi} \\ \tilde{q} \end{bmatrix}, \tag{2.17}$$

fluxes

$$\mathbf{F}^j = \begin{bmatrix} -\beta^j \tilde{E}^i + \alpha(\gamma^{ij}\tilde{\psi} - \varepsilon_{(3)}^{ijk} \tilde{B}_k) \\ -\beta^j \tilde{B}^i + \alpha(\gamma^{ij}\tilde{\phi} + \varepsilon_{(3)}^{ijk} \tilde{E}_k) \\ -\beta^j \tilde{\psi} + \alpha \tilde{E}^j \\ -\beta^j \tilde{\phi} + \alpha \tilde{B}^j \\ \tilde{J}^j - \beta^j \tilde{q} \end{bmatrix}, \tag{2.18}$$

and source terms

$$\mathbf{S} = \begin{bmatrix} -\alpha\sqrt{\gamma}J^i - \tilde{E}^j\partial_j\beta^i + \tilde{\psi}(\gamma^{ij}\partial_j\alpha - \alpha\gamma^{jk}\Gamma^i_{jk}) \\ -\tilde{B}^j\partial_j\beta^i + \tilde{\phi}(\gamma^{ij}\partial_j\alpha - \alpha\gamma^{jk}\Gamma^i_{jk}) \\ \tilde{E}^k\partial_k\alpha + \alpha\tilde{q} - \alpha\tilde{\psi}(K + \kappa_\psi) \\ \tilde{B}^k\partial_k\alpha - \alpha\tilde{\phi}(K + \kappa_\phi) \\ 0 \end{bmatrix}, \tag{2.19}$$

where Γ^i_{jk} are the Christoffel symbols associated with the spatial metric. A prescription for the electric current density J^i (Ohm's law) needs to be supplied to close the system.

2.2.2 Force-free limit

In the magnetospheres of neutron stars and black holes, we expect copious production of electron-positron pairs (Goldreich and Julian, 1969). The resulting plasma will be highly conductive, effectively screening electric field components parallel to the magnetic field. In addition, the magnetization of the plasma will be very high, allowing us to consider the limit in which the Lorentz force density vanishes and the plasma becomes force-free.

The force-free conditions are given as

$$F^{ab}\mathcal{J}_b = 0, \tag{2.20}$$

$$^*F^{ab}F_{ab} = 0, \tag{2.21}$$

$$F^{ab}F_{ab} > 0. \tag{2.22}$$

In terms of E^i, B^i, q and J^i, these conditions are

$$qE^i + \varepsilon^{ijk}_{(3)}J_jB_k = 0, \tag{2.23}$$

$$E^aB_a = E^iB_i = 0, \tag{2.24}$$

$$B^2 - E^2 > 0, \tag{2.25}$$

where $E^2 = E_aE^a = E_iE^i$ and $B^2 = B_aB^a = B_iB^i$. The first condition (2.23) corresponds to the vanishing Lorentz force density, and the second one (2.24) shows the screening of electric field along magnetic field lines. The third condition (2.25) is called magnetic dominance, and violation of this constraint flags the breakdown of force-free electrodynamics; characteristic speeds associated with Alfvén modes become complex and Maxwell equations are no longer hyperbolic (Pfeiffer and MacFadyen, 2013). Physically, $E^2 \approx B^2$ means that the plasma drift speed approaches the speed of light, beyond which the FFE approximation breaks down.

The force-free conditions also give constraints on the electric current density. Eq. (2.23) gives J^i in the form

$$J^i = q\frac{\varepsilon_{(3)}^{ijk} E_j B_k}{B^2} + \frac{(J_l B^l)}{B^2} B^i, \tag{2.26}$$

which leaves the parallel component $J_l B^l$ undetermined. The first term on the right hand side of (2.26), the drift current, is perpendicular to both electric and magnetic fields and shows that electric charge moves collectively with the drift velocity $v_d = \varepsilon_{(3)}^{ijk} E_j B_k / B^2$.

Requiring Eq. (2.24) to always be satisfied, we obtain a closed form expression of the parallel current $J_l B^l$ as (McKinney, 2006a; Paschalidis and Shapiro, 2013)

$$J_l B^l = \epsilon_{(3)}^{ijk} \left(B_i D_j B_k - E_i D_j E_k \right) - 2 E^i B^j K_{ij}, \tag{2.27}$$

which reduces to

$$J_l B^l = B_i (\nabla \times B)^i - E_j (\nabla \times E)^j \tag{2.28}$$

in the special relativistic limit (Gruzinov, 1999).

The parallel current Eq. (2.27) contains the spatial derivatives of E and B, the dynamical variables that we evolve. Including these derivatives in the source terms changes the principal part of the Maxwell PDE system, and the resulting system of equations is not strongly hyperbolic (Pfeiffer and MacFadyen, 2013).

A straightforward way to keep the force-free conditions satisfied in numerical simulations is to algebraically impose Eq. (2.24) and (2.25) in the time evolution (Spitkovsky, 2006; Palenzuela, Garrett, et al., 2010; Petri, 2012; Parfrey, Beloborodov, and Hui, 2012; Cao, L. Zhang, and Sun, 2016; A. Y. Chen, Yuan, and Vasilopoulos, 2020; Mahlmann, Aloy, et al., 2021a). This commonly employed approach exactly ensures the force-free conditions, but reduces the numerical accuracy to first-order convergence in time.

As we aim to implement a higher-order numerical scheme for GRFFE, we consider an alternative strategy. We adopt the driver term approach first implemented in Alic et al. (2012) and Moesta et al. (2012) and applied in later studies (e.g. Most and Philippov, 2020; Most and Philippov, 2022). In this method, a stiff relaxation term is added to the electric current density J^i to continuously damp the violation of the force-free conditions. We adopt the following electric current density prescription (Most and Philippov, 2022)

$$J^i = q\frac{\varepsilon^{ijk}_{(3)}E_j B_k}{B^2} + \eta\left[\frac{E_j B^j}{B^2}B^i + \frac{\mathcal{R}(E^2 - B^2)}{B^2}E^i\right], \tag{2.29}$$

where $\mathcal{R}(x) \equiv \max(x, 0)$ is the rectifier function and η is a relaxation parameter. The parallel current consists of the terms in the square bracket in Eq. (2.29), each being proportional to the violation of the force-free conditions (2.24) and (2.25). They are coupled to the evolution of electric field and drive the solution to the force-free limit with the characteristic damping time scale η^{-1}. The limiting case $\eta \to \infty$ corresponds to the ideal force-free limit.

A caveat to the FFE simulations with a parallel electric current is that the energy loss from an Ohmic dissipation $J_i E^i$ is removed out from and no further tracked in simulations; therefore, total electromagnetic energy is not conserved.[4] While numerical dissipation will also contribute to the energy loss, the amount of energy dissipation in current sheets (corresponding to the rectifier term in Eq. (2.29)) dominates, albeit likely at a different rate compared to a full kinetic reconnection model (e.g. Cerutti, Philippov, Parfrey, et al., 2015; Philippov, Cerutti, et al., 2015).

2.3 Numerical implementation

In this section, we describe the details of our numerical scheme and its implementation. We present our method of spatial discretization in Sec. 2.3.1, time integration in Sec. 2.3.2, and the adaptive discontinuous Galerkin-finite difference hybrid solver in Sec. 2.3.3. Our numerical scheme described here is implemented in the open source numerical relativity code `SpECTRE` (Deppe, Throwe, et al., 2025).

2.3.1 Domain decomposition and spatial discretization

The computational domain typically used in astrophysics or numerical relativity simulations is simple enough to be decomposed into a set of non-overlapping deformed cubes. We divide the domain into these deformed cubes, which are called subdomain elements (hereafter simply *elements*). Neighboring elements share their boundaries at an element interface between them.

Within each element, a spectral expansion can be performed to represent a field of interest. We also need to define a prescription for handling boundary corrections

[4] In a MHD model, it is captured as the same amount of increase in the internal (thermal) energy of the plasma.

from element interfaces. This family of numerical methods is broadly called spectral element methods (Kopriva, 2009). We choose to adopt the nodal discontinuous Galerkin discretization (Hesthaven and Warburton, 2007), so our approach is formally referred to as a discontinuous Galerkin spectral element method (DG-SEM), which is often simply called a discontinuous Galerkin (DG) method.

Each element is mapped to a reference cube spanning $\{\xi^1, \xi^2, \xi^3\} \in [-1,1]^3$ in the reference coordinate system $\{\xi^i\}$. A coordinate map $x^i(\xi^j)$ relates the reference coordinates ξ^j to physical coordinates x^i. A set of collocation points $\{\xi^1_i, \xi^2_j, \xi^3_k\}$ are chosen to represent the solution

$$u(\xi) = \sum_{i,j,k} u_{i,j,k} \phi_{i,j,k}(\xi) \tag{2.30}$$

where $u_{i,j,k} = u(\xi^1_i, \xi^2_j, \xi^3_k)$ is the value of the solution at the collocation point $(\xi^1_i, \xi^2_j, \xi^3_k)$, and $\phi_{i,j,k}(\xi)$ is the nodal basis function

$$\phi_{i,j,k}(\xi^1_l, \xi^2_m, \xi^3_n) = \left\{ \begin{matrix} 1, & \text{for } i = l, j = m, k = n \\ 0, & \text{otherwise} \end{matrix} \right\}. \tag{2.31}$$

We use the tensor product basis

$$\phi_{i,j,k}(\xi) = l_i(\xi^1)\, l_j(\xi^2)\, l_k(\xi^3) \tag{2.32}$$

where $l_d(x)$ is the 1D Lagrange polynomial interpolating collocation points along the d-th axis. We choose to use an isotropic DG mesh with the same polynomial degree N for each spatial dimension. The resulting nodal expansion of the solution is

$$u(\xi) = \sum_{i=0}^{N} \sum_{j=0}^{N} \sum_{k=0}^{N} u_{i,j,k}\, l_i(\xi^1) l_j(\xi^2) l_k(\xi^3). \tag{2.33}$$

The solution (2.33) can be also represented in a modal form

$$u(\xi) = \sum_{p=0}^{N} \sum_{q=0}^{N} \sum_{r=0}^{N} c_{p,q,r}\, L_p(\xi^1) L_q(\xi^2) L_r(\xi^3). \tag{2.34}$$

where $L_p(x)$ is the Legendre polynomial of degree p. See also Teukolsky (2016) for a detailed derivation of formulating the DG scheme in a curved spacetime.

In this article, we denote a scheme using the N-th degree polynomial basis (i.e. $N+1$ collocation points) in each spatial dimension as a DG-P_N scheme. For instance, a DG-P_5 scheme uses 6^3 collocation points in each element and a solution is approximated as a fifth degree polynomial in each spatial direction. When the solution is smooth, a DG-P_N scheme exhibits $O(L^{N+1})$ spatial convergence where L is the spatial size of an element.

We mainly use a DG-P_5 scheme, although we present results for different DG orders where necessary. We use the Legendre-Gauss-Lobatto collocation points with the mass lumping approximation (Teukolsky, 2015a). For a reduced aliasing error, an exponential filter is applied to rescale the modal coefficients $c_{p,q,r}$ in Eq. (2.34):

$$c_{p,q,r} \to c_{p,q,r} \prod_{n=\{p,q,r\}} \exp\left[-a\left(\frac{n}{N}\right)^{2b}\right] \tag{2.35}$$

after every DG time (sub)step. We use $a = 36$ and $b = 50$, which effectively zeros only the highest mode ($i = N$) and leaves other modes intact. Filtering out the highest mode reduces expected spatial converge of a DG-P_N scheme from $O(L^{N+1})$ to $O(L^N)$. We note that this is a common practice adopted in spectral methods for curing aliasing and has marginal effects on capturing discontinuities, since typically a Gibbs phenomenon near a discontinuity excites not only the highest mode but multiple high modes simultaneously.

2.3.2 Time integration

Based on the spatial discretization presented in the previous section, evolution equations can be integrated over time using the method of lines.

The maximum admissible time step size for a DG-P_N scheme is (Cockburn and Shu, 2001; Dumbser, Zanotti, Loubère, et al., 2014)

$$\Delta t \leq \frac{L}{\lambda_{\max}(2N+1)} \frac{c}{D} \tag{2.36}$$

where L is the minimum (Cartesian) edge length of an element, $\lambda_{\max}$ is the maximum characteristic speed inside the element, c is a stability constant specific to a time stepper, which is usually of order unity,[5] and D is the number of spatial dimensions.

However, usage of a nontrivial coordinate map $x(\xi)$ and a complex geometry of elements deforms the spatial distribution of grid points, and an actual upper bound can differ from Eq. (2.36). As a practical strategy, we adopt the following expression

$$\Delta t = f \frac{(\Delta x)_{\min}}{\lambda_{\max}} \frac{c}{D} \tag{2.37}$$

[5]For example, the classic 4th-order Runge-Kutta method has $c \approx 1.39$ (Hairer, Nørsett, and Wanner, 1993).

for the DG time step size, where $(\Delta x)_{\min}$ is the minimum grid spacing between DG collocation points in physical coordinates and f is the CFL factor.

In order to keep the force-free constraint violations as small as possible during evolution, we aim to use a large value of the damping coefficient η for the driver term in Eq. (2.29), possibly up to $\eta\Delta t \gtrsim 10$. This implies that the characteristic time scale of constraint damping η^{-1} is smaller than the time step size, which introduces stiffness in evolution equations and makes explicit time integration unstable unless an unreasonably small time step is used.

To address the stiffness from rapid constraint damping, we adopt the implicit-explicit (IMEX) time stepping technique. In particular, we make use of the IMEX-SSP3(4,3,3) scheme by Pareschi and Russo (2005), which is third order in time. In this IMEX approach, we evolve all quantities explicitly using a standard 3rd-order Runge-Kutta scheme, and treat only the stiff part of the source terms (2.19) implicitly. Specifically, in the evolution of electric fields this requires us to solve the following nonlinear algebraic equation at all substeps,

$$E^i = (E^i)^* - \alpha\eta\Delta t' \left[\frac{E_j B^j}{B^2} B^i + \frac{\mathcal{R}\left(E^2 - B^2\right)}{B^2} E^i \right] \tag{2.38}$$

where $(E^i)^*$ are provided values and $\Delta t'$ is an IMEX-scheme-dependent corrector step size. When $E^2 < B^2$, the solution to this equation is analytical whereas in general cases we employ a three-dimensional Newton-Raphson solver with a specific initial guess.

In addition to the stiff electric current, we also apply the IMEX time integration to the hyperbolic divergence cleaning parts to ensure stability,

$$\psi = \psi^* - \kappa_\psi \Delta t' \psi, \tag{2.39}$$

$$\phi = \phi^* - \kappa_\phi \Delta t' \phi, \tag{2.40}$$

which are linear equations and have exact analytic inversions.

Because of the simplicity of the implicit equations in our evolution system, the cost overhead from using an IMEX scheme is less than 5% of the total runtime. Being able to use much larger time steps more than compensates for this.

2.3.3 The discontinuous Galerkin-finite difference hybrid method

This section describes our implementation of the DG-FD hybrid solver for GRFFE equations. We closely follow the original implementation of Deppe, Hébert, et al.

(2022), which was designed for GRMHD, with several improvements and adaptations.

Overview of the algorithm

Consider an element performing a time step on the DG grid. After each substep of the time integrator, the candidate solution is monitored by the *troubled cell indicator* (TCI) to check if the solution is admissible on the DG grid. If it is admissible, we continue with the updated solution on the DG grid. If the candidate solution is inadmissible, the troubled cell indicator is flagged, we undo the DG substep, project the DG solution onto the sub-element FD grid, then repeat the substep using the FD solver. Evolution on the FD grid proceeds in a similar way; after every time step the solution gets monitored by the troubled cell indicator, which determines whether the solution needs to stay on the FD grid or it is admissible on the DG grid. If the candidate solution looks admissible on the DG grid, the solution is projected back to the DG grid and the evolution proceeds using the DG solver.

An optimal number of sub-element finite-difference grid points for a DG-P_N scheme is $2N + 1$ (Dumbser, Zanotti, Loubère, et al., 2014). We follow such a prescription, and an element with $(N + 1)^D$ collocation points on the DG grid is switched to $(2N + 1)^D$ FD cells with a uniform grid spacing $\Delta\xi^i = 2/(2N + 1)$ in the reference coordinates.

At the code initialization phase, all physical quantities are evaluated on the FD grid to avoid potential spurious oscillations arising from a spectral representation of the initial data. Next, each element projects evolved variables onto the DG grid, then either switches to the DG grid or stays on the FD grid depending on the decision made by the troubled cell indicator.

The projection algorithm of scalar and tensor quantities between DG and FD grids is described in detail in Deppe, Hébert, et al. (2022). We use a general sixth-order accurate interpolation scheme. Since the scheme is general and does not respect the physical constraints,[6] repeated applications (i.e., switching back and forth between DG and FD too frequently) can introduce spurious errors in the solution. To suppress this behavior, we need to design the troubled cell indicator to apply tighter criteria when switching back from FD to DG grid.

[6]For example, the interpolation scheme between the DG and FD grids does not strictly preserve the force-free conditions or the divergence (Gauss) constraints.

Finite difference solver

Evolution on the finite-difference grid is performed using a conservative finite-difference scheme (Shu and Osher, 1988; Shu and Osher, 1989). For an element using a DG-P_N scheme, we divide the reference coordinate interval $[-1, 1]$ into $2N + 1$ finite-difference cells and project a solution from the DG grid onto cell-centered values $\{U_{\hat{\imath}}\}$. A flux-balanced law (2.16) is discretized as

$$\frac{dU_{\hat{\imath}}}{dt} + \left(\frac{\partial \xi^k}{\partial x^j}\right) \frac{\hat{F}^j_{\hat{\imath}+1/2} - \hat{F}^j_{\hat{\imath}-1/2}}{\Delta \xi^k} = S(U_{\hat{\imath}}) \tag{2.41}$$

where we used hat indices to label FD cells and plain indices to label spatial directions.

Computation of a numerical flux $\hat{F}^j_{\hat{\imath}+1/2}$ is dimensionally split, and closely follows that of the ECHO scheme (Del Zanna, Zanotti, et al., 2007). At the left and right sides of the FD cell interface $x_{\hat{\imath}+1/2}$, evolved variables are reconstructed using their cell-centered values $\{U_{\hat{\imath}}\}$. In our implementation, densitized electric current density $\tilde{J}^i$ is also reconstructed to compute fluxes associated with $\tilde{q}$ (see also Palenzuela, 2013).

Once face-centered values $U^{L,R}_{\hat{\imath}+1/2}$ are reconstructed, the interface Riemann flux $F^*_{\hat{\imath}+1/2}$ is computed using the Rusanov (local-Lax-Friedrichs) flux formula (Rusanov, 1962). Since the principal part of our equations is linear, this solver will reduce to the exact solution (see Dedner et al., 2002).

In order to achieve high-order accuracy, a high-order derivative corrector is added to the interface Riemann flux to obtain the final numerical flux:

$$\hat{F}_{\hat{\imath}+1/2} = F^*_{\hat{\imath}+1/2} - G^{(4)}_{\hat{\imath}+1/2}. \tag{2.42}$$

The original ECHO scheme uses the Riemann fluxes from cell interfaces (e.g. $F^*_{\hat{\imath}\pm 3/2}$) for the higher-order correction term $G^{(4)}_{\hat{\imath}+1/2}$. Since we do not employ a constrained-transport algorithm requiring a consistent and fixed stencil, we opt for simpler cell-centered fluxes (e.g., $F_{\hat{\imath}\pm 1}$) for a more compact stencil and reduced amount of data communications (see Nonomura and Fujii, 2013; Y. Chen, Tóth, and Gombosi, 2016).

For the simulations presented in this work, we use the WENO5-Z reconstruction with the nonlinear weight exponent $q = 2$ (Borges et al., 2008). The high-order finite-difference corrector is currently implemented only on Cartesian meshes. We therefore use it for all of our one-dimensional test problems, where we assess numerical convergence of the scheme, and defer to future work its applications in multi-dimensional contexts. Consistent with previous assessments, we find it sufficient to use only a fourth-order accurate derivative correction when combined with WENO5-Z (Most, Papenfort, and Rezzolla, 2019).

Troubled cell indicator

In order to decide when to switch between DG and FD grids, our numerical scheme requires a robust criterion to identify regions of non-smoothness. Such an approach somewhat shares its idea with popular adaptive-mesh-refinement criteria. These criteria are inherently problem dependent, and an optimal design of the troubled cell indicator is at the heart of the DG-FD hybrid method. Requirements on the indicator include

(i) A relatively low computational cost

(ii) Early and robust detection of spurious oscillations developing on the DG grid.

(iii) Being unflagged as soon as the oscillation no longer exists, so that evolution can be performed by a more efficient DG solver.

A solution approximated with an N-th degree polynomial on the DG grid has nodal and modal representations where $L_p(x)$ is the Legendre polynomial of degree p. Motivated by the idea of the modal shock indicator devised by Persson and Peraire (2006), we adopt the oscillation detection criterion

$$\sqrt{\frac{\sum_i \hat{u}_i^2}{\sum_i u_i^2}} > (N+1-M)^{-\alpha}, \tag{2.43}$$

where $\hat{u}$ is the solution with the lowest M modes filtered out i.e.

$$\hat{u}(\xi) = \sum_{p=M}^{N} \sum_{q=M}^{N} \sum_{r=M}^{N} c_{p,q,r} \, L_p(\xi^1) L_q(\xi^2) L_r(\xi^3), \tag{2.44}$$

and the summations $\sum_i$ in Eq. (2.43) with the nodal values $u_i, \hat{u}_i$ are performed over all DG grid points. The exponent α in the criterion (2.43) controls the sensitivity of the indicator. Since we filter out the highest mode on the DG grid, the troubled cell indicator needs to use $M \geq 2$. We use $M = 3$ for the troubled cell indicator, effectively monitoring power from the second and third highest modes. Empirically we find that $M \lesssim \lfloor (N+1)/2 \rfloor$ provides robust detections of discontinuities without the indicator being excessively triggered. We use $\alpha = 4.0$ following Deppe, Hébert, et al. (2022) and Deppe et al. (2022).

To avoid an element switching back and forth between DG and FD grid in an unnecessarily frequent manner, we use $\alpha' = \alpha + 1$ when an element is evolving on FD grid. The tighter bound α' ensures an extra smoothness of solution when the grid is switched back to DG, preventing it from switching again to FD within only a few time steps.

Depending on the specific type of an evolved system, one may consider additional physical admissibility criteria (e.g. positivity of the mass density in the case of hydrodynamics) for the troubled cell indicator. Since the only physical constraints in our evolution system, the force-free conditions, are handled by the stiff parallel electric current, we do not impose any physics-motivated criteria.

In our implementation of the DG-FD hybrid scheme for GRFFE, we adopt only one criterion for the troubled cell indicator: application of the modal sensor (2.43) to the magnitude of $\tilde{B}^i$. While it looks somewhat oversimplified that the information of a single scalar quantity is used for monitoring a system with nine evolution variables $\{\tilde{E}^i, \tilde{B}^i, \tilde{\psi}, \tilde{\phi}, \tilde{q}\}$, we show in Sec. 2.4 that it is capable of detecting troubled elements in a satisfactory manner.

2.3.4 Outer boundary condition

In 3D simulations, the outer boundary of the computational domain is usually placed far out to avoid spurious boundary effects leaking into the internal evolution. Still, in order to suppress potential unphysical noise or reflections at the outer boundary, we implement a no-incoming Poynting flux boundary condition as follows. The evolved variables at the outer boundary $\mathbf{U}_{\text{out}} = (\tilde{E}^i, \tilde{B}^i, \tilde{\psi}, \tilde{\phi}, \tilde{q})_{\text{out}}$ are prescribed as follows. First, we copy the values of $\{\tilde{E}^i, \tilde{B}^i, \tilde{q}\}$ from the outermost grid points. Then, if the Poynting flux is pointing inward, we set $(\tilde{E}^i)_{\text{out}}$ to zero. Divergence cleaning scalar fields $(\tilde{\psi})_{\text{out}}$ and $(\tilde{\phi})_{\text{out}}$ are always set to zero.[7] On the DG grid, $\mathbf{U}_{\text{out}}$ is fed as an external state when computing the boundary correction terms. On the FD grid, ghost zones are filled with $\mathbf{U}_{\text{out}}$ during the FD reconstruction step.

[7]Normally, the level of errors associated with the divergence cleaning part (ψ, ϕ) is much smaller than that of the physical variables (E^i, B^i, q). Spurious reflections, if any, in the divergence cleaning parts are subdominant to Poynting fluxes transmitting through the outer boundaries.

Table 2.1: Simulation setup for 1D tests in Sec. 2.4.1. Grid resolution is increased with $n = 0$ (Low), $n = 1$ (Med), and $n = 2$ (High). For the FFE breakdown problem, we use $n = 3$ as a reference solution. Each resolution, if all elements are switched to FD, is equivalent to 352×2^n finite-difference grid points along the x axis.

	Domain size ($\times[-0.1, 0.1]^2$)	DG Grid points ($\times 6^2$)	η	CFL factor	Δt ($\times 2^{-n}$)
Fast wave	$[-0.5, 1.5]$	(192×2^n)	10^6	0.3	9.22×10^{-4}
Alfvén wave	$[-1.5, 1.5]$				1.38×10^{-3}
FFE breakdown	$[-0.5, 0.5]$				4.61×10^{-4}

2.4 Results

In this section, we test and assess our implementation of the DG-FD hybrid method for evolving GRFFE equations with a suite of robust code validation problems. We perform 1D tests in Sec. 2.4.1, curved spacetime tests with black holes in Sec. 2.4.2, and pulsar magnetosphere tests in Sec. 2.4.3. We also discuss accuracy and efficiency aspects of the DG-FD hybrid method in Sec. 2.4.4.

2.4.1 One-dimensional test problems

One-dimensional test problems evolve initial data that only has dependence in the x direction. We use a computational domain consisting of a single element along the y and z axes, and impose periodic boundary condition on those directions. Our lowest grid resolution has 32 elements along the x axis, resulting in 192 DG grid points. To facilitate comparisons with other results available in the literature, we note that this resolution is equivalent to 352 grid points if all elements are switched to an FD grid. The number of elements along the x axis is increased by a factor of two to run medium (64 elements) and high (128 elements) resolutions. Dirichlet boundary conditions are applied at both ends of the x axis. We use the CFL factor 0.3 and parallel conductivity $\eta = 10^6$. Simulation setups are summarized in Table 2.1.

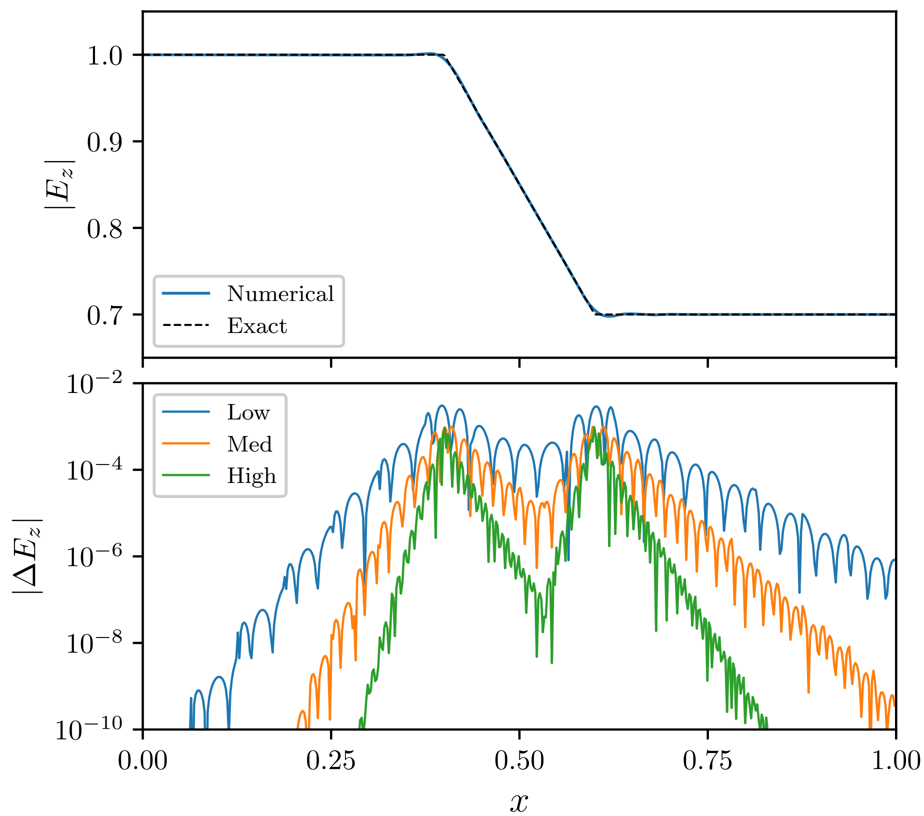

Figure 2.1: Fast wave at $t = 0.5$. Top: comparison between the exact solution and a numerical solution with the lowest grid resolution. Bottom: error of E_z for three different grid resolutions.

Fast wave

Originally due to Komissarov (2002), this test problem evolves a pure fast mode propagating in an electrovacuum. The initial profile

$$
\begin{aligned}
B^x &= 1.0, \\
B^y &= \left\{ \begin{array}{ll} 1.0 & \text{if } x < -0.1 \\ -1.5x + 0.85 & \text{if } -0.1 < x < 0.1 \\ 0.7 & \text{if } x > 0.1 \end{array} \right\}, \\
B^z &= 0, \\
E^x &= 0, \;\; E^y = 0, \;\; E^z = -B^y,
\end{aligned} \tag{2.45}
$$

advects to the $+x$ direction with the wave speed $\mu = 1$. The analytic solution is $Q(x,t) = Q(x-t,0)$ for any physical quantity Q.

As shown in Figure 2.1, our scheme shows good convergence in flat regions with increasing grid resolution. We observe that the accuracy and numerical convergence

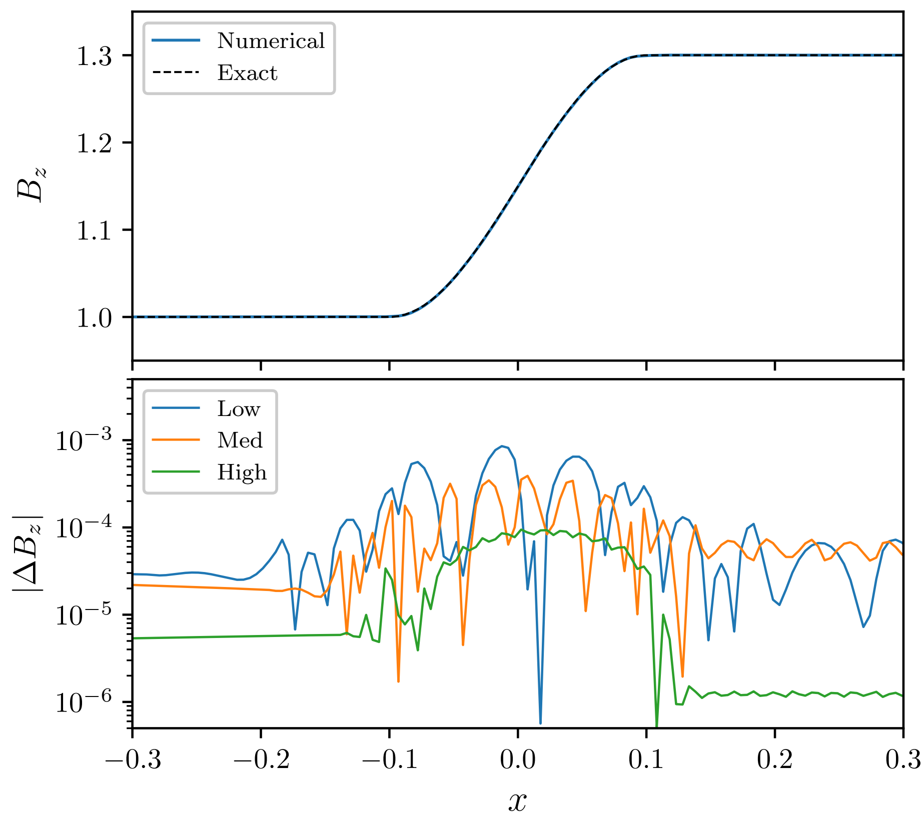

Figure 2.2: Stationary Alfvén wave at $t = 2.0$. Same plot description as Fig. 2.1.

of the solution is substantially lost around two kinks present in the initial data (corresponding to $x = 0.5 \pm 0.1$ in Fig. 2.1) at which spatial derivatives of fields are discontinuous.

Alfvén wave

The stationary Alfvén wave problem (Komissarov, 2004a) has a transition layer $|x| < 0.1$ that maintains a strong parallel current, and the accuracy of the test results essentially reflects how well a numerical scheme can maintain the force-free conditions.

In the rest frame of the wave, electric and magnetic fields are

$$
\begin{aligned}
B_x &= B_y = 1.0, \\
B_z &= \left\{ \begin{array}{ll} 1.0 & \text{if } x < -0.1 \\ 1.15 + 0.15 \sin(5\pi x) & \text{if } |x| < 0.1 \\ 1.3 & \text{if } x > 0.1 \end{array} \right\}, \qquad (2.46) \\
E_x &= -B_z, \;\; E_y = 0, \;\; E_z = 1.0.
\end{aligned}
$$

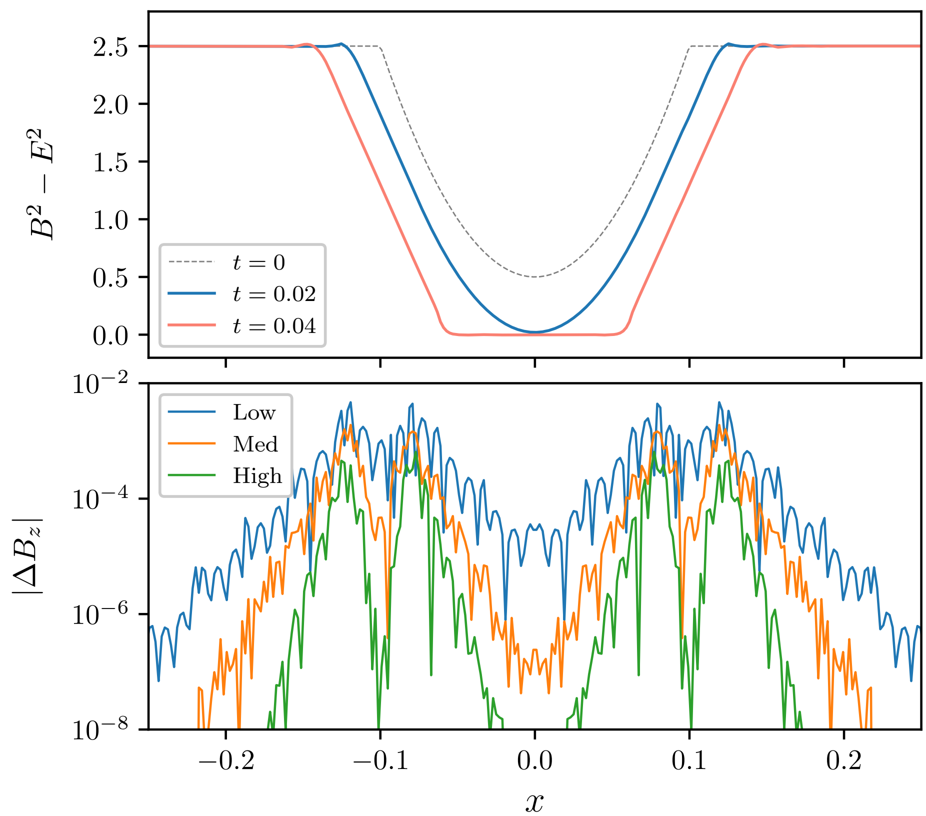

Figure 2.3: FFE breakdown problem. Top: initial data ($t = 0$) and a numerical solution with the lowest grid resolution at $t = 0.02$ and $t = 0.04$. Bottom: Error of B_z with respect to the reference solution.

The case with a nonzero wave speed $-1 < \mu < 1$ can be tested by performing an appropriate Lorentz boost to the initial conditions (2.46) (see e.g. Paschalidis and Shapiro, 2013).

We show the result at $t = 2.0$ in Figure 2.2. It needs to be noted that time derivatives of fields at $t = 0$, from the initial condition (2.46), vanish only if the parallel current $J_i B^i$ equals Eq. (2.27). In our approach, the region $|x| < 0.1$ initially develops a small transient until the stiff relaxation term becomes fully active within several time steps and effectively recovers the same value of $J_l B^l$. The amplitude of the initial transient rapidly decreases at higher grid resolutions. Owing to the higher-order accuracy of the discontinuous Galerkin discretization, our result shows good convergence and low amounts of grid dissipation.

FFE breakdown

The force-free electrodynamics breakdown problem, originally designed by Komissarov (2002), demonstrates that a state initially satisfying the force-free conditions can later develop into a state violating them. The initial state is

$$\begin{aligned} B^x &= 1, \\ B^y = B^z &= \left\{ \begin{array}{ll} 1 & \text{if } x < -0.1 \\ -10x & \text{if } -0.1 < x < 0.1 \\ -1 & \text{if } x > 0.1 \end{array} \right\}, \\ E^x &= 0, \;\; E^y = 0.5, \;\; E^z = -0.5. \end{aligned} \tag{2.47}$$

$B^2 - E^2$ decreases over time toward zero in the transition layer $|x| < 0.1$ and the magnetic dominance condition eventually breaks down.

Figure 2.3 shows numerical results. At $t \gtrsim 0.02$, the rectifier term restoring the $B^2 - E^2 > 0$ condition is switched on and robustly maintains the magnetic dominance at later times. Since this problem does not have a closed form solution, we perform an additional higher resolution run using 256 elements along the x axis and use it as a reference solution to check the convergence. Similar to the fast wave test, we note the loss of accuracy and numerical convergence near the kinks present in the solution.

2.4.2 Three-dimensional tests: Black hole magnetospheres

We perform a set of 3D tests in a curved spacetime using black hole magnetosphere problems. The grid structure of the computational domain is portrayed in Figure 2.4. A spherical shell spanning the radius $[r_{\text{in}}, r_{\text{out}}]$ is split into six cubed-sphere wedges, which are then further refined into elements. We use an equiangular coordinate map along angular directions and a logarithmic map along the radial direction.

Exact Wald solution

Wald (1974) found a stationary electrovacuum solution of Maxwell's equations in the Kerr spacetime. The solution for the 4-potential is given as

$$A_b = \frac{B_0}{2}[(\partial_\phi)_b + 2a(\partial_t)_b], \tag{2.48}$$

where B_0 is the field amplitude, ∂_t and ∂_ϕ are the Killing vector fields in time and azimuthal directions, and $a = J/M$ is the rotational parameter of the Kerr black

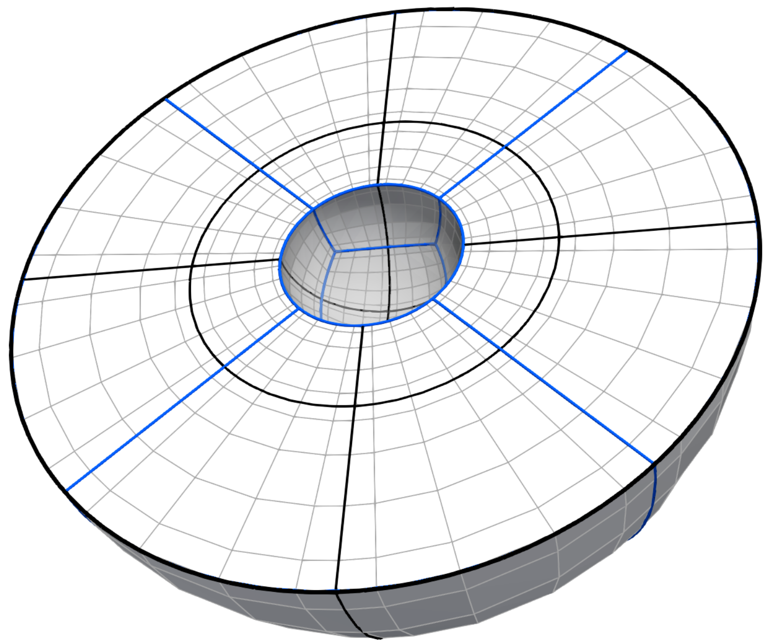

Figure 2.4: A half-cut illustration of the spherical grid used for black hole tests in Sec. 2.4.2. Blue lines show boundaries between the cubed-sphere wedges, where black lines show boundaries between each element (in this example, there are 8 elements in each wedge). The DG-P_5 mesh consisting of 6^3 Legendre-Gauss-Lobatto collocation points is shown with gray lines. The total number of elements in this example is $N_r \times N_\Omega = 2 \times 24$.

hole. See Appendix B for the explicit expressions of the Wald solution (2.48) in the spherical Kerr-Schild coordinates.

The Wald solution with $a = 0$ satisfies the force-free conditions outside the horizon. Electric and magnetic fields in Kerr-Schild coordinates are given by

$$
\begin{aligned}
&\tilde{B}^x = \tilde{B}^y = 0, \;\; \tilde{B}^z = B_0, \\
&\tilde{E}^x = -\frac{2MB_0 y}{r^2}, \;\; \tilde{E}^y = \frac{2MB_0 x}{r^2}, \;\; \tilde{E}^z = 0.
\end{aligned}
\tag{2.49}
$$

We evolve the initial condition (2.49) to $t = 5M$ and measure the L2 error norm

$$
L_2(v^i) \equiv \sqrt{\frac{1}{n}\sum_{k=1}^{n}\left[(v_k^x)^2 + (v_k^y)^2 + (v_k^z)^2\right]}, \tag{2.50}
$$

where $v^i = \tilde{B}^i_{\mathrm{numerical}} - \tilde{B}^i_{\mathrm{exact}}$ and n is the number of grid points. The inner domain boundary is placed at $r_{\mathrm{in}} = 1.99M$, at which no specific boundary condition is imposed. A Dirichlet boundary condition is imposed at the outer boundary $r_{\mathrm{out}} = 20M$. Conductivity of the magnetosphere is turned off by setting $\eta = 0$.

Table 2.2: Convergence tests of different DG-P_N schemes on the exact Wald solution (Sec. 2.4.2). For each level of grid resolution, we show the number of elements used in radial and angular directions, time step size $\Delta t/M$, L2 error norm of $\tilde{B}^i$ at $t = 5M$, and the measured order of numerical convergence.

	Resolution	Elements ($N_r \times N_\Omega$)	$\Delta t/M$	Error($\tilde{B}^i$)	Convergence order
DG-P_5	Low	1×6	2.90×10^{-2}	8.71×10^{-4}	
	Medium	2×24	1.15×10^{-2}	2.74×10^{-5}	4.99
	High	4×96	5.76×10^{-3}	4.11×10^{-8}	4.72
DG-P_7	Low		1.62×10^{-2}	1.23×10^{-5}	
	Medium		6.29×10^{-3}	1.51×10^{-7}	6.35
	High		3.14×10^{-3}	1.29×10^{-9}	6.87
DG-P_9	Low		1.03×10^{-2}	2.75×10^{-7}	
	Medium		3.95×10^{-3}	2.03×10^{-9}	7.08
	High		1.97×10^{-3}	8.04×10^{-12}	7.98

In Table 2.2, we show convergence studies for different orders of DG schemes $N = 5, 7, 9$. Measured convergence of DG-P_5 and DG-P_7 schemes is consistent with the order of DG discretization. A somewhat slower convergence of the DG-P_9 scheme can be attributed to other limiting factors such as the truncation error from time integration or the sixth-order interpolation from the initial FD grid to DG grid. In all test cases shown in Table 2.2, all elements stayed on the DG grid throughout the evolution.

Vacuum Wald problem

A time-dependent evolution of electromagnetic fields around a Kerr black hole can be simulated with the initial magnetic fields given by the Wald solution (2.48) where electric fields are set to zero at $t = 0$. The system reaches a steady state that depends on the spin of the black hole and electrical conductivity of the magnetosphere.

We first simulate the electrovacuum case. The background spacetime is the Kerr metric with $a = 0.999M$ in spherical Kerr-Schild coordinates. The electrical conductivity of the magnetosphere is switched off by setting $\eta = 0$. We use $N_r \times N_\Omega = 16 \times 96$ elements and use CFL factor 0.25, resulting in the time step size $\Delta t = 1.97 \times 10^{-3} M$. The inner domain boundary is located at $r_{\text{in}} = M$, and the no-incoming Poynting flux boundary condition (see Sec. 2.3.4) is applied at the outer domain boundary $r_{\text{out}} = 125M$.

The evolution reaches a stationary state after $t \gtrsim 80M$. We show the structure

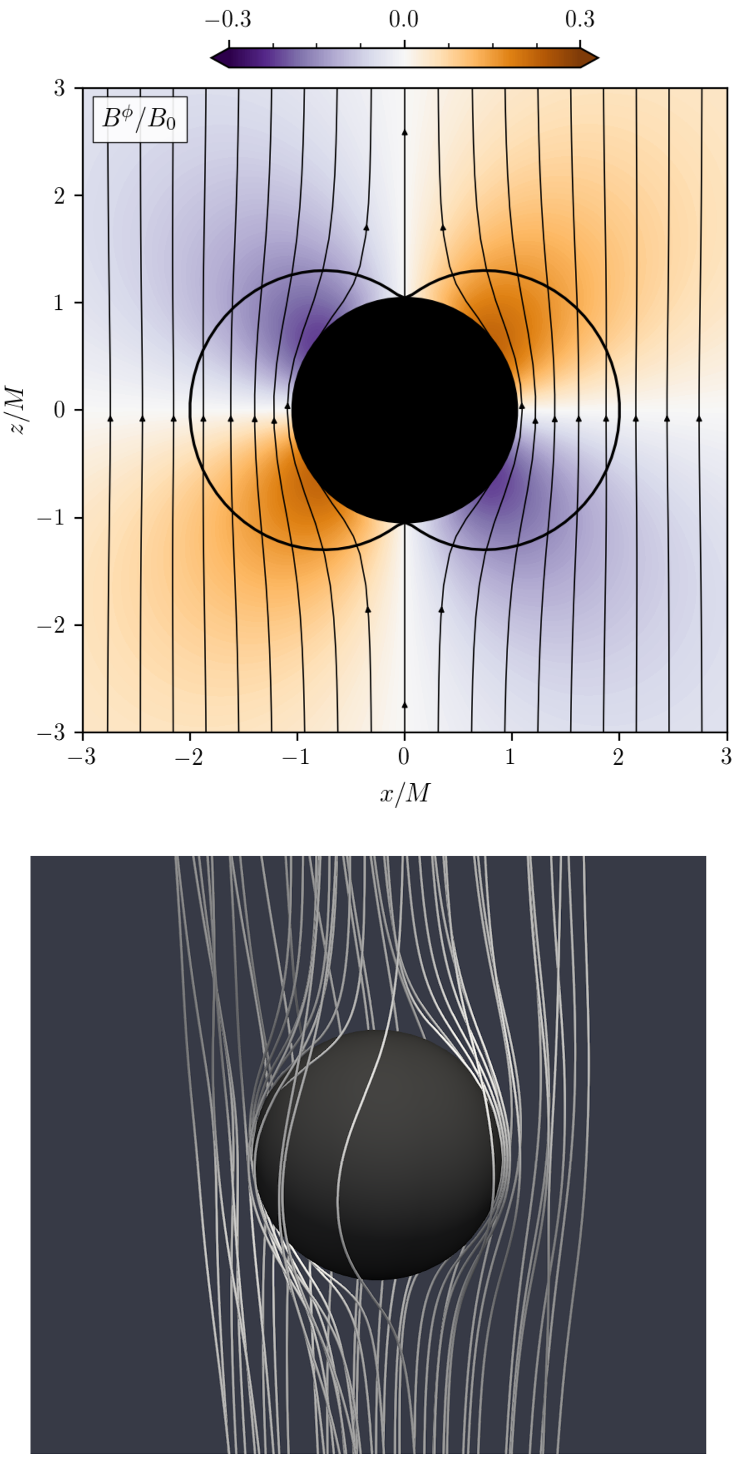

Figure 2.5: Vacuum Wald problem (at $t = 125M$) with black hole spin $a = 0.999M$. Top: Toroidal component of the magnetic field and its in-plane field lines on the meridional plane. We show the interior of the outer horizon $r = r_+$ with a black disk and the ergosphere with black solid lines. Bottom: A three-dimensional visualization illustrates the magnetic field lines (silver lines) expelled from the horizon (black sphere).

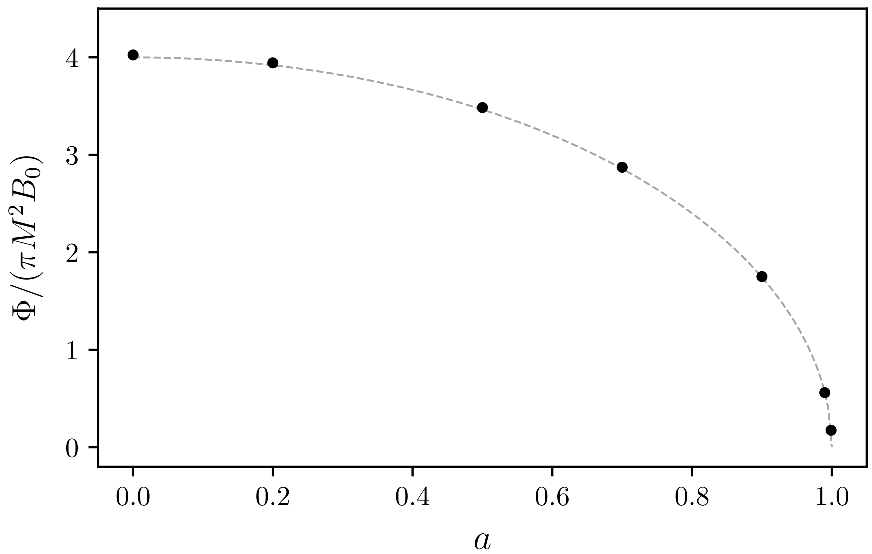

Figure 2.6: Vacuum Wald problem: total magnetic flux through the upper hemisphere of the outer horizon versus the spin of the Kerr black hole. Numerical results at $t = 125M$ (black dots) are shown on top of the analytic prediction (dotted line, Eq. (2.51)).

of magnetic fields at $t = 125M$ in Figure 2.5. The Kerr black hole expels magnetic field lines, successfully demonstrating the "Meissner effect" of black hole electrodynamics (Komissarov and McKinney, 2007).

In a stationary state, total magnetic flux through the upper hemisphere of the outer horizon has an analytic expression (King, Lasota, and Kundt, 1975)

$$\Phi = \oint_{r=r_+,\, z>0} B^i d\Sigma_i = \pi r_+^2 B_0 \left(1 - \frac{a^4}{r_+^4}\right), \tag{2.51}$$

where a is the rotational parameter of the Kerr black hole and $r_+ = M + \sqrt{M^2 - a^2}$ is the outer horizon radius in spherical Kerr-Schild coordinates. We perform additional simulations varying the black hole spin a using the same grid setup, all reaching stationary states at $t \gtrsim 80M$. We plot the obtained magnetic flux at $t = 125M$ in Figure 2.6; our numerical results are in an excellent agreement with the analytic prediction. The troubled cell indicator is flagged at several innermost elements only for the highly spinning cases with $a/M \geq 0.90$.

Magnetospheric Wald problem

First performed by Komissarov (2004a), this problem models a highly conductive magnetosphere around a Kerr black hole. The initial condition is the same as the

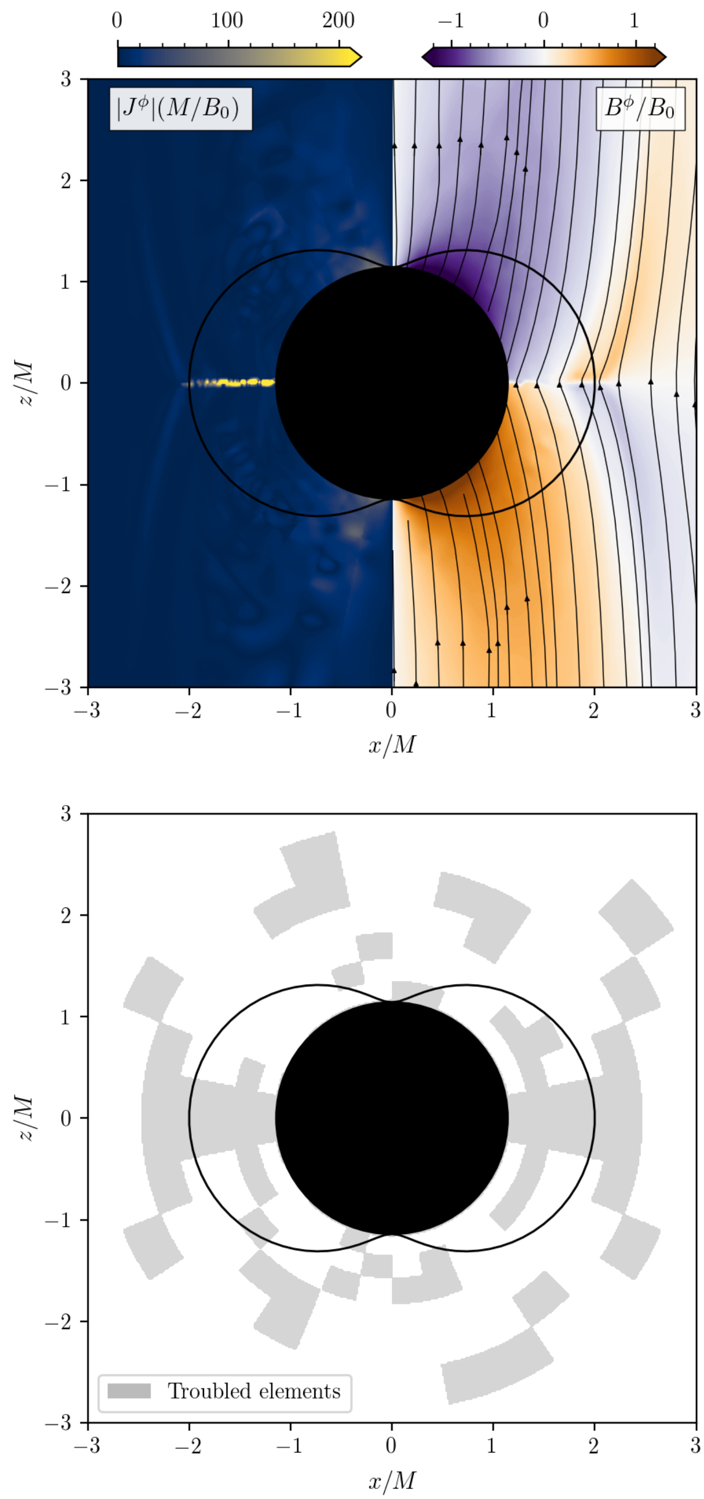

Figure 2.7: Magnetospheric Wald problem at $t = 125M$. In both panels, the interior of the outer horizon and the ergosphere are shown with a black disk and a thick black line, respectively. Top: toroidal component of the electric current density and magnetic field. In-plane magnetic field lines are shown with thin black lines in the right half. Bottom: distribution of troubled elements evolved on the FD grid.

vacuum Wald problem but now the electrical conductivity of the magnetosphere is switched on. Compared to the electrovacuum case, the presence of highly conductive plasma dramatically changes the behavior of the magnetosphere, since the parallel components of electric fields $E_i B^i$ can be neutralized by the parallel electric current. There is no analytic solution to the evolution of this initial value problem, where numerical simulations (e.g. Komissarov, 2004a; Paschalidis and Shapiro, 2013; Etienne, Wan, et al., 2017; Parfrey, Philippov, and Cerutti, 2019; Mahlmann, Aloy, et al., 2021a) show that the system reaches a quasisteady state that resembles the analytically derived solutions of a stationary force-free magnetosphere (Nathanail and Contopoulos, 2014).

We perform a test with the black hole spin $a = 0.999M$ using $N_r \times N_\Omega = 32 \times 384$ elements with the CFL factor 0.25 ($\Delta t = 9.86 \times 10^{-4} M$). At this grid resolution, if all elements are on the FD grid, there are 176 FD grid points along the θ direction with the minimum radial grid spacing $\Delta r = 0.014M$ at the inner boundary $r = M$. Parallel conductivity is set to $\eta = 10^5 M^{-1}$. Small numerical errors and resulting constraint violations naturally introduce electric charge density into the computational domain via the parallel current Eq. (2.29), filling up the magnetosphere. The system reaches a stationary state at $t \gtrsim 80M$.

We show the result at $t = 125M$ in Figure. 2.7. Inside the ergosphere, magnetic field lines are dragged by the rotation of the black hole and a thin current sheet is formed in the equatorial plane. The overall configuration and topology of the magnetic fields agree well with previous results reported in the literature. The troubled cell indicator is always flagged at the elements encompassing the equatorial current sheet, while several more elements sparsely distributed near the ergosphere are also switched to the FD grid (bottom panel of Fig. 2.7).

In the high electrical conductivity limit, magnetic field lines entering the ergosphere end up crossing the outer horizon (Komissarov, 2007; Parfrey, Philippov, and Cerutti, 2019), apart from a small portion reconnecting at the equatorial current sheet. Because of a large grid resistivity in our setup (the ergosphere is radially $\sim$50 FD grid points across on the equatorial plane), we see that only about half of the magnetic field lines penetrate the horizon. Some temporal variations of the current sheet and magnetic field lines near the ergosphere are observed, but the details of magnetic reconnection and plasmoid formations at the equatorial current sheet (Parfrey, Philippov, and Cerutti, 2019) are not fully resolved at the current grid resolution.

2.4.3 Three-dimensional tests: Pulsar magnetospheres

A conducting sphere threaded with a dipolar magnetic field and rotating in free space serves as a toy model of pulsars. In the flat spacetime, we set the initial dipolar magnetic field as

$$A_\phi = \mu \frac{(x^2 + y^2)}{(r^2 + \delta^2)^{3/2}}, \tag{2.52}$$

where μ is the magnetic dipole moment, $r^2 = x^2 + y^2 + z^2$, and δ is a small number to regularize the field at $r = 0$. All other variables, including electric fields, are set to zero everywhere in the initial data.

Rotation of the star is turned on at $t = 0$ with a fixed angular velocity $\Omega\hat{z}$. Inside the star ($r \leq R$), we enforce the perfect conductor condition

$$E^i + \varepsilon_{(3)}^{ijk} v_j B_k = 0, \tag{2.53}$$

with the (rigid) rotation velocity field $v^i = \varepsilon_{(3)}^{izj} \Omega x_j$. In practice this is implemented by overwriting electric fields E^i with those consistent with (2.53) at every substep of time integration. By this means, the magnetic field is effectively anchored and corotates within $r \leq R$, whereas fields at $r > R$ are freely evolved. For consistent behavior of other evolved variables, we also fix $\tilde{\psi} = 0$ and $\tilde{q} = 0$ inside the star. The magnetic part of the evolution equations is freely evolved everywhere. We use $\delta = 0.1R$ for this test.

Denoting the grid refinement level by an integer l, the computational domain consists of an inner cube (2^{3l} elements) and six cubed-sphere wedges ($N_r \times N_\Omega = 2^{l-3} \times 2^{2l}$ elements for each) surrounding it, wrapped with an outer spherical shell ($N_r \times N_\Omega = 2^{l-3} \times (6 \times 2^{2(l-1)})$). The outer shell uses a logarithmic map along the radial direction and is fixed to stay on the DG grid. Figure 2.8 shows the grid structure for $l = 4$. The wedges and the outer shell use an equiangular map for the angular directions, leading to non-uniform sizes of the elements in the inner cube: elements closer to the origin have smaller sizes. Vertices of the inner cube are located at $r_{\text{cube}} = 10\sqrt{3}R$, and the cubed-sphere wedges fill the region up to $r_{\text{in}} = 20R$. The outer shell extends to the outer domain boundary $r_{\text{out}} = 60R$, at which the no-incoming Poynting flux boundary condition is imposed. At the $l = 4$ grid resolution, the total number of grid points is $n_{\text{grid}}^{1/3} \approx 120$ on the DG grid, and the radius of the rotator R is a single element wide at the center.

We test with the angular velocity $\Omega = (5R)^{-1}$ and use a parallel conductivity $\eta = 10^5 R^{-1}$. Our simulation grid is rotated along the z axis with the same angular speed as the rotator.

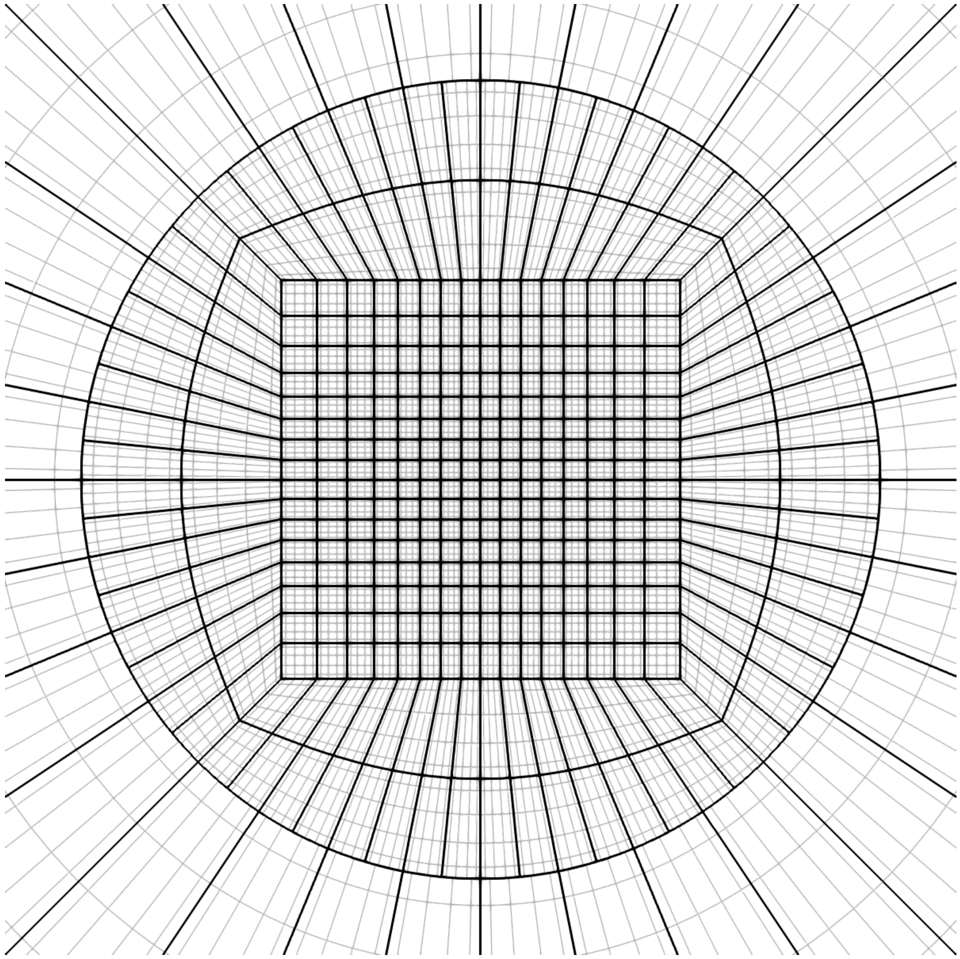

Figure 2.8: A zoom-in view of the computational domain used for the pulsar magnetosphere tests in Sec. 2.4.3. A sphere domain is divided into an inner cube at the center, a layer of cubed-sphere wedges, and an outer spherical shell (not fully shown in this figure).

Aligned rotator

An aligned rotator ($\theta = 0$) is a simple model of a rotating magnetized neutron star with magnetic moment aligned with the axis of rotation. This problem is relatively simple because it is axisymmetric, and has been treated in a large volume of studies (e.g., Goldreich and Julian, 1969; Contopoulos, Kazanas, and Fendt, 1999; Spitkovsky, 2006; Komissarov, 2006; McKinney, 2006b; Parfrey, Beloborodov, and Hui, 2012; Cao, L. Zhang, and Sun, 2016)

We use the $l = 5$ resolution, which has 22 FD grid points across the rotator radius and $n_{\rm grid}^{1/3} \approx 240$ total grid points across the DG grid, along with the CFL factor 0.25 ($\Delta t = 6.03 \times 10^{-3} R$). Following an initial numerical transient, the magnetosphere

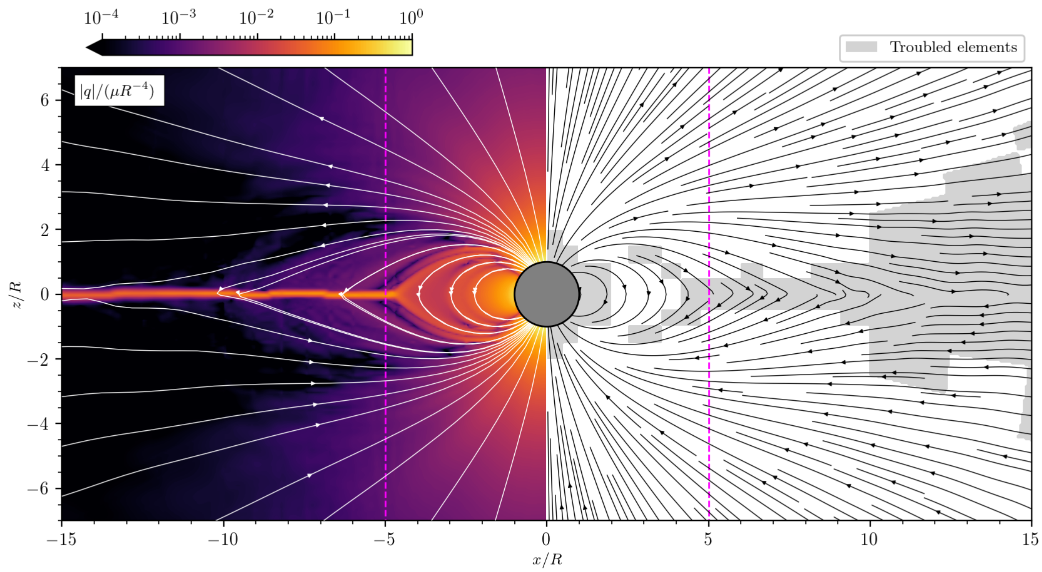

Figure 2.9: Aligned rotator after two rotation periods. Magnetic field lines are shown with white solid lines on the left half and black solid lines on the right. Electric charge density is shown with a colormap on the left, and the distribution of troubled elements is shown with gray shades on the right. The light cylinder radius ($r_{\rm LC} = \Omega^{-1}$) is shown with magenta dashed lines.

of the rotator gradually expands and the system reaches a quasi-steady state after one rotation period.

In Figure 2.9, we show the distribution of electric charge density and the structure of magnetic fields after two rotation periods ($t = 20\pi R$). Our scheme successfully reproduces all characteristic features of the aligned rotator magnetosphere. An equatorial current sheet is formed outside the light cylinder radius $r_{\rm LC} = \Omega^{-1}$, and magnetic field lines far from the equatorial plane open up to form a monopole-like configuration. Because of the grid resistivity, magnetic field lines $r \gtrsim 2r_{\rm LC}$ spuriously reconnect through the equatorial current sheet. The troubled cell indicator faithfully tracks the current sheet and the regions with rapid variations of the magnetic field, which are likely to develop oscillations on the DG grid, switching elements to the more robust FD grid. The widening of the distribution of the troubled elements is observed in the outer region $r > 10$. While elements near the center of the domain has a cubic shape, the elements in this outer region are deformed (curved) cubes that build up an outer spherical shell (see Fig. 2.8), and the Jacobian matrix that maps logical and physical coordinates is no longer constant within an element. Ideally, this should have marginal effects on the behavior of the troubled cell indicator, where empirically we find that the indicator becomes slightly more sensitive on the elements with curved shapes.

Oblique rotator

Having a misalignment angle between the magnetic moment and the rotation axis, an oblique rotator serves as a more realistic model of astrophysical pulsars (Spitkovsky, 2006; Kalapotharakos and Contopoulos, 2009; Petri, 2012; Petri, 2016; Carrasco, Palenzuela, and Reula, 2018). Since the configuration is no longer axisymmetric, a full 3D simulation is required to study this problem.

We use the same simulation setup as the aligned rotator test, but tilt the initial magnetic field by an inclination angle $\theta = \pi/4$. The system reaches a steady state after about one rotation period.

Figure 2.10 shows simulation snapshots on the equatorial plane (left panel) and meridional plane (right panel) after two periods of rotation. Generic features of the solution are similar to the aligned rotator. Beyond the light cylinder radius, a current sheet is formed and magnetic field lines are opened up. Now that the magnetic axis is misaligned with the rotation axis, the current sheet has a periodically modulated curved 3D geometry, appearing as a spiral pattern on the equatorial plane. It is clearly visible that the troubled cell indicator robustly captures and tracks magnetic reconnection points and the spiral current sheet so that the solution can be evolved on the FD grid in those regions. The remainder of the domain keeps evolving on the DG grid, which is computationally more efficient.

One can compute the spin-down luminosity of the rotator

$$L = \oint S_i d\Sigma^i, \tag{2.54}$$

where

$$S^a = \frac{E^2 + B^2}{2} n^a + \varepsilon_{(3)}^{abc} E_b B_c \tag{2.55}$$

is the Poynting vector. We perform simulations with a lower grid resolution $l = 4$ for different inclination angles and compute the spin-down luminosity Eq. (2.54) after two rotation periods at $r = 6R$. Figure 2.11 shows the measured values. The inclination dependence of the spin-down luminosity L is well fitted with the relation (Spitkovsky, 2006)

$$L = L_0(k_1 + k_2 \sin^2 \theta) \tag{2.56}$$

yielding $k_1 = 1.04$ and $k_2 = 1.24$, where L_0 is the luminosity of the aligned configuration ($\theta = 0$).

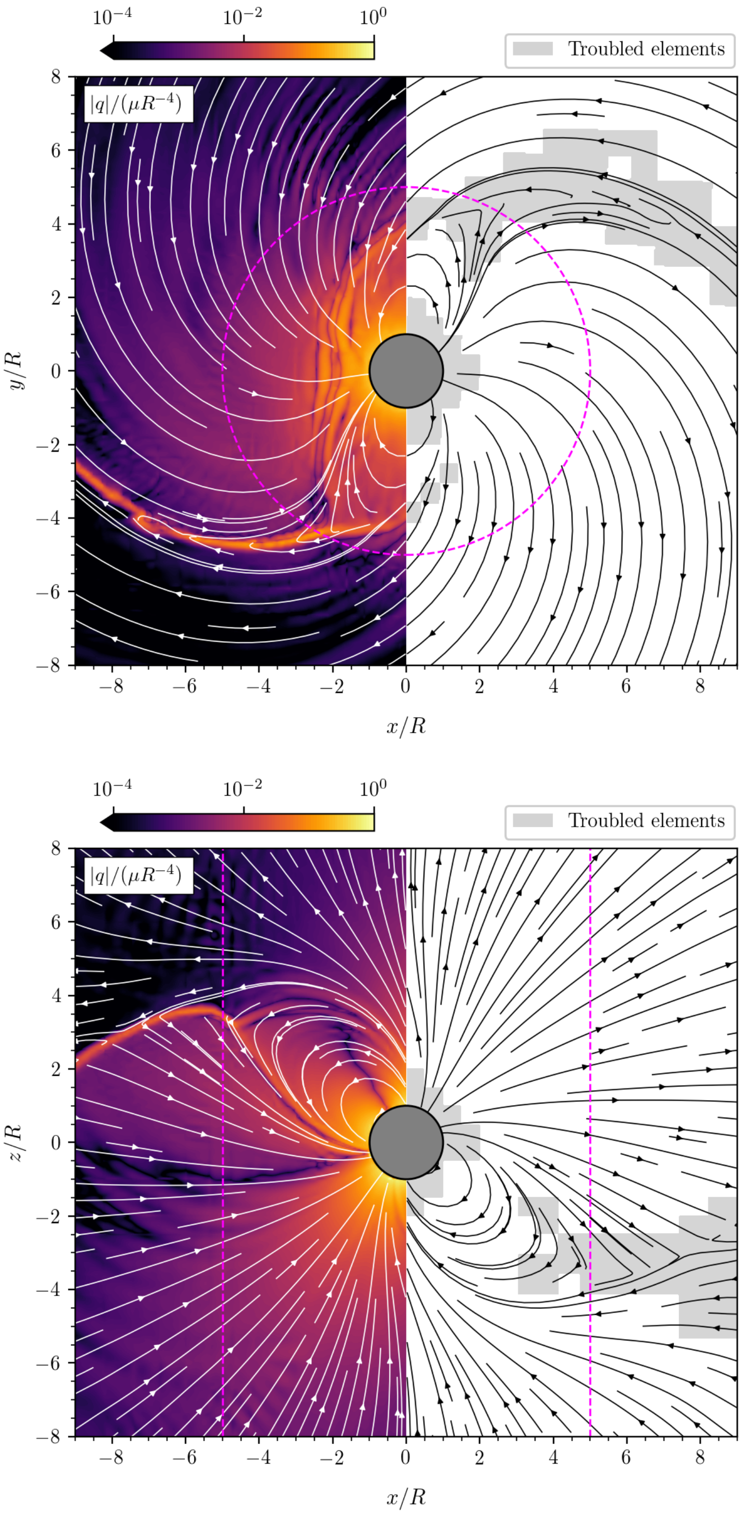

Figure 2.10: Oblique rotator: Simulation snapshot on the equatorial (top) and meridional (bottom) plane after two periods of rotation. Plotted physical quantities and their visualizations are the same as Fig. 2.9.

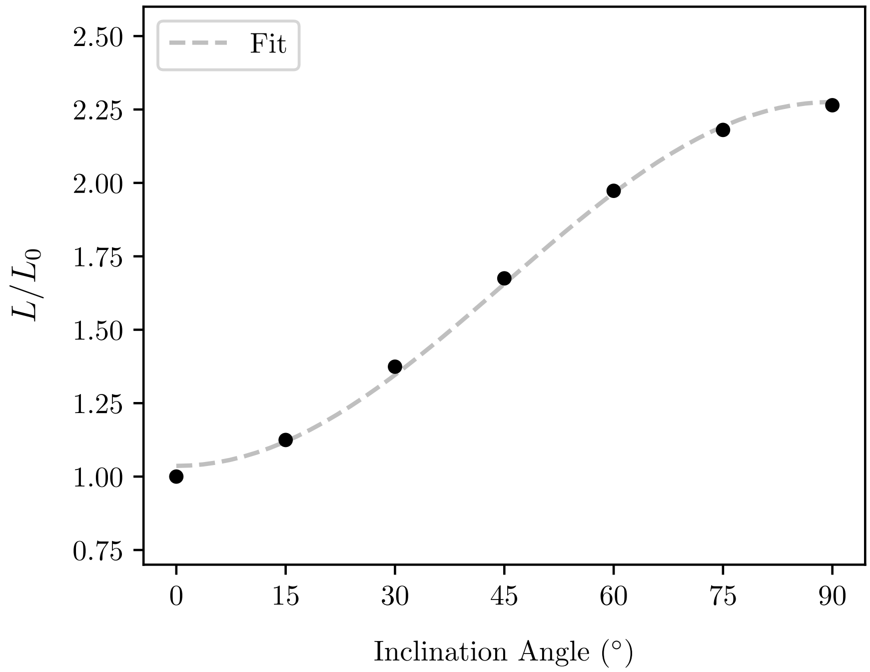

Figure 2.11: Oblique rotator: Inclination angle dependence of the spin-down luminosity. Numerical results (black dots) are fitted with the formula (2.56), shown with a gray dashed line.

2.4.4 Performance comparison between DG and FD grids

One of the main goals of this work is to assess the performance and cost-saving potential of using a DG-FD hybrid method for global FFE simulations of compact binary magnetospheres. We do so in two steps. First, we establish an accuracy benchmark to identify corresponding DG and FD resolution requirements for the same level of accuracy. Second, using this optimal choice, we estimate the cost-savings/speed-up factor of the DG-FD hybrid methods over traditional FD approaches for the problems presented in this work.

Accuracy comparison

Depending on which scheme is taken as the baseline, the DG-FD hybrid method can be interpreted either as a sophisticated shock-capturing technique for the DG method, or an FD method that compresses a group of cells into a high-order spectral representation on smooth regions (Deppe et al., 2022). The 'exchange ratio' between these two grids, namely $(N+1)^D$ DG grid points and $(2N+1)^D$ FD grid points, has been determined by equalizing the maximum admissible time step sizes (Dumbser, Zanotti, Loubère, et al., 2014).

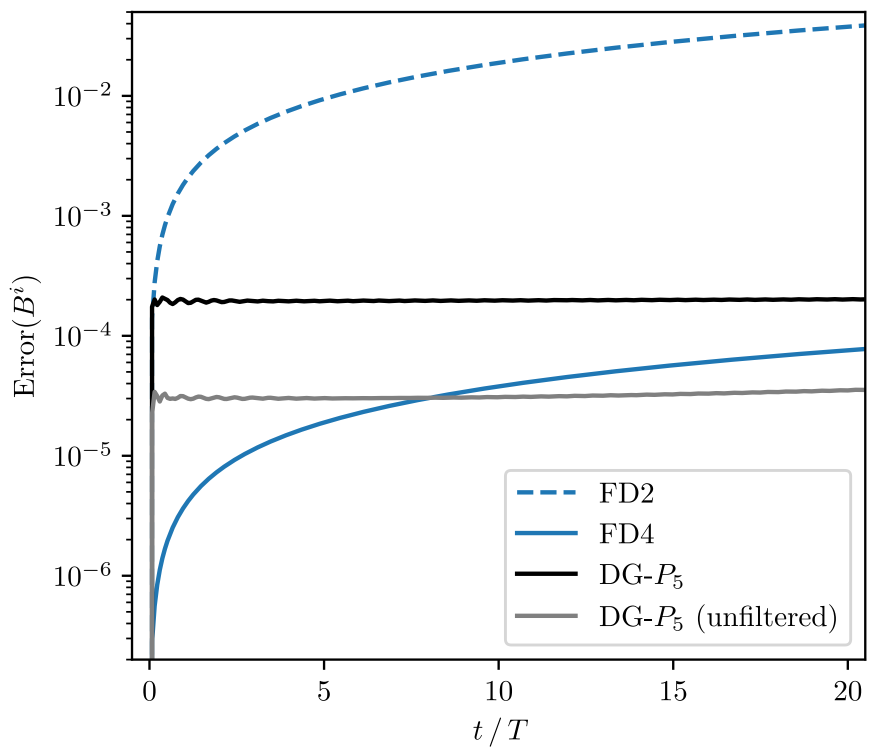

Figure 2.12: Error norm of magnetic field over time from a test evolving a sinusoidal fast wave in a periodic box (described in Sec. 2.4.4). For the FD runs, we perform the test without (FD2) and with (FD4) the high-order flux correction.

An important follow-up question is comparing the accuracy between the DG and FD grids when the number of grid points is subject to the above ratio. For example, does a compression of 11^3 FD grid points into a P_5 DG mesh with 6^3 grid points in a smooth region lead to an increase or decrease in accuracy? Clearly, the answer is highly dependent on the details of DG (e.g. order of the polynomial, how filtering is applied) and FD solvers (e.g. reconstruction scheme, high-order corrections), which needs to be assessed on a case-by-case basis.

However, it is desirable that the DG and FD solvers have similar levels of accuracy in smooth regions. For instance, coupling a low-order DG scheme with a very high-order FD reconstruction is not ideal since the evolution on the FD grid is computationally too expensive considering the overall achievable accuracy with such a choice. This may possibly make adopting a low-order FD scheme and using an increased number of elements overall more efficient. On the other hand, hybridizing a high-order DG scheme with a low-order FD scheme introduces a relatively large numerical diffusion on the FD grid, artificially smearing out important features, especially on smooth regions close to a discontinuity. In this case, the quality of the solution from the DG-FD hybridization, despite its algorithmic complication, might be no better than simply applying an aggressive DG limiter.

A desired sweet spot is setting the DG and FD discretization to have the same order of convergence. As a fiducial case, we consider the same setup used for the 1D test problems: a DG-P_5 with the highest mode filtered out and a FD solver using the WENO5-Z reconstruction with $q = 2$ along with the fourth-order derivative corrector. Both discretizations are fifth-order convergent for smooth solutions.

We perform a simple numerical experiment as follows. The 1D fast wave problem in Sec. 2.4.1 is modified to a smooth initial profile $E_z = -B_y = \sin(2\pi x/\lambda)$ with the wavelength $\lambda = 2$. The computational domain $[0, \lambda]^3$ is split into four elements in each spatial direction. The initial condition is evolved up to 20 wave crossing times using periodic boundary condition.

Figure 2.12 shows the time evolution of the error norm of the magnetic field. While both the DG and FD discretizations used in this test have the same fifth-order convergence, the FD grid has a twice smaller grid spacing and shows better accuracy for $t \leq 20\lambda$. We note the boundedness of the error norm on the DG grid, demonstrating a lower numerical dissipation and its resulting suitability for problems involving long-range wave propagation. By contrast, the error norm on the FD grid increases monotonically with time, approaching the same level of error as the DG grid at $t \geq 20\lambda$.

We cautiously interpret this result in the following way. In long-term magnetospheric simulations, replacing the group of $(2N + 1)^D$ FD cells with a DG-P_N spectral mesh in smooth regions likely does not harm global accuracy. In simulations with realistic astrophysical scenarios, the solution is not smooth everywhere but will have localized large gradients such as current sheets separated by smooth regions. The global numerical error will then be dominated by the regions with large gradients, since a shock-capturing FD scheme (such as WENO5-Z) will fall back to a lower order.

As an additional example, in Fig. 2.12 we also show results from an unfiltered DG-P_5 scheme and an FD scheme without the high-order flux correction. The accuracy of the solution on the FD grid is significantly lower without the high-order corrections, the error being even higher than the DG grid using twice fewer grid points per spatial dimension. The unfiltered DG-P_5 has a sixth-order convergence

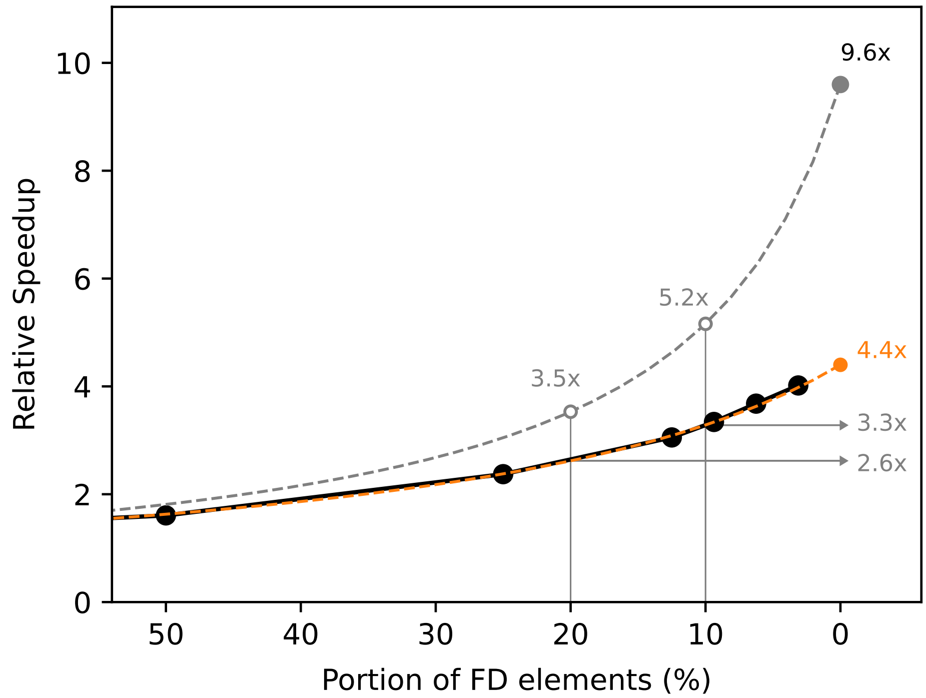

Figure 2.13: Single-core wall-clock speedup of the 1D Alfvén wave problem for different fractions of elements using the FD grid. An ideal scaling between all-DG and all-FD is shown with a dashed gray line. The measured scaling (yellow dashed line) fit shows that a DG element runs 4.4× faster on average than an FD element. 10%/20% fraction of FD elements give 3.3× (5.2×) / 2.6× (3.5×) overall (ideal) speedup as shown by the solid (dashed) gray line.

and shows smaller error than the FD grid at $t \gtrsim 10\lambda$. As soon as the DG grid has a higher order of discretization than the order of FD discretization, DG shows a better accuracy in spite of having fewer grid points.

In summary, in particular for the hybridization of a DG-P_5 and a WENO5-Z FD scheme, we conclude that switching from the FD to the DG grid results in a marginal loss of local accuracy in smooth regions, which is unlikely to affect the global error in actual simulations.

Efficiency

Having confirmed that the DG and FD grids show a comparable level of accuracy in the setup we use, we now assess potential computational cost savings when using the hybrid scheme. Since the number of grid points on the DG grid is fewer than the FD grid by a factor of $(11/6)^3 = 6.2$ in 3D, a similar amount of computational speedup is naturally anticipated. In order to quantify the actual speedup in our implementation, we run the stationary Alfvén wave test (Sec. 2.4.1) using $(N_x, N_y, N_z) = (8, 32, 8)$ elements. We manually force elements to stay on the DG grid for $y > 0$ and on the FD grid for $y < 0$.[8] The fraction of elements running on the FD grid is changed by shifting the upper and lower bounds of the y coordinate. This allows us to vary the fraction of FD to DG grid points in a controlled way. We additionally disable parallelization and carry out all tests in this section on a single CPU core to disentangle parallel scaling from algorithmic performance. Our fiducial benchmark is then given by the overall wall-clock time of the evolution algorithm.

Figure 2.13 shows the relative speedup compared to the case when all elements are using the FD grid. Since the DG solver does not involve computationally expensive reconstruction steps and has less data communication, it can perform ~50% more grid point updates per second compared to the FD solver, which results in a combined 9.6× overall speedup. In absolute terms, the measured zone-cycles per CPU second are 108K when all elements are on the DG grid, and 69K when all elements are on the FD grid.

Assuming perfect scaling, the overall speedup relative to the all-FD case can be estimated with the simple formula

$$\frac{1}{x + (1 - x)/f} \tag{2.57}$$

where x is the portion of elements using the FD grid and f is the speedup factor of the DG grid with respect to the FD grid. In Fig. 2.13, we show the ideal speedup scaling with $f = 9.6$ (gray dashed curve). However, our measurements show that as soon as there is any portion of FD elements, the effective speedup factor drops down to $f = 4.4$, implying the presence of an algorithmic bottleneck. When half the elements are using the FD grid, measured zone-cycles per second are 65K, even a bit slower than the all-FD case. This somewhat unexpected drop in performance is likely to be related to an extra interpolation step required at the interface between DG and FD elements to convert the ghost zone data sent between the elements. As a representative number, we quote the achievement of 3.3× (5.2×) / 2.6× (3.5×) overall (ideal) speedup when 10% / 20% of elements are using the FD grid.

A separate, detailed profiling of the code suggests at most 10% overhead from the controlling part of the DG-FD hybrid algorithm (applying the TCI to the solution and

[8]Therefore, in this controlled experiment, the overhead related to (i) execution of the TCI and (ii) rolling back the time step on troubled elements are excluded. Each element still sends out ghost-zone data to neighboring elements at every time step.

undoing a time step if an element is troubled), which was excluded in the speedup test described above. Comparing simulations of a smooth wave solution using the DG grid on all elements with the adaptive DG-FD scheme turned on and off showed less than 4% of difference in total runtime.

2.5 Conclusions

We have developed a new numerical scheme for general-relativistic FFE based on a DG-FD hybrid method. The numerical scheme combines a high-order spatial discretization with IMEX time stepping to handle stiff source terms associated with maintaining the FFE constraints. We have further implemented a troubled cell indicator capable of flagging spurious features in the DG evolution, allowing the associated elements to transition to a more dissipative conservative FD scheme. In this way, the scheme achieves high-order convergence for smooth problems while robustly tracking and capturing large gradients present in solutions such as current sheets. Our implementation is based on the open-source `SpECTRE` code and successfully passes and reproduces a suite of standard test problems in one- and three-dimensions. In particular, we achieve up to eighth-order numerical convergence in smooth vacuum problems. A quantitative measure of the numerical resistivity in our scheme, in particular using the approaches by (Rembiasz et al., 2017; Mahlmann, Aloy, et al., 2021b), will be explored in future works.

In order to assess potential cost savings of this approach over more traditional FD-only schemes, we have performed a quantitative assessment of its accuracy and efficiency. We find that our approach has a potential to speed up FD simulations by the factor of 2–3 with little to no loss of accuracy. We further demonstrate an additional optimization potential of (in some cases) up to a factor 2, when compared to the ideal speed up of the code. Similar or even larger performance gains have been reported when adopting GPU-based parallelization strategies (e.g. Liska et al., 2022; Del Zanna, Landi, et al., 2024; Grete, Glines, and B. W. O'Shea, 2021). Additional improvements may come from a more optimal set of troubled cell indicator criteria or a dynamic power monitor (e.g. see Szilágyi, 2014), which can potentially facilitate a more economical grid switching between DG and FD.

The DG-FD hybrid scheme presented here is particularly well suited to study wave propagation as well as accuracy-limited problems, such as steady-state twists or magnetospheric explosion dynamics that evolve on long timescales (e.g. Parfrey, Beloborodov, and Hui, 2013; Yuan, Spitkovsky, et al., 2019; Yuan, Y. Levin, et al., 2021). Such studies will be the subject of future work.

Acknowledgements

We are grateful to Kyle Nelli and Nils Vu for helpful discussions and technical support during various stages of this project. Y.K. acknowledges Cristòbal Armaza for encouraging conversations. Computations were performed on the Wheeler cluster and Resnick HPC Center at Caltech.

Chapter 3

GENERAL RELATIVISTIC MAGNETIZED BONDI-HOYLE-LYTTLETON ACCRETION

Kim, Yoonsoo and Elias R. Most (2025). "General relativistic magnetized Bondi-Hoyle-Lyttleton accretion with a spin-field misalignment: Jet nutation, polarity reversals, and Magnus drag". In: *Physical Review D* 111 (8), p. 083025. DOI: 10.1103/PhysRevD.111.083025. URL: https://link.aps.org/doi/10.1103/PhysRevD.111.083025.

The dynamics of a black hole traveling through a plasma – a general relativistic extension of the classic Bondi-Hoyle-Lyttleton accretion problem – can be related to a variety of astrophysical contexts, including the aftermath of binary black hole (BBH) mergers in gaseous environments. We perform three-dimensional general relativistic magnetohydrodynamics simulations of Bondi-Hoyle-Lyttleton accretion onto a spinning black hole when magnetic field of the incoming wind is inclined to the spin axis of the black hole. Irrespective of inclination but dependent on the wind speed, we find that the accretion flow onto the black hole can become magnetically arrested, launching an intermittent jet whose formation is assisted by a turbulent dynamo-like process in the inner disk. The upstream ram pressure of the wind bends the jet, and confines the angular extent into which the magnetic flux tubes ejected from quasi-periodic eruptions are released. Recoil from magnetic flux eruptions drives strong oscillations in the inner accretion disk, resulting in jet nutation at the outer radii and occasionally ripping off the inner part of the accretion disk. When the incoming magnetic field is perpendicular to the spin axis of the black hole, we find that the magnetic polarity of the jets can undergo a stochastic reversal. In addition to dynamical friction, the black hole experiences a perpendicular drag force analogous to the Magnus effect. Qualitative effects of the incoming magnetic field orientation, the strength of the magnetization, and the incoming wind speed are investigated as well.

3.1 Introduction

3.1.1 BBH merger remnant in AGN disk

The merger of a binary black hole (B. P. Abbott et al., 2016; B. P. Abbott et al., 2019; R. Abbott et al., 2021a; R. Abbott et al., 2023) within the accretion disk of an active galactic nucleus (AGN) (N. C. Stone, Metzger, and Haiman, 2017; Tagawa, Haiman, and Kocsis, 2020; Gröbner et al., 2020; Ishibashi and Gröbner, 2020; McKernan et al., 2022; Ford and McKernan, 2022; Kaaz, Schrøder, et al., 2023) is thought to be one of major channels of the observed BBH mergers, but is also an interesting astrophysical scenario within the context of multi-messenger astronomy. If asymmetry is present in a black hole binary, the resulting anisotropic emission of gravitational waves from the merger can impart a recoil onto the post-merger remnant black hole (Gonzalez, Sperhake, et al., 2007; Campanelli et al., 2007a). Since the kicked remnant will be moving through a gas-rich environment, a luminous accretion flow onto or a relativistic jets from the BH may give rise to an observable post-merger electromagnetic signal (Graham et al., 2020; K. Chen and Z.-G. Dai, 2024).

The gaseous environment of the AGN disk can affect the long-term evolution of an embedded BBH, often putting constraints on its orbital configuration. Newtonian studies suggest that orbital and spin axes of a BBH embedded in a gaseous environment align over time (Bogdanovic, Reynolds, and Miller, 2007; Coleman Miller and Krolik, 2013), and the orbit is driven to be aligned with the AGN disk plane as well (Dittmann, Dempsey, and H. Li, 2024). These findings, put together, indicate that both the orbital angular momentum and spin of the BBH are likely aligned with the AGN disk. Unless anisotropic gravitational radiation induces a significant torque on the system, the remnant would retain its prior spin direction.

Recent large-scale cosmological simulations revealed that the magnetic field of AGN disks are predominantly toroidal (parallel to the disk plane) (Hopkins, Grudic, et al., 2024; Hopkins, Squire, et al., 2024); see also Gaburov, Johansen, and Y. Levin (2012) for an earlier work. The presence of mixed poloidal-toroidal configurations is also in line with simulations of magnetized circumbinary disks around BBHs as well (Most and H.-Y. Wang, 2024b; Most and H.-Y. Wang, 2024a). Overall, this motivates a theoretical investigation on a recoiled black hole flying through a plasma embedded with a magnetic field misaligned with the spin of the black hole.

3.1.2 Bondi-Hoyle-Lyttleton accretion

Bondi-Hoyle-Lyttleton (BHL) accretion (Bondi, 1952; Hoyle and Lyttleton, 1939) is a classic problem in astrophysics involving a gravitational accretor traveling through a uniform fluid. Despite being highly simplified, it can be applied to a wide range of astrophysical systems including common envelope phases of binary star evolution (MacLeod and Ramirez-Ruiz, 2015; MacLeod, Antoni, et al., 2017; Murguia-Berthier et al., 2017; López-Cámara, Moreno Méndez, and De Colle, 2020), wind-fed X-ray binaries (El Mellah, Sundqvist, and Keppens, 2018), star clusters (Kaaz, Antoni, and Ramirez-Ruiz, 2019) or protoplanetary disks (Moeckel and Throop, 2009).

Owing to its astrophysical significance, a large volume of analytical and numerical studies exist in the literature on Newtonian (see Edgar, 2004; Foglizzo, Galletti, and Ruffert, 2005 for a review) and relativistic regimes (Petrich, Shapiro, and Teukolsky, 1988; Petrich, Shapiro, Stark, et al., 1989; Font and Ibanez, 1998b; Font, Ibanez, and P. Papadopoulos, 1999; Font and Ibanez, 1998a; Dönmez, Zanotti, and Rezzolla, 2011; Dönmez, 2012; Zanotti, Roedig, et al., 2011; Penner, 2011; Penner, 2013; Lora-Clavijo and Guzman, 2013; Koyuncu and Dönmez, 2014; Lora-Clavijo, Cruz-Osorio, and Méndez, 2015; Blakely and Nikiforakis, 2015; Cruz-Osorio, Lora-Clavijo, and Guzman, 2012; Cruz-Osorio and Lora-Clavijo, 2016; Tejeda and Aguayo-Ortiz, 2019; Cruz-Osorio and Rezzolla, 2020; Gracia-Linares and Guzmán, 2015; Kaaz, Murguia-Berthier, et al., 2023; Gracia-Linares and Guzmán, 2023).

Basic physical scales associated with BHL accretion are the accretion radius[1]

$$R_a = \frac{2GM}{v_\infty^2}\,, \tag{3.1}$$

the accretion timescale

$$\tau_a = \frac{R_a}{v_\infty} = \frac{2GM}{v_\infty^3}\,, \tag{3.2}$$

and the Bondi-Hoyle-Lyttleton mass accretion rate

$$\dot{M}_{\rm BHL} = \pi R_a^2 \rho_\infty v_\infty = \frac{4\pi G^2 M^2 \rho_\infty}{v_\infty^3}\,, \tag{3.3}$$

where G is the gravitational constant, M is the mass of the accreting object, v_∞ is the asymptotic relative velocity, and ρ_∞ is the asymptotic mass density of the fluid.

A major challenge in computational approaches to this problem is its inherent multi-scale nature, namely simultaneously resolving the size of the accreting object r_0 and

[1] An alternate definition of the accretion radius exists in the literature

$$R_a = \frac{2GM}{c_{s,\infty}^2 + v_\infty^2},$$

where $c_{s,\infty}$ is the asymptotic sound speed of the incoming fluid. We adopt the definition (3.1) throughout this chapter.

the accretion radius R_a on a single numerical grid. For example, a black hole with mass M has $r_0 \approx r_g$ where

$$r_g = \frac{GM}{c^2} \tag{3.4}$$

is the gravitational radius of the black hole. The ratio between the two length scales is

$$\frac{R_a}{r_g} \sim \left(\frac{v_\infty}{c}\right)^{-2}. \tag{3.5}$$

Also, time integration needs to be performed at least several times of τ_a to reach a steady state, which is longer than the dynamical timescale associated with the black hole by a factor of

$$\frac{\tau_a}{(r_g/c)} \sim \left(\frac{v_\infty}{c}\right)^{-3}. \tag{3.6}$$

A large separation in both length and time scales, which is especially severe for a compact accretor such as a black hole, rapidly increases the computational cost for realistic values of v_∞. As a result, many studies are often forced to assume an unrealistically fast velocity of the BH relative to the fluid. Due to its high computational cost, most numerical studies on general relativistic BHL accretion have considered hydrodynamic flows on either 2D planar or 3D axisymmetric geometry. However, inclusion of magnetic fields can dramatically alter the flow morphology, and a restrictive nature of the assumed spatial symmetry might fail to fully capture multi-dimensional effects. Following the first study of 2D magnetohydrodynamic (Penner, 2011) and 3D hydrodynamic (Gracia-Linares and Guzmán, 2015) flows, the first simulations of general relativistic magnetohydrodynamics (GRMHD) Bondi-Hoyle-Lyttleton accretion in full 3D have been carried out only recently by Kaaz, Murguia-Berthier, et al. (2023) and Gracia-Linares and Guzmán (2023). Each of these studies respectively explored jet launching from the BH (Kaaz, Murguia-Berthier, et al., 2023) and the effect of the BH spin-wind orientation on the shock morphology (Gracia-Linares and Guzmán, 2023), which can only be properly captured in a 3D MHD simulation.

In this work, we perform GRMHD simulations of a spinning black hole traveling through a fluid embedded with a magnetic field inclined to the spin axis of the BH. The physical scenario is approximated by a relativistic Bondi-Hoyle-Lyttleton accretion problem with a magnetized wind. We examine large-scale morphology and temporal evolution of the accretion flow, both of which are closely related to intermittent jet launching and magnetic flux eruptions from the BH. The impacts of magnetic field orientation, magnetization, and the wind speed are assessed by systematically varying simulation parameters.

Another purpose of our numerical experiment is to measure the outflow luminosity (power) and determine the efficiency with which $\dot{M}_{\rm BHL}c^2$ can be converted into an energy outflow. The drag force exerted on the accreting BH is also measured and its astrophysical implications are discussed.

This chapter is organized as follows. In Sec. 3.2, we describe our numerical setup and methods. We present our results in two steps, focusing on a specific parameter set first in Sec. 3.3, before generalizing it in Sec. 3.4. We present discussions on the results in Sec. 3.5, then summarize our main findings along with limitations and future perspectives in Sec. 3.6.

3.2 Methods

The background spacetime is set to the Kerr metric in (Cartesian) Kerr-Schild coordinates (see also Appendix A). The spin of the black hole is aligned with the $\hat{z}$ axis of the computational domain. The exact form of the spacetime metric is

$$\begin{aligned} ds^2 = -c^2dt^2 + dx^2 + dy^2 + dz^2 + \frac{2GMr^3/c^2}{r^4 + a^2z^2} \\ \times \left[c\,dt + \frac{r(xdx + ydy) + a(ydx - xdy)}{r^2 + a^2} + \frac{zdz}{r}\right]^2 , \end{aligned} \tag{3.7}$$

where M is the mass and a is the spin parameter of the black hole (with the unit of length). The coordinate variable r is defined as

$$\frac{x^2 + y^2}{r^2 + a^2} + \frac{z^2}{r^2} = 1\,. \tag{3.8}$$

We solve the equations of ideal GRMHD, which are given in terms of the rest-mass density current

$$J^\mu = \rho u^\mu\,, \tag{3.9}$$

and the stress-energy tensor,

$$T^{\mu\nu} = \left(\rho + e + p + b^2\right) u^\mu u^\nu + \left(P + \frac{b^2}{2}\right) g^{\mu\nu} - b^\mu b^\nu\,, \tag{3.10}$$

with its electromagnetic component

$$T^{\mu\nu}_{\rm EM} = b^2 u^\mu u^\nu + \frac{b^2}{2} g^{\mu\nu} - b^\mu b^\nu\,, \tag{3.11}$$

where ρ is the rest mass density, e is the internal energy density, p is the pressure, u^μ is the four-velocity, and b^μ the comoving magnetic field of the fluid, with $b^2 = b^\mu b_\mu$. The electromagnetic field is evolved using the dual field strength tensor,

$$^*F^{\mu\nu} = b^\mu u^\nu - u^\mu b^\nu \,. \tag{3.12}$$

The evolution equations are

$$\nabla_\mu J^\mu = 0\,, \tag{3.13}$$

$$\nabla_\mu {}^*F^{\mu\nu} = 0\,, \tag{3.14}$$

$$\nabla_\mu T^{\mu\nu} = 0\,. \tag{3.15}$$

We find it advantageous to define a normal magnetic field as[2]

$$\bar{B}^i = {}^*F^{0i}\,. \tag{3.16}$$

We further model the gas dynamics using an ideal fluid equation of state

$$p = e\,(\Gamma - 1)\ , \tag{3.17}$$

where $\Gamma = 5/3$ is the adiabatic index.

3.2.1 Numerical setup

We numerically solve the ideal GRMHD system using `AthenaK` (J. M. Stone, Mullen, et al., 2024), a rewrite of `Athena++` code (J. M. Stone, Tomida, et al., 2020) with a performance portability library `Kokkos` (Trott et al., 2022).

The computational domain $[-40960r_g, 40960r_g]^3$ is discretized into a uniform Cartesian grid with the base grid resolution 256^3. 13 levels of static mesh refinement are applied around the coordinate origin, with the innermost mesh $[-5r_g, 5r_g]^3$ providing a resolution of ~26 grid points per r_g. Time integration is performed using a second order Runge-Kutta stepper, piecewise parabolic reconstruction (Colella and

[2]This definition of the magnetic field is not covariant, as it is different by a factor of α (the lapse function in 3+1 decomposition) from the Eulerian magnetic field B^i commonly adopted in numerical relativity or relativistic electrodynamics literature (e.g., Baumgarte and Shapiro, 2010; Paschalidis and Shapiro, 2013; Komissarov, 2004a). However, we adopt the definition (3.16) here since it simplifies the handling of the solenoidal (divergence-free) constraint on the magnetic field as,

$$\partial_i \bar{B}^i = 0\,,$$

in the Kerr-Schild coordinates.

Woodward, 1984), an HLLE Riemann solver (Harten, Lax, and Leer, 1983; Einfeldt et al., 1991), and a constrained transport algorithm (Gardiner and J. M. Stone, 2008). We use the mass density and internal energy floor values $\rho_{\text{floor}} = 10^{-14}\rho_\infty$, $e_{\text{floor}} = \rho_{\text{floor}} c^2/3$, and cap the maximum Lorentz factor of the fluid to $W_{\text{max}} = 20$. The drift frame flooring technique (Ressler, Tchekhovskoy, et al., 2017) is applied to limit the comoving magnetization to $\sigma_{\text{max}} = 50$.

`AthenaK` can be compiled and run on graphics processing unit (GPU) devices at scale, providing $\mathcal{O}(10^7)$ cell updates per second per each GPU card for large scale GRMHD simulations. The simulations presented here overall have been performed on 132 GPU nodes (792 NVIDIA Volta cards) at OLCF Summit cluster, costing 900 node hours per $10^4 r_g/c$ integration time on average. The total computational cost used for all simulations is about 34,000 node hours.

3.2.2 Initial data

Over the whole computational domain, matter profile is initialized with a uniform rest mass density ρ_∞ and spatial velocity

$$u^{i'} = \left(-\frac{v_\infty}{\sqrt{1 - v_\infty^2/c^2}}, 0, 0\right), \tag{3.18}$$

where v_∞ is the asymptotic incoming speed of the fluid, c is the speed of light, and $u^{i'} = u^i + \beta^i u^0$ is the normal-frame spatial velocity which is a primitive variable used in the code.[3] Given the sound speed $c_{s,\infty}$, the fluid internal energy density

$$e_\infty = \frac{c_{s,\infty}^2 \rho_\infty}{\Gamma(\Gamma - 1 - c_{s,\infty}^2/c^2)}, \tag{3.19}$$

and pressure

$$p_\infty = e_\infty(\Gamma - 1), \tag{3.20}$$

can be initialized accordingly.

The inclination between the magnetic field of the incoming wind and its velocity can be arbitrary in general. In this study, in order to narrow down the parameter space and focus on the misalignment between the BH spin and the magnetic field, we assume that the incoming magnetic field is perpendicular to the wind velocity. We initialize the magnetic field as

$$\bar{B}^i = B_0(0, \sin\theta_B, \cos\theta_B), \tag{3.21}$$

[3] See section 4 of J. M. Stone, Tomida, et al. (2020) for the definition of GRMHD primitive variables used in `Athena++` or the section 3 of J. M. Stone, Mullen, et al. (2024) for `AthenaK`.

where B_0 is the field strength and θ_B is the inclination angle between the BH spin and the magnetization of the incoming fluid.

In the asymptotic limit ($x^i \to \infty$), the magnetic field strength B_0 is related to the magnetization of the fluid σ as

$$\sigma_\infty = \frac{(b^2)_\infty}{(\rho c^2 + e + p)_\infty} = \frac{B_0^2/(1 - v_\infty^2/c^2)}{\rho_\infty c^2 + \Gamma e_\infty} . \tag{3.22}$$

The plasma β-parameter and the magnetization σ are related via

$$\beta_\infty = \frac{p_{\rm gas}}{p_b} = \frac{p_\infty}{(b^2)_\infty/2} = \frac{2}{\Gamma}\frac{(c_{s,\infty}/c)^2}{\sigma_\infty}. \tag{3.23}$$

Input parameters of our simulations are the asymptotic fluid mass density ρ_∞, accretion radius R_a, asymptotic sound speed $c_{s,\infty}$, the plasma parameter β_∞, and the magnetic field inclination angle θ_B. The incoming speed of the fluid v_∞ is computed from $v_\infty^2 = 2GM/R_a$ and used to initialize the spatial velocity (3.18). From the sound speed $c_{s,\infty}$, both internal energy density and pressure can be initialized using (3.19) and (3.20). The plasma parameter β_∞ determines the relativistic magnetization σ_∞ via (3.23), in turn giving B_0 from (3.22), which we use to initialize the magnetic fields as (3.21). Primitive variables are initialized everywhere in the computational domain with the values prescribed as above.

Simulation parameters are listed in Table 3.1. We particularly focus on the cases that the magnetic field of the incoming wind is perpendicular or inclined with respect to the BH spin (see Kaaz, Murguia-Berthier, et al., 2023 for the aligned magnetic field configuration). For all simulations we adopt a BH spin $a/r_g = 0.9$ and the asymptotic sound speed $c_{s,\infty} = 0.05c$. Our representative, fiducial model assumes $\beta_\infty = 10$ with a horizontal orientation of the magnetic field $\theta_B = 90^\circ$, along with the fluid incoming speed $v_\infty = 0.1c$ corresponding to $R_a = 200r_g$; this model is labeled as β_{10}-θ_{90}-R_{200}. To explore the influence of magnetic field orientation relative to the BH spin, we run the identical setup but varying $\theta_B = 22.5^\circ, 45^\circ, 67.5^\circ$, each of which is labeled with θ_{23}, θ_{45}, and θ_{68}. We perform an experiment on the effect of a weaker magnetization $\beta_\infty = 100$ while keeping other parameters fixed from the fiducial model. Lastly, we run two more models with a smaller ($R_a = 50r_g$) and a larger ($R_a = 400r_g$) accretion radius to test the influence of the fluid incoming speed, also keeping the other parameters fixed to the same values as the fiducial model.

Table 3.1: List of the models and parameters considered in this work. Each column denotes the accretion radius R_a, asymptotic fluid incoming speed v_∞, asymptotic Mach number $\mathcal{M}$, accretion time scale τ_a, the plasma beta parameter of the incoming fluid β_∞, and the magnetic field inclination angle θ_B. The spin of the BH is set to $a = 0.9 r_g$ for all simulations.

Label	R_a $[r_g]$	v_∞/c	$\mathcal{M}$	τ_a $[r_g/c]$	β_∞	θ_B	Comments
β_{10}-θ_{90}-R_{200}	200	0.1	2.0	2000	10	90°	Fiducial setup
β_{10}-θ_{68}-R_{200}	200	0.1	2.0	2000	10	67.5°	Varying θ_B
β_{10}-θ_{45}-R_{200}	200	0.1	2.0	2000	10	45°	
β_{10}-θ_{23}-R_{200}	200	0.1	2.0	2000	10	22.5°	
β_{100}-θ_{90}-R_{200}	200	0.1	2.0	2000	100	90°	High β
β_{10}-θ_{90}-R_{50}	50	0.2	4.0	250	10	90°	Faster v_∞
β_{10}-θ_{90}-R_{400}	400	0.07	1.4	5660	10	90°	Slower v_∞

3.2.3 Boundary conditions

At the outer boundary of the computational domain facing the $+\hat{x}$ (upstream) direction, we impose a Dirichlet boundary condition injecting a constant wind profile same as the initial data. At all other sides of the domain boundary, primitive variables at the outermost grid points are copied into the ghost zones to impose a free streaming boundary condition.

3.2.4 Analysis

In addition to the magnetohydrodynamics variables evolved on the grid, we compute following integral quantities from simulation data in order to monitor time evolution of the system:

- Mass accretion rate
$$\dot{M} = \oint (-\rho u^r)\sqrt{-g}\, d\theta d\phi, \tag{3.24}$$
  where ρ is the rest mass density and u^r is the radial component of the four-velocity. Note the minus sign in the integrand, which makes a positive value indicate mass inflow.

- Total energy (in-)flux
$$\dot{E} = \oint T^r{}_t \sqrt{-g}\, d\theta d\phi\,. \tag{3.25}$$

- Angular momentum (out-)flux

$$\dot{J} = \oint T^r{}_\phi \sqrt{-g}\, d\theta d\phi. \tag{3.26}$$

- Total magnetic fluxes threading the horizon

$$\Phi_{\rm BH} = \frac{1}{2}\oint_{\rm horizon} |\bar{B}^r| \sqrt{-g}\, d\theta d\phi. \tag{3.27}$$

For our discussions presented here and in the following sections, we will often refer to the dimensionless total magnetic fluxes threading the BH horizon

$$\phi_{\rm BH} \equiv \frac{\Phi_{\rm BH}}{\sqrt{\dot{M} r_g^2 c}}\,. \tag{3.28}$$

The dimensionless magnetic flux can be used as an indicator for the accretion state, showing that for $\phi_{\rm BH} \gtrsim 20$ jets can be launched (Tchekhovskoy, Narayan, and McKinney, 2011). For larger values of $\phi_{\rm BH}$, the accretion flow will become fully magnetically arrested (e.g., Tchekhovskoy, Narayan, and McKinney, 2011; McKinney, Tchekhovskoy, and Blandford, 2012; White, J. M. Stone, and Quataert, 2019; Chatterjee and Narayan, 2022).

- Drag force exerted on the BH

$$F^i = -F^i_{\rm mom} + F^i_{\rm grav}, \tag{3.29}$$

where $F^i_{\rm mom}$ is the total momentum (out-)flux through a spherical surface

$$F^i_{\rm mom} = \oint T^r{}_i \sqrt{-g}\, d\theta d\phi, \tag{3.30}$$

and $F^i_{\rm grav}$ is the gravitational drag computed with a modified Newtonian formula (Cruz-Osorio and Rezzolla, 2020; Kaaz, Murguia-Berthier, et al., 2023)

$$F^i_{\rm grav} = \int \rho \frac{x^i}{r^3} dV. \tag{3.31}$$

A minus sign on the right hand side of Eq. (3.29) accounts for that the momentum loss in a closed volume results in a reaction force to the opposite direction. For example, in our simulation setup in which BH travels to $+x$ direction, $F^x_{\rm mom} > 0$ corresponds to the deceleration of the BH with respect to the ambient medium, where $F^x_{\rm grav} > 0$ corresponds to the acceleration.

The flow in the vicinity of the BH is strongly magnetized in our simulations, frequently triggering density and energy floors on troubled grid cells. Since the artificial injection of mass and energy density from numerical flooring can contaminate some of the diagnostics introduced above, we perform surface integrals around the BH at a slightly larger radius than the outer event horizon (e.g., Kaaz, Murguia-Berthier, et al., 2023). In our analysis, the horizon magnetic fluxes $\Phi_{\rm BH}$ is integrated over the outer event horizon whereas $\dot{M}$, $\dot{E}$, $\dot{J}$, and $F^i_{\rm mom}$ are extracted at $r = 3r_g$. The gravitational drag $F^i_{\rm grav}$ is integrated over the whole volume of the computational domain excluding $r < 3r_g$ in the same regard. We find this approach has no significant effect our diagnostics, see Appendix 3.A for a detailed analysis.

The turbulent nature of the accretion flow leads to high-frequency fluctuations of the time series data. For improved readability, we have averaged all time series data over a sliding time window of $100r_g/c$, unless otherwise stated.

Computations are performed in a scale-free manner by setting $c = GM = \rho_\infty = 1$. From simulation results, physical values can be recovered as

$$x^i = r_g\,\hat{x}^i \tag{3.32}$$

$$t = (r_g/c)\,\hat{t} \tag{3.33}$$

$$\rho = \rho_\infty\,\hat{\rho} \tag{3.34}$$

$$\dot{M} = (r_g^2\rho_\infty c)\hat{\dot{M}} \tag{3.35}$$

$$\dot{E} = (r_g^2\rho_\infty c^3)\hat{\dot{E}} \tag{3.36}$$

$$\dot{J} = (r_g^3\rho_\infty c^2)\hat{\dot{J}} \tag{3.37}$$

$$B^i = (\rho_\infty^{1/2} c)\hat{B}^i \tag{3.38}$$

$$\Phi_{\rm BH} = (r_g^2\rho_\infty^{1/2} c)\hat{\Phi}_{\rm BH} \tag{3.39}$$

$$F^i = (r_g^2\rho_\infty c^2)\hat{F}^i \tag{3.40}$$

where hat variables are the results in the (scale-free) code unit.

3.3 Fiducial model: Jet launching from horizontally magnetized wind

In this section, we analyze the results from the baseline model β_{10}-θ_{90}-R_{200} in detail to highlight several key phenomena observed in the simulation. This model features a wind speed $v_\infty = 0.1c$ and a magnetic field perpendicular (horizontal) to the black hole spin axis, with its strength set by the plasma parameter $\beta = 10$.

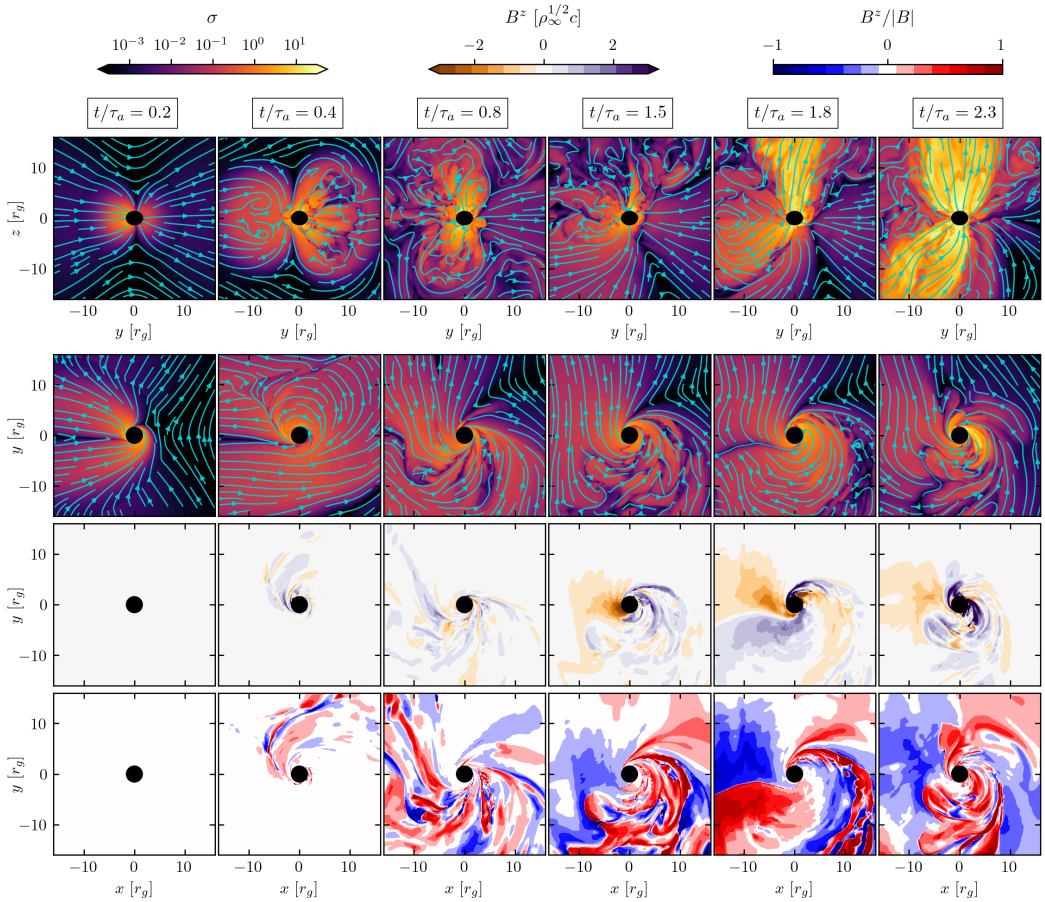

Figure 3.1: Initial jet launching process in the β_{10}-θ_{90}-R_{200} simulation. Shown here are in-plane magnetic field lines (cyan solid lines), magnetization σ, vertical magnetic field B^z, and its normalized value $B^z/|B|$. Each column displays physical quantities on the vertical (yz, the face-on direction with respect to the incoming wind) and the equatorial (xy) plane at each simulation time.

3.3.1 Overview

Initial jet launching process

Shortly following the beginning of the simulation, a shocked region around the BH quickly expands and forms a bow-shaped shock front, which is a common characteristic of supersonic BHL accretion flows (e.g., Foglizzo, Galletti, and Ruffert, 2005; Edgar, 2004; Shima et al., 1985; Font and Ibanez, 1998b). This initial accretion phase is largely hydrodynamical. Over time, the spin of the BH drags the flow into rotation around the horizon, starting to form an accretion disk, and magnetic flux is accumulated around the BH.

In Figure 3.1, we show simulation snapshots at an early time ($t \lesssim 2.5\tau_a$) focusing on the evolution of magnetic fields near the BH. While the magnetic field is initially perpendicular to the BH spin, turbulent fluid motion developing in the accretion flow generate vertical (poloidal) magnetic flux, akin to an MHD dynamo. This can be seen from the third and fourth rows of Fig. 3.1, showing the vertical magnetic field (B^z) on the equatorial plane. As the turbulent dynamo continues to supply vertical magnetic fluxes into the accretion flow with various eddy sizes, we find that a coarse large-scale magnetic flux separation emerges at $t \approx 1.8\tau_a$ (the fifth column in Fig. 3.1, appearing as a two-sided spiral shape). This serves as a reservoir of unilateral vertical magnetic field lines attached to the BH, which enables jet launching via the Blandford-Znajek mechanism (Blandford and Znajek, 1977).

From the time series plots in Fig. 3.3, we can see that the magnetization around the BH quickly reaches half-MAD ($\phi_B \simeq 25$) levels within $t \approx 3\tau_a$, as indicated by the dimensionless magnetic flux $\phi_{\rm BH}$, where a magnetically arrested disk (MAD) state is characterized by $\phi_{\rm BH} \simeq 50$ (Tchekhovskoy, Narayan, and McKinney, 2011). This built-up of magnetic flux coincides with the formation of a magnetized polar funnel region near the black hole as described above.

Large-scale flow morphology

Fig. 3.2 shows hydrodynamic and magnetic properties of the accretion flow on the meridional (xz) and equatorial (xy) plane at $t = 20400 r_g/c \approx 10\tau_a$. Relativistic jets powered by the BH appear as low-density, highly magnetized ($\sigma \gg 1$) funnel regions traversing the shock cone. The wind from the upstream collides with the jets and deflect them downstream with its ram pressure. The amount of jet bending correlates directly with the wind speed. A pair of these bent, relativistic jets are observed from tailed radio sources such as bent-tail radio galaxies (e.g. Hardcastle and Sakelliou, 2004; O'Dea and Owen, 1986; Miley, Wellington, and van der Laan, 1975; Giacintucci and Venturi, 2009).

An accretion disk forms around the BH with the same direction of rotation as the BH spin, and spans out to $r \sim 30 r_g$ on the equatorial plane although its spatial extent is varying over time. At the outermost radius of the disk, its circulatory flow is mixed with the regular downstream flow entering the shock cone, forming a stagnation point, as can be seen from the distribution of velocity streamlines near $(x, y) = (-20, -30) r_g$ of the lower left panel of Fig. 3.2. The matter inflow entering the shock cone on the co-rotating side ($+y$) is smoothly connected to the circulatory accretion flow, where that on the counter-rotating side ($-y$) collides with

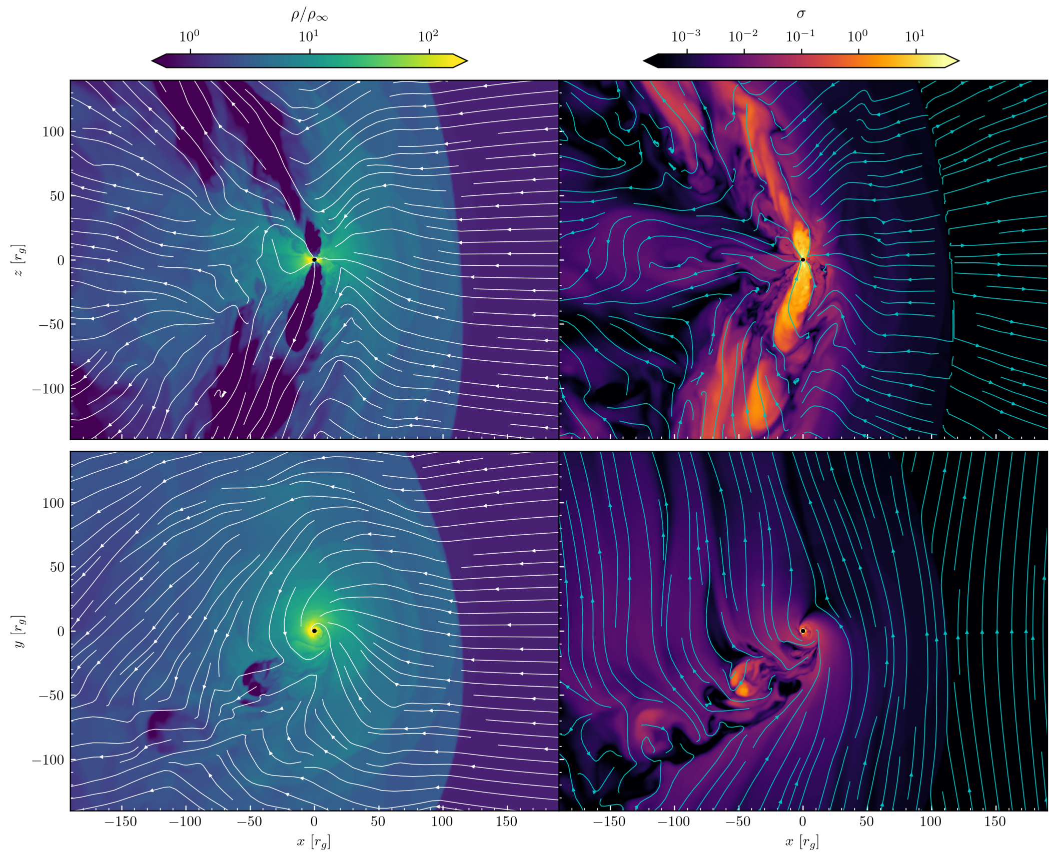

Figure 3.2: Transient jets and magnetic flux eruptions in GRMHD Bondi-Hoyle-Lyttleton accretion. Shown here are mass density, ρ, (left) and relativistic magnetization, σ, (right) on the meridional plane (top) and the equatorial plane (bottom) from the fiducial model β_{10}-θ_{90}-R_{200} at $t = 20400\, r_g/c$. The in-plane velocity and magnetic fields are shown with white and cyan streamlines on the left and right panels, respectively.

the accretion flow to be pushed radially outward. This leads to the bulk motion of the downstream flow being deflected into $-\hat{y}$ direction. In contrast to accretion simulations initialized or supplied with a finite angular momentum,[4] the incoming flow has zero net angular momentum in our setup. Spin-induced frame dragging of the BH is the only source of angular momentum imparted onto the flow, naturally limiting the radial size of the accretion disk.

The BH is in a near MAD state (Igumenshchev, Narayan, and Abramowicz, 2003; Narayan, Igumenshchev, and Abramowicz, 2003). MAD states feature the built-up of strong magnetic flux near the horizon, leading to the establishment of a mag-

[4]e.g., Fishbone-Moncrief torus (Fishbone and Moncrief, 1976), or BHL accretion scenarios with a density/velocity gradient (Lora-Clavijo, Cruz-Osorio, and Méndez, 2015; Cruz-Osorio and Lora-Clavijo, 2016)

netically arrested flow structure near the innermost stable circular orbit. Once the horizon magnetic flux rises above a threshold, reconnection triggers an ejection of magnetic flux bundles from the BH magnetosphere, accompanied by decay of the horizon magnetic flux (Ripperda, Bacchini, and Philippov, 2020; Ripperda, Liska, et al., 2022; Chatterjee and Narayan, 2022). Shearing instabilities, such as the Rayleigh-Taylor instability (Kulkarni and Romanova, 2008), ultimately trigger a magnetic flux eruption with a simultaneous mass accretion inwards, via interchanging magnetically buoyant low-density bubbles with less magnetized, dense parcel of fluid (Igumenshchev, 2008). Through this process a MAD state is re-established over the viscous timescale of the accretion flow. As a consequence, the BH does not sustain steady outflows but exhibits fluctuations in the jet power and intermittent flux eruptions.

The quasi-periodic MAD cycle results in two notable features in the flow morphology compared to unmagnetized axisymmetric BHL accretion flows.

(1) Each eruption event launches a pressure wave that expands outward from the black hole. This wavefront with a relatively higher density pushes the boundary of the bow shock further upstream, expanding the shock cone, before it shrinks back due to the ram pressure of the incoming fluid. As a consequence, the bow shock exhibits a breathing motion in lockstep with each of the magnetic flux eruptions. This results in a deformed morphology of the shockfront, rather than a smooth parabolic shape commonly observed from unmagnetized cases (e.g., Shima et al., 1985; Penner, 2013; Lora-Clavijo and Guzman, 2013; Gracia-Linares and Guzmán, 2015). This eruption-driven expansion of the bow shock and multiple pressure waves approaching the bow shock can be seen from the left panels of Fig. 3.2 or in Fig. 3.5.

(2) A series of magnetic flux tubes with high magnetization are formed near the BH and drift downstream on the equatorial plane as they are released, a few of which can be identified from the region $x < 0$, $y < 0$ in the lower panels of Fig. 3.2. This situation is reminiscent of unboosted MAD BH flows (e.g., Chatterjee and Narayan, 2022; Ripperda, Liska, et al., 2022; Porth et al., 2021). When a flux eruption event occurs, magnetic pressure pushes the matter outward via an interchange instability and forms highly magnetized, hot, low-density voids near the horizon (e.g., see the simulation snapshots included in Fig. 3.3 and Fig. 3.4). The ejected flux tubes are spiralling outwards

from the BH (Porth et al., 2021), getting sheared and ultimately reach the stagnation point, where they are fragmented by ram pressure and released into the downstream flow as a mushroom-shaped feature. In magnetic flux eruptions of axially symmetric accretion flows, flux tubes would have been launched without a preferred direction. Here, due to a preferential direction of the ambient flow, the flux tubes can be only released toward a particular range of angle relative to the direction of the upstream wind. The ejected flux tubes are filled with hot non-thermal plasma produced by the near-horizon magnetic reconnection that initially created the tubes (Ripperda, Bacchini, and Philippov, 2020; Ripperda, Liska, et al., 2022). This plasma has the potential to power TeV and X-ray flares (Porth et al., 2021; Hakobyan, Ripperda, and Philippov, 2023), in a similar manner to what has been proposed as an explanation for galactic flares near Sgr A* (Dexter et al., 2020; Antonopoulou, Loules, and Nathanail, 2025).

Time evolution

Having described the overall properties of the accretion flow, we now focus on its time variability. In Fig. 3.3, we provide the time series data of the dimensionless horizon magnetic flux $\phi_{\rm BH}$, mass accretion rate $\dot{M}$, energy outflow efficiency $\eta = (\dot{M} - \dot{E}/c^2)/\dot{M}$, (outwards directed) angular momentum flux $\dot{J}$, and the total drag force F^i. Based on these, we examine the time evolution of our fiducial accretion flow setup in this section.

After the initial development of relativistic polar outflows from the BH ($t \sim 3\tau_a$), the accretion flow undergoes an oscillatory MAD cycle showing a transient behavior of $\phi_{\rm BH}$ associated with episodes of magnetic flux eruptions. In active phases, when the jet is present, the mass accretion rate is suppressed, whereas it is enhanced in quiet (accreting) phases when the jet is absent. The overall evolution observed in this model is broadly consistent with previous studies on MADs (e.g. White, J. M. Stone, and Quataert, 2019; Porth et al., 2021; Chatterjee and Narayan, 2022; Tchekhovskoy, Narayan, and McKinney, 2011). The continued eruption cycle is maintained until $t \sim 10\tau_a$, which we hereafter refer to as the first eruption epoch.

Following the final flux eruption of the first eruption epoch at $t \sim 10\tau_a$, the magnetic flux of the BH drops and the system enters a fully quiescent period, $10\tau_a \le t \le 12\tau_a$ with the jet being fully quenched. The accretion flow temporarily enters a standard

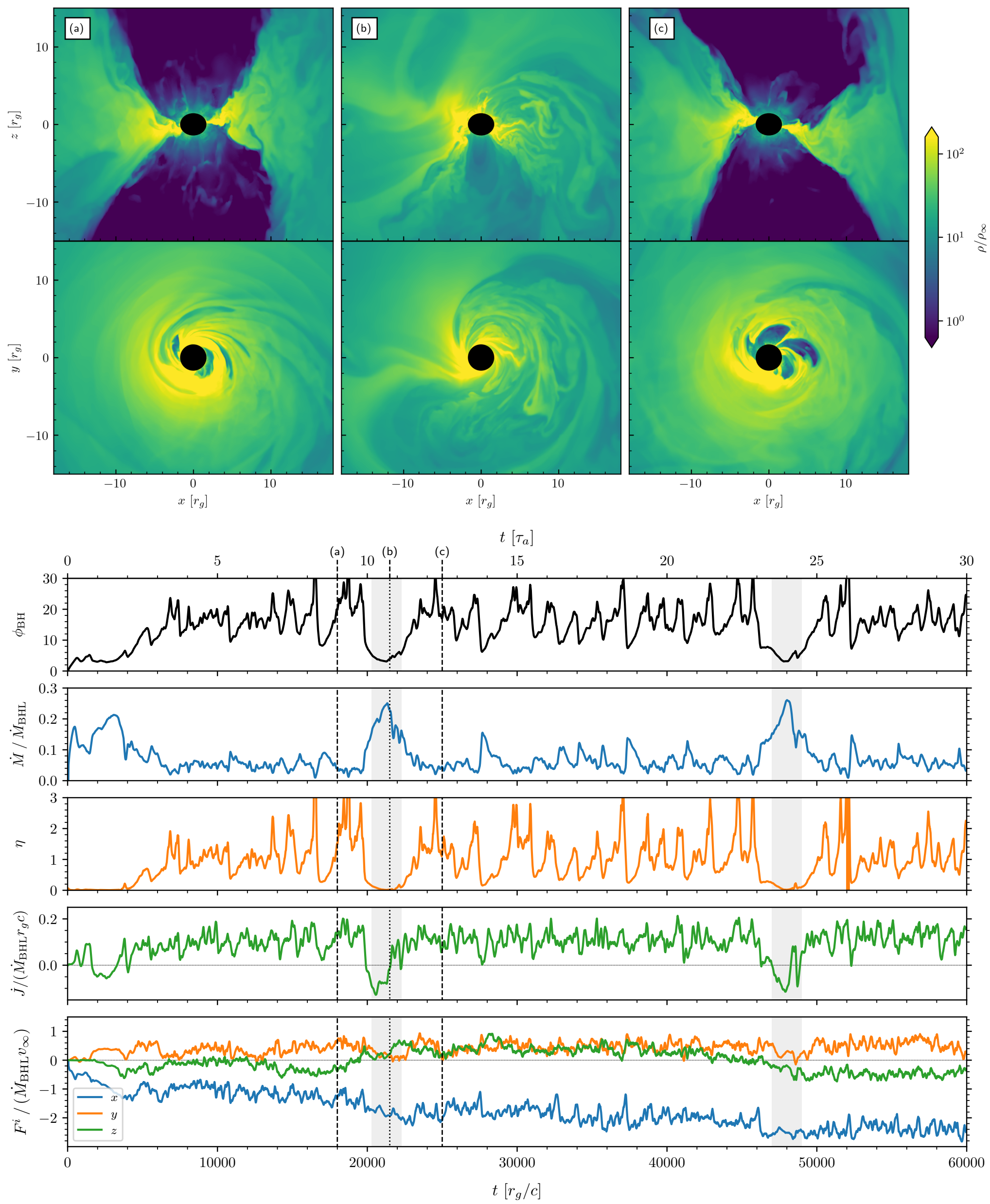

Figure 3.3: Time evolution of physical quantities for the representative (β_{10}-θ_{90}-R_{200}) model. Each panel of the line plots, from top to bottom, presents the dimensionless horizon magnetic flux $\phi_{\rm BH}$, mass accretion rate $\dot{M}$, energy outflow efficiency η, angular momentum flux $\dot{J}$, and the total drag force F^i. Quiescent periods (shaded) with a duration $\sim 2000 r_g/c$ are separated by an epoch of continued flux eruptions lasting $\sim 24000 r_g/c$. Color plots on top of this figure show the mass density, ρ, on the xz (first row) and xy (second row) plane in active states $t_{(a)} = 1.8 \times 10^4 r_g/c$, $t_{(c)} = 2.5 \times 10^4 r_g/c$ and a SANE-like quiescent state $t_{(b)} = 2.15 \times 10^4 r_g/c$, which are indicated with dashed and dotted vertical lines in the line plots.

and normal evolution (SANE, Narayan, Sadowski, et al., 2012) regime in which magnetized polar funnel are replaced by a smooth inflow of matter toward the BH and the accretion exhibits a relavitely laminar flow on the equatorial plane (with only mild turbulent eddies) without a strong vertical stratification (Chatterjee and Narayan, 2022). As a result, the mass accretion rate is notably increased and the BH experiences a temporary spin up ($\dot{J} < 0$) from the falling matter.

In the middle of the SANE-like quiescent period, the horizon magnetic flux and the energy outflow efficiency rises again, mass accretion decreases, and the angular momentum flux transitions from inflow (−) to outflow (+). The evolution of the system in this time window is similar to the process of the first jet launching phase, indicating the revival of it. This revival process takes roughly a viscous time scale of the disk. The system re-enters the MAD state and the jet is launched again at $t \sim 12\tau_a$, which marks the beginning of the second eruption epoch lasting $12\tau_a \leq t \leq 23\tau_a$.

In the upper half of Fig. 3.3, we include simulation snapshots displaying the mass density distribution of the accretion flow at three different times $t_{(a)} = 1.8\times10^4 r_g/c$, $t_{(b)} = 2.15 \times 10^4 r_g/c$, and $t_{(c)} = 2.5 \times 10^4 r_g/c$, each of which corresponds to (a) a MAD-like active state by the end of the first eruption epoch, (b) a quiet SANE-like state with no jet present, and (c) an active state in the second eruption epoch after the revival. This process overall repeats periodically.

3.3.2 Magnetic flux eruptions

In the preceding sections, we have described the global dynamics leading to the establishment of a MAD accretion state and subsequent magnetic flux eruption events. In the following, we provide a detailed description of the flux eruption event at $t = 16500 r_g/c$ as a representative example of the process, and elucidate its effect on the jet morphology.

Near black-hole dynamics

Along with the three sections of plots comprising Fig. 3.4, we now illustrate a comprehensive picture of a single magnetic flux eruption event.

- *Evolution of the horizon magnetic flux* (Fig. 3.4, top panel): The eruption cycle begins with a magnetically relaxed state after the previous eruption has settled down. The horizon magnetic flux $\phi_{\rm BH}$ starts to increase from $t = 15500 r_g/c$,

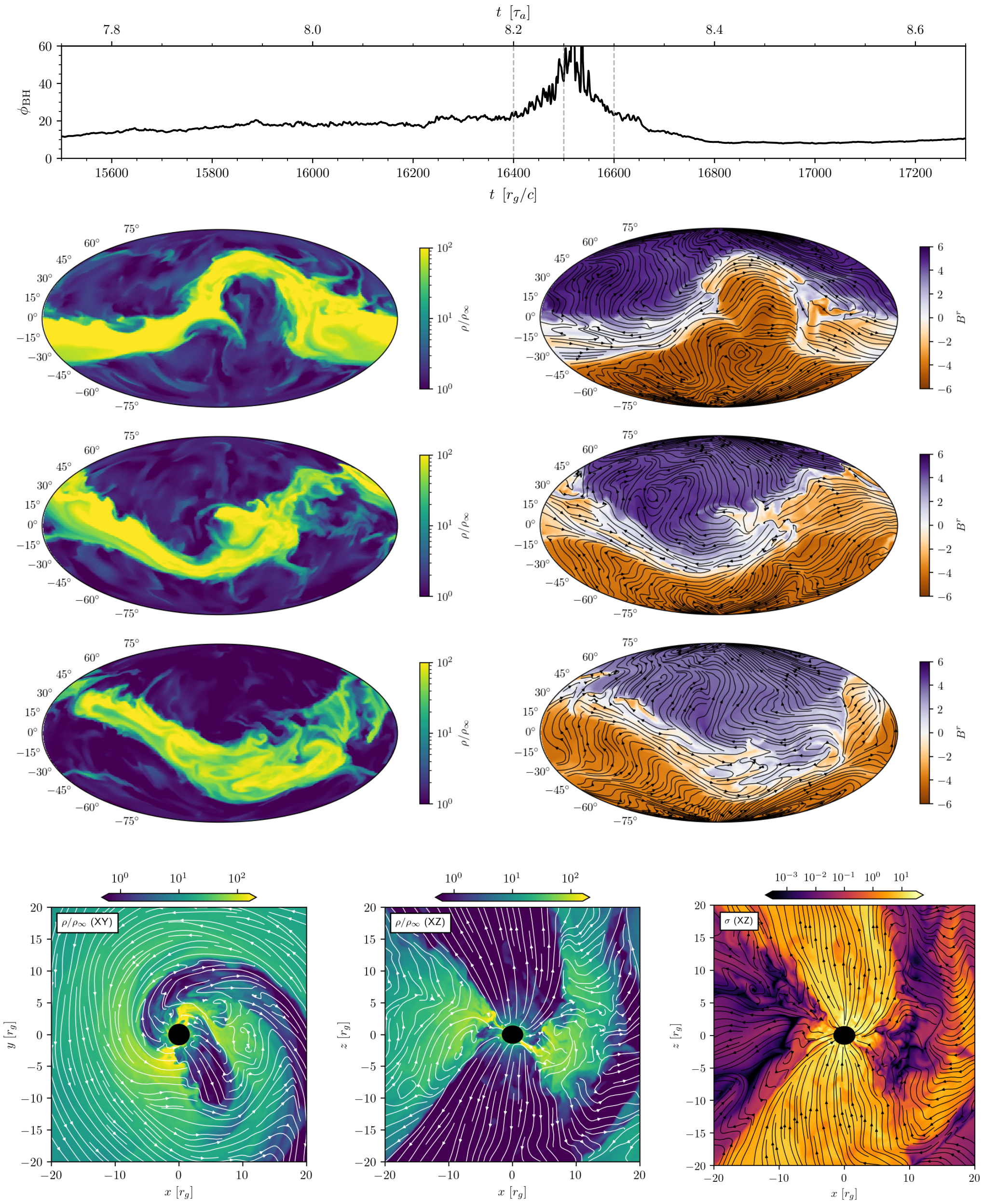

Figure 3.4: A magnetic flux eruption event at $t = 16500 r_g/c$. Top panel: change of dimensionless magnetic flux $\phi_{\rm BH}$ on the black hole (BH) over the eruption. Three vertical dashed lines mark $t = 16400, 16500, 16600\, r_g/c$ respectively. Data points are displayed without smoothing. Middle panels: mass density, ρ, (left) and radial magnetic field B^r in units ($[\rho_\infty^{1/2} c]$), (right) on a spherical surface $r = 5r_g$ are shown with the Mollweide projection aligned with the BH spin axis. The radial component of the magnetic field is shown in color and the angular components are shown with black streamlines. The center of the plot corresponds to the $+\hat{x}$ direction. From top to bottom, each row corresponds to $t = 16400, 16500, 16600\, r_g/c$. Bottom panels: mass density on the equatorial plane (left), on the meridional plane (center), and the relativistic magnetization σ on the meridional plane (right) at $t = 16500 r_g/c$. In-plane velocity and magnetic field are shown with white and black streamlines.

reaching $\phi_{\rm BH} \approx 20$ at $16300 r_g/c$. Then it rapidly rises to $\phi_{\rm BH} > 50$ around $t = 16500 r_g/c$, and relaxes down to $\phi_{\rm BH} \approx 10$ at $t = 16700 r_g/c$ after the eruption.

- *Nutation of the accreting plane* (middle panels in the Mollweide projection in Fig. 3.4): These panels, showing mass density and magnetic field on a spherical surface $r = 5r_g$ at $t = 16400 r_g/c$, $16500 r_g/c$ and $16600 r_g/c$, visualize angular distribution of the accretion flow and the geometry of magnetic field near the BH during the eruption event. In the pre-eruption stage, the accretion disk develops precession with an increasingly large amplitude over time. Left column of the panels shows that the accretion disk is subject to a significant tilt and distortion during the eruption (which otherwise would appear as a smooth strip along the equator). The ejection of the magnetic flux tube during the eruption is off the equator and exerts a strong recoil (and corresponding torque) onto the system, which leads to a nutation of the accretion disk.

- *Tearing of accretion disk* (bottom panels of Fig. 3.4): The asymmetric ejection of the magnetic flux tube (low density/high magnetization region) and the resulting recoil strongly tilting and tearing the inner accretion flow can be clearly seen from the figure. The dynamical time scale of the fluid at which the accretion disk is torn can be estimated via the local Keplerian orbital period as

$$T \approx \frac{2\pi}{\Omega_K} = 2\pi \left(\frac{r^3}{GM}\right)^{1/2} = 370 r_g/c \tag{3.41}$$

for $r = 15r_g$, which is in good agreement with the disk precession period $\approx 400 r_g/c$, which we estimate empirically. While the inner part of the accretion disk has a shorter dynamical timescale ($r < 15r_g$) than the driving frequency ($T \approx 400 r_g/c$) and is able to reorganize itself, the outer part of the disk with a longer dynamical timescale ($r > 15r_g$) cannot dynamically react (synchronize) to the driving and is decoupled from the inner part. In a different context, highly tilted accretion disks have been observed to suffer more tearing, precession, and fragmentation, when the inner part of the disk is subject to torque (Liska et al., 2021).

Jet morphology

High-resolution simulations of tilted accretion disks have shown that the motions of the disk and the jet are coupled (Liska et al., 2018; Liska et al., 2021), and we

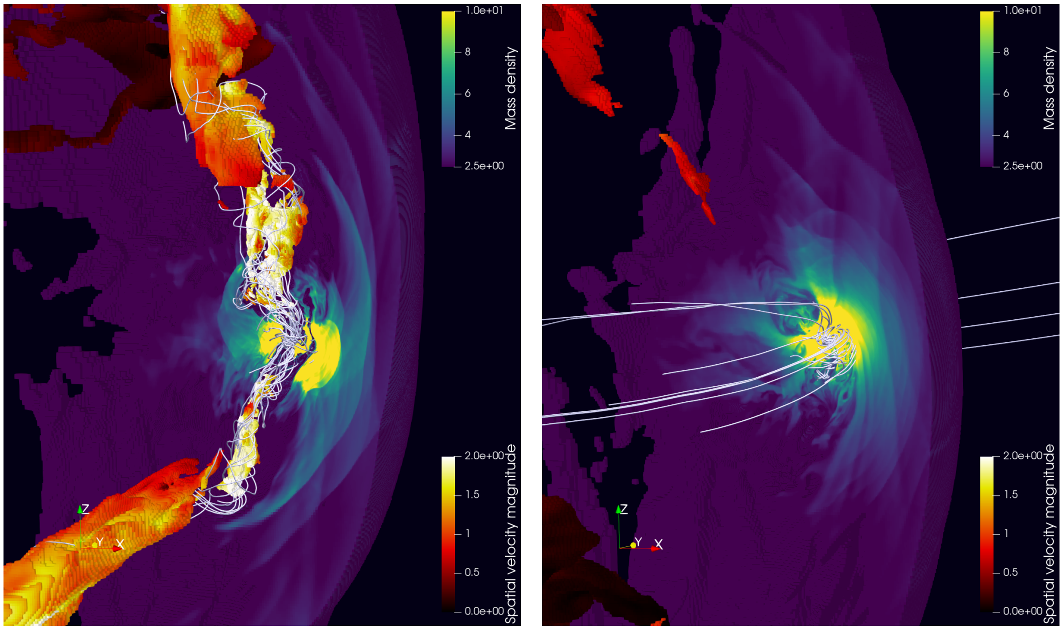

(a) $t = 16500 r_g/c$ (b) $t = 21500 r_g/c$

Figure 3.5: A three-dimensional rendering of the simulation depicting an active state (left) and a quenched state (right). Shown here are low-density, highly magnetized outflow (filtered by $\rho < 0.05\rho_\infty$, red-white colors), accretion flow inside the bow shock (filtered by $\rho > 2\rho_\infty$ and half-cut to vertical, blue-yellow colors), and magnetic field lines emanating from the accretion disk. Each colormap shows the magnitude of the spatial components of the four-velocity and the normalized mass density ρ/ρ_∞. A vertical tearing of the accretion disk (see Sec. 3.3.2) is visible in the left panel.

observe a similar phenomenon in our simulations. While the structure of the jet remains more or less aligned with the BH spin very close the horizon ($r \lesssim 5r_g$), the rapid nutation of the accretion disk and a consequent wobbling of the the polar funnels surrounded by the accretion flow results in fluctuations in the direction of the jet at $r \gtrsim 10r_g$ (see also Liska et al., 2018). From a three-dimensional visualization in Fig. 3.5, one can observe the twisted morphology of the jet associated with the nutation of the near-BH accretion flow. This non-smooth jet morphology may further enhance kink-like instabilities naturally present in these systems (Appl, Lery, and Baty, 2000; L.-X. Li, 2000; Narayan, J. Li, and Tchekhovskoy, 2009; Bromberg and Tchekhovskoy, 2016). At larger distances, the interaction with the ambient wind gradually smooths out these features. We can also see how the jet is quenched at a later time.

In Fig. 3.6, we show the distribution of the radially outgoing electromagnetic flux $(T_{\rm EM})^t{}_r$ at $r = 100r_g$. The opening angle of the jet shows variations between 15°

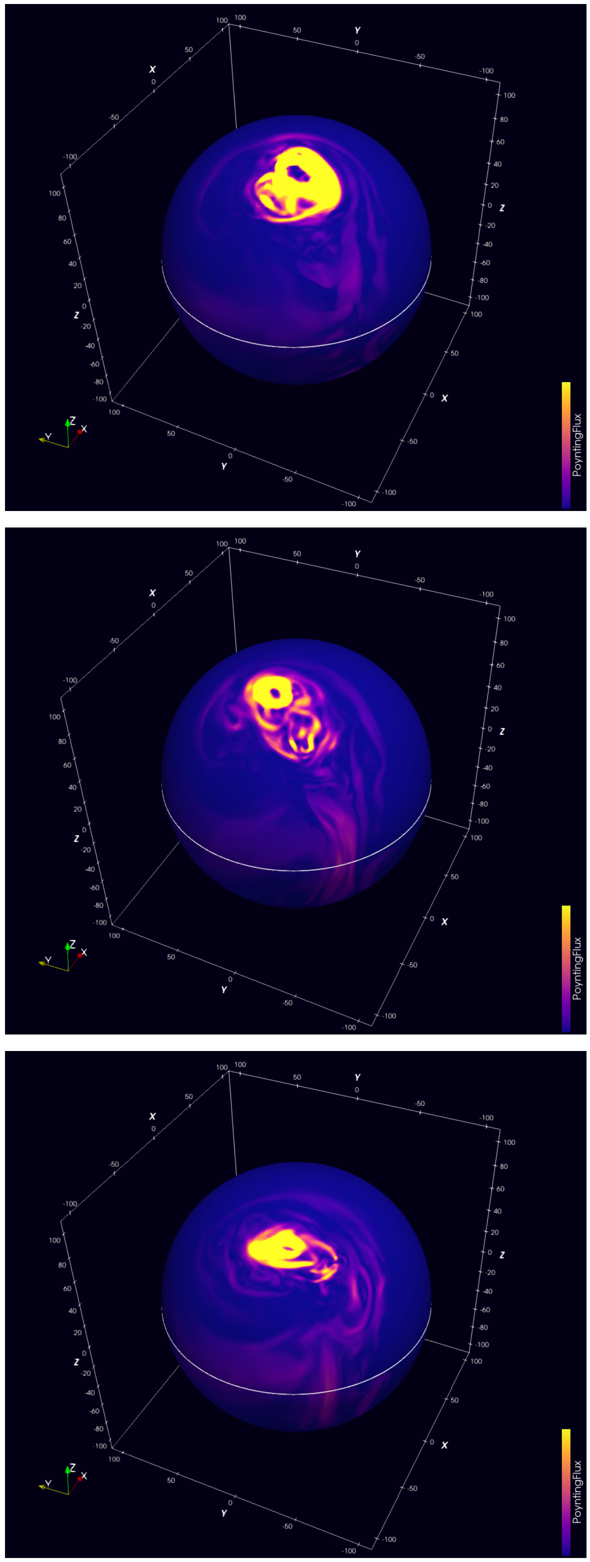

Figure 3.6: Distribution of the radial Poynting flux, $(T_{\mathrm{EM}})^{t}{}_{r}$, on the upper hemisphere of a spherical surface $r = 100 r_g$ at $t = 19600\, r_g/c$ (top), $t = 19800\, r_g/c$ (center), and $t = 20000\, r_g/c$ (bottom).

and 25°, where the position of the peak Poynting flux (center of the jet) precesses with an amplitude $\lesssim 15°$. While the jet still exhibits an oscillatory behavior at this radius to some extent, its angular variations remain much smaller than the inner accretion disk attached to the BH. We expect that these variations will be further attenuated at a larger radius.

3.3.3 Drag and spin-down

Here we look into the transport of linear and angular momentum between the BH and the accretion flow, which are responsible for the deceleration and spin-down of the BH. A time scale which we will frequently refer to for the discussions in this section is the mass doubling timescale $\tau_M = M/\dot{M}$, which can be rescaled using the BHL mass accretion rate $\dot{M}_{\rm BHL}$ as

$$\begin{aligned} \tau_M = 2.8 \times 10^4 \left(\frac{\dot{M}}{\dot{M}_{\rm BHL}} \right)^{-1} \left(\frac{v_\infty}{1000\,{\rm km\,s^{-1}}} \right)^3 \\ \times \left(\frac{\rho_\infty}{10^{-10}\,{\rm g\,cm^{-3}}} \right)^{-1} \left(\frac{M}{100 M_\odot} \right)^{-1} {\rm yr}\,. \end{aligned} \tag{3.42}$$

The normalized mass accretion rate is $\dot{M}/\dot{M}_{\rm BHL} \sim 0.1$ in our simulation (see Fig. 3.3).

Drag force

An accretor traveling through a gaseous medium is subject to a dynamical friction (Chandrasekhar, 1943). The reference scale of this drag is $\dot{M}_{\rm BHL} v_\infty$, which is the drag force in the ballistic (dust) limit, and a multiplicative correction factor needs to be included in generic cases.[5] For convenience, we define the fudge factor

$$f^i_{\rm BHL} \equiv F^i / (\dot{M}_{\rm BHL} v_\infty) \tag{3.43}$$

where F^i is the measured drag force in each directions. Since our simulation is performed in a fixed spacetime and does not consistently capture the slow-down of the BH in dynamical general relativity, the drag force is estimated by means of an approximate formula Eq. (3.29).

The bottom panel of Fig. 3.3 shows the time variation of the total drag force normalized with the BHL drag scale $\dot{M}_{\rm BHL} v_\infty$, effectively displaying the factor $f^i_{\rm BHL}$ for each spatial directions. The tangential drag (dynamical friction) reaches a

[5]Newtonian studies suggest that the correction is not expected to exceed a factor of ten in hydrodynamic BHL accretion (Edgar, 2004).

steady value of $f^x_{\rm BHL} \sim 2.5$ around $t = 5\times10^4 r_g/c$. The linear momentum accretion rate $F^x_{\rm mom}$ is nearly zero when time averaged, yet it is very oscillatory. It is the gravitational drag $F^x_{\rm grav}$ that constitutes a dominant net portion of the total drag. See Appendix 3.A for the raw time series data of $F^x_{\rm mom}$ and $F^x_{\rm grav}$. A similar trend is observed for F^y and F^z as well, suggesting that the accretion flow plunging into the BH is mostly symmetric when averaged over time. However, we note that $F^y_{\rm mom}$ shows a small positive average $\sim 0.1\dot{M}_{\rm BHL}v_\infty$.

The drag force results in a slow-down of the BH relative to the surrounding medium. The deceleration time scale can be estimated by dividing the initial BH linear momentum by the drag force

$$\tau_{\rm dec} = \frac{M v_\infty}{f_{\rm BHL}(\dot{M}_{\rm BHL} v_\infty)} = (f_{\rm BHL})^{-1}\,\tau_M \tag{3.44}$$

where the mass doubling timescale τ_M is given as Eq. (3.42). Plugging in $\dot{M}/\dot{M}_{\rm BHL} \sim 0.1$ and $f_{\rm BHL} \sim 2.5$ from our fiducial simulation, we get $\tau_{\rm dec} \sim 10^5$ yr for the representative values of v_∞, ρ_∞, M chosen in (3.42).

On top of the drag force F^x tangential to the direction of BH motion, there exist nonzero transverse drag (F^y) and vertical drag (F^z) which are perpendicular and parallel to the BH spin. These drags can potentially induce a deflection or oscillatory features in the trajectory of the accreting BH. The transverse drag force F^y shows an average magnitude $\approx 0.5\dot{M}_{\rm BHL}v_\infty$, which is about 20% of the tangential drag F^x. The vertical drag F^z has a similar magnitude as the transverse part F^y. The transverse drag F^y maintains a positive finite value where the vertical drag periodically flips its sign between eruption epochs. Each of these components are intimately related with the gravitational Magnus effect (Sec. 3.5.2) and the magnetic reversal of jets (Sec. 3.3.4) observed in our simulations.

Spin-down

As previously noted, in our setup, the spin effect from the BH is the only physical origin of circulation introduced in the accretion flow. From Fig. 3.3, we see that the angular momentum transport rate from the BH into accretion flows is $\dot{J} \approx 0.1\dot{M}_{\rm BHL} r_g c$ during eruption epochs where it is reversed during quiescent periods. Angular momentum in the disk is mainly transported in flux eruption episodes (Chatterjee and Narayan, 2022), where the overall spin-down of the BH is largely affected by the jet as well (Lowell et al., 2024). Since our problem setup (BHL accretion) is different from a commonly referenced MAD configuration which is being reached starting from an accreting torus, it is noted that an additional feedback mechanism might contribute to the angular momentum transport.

A systematic investigation on the spin-down of a BH in the MAD state showed that the characteristic decaying time of the BH dimensionless spin $Jc/GM^2 = a/r_g$ is about 10% of the mass doubling time scale (Lowell et al., 2024). To explore the same aspect but for the BHL accretion, we estimate the spin-down rate of the BH during an active phase in our simulation as follows. The angular momentum loss timescale of the BH can be estimated as

$$\tau_J = \frac{J}{\dot{J}} = \left(\frac{\dot{J}}{\dot{M}_{\mathrm{BHL}} r_g c}\right)^{-1} \left(\frac{\dot{M}}{\dot{M}_{\mathrm{BHL}}}\right) \left(\frac{a}{r_g}\right) \tau_M \, . \tag{3.45}$$

Our simulation results (Fig. 3.3) shows $\dot{J}/(\dot{M}_{\mathrm{BHL}} r_g c) \approx 0.1$ and $\dot{M}/\dot{M}_{\mathrm{BHL}} \approx 0.05$, indicating $\tau_J \sim \tau_M/2$. Then the spin-down timescale of the dimensionless spin a/r_g can be estimated as

$$\frac{a}{r_g} \propto \frac{J}{M^2} \propto \frac{e^{-t/\tau_J}}{e^{2t/\tau_M}} \sim e^{-4t/\tau_M} \, , \tag{3.46}$$

yielding a slightly longer spin-down timescale $\tau_M/4$ than $\approx \tau_M/10$ from Lowell et al. (2024). This rather lower rate of the angular momentum extraction from the BH can be attributed to the fact that in our case the accretion flow stays in a mildly MAD state ($\phi_{\mathrm{BH}} \approx 20$).

3.3.4 Magnetic reversal

Within the simulation time of the model ($t \leq 6 \times 10^4 \, r_g/c$), the BH and the accretion flow undergo two quiescent periods at $t = 10\tau_a$ and $t = 24\tau_a$. While all other quantities show a recurring pattern of rise and fall in every eruption epoch, the vertical drag force F^z (see the bottom line plot of Fig. 3.3) shows a distinct behavior in that it flips its sign during a quiescent period and maintains that opposite sign for the next eruption epoch, before coming back to the original sign after another quiescent period.

We find that the polarity of the horizon magnetic fluxes and jets is reversed during these quiescent periods, namely that the MAD state experiences a magnetic reversal between eruption epochs; see Fig. 3.7. This reversal behavior is observed from all models with a purely horizontal magnetic field ($\theta_B = 90°$) of the incoming fluid. Unfortunately, our simulation is too short to conclusively decide whether the polarity selection always alternates or is stochastic. We postpone a detailed discussion on the origin of this phenomena to future studies.

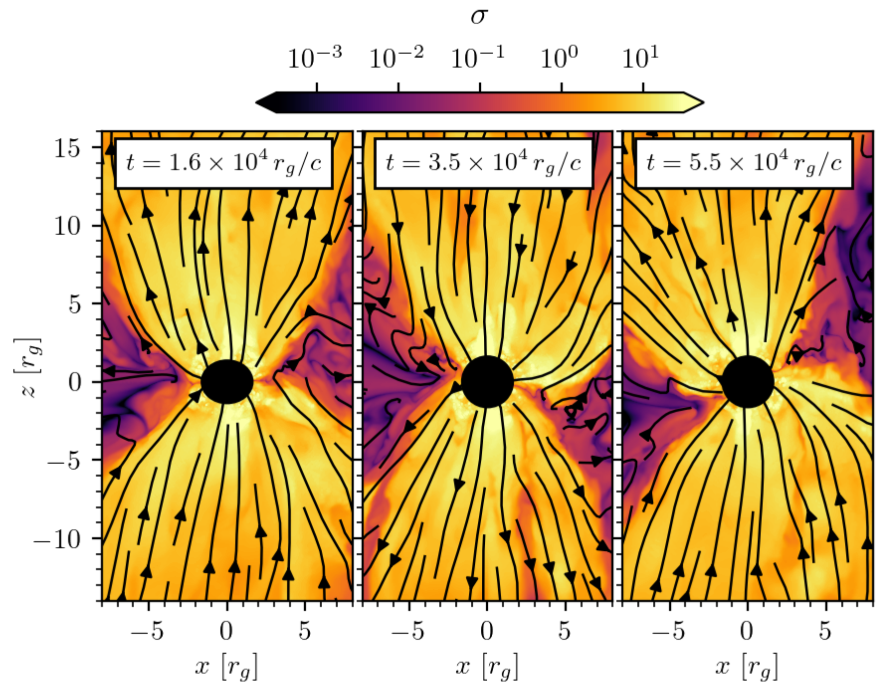

Figure 3.7: Magnetic field reversal of the jets between three eruption epochs in the fiducial model (β_{10}-θ_{90}-R_{200}). The relativistic magnetization σ is shown in color and the in-plane components of the magnetic field are shown with black streamlines.

3.4 Dependence on accretion parameters

In this section, we present a systematic survey of the accretion parameters. We change the inclination angle θ_B between the incoming magnetic field and the BH spin (Sec. 3.4.1), then explore a weakly magnetized case with $\beta_\infty = 100$ (Sec. 3.4.2), followed by different incoming speeds of the fluid v_∞ (Sec. 3.4.3). Rather than delving into the same level of detail as the previous section, here we provide a broader overview on qualitative impacts of the physical parameter chosen to be varied.

3.4.1 Mixed magnetic fields

Keeping other parameters fixed as the fiducial setup, the inclination angle of the initial magnetic field was varied to $\theta_B = 22.5°, 45°, 67.5°$. The purpose of this experiment is to investigate how much the inclination of the incoming magnetic field relative to the BH spin affects jet launching and the time evolution of accretion flow.

In Fig. 3.8, we present the time series data from the three simulations varying θ_B. The result from the fiducial model β_{10}-θ_{90}-R_{200} is overlayed with a transparent

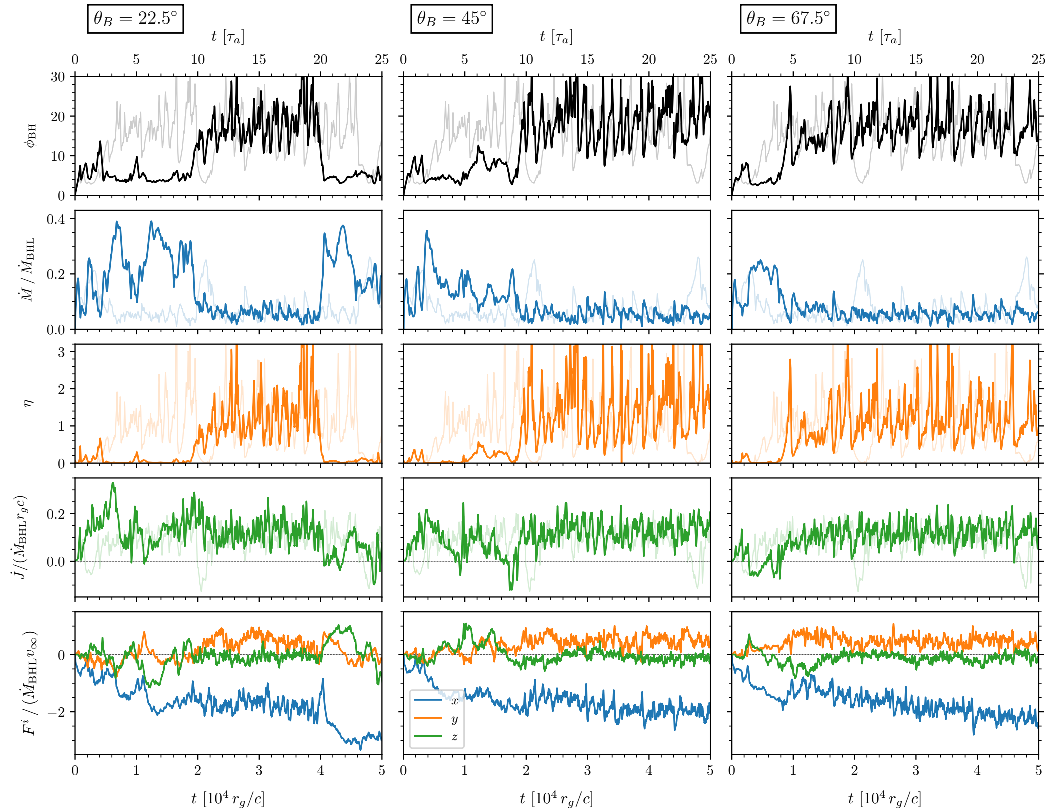

Figure 3.8: Time evolution of physical quantities for three models with $\theta_B = 23.5°$, $45°$ and $67.5°$, all with $\beta = 10$ and $R_a = 200$. See Fig. 3.3 for a description of the quantities shown. The result from the $\theta_B = 90°$ (fiducial) model is overlayed with a transparent line.

line in each panels to highlight deviations. While the overall correlations between each physical quantities is similar to that of the fiducial setup, we compile several observations below.

(i) The time it takes from the beginning of the simulation to the first successful jet launching and transition to the MAD state is longer for smaller inclination angle, namely when the incoming magnetic field has more vertical component. Interestingly, the maximally misaligned case (θ_{90}) launches the jet the earliest.rm

(ii) Within the simulation time $t \leq 5 \times 10^4 r_g/c$, both $\theta_B = 45°$ and $\theta_B = 67.5°$ models did not show any quiescent period; the first eruption epoch continued throughout the final time. In contrast, the $\theta_B = 22.5°$ model turned into a quiescent state after a single eruption epoch of a duration $10\tau_a$, and did not revive its jet activity until the end of the simulation, showing a quiescent

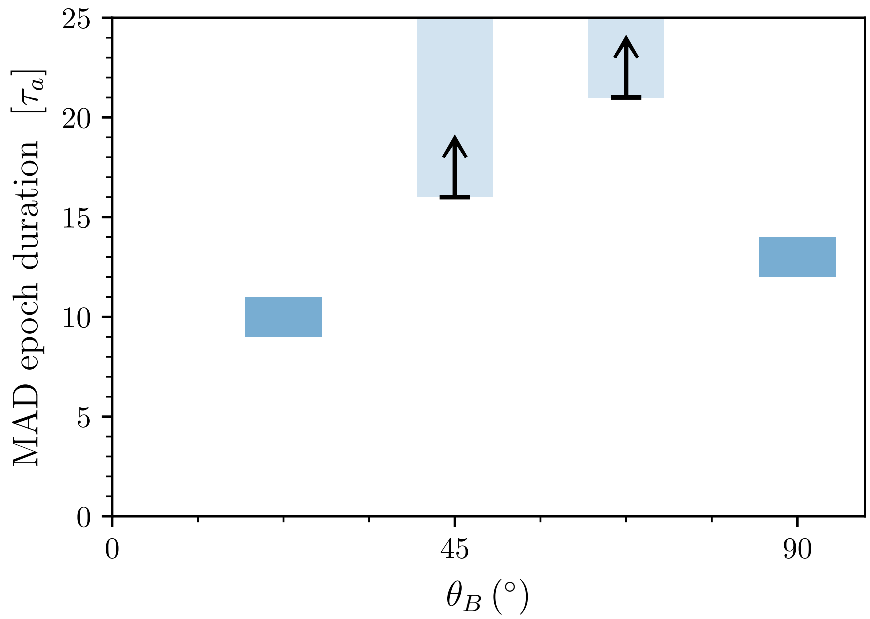

Figure 3.9: Duration of a magnetically arrested accretion epoch in units of the accretion timescale $\tau_a = 2000 r_g/c$ for the four models with $R_a = 200 r_g$ and $\beta_\infty = 10$.

period with the duration at least longer than $5\tau_a$. The BH fails to establish a MAD state during this quiescent period, where its episodic launching of weak outflows ($\eta \lesssim 10\%$) into random directions appears to be very similar to what was observed from low angular momentum accretion flows (Ressler, Quataert, et al., 2021; Kwan, L. Dai, and Tchekhovskoy, 2023; Lalakos et al., 2024; Galishnikova et al., 2025).

(iii) However, once the BH enters the eruption (MAD) state, values of $\phi_{\rm BH}$, $\dot{M}$, η and $\dot{J}$ are almost same as the $\theta_B = 90°$ case for all models. This implies that quasi-stationary properties of the MAD state in this setup do not depend on the large scale magnetic field geometry, which only determines the time period between eruption epochs.[6] In Fig. 3.9, we plot the θ_B dependence of the duration of eruption epochs we could observe from our simulations, while we could only constrain lower bounds for $\theta_B = 45°$ and $\theta_B = 67.5°$ cases. Our results indicate a non-monotonic behavior of the eruption epoch duration

[6] Kaaz, Murguia-Berthier, et al. (2023) adopts a similar parameter regime as in this work, apart from $\mathcal{M} = 2.45$ and $\theta_B = 0°$. In an active (jet) state, the mass accretion rate $\dot{M}/\dot{M}_{\rm BHL} \approx 0.05$ and the energy outflow efficiency $1 \lesssim \eta \lesssim 3$ observed in our simulation agree with those from Kaaz, Murguia-Berthier, et al., 2023, while the average value of $\phi_{\rm BH}$ appears to be somewhat lower in our study.

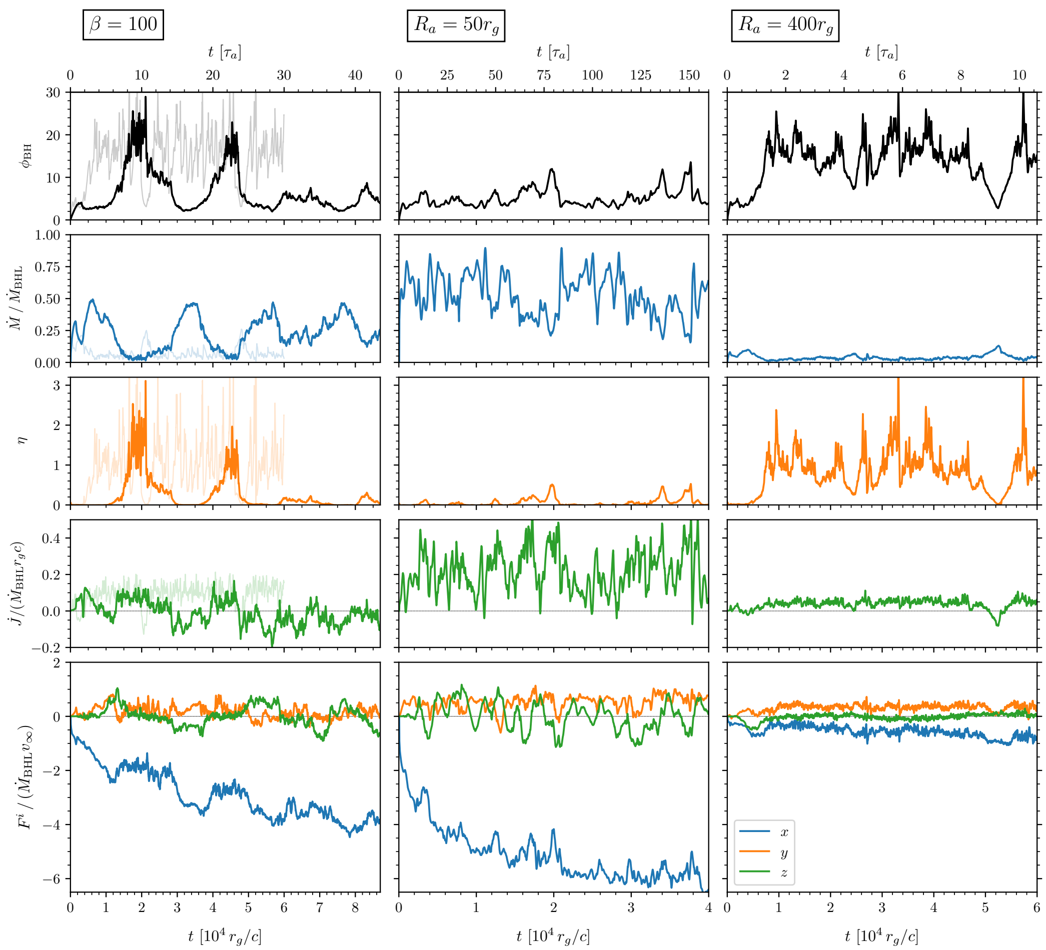

Figure 3.10: Time series data for the β_{100}-θ_{90}-R_{200} (left), β_{10}-θ_{90}-R_{50} (center), and β_{10}-θ_{90}-R_{400} (right) models. See Fig. 3.3 for a description of the quantities shown. We overlay the result from the fiducial (β_{10}-θ_{90}-R_{200}) model with a transparent line only for the β_{100}-θ_{90}-R_{200} model (first column).

with the magnetic field orientation θ_B, but an exact functional relationship between them is highly uncertain due to an insufficient number of data points and limited numerical resolution surveys.

3.4.2 Lower magnetization

The first column of Fig. 3.10 shows the time series of accretion quantities for the model β_{100}-θ_{90}-R_{200}, which has ten times weaker magnetization of the incoming fluid compared to the fiducial model. Several peculiar features observed in this model compelled us to perform a longer time integration up to $t = 8.7 \times 10^4 r_g/c$. We outline those below.

The evolution of the horizon magnetic flux $\phi_{\rm BH}$ roughly follows a similar cycle.

However, it undergoes more gradual increase and fall of $\phi_{\rm BH}$ between eruption and quiescent periods, exhibiting relatively short duration of eruptions and a longer quiescent period. The BH cannot sustain the MAD state long enough as the $\beta = 10$ case and takes longer to revive jets once it goes quiescent, which is consistent with the upstream wind providing a smaller amount of magnetic flux per time. These trends, along with an increased $\dot{M}/\dot{M}_{\rm BHL} \approx 0.5$ in a quiescent period and decreased average values of $\phi_{\rm BH}$, η during an active period, is similar to the results of Kaaz, Murguia-Berthier, et al. (2023) despite a different incoming magnetic field geometry.

Another observation that can be made from the result, owing to a prolonged duration of a quiescent period, is a reduced (or a reduced accumulation of) dynamical drag F^x over an eruption period. A strong, low-density bipolar jets launched from the BH pushes the gas outward, dropping the average mass density in the region trailing behind the BH (X. Li et al., 2020).

The third eruption epoch ($28\tau_a \lesssim t \lesssim 36\tau_a$), though not as conspicuous as the first two, ends up staying only in the mildly MAD regime $\phi_{\rm BH} \leq 10$. We observe the fourth round of rising magnetic fluxes at $t = 40\tau_a$ during which horizon magnetic fluxes also stayed below $\phi_{\rm BH} = 10$. In brief, the system exhibits a periodic eruption-quiescence cycle similar to what is observed in our fiducial model, but with a decreasing level of activity over time. We caution that the decay we see may be correlated with numerical resolution and scale separation between the BH and the outer simulation domain boundary.

3.4.3 Faster/slower incoming speed

Time evolution of the models with a faster ($R_a = 50r_g$, $v_\infty = 0.2c$) and a slower ($R_a = 400r_g$, $v_\infty = 0.07c$) speed of the incoming fluid are shown on the second and third columns in Fig. 3.10. We show the mass density distribution on the meridional plane for the two models in Fig. 3.11, highlighting differences in the shape and radius of the bow shock, as well as the bending angle of outflows from the BH.

We first examine the case with a faster incoming speed ($R_a = 50r_g$). The outflow launched in the polar directions is choked by a strong ram pressure. The BH exhibits sporadic flux eruptions and launches outflows intermittently, but fails to maintain a continuous jet. While the horizon magnetic flux is kept below $\phi_{\rm BH} \leq 10$, the mass accretion rate shows a large oscillation between 0.3–0.9 $\dot{M}_{\rm BHL}$, highly anti-correlated with $\phi_{\rm BH}$. While the dynamical time of the accretion flow around the BH is the same independent of the wind speed, the replenishing timescale of the flux changes

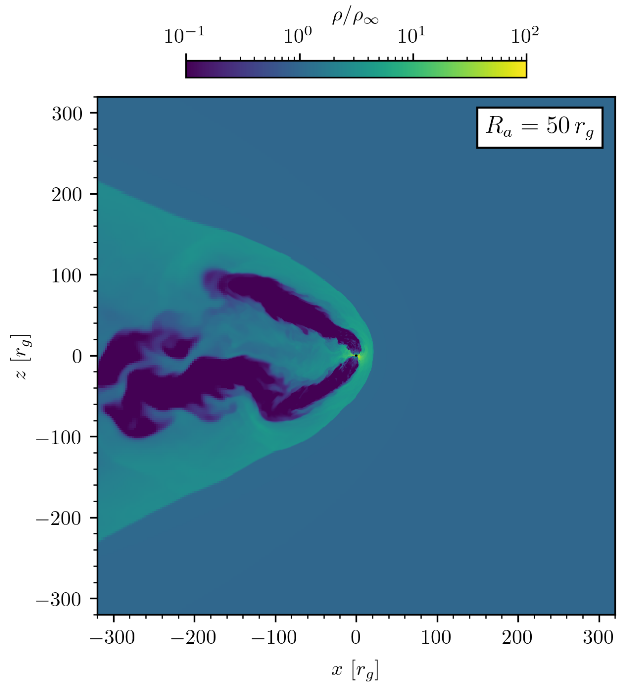

(a) $R_a = 50r_g$ (at $t = 2 \times 10^4\, r_g/c$)

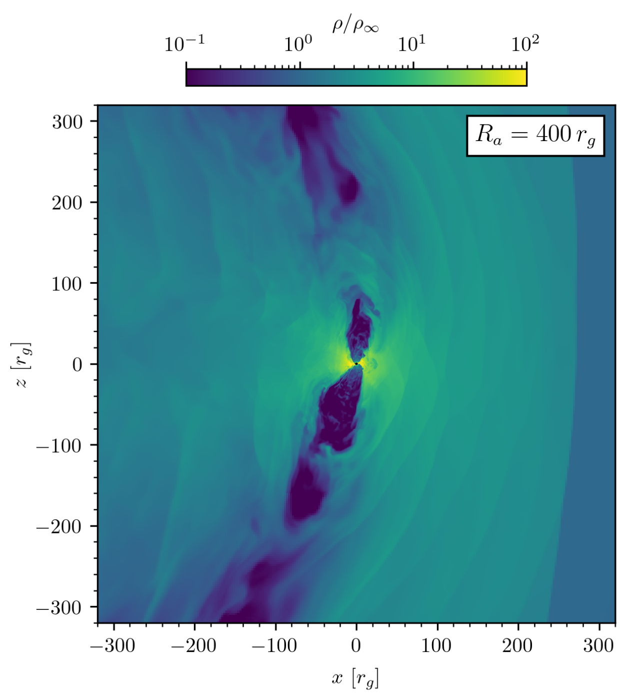

(b) $R_a = 400r_g$ (at $t = 4 \times 10^4\, r_g/c$)

Figure 3.11: Distribution of the mass density ρ in the meridional plane for the simulations β_{10}-θ_{90}-R_{50} (top) and β_{10}-θ_{90}-R_{400} (bottom). R_a is the accretion radius, r_g is the gravitational radius of the black hole, and ρ_∞ is asymptotic mass density of the wind.

with R_a. For faster wind speeds, the cross section of the bow shock shrinks, with less mass being accreted on the BH, though more relative to the changed reference rate, $\dot{M}_{\rm BHL}$. The BH then preferentially accretes in a SANE regime, even if the magnetic properties of the wind at large scales remain the same. This likely implies that questions about flux accumulation on the black hole horizon in BHL accretion cannot be separated from the effective speed of the black hole. We also observe that the tangential drag reaches $f^x_{\rm BHL} \approx 6$ by the end of the simulation; recall that $f^x_{\rm BHL} \approx 2.5$ in our fiducial model with $R_a = 200r_g$.

Next, we examine the model with a slower incoming speed of fluid ($R_a = 400r_g$). The accretion flow reaches the MAD state relatively early at $t \sim 1.5\tau_a$. The shorter time for the flow to become magnetically arrested is consistent with the scaling argument presented in Kaaz, Murguia-Berthier, et al. (2023),

$$\tau_{\rm MAD}/\tau_a \propto R_a^{-3/4}, \tag{3.47}$$

while we note the exponent can be slightly different for an inclined magnetization of the inflow. The accretion flow enters a quiescent period at $t \sim 9\tau_a$ and revives jets at $t \sim 10\tau_a$, also showing a magnetic reversal behavior. The overall time evolution of this model is qualitatively very similar to the fiducial model discussed in Sec. 3.3. The dynamical friction measured by the end of the simulation was $f^x_{\rm BHL} \sim 1.0$. However, we expect a higher value in practice as the measured value of the drag had not fully reached a steady state during our integration time. We also observe that the magnitude of the vertical drag is reduced to $|f^z_{\rm BHL}| \sim 0.1$ and the correlation of its sign and the magnetic polarity of the jet has become weaker compared to the fiducial model. The vertical drag occasionally turns to a positive value during $2.5\tau_a \leq t \leq 4.5\tau_a$ where the direction of magnetic field threading the BH and the jet has been steadily kept to $+\hat{z}$ during the period. Considering that the astrophysically realistic speed of the BH is still much beyond the lower limit of v_∞ explored in this study, it follows that the vertical drag F^z may be effectively uncorrelated or only weakly correlated with the magnetic polarity of jets in realistic situations.

3.5 Discussion

3.5.1 Energy outflow

Fig. 3.12 compares the net energy outflow power $P = \dot{M}c^2 - \dot{E}$ for all models. Once the accretion enters the MAD state, the energy outflow power does not show much dependence on the inclination angle θ_B of the incoming magnetic field. A slight decrease in the power is observed when the magnetization of the incoming medium

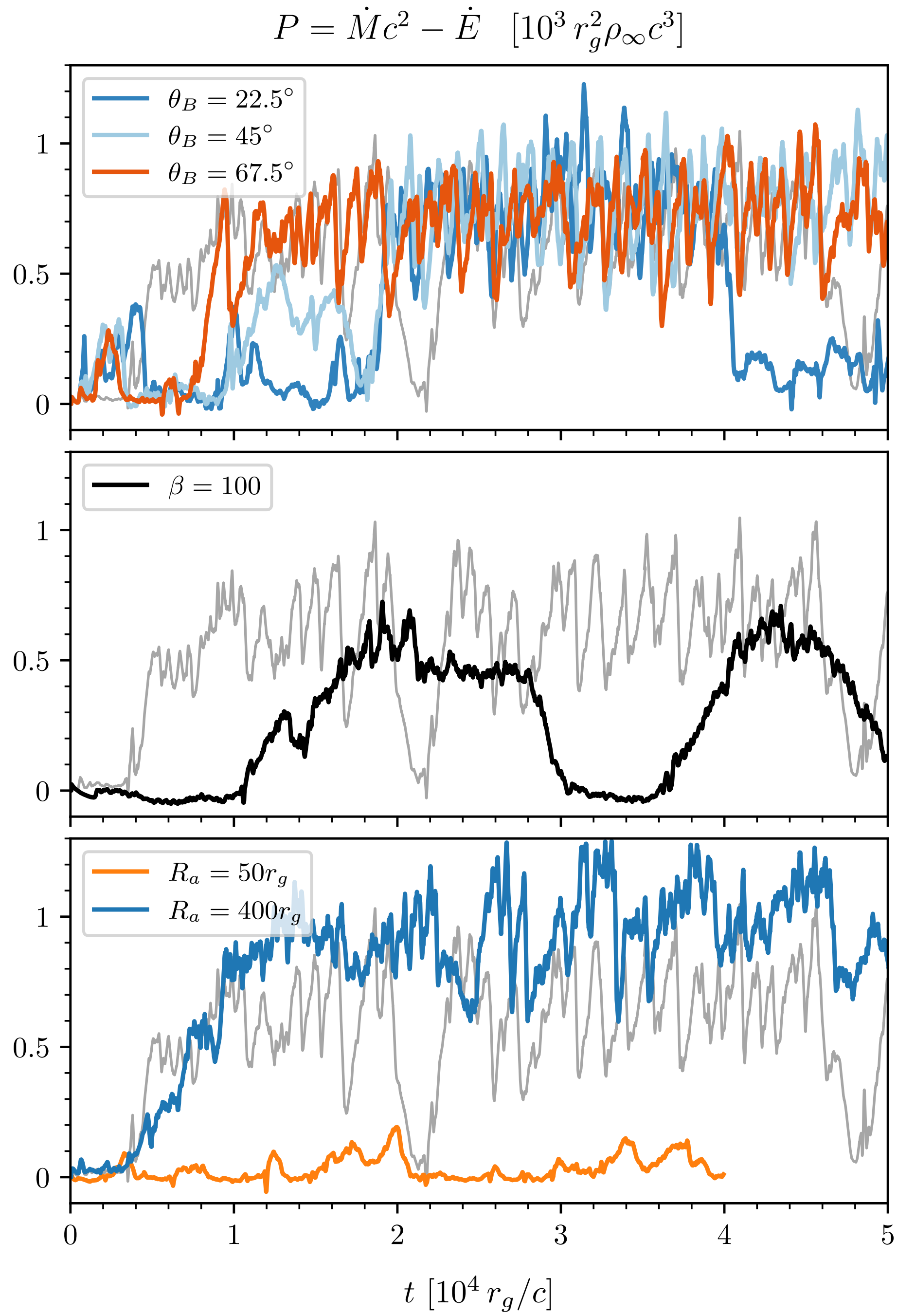

Figure 3.12: The energy outflow power $P = \dot{M}c^2 - \dot{E}$ from all simulations. The gray line shows the result from the fiducial model. For the scaled efficiency $\eta\dot{M}/\dot{M}_{\rm BHL}$, see Fig. 3.13.

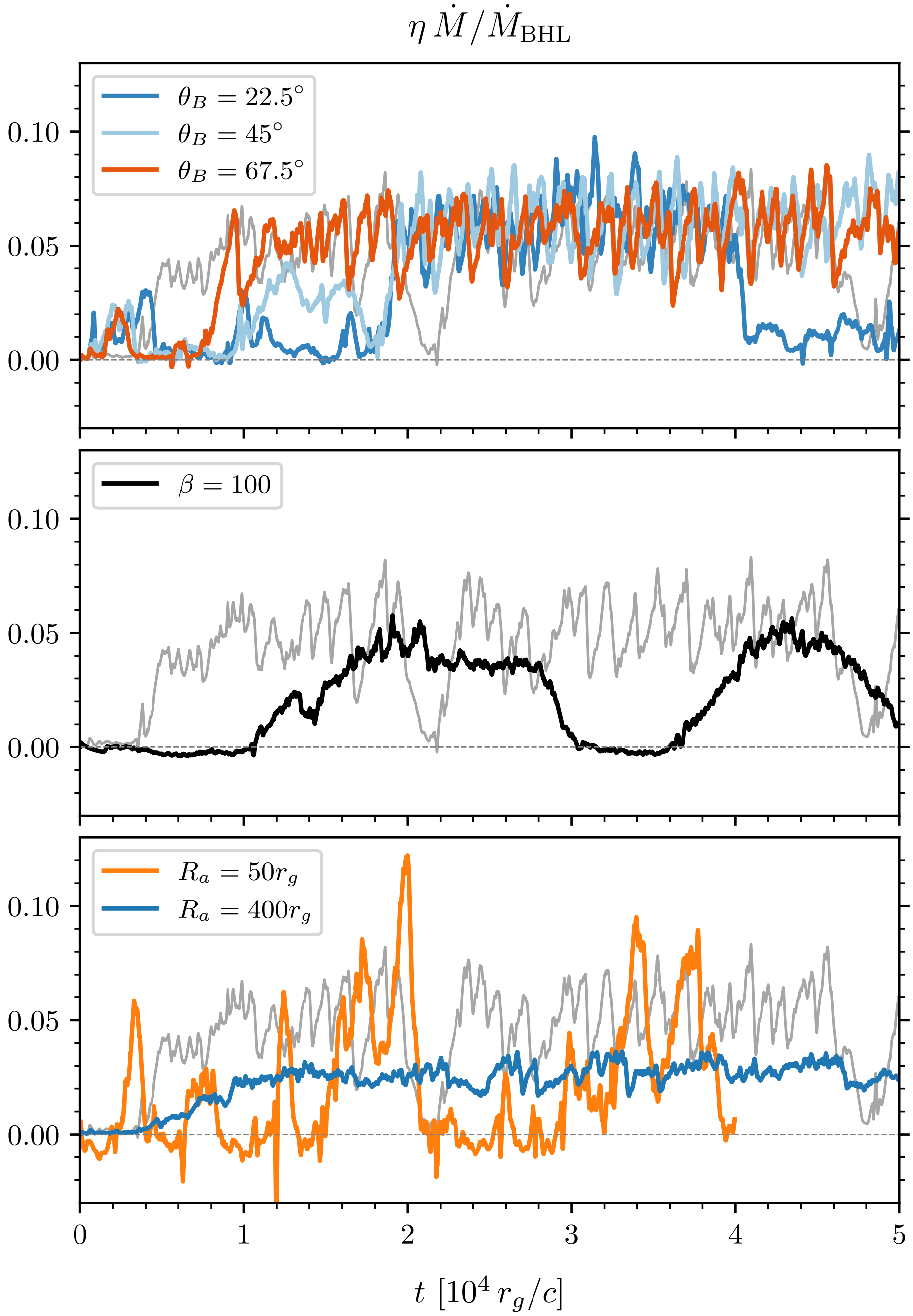

Figure 3.13: The energy conversion efficiency $\eta\dot{M}/\dot{M}_{\rm BHL}$ from all simulations. The gray line shows the result from the fiducial model β_{10}-θ_{90}-R_{200}.

is lower, which can be attributed to a reduced supply of magnetic energy to the BH per unit time. Likewise, an increased energy outflow for a slower speed of incoming fluid can be understood as that of a slowly moving BH with a large accretion radius, leading to a higher mass accretion rate ($\dot{M}_{\rm BHL} \propto v_\infty^{-3}$), and consequently a higher rate of magnetic flux injection onto BH, resulting in a more powerful energy outflow (and vice versa).

Our results indicate that among the accretion parameters varied in this study, the energy outflow is most significantly influenced by the fluid speed v_∞ and to a lesser extent by the magnetization of the incoming matter (note that the BH speed is v_∞ varied by a factor of two at most, where magnetization is set to be ten times weaker in the $\beta = 100$ model). The magnetic field inclination angle θ_B has a negligible impact on the outflow power during eruption epochs. However, it largely effects the time evolution and the intermittency of the jet activity, as previously discussed in Sec. 3.4.1.

The finding from this comparative analysis, namely that the BH speed v_∞ is a primary factor in determining the outflow luminosity, also aligns with the fact that basic physical scales of the BHL accretion e.g., Eq. (3.1)–(3.3) possess a strong dependence in v_∞ with the highest power exponent.

A reference scale of the energy outflow power in physical units can be written as

$$
\begin{aligned}
P &= \eta \left(\frac{\dot{M}}{\dot{M}_{\rm BHL}} \right) \dot{M}_{\rm BHL} c^2 \\
&= 1.0 \times 10^{43} \left(\frac{\eta \dot{M} / \dot{M}_{\rm BHL}}{0.05} \right) \left(\frac{M}{100 M_\odot} \right)^2 \left(\frac{\rho_\infty}{10^{-10}\,{\rm g\,cm^{-3}}} \right) \\
&\qquad \times \left(\frac{v_\infty}{1000\,{\rm km\,s^{-1}}} \right)^{-3} {\rm erg\,s^{-1}} \, .
\end{aligned}
\tag{3.48}
$$

The factor $\eta \dot{M} / \dot{M}_{\rm BHL}$ corresponds to an effective energy conversion efficiency with which the rest mass energy inflow $\dot{M}_{\rm BHL} c^2$ is converted into a net energy outflow. Our baseline setup (β_{10}-θ_{90}-R_{200}) shows the conversion efficiency ≈ 0.05 during an eruption epoch. See Fig. 3.13 for the values of $\eta \dot{M} / \dot{M}_{\rm BHL}$ from all models.

3.5.2 Magnus effect

As can be seen from Fig. 3.2, the downstream flow trailing the BH is deflected to the $-\hat{y}$ direction owing to the spin of the BH and a resulting circulatory flow surrounding it. This can result in two effects on the transverse drag force F^y: (1) the conservation of linear momentum requires the BH to experience a reaction force to

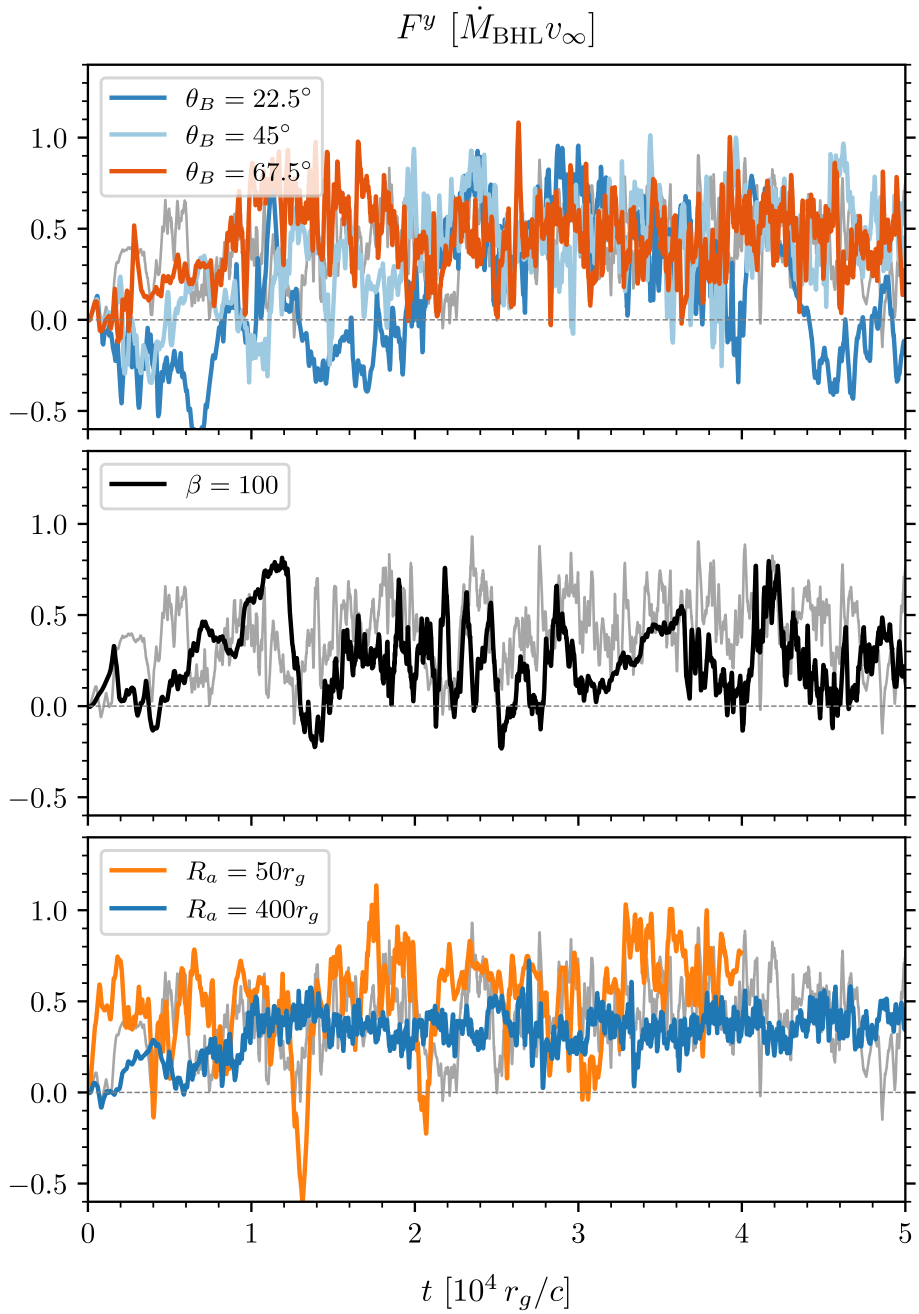

Figure 3.14: The drag force to the transverse (y) direction (Magnus force) in all simulations. The gray line shows the result from the fiducial model. A negative value corresponds to the anti-Magnus effect.

$+\hat{y}$ direction, where (2) since a more amount of matter is deposited to $y < 0$ region of the downstream, a net gravitational pull from the flow is enhanced toward $-\hat{y}$ direction. These two effects are competing with each other, and the direction of the net drag will be highly dependent on the nature of the accretion flow.

A nonzero transverse drag F^y is the manifestation of the (general-relativistic analog of the) Magnus effect, the phenomenon in the classical fluid dynamics that a spinning body moving through a fluid experiencing a drag force normal to both the direction of its motion and spin. Although its physical origin is different, a similar effect is expected to be present in general relativity when a spinning compact object is immersed in a mass-energy current not aligned with its spin axis (e.g., Font, Ibanez, and P. Papadopoulos, 1999; Okawa and Cardoso, 2014; Costa, Franco, and Cardoso, 2018).

However, the precise direction of this gravitational Magnus effect has been under debate when considering non-hydrodynamical types of matter (Okawa and Cardoso, 2014; Cashen, Aker, and Kesden, 2017; Costa, Franco, and Cardoso, 2018; Dyson et al., 2024; Z. Wang et al., 2024). Costa, Franco, and Cardoso (2018) argues that the gravitational Magnus force consists of two distinctive components (which they name as 'Magnus' and 'Weyl' respectively therein) and especially the Weyl component can be highly dependent on the specific scenario and boundary conditions of the physical system under consideration. A recent fully relativistic analysis (Dyson et al., 2024) has shown that the drag is always anti-Magnus for a collisionless particle-like matter field, where a wave-like scalar field shows a mixed behavior. A numerical relativity simulation on the BHL accretion of scalar dark matter (Z. Wang et al., 2024) has reported an anti-Magnus effect.

Font, Ibanez, and P. Papadopoulos (1999), to the best of our knowledge, is the only numerical study commenting on this phenomenon in the hydrodynamic regime, and suggested that the enhanced pressure of the accretion flow on the counter rotating side of the Kerr BH gives rise to the (pro-) Magnus effect, albeit without a quantitative argument.

We report in here that our physical scenario—3D GRMHD BHL accretion onto a spinning BH—yielded the positive sign of the Magnus force, analogous to the one in classical fluid dynamics. Fig. 3.14 collects and compares the Magnus force F^y from all models. For all the cases, the Magnus drag maintained a positive value for the most of the simulation time. While the gravitational drag force Eq. (3.31) we compute is not a fully general relativistic formula (see e.g., Costa, Franco, and Cardoso, 2018; Dyson et al., 2024; Z. Wang et al., 2024), it is very unlikely to change the direction of the Magnus effect we observe from simulations. We mention that previous numerical studies on the gravitational Magnus effect in a scalar field (Okawa and Cardoso, 2014; Z. Wang et al., 2024) have been carried out in a boosted metric, unlike our setup in which the black hole is fixed and the inflow is imposed in terms of fluid velocity, potentially causing a quantitative difference in the drag force.

It is also noteworthy that the magnitude of the Magnus force is not small, often rising to a level comparable to the BHL drag force scale $\dot{M}_{\rm BHL} v_\infty$. Across all models, we quote a conservative overall estimate that the Magnus force has been observed to be about 10% of the dynamical friction. In the circumstances that the initial linear momentum of the BH has been substantially lost by the dynamical friction, its traveling trajectory could have been largely deflected from its original direction of motion.

Our results have implications for a number of astrophysical contexts. In an extreme mass-ratio inspiral of binary black hole, if a secondary BH has spin and is surrounded by gaseous medium, the gravitational Magnus force on the secondary can alter its trajectory or excite an eccentricity to the orbit. The resulting features in gravitational waves can be potentially detectable with next generation gravitational wave detectors e.g., LISA (Afshordi et al., 2023). In the common envelope phase of a binary star, the drag force inside the gaseous envelope is responsible for the orbital decay and expansion of the envelope (Livio and Soker, 1988; Taam and Sandquist, 2000; Ivanova et al., 2013). Our findings imply that the BH orbiting within the envelope could experience the Magnus force when spiralling around the core of the companion star. Depending on the relative orientation of the BH spin to its direction of motion, the Magnus force can increase orbital eccentricity or induce precession of the orbital plane. This may have a considerable impact on the evolution of the BH orbit over long periods and the final configuration of the binary after the common envelope phase. We note that in this context a wind profile varying in the transverse direction needs to be taken into consideration as well, since the nonzero gradient in mass density or velocity leads to a misaligned, rotated shock cone geometry (Cruz-Osorio and Lora-Clavijo, 2016; Cruz-Osorio and Rezzolla, 2020; Lora-Clavijo, Cruz-Osorio, and Méndez, 2015) which in turn can significantly alter the direction of the total drag force.

3.6 Conclusion

We have conducted three-dimensional general-relativistic magnetohydrodynamic simulations of Bondi-Hoyle-Lyttleton accretion onto a spinning black hole when the magnetic field of the surrounding plasma is inclined with respect to the spin of the BH. Our primary motivation was to investigate the dynamics of a BBH merger remnant kicked into the disk of an active galactic nucleus, but owing to the ubiquitous applicability of the Bondi-Hoyle-Lyttleton accretion problem, our results are also applicable to broader astrophysical contexts. We summarize our main findings below.

- The accumulation of magnetic flux onto the BH establishes a magnetically arrested state of the accretion flow and launches relativistic outflows to polar directions, which are bent toward the downstream at a larger radius. The accretion disk surrounding the BH extends up to a few tens of r_g from the horizon, and is encompassed by a large-scale downstream flow in the shock cone.

- Quasi-periodic magnetic flux eruptions from the BH launch pressure waves expanding the bow-shaped shock cone, and release strongly magnetized blobs (flux tubes)—which can potentially power flare-type electromagnetic transients (e.g., Hakobyan, Ripperda, and Philippov, 2023; Zhdankin, Ripperda, and Philippov, 2023) —along the equatorial plane into a narrow range of angles relative to the wind direction.

- Anisotropic recoil from the magnetic flux eruptions drive a strong nutation on the accretion disk, often ripping its inner region off from the outer part. Nutation of the accretion disk is imprinted on the jet as its twisted morphology, potentially aiding the development of a kink instability (Bromberg and Tchekhovskoy, 2016).

- For a purely horizontal magnetized wind ($\theta_B = 90°$), the system periodically undergoes a quiescent period with the duration $\gtrsim \tau_a$, during which jet is quenched and the accretion flow relaxes to the SANE state. Magnetic polarity inversion is observed during this period.

- With an increasing inclination of the magnetic field relative to the BH spin, the jet is launched earlier. However, the energy outflow power and efficiency did not show significant differences once the system establishes a MAD state. The orientation of the incoming magnetic field appears to hardly affect steady-state properties of the jet, but determines the temporal behavior of its active and quiescent periods.

- The model with a lower magnetization $\beta = 100$ shows a more gradual evolution of ϕ_{BH} over active and quiescent epochs, as well as a slightly decreased energy outflow, which can be explained by a reduced supply of magnetic fluxes from the accretion flow.

- When subjected to a faster wind speed, a decreased dynamical cross section and an increased ram pressure on the BH results in the suppression of jet launching. On the other hand, the model with a slower wind speed reached the MAD state earliest relative to the accretion timescale τ_a, which is consistent with a qualitative argument made in Kaaz, Murguia-Berthier, et al. (2023). Energy outflow shows the strongest dependency in the wind speed among all parameters considered in this work. This strong dependence of the overall flow dynamics on the wind speed suggests that realistic values of v_∞ will be a crucial element for improved models of GRMHD BHL accretion.

- The gravitational Magnus effect is observed across all models, with the magnitude of a few tens of percents of the reference drag scale $\dot{M}_{\mathrm{BHL}} v_\infty$. The direction of the Magnus force is the same as its classical aerodynamic counterpart.

Whereas the accretion radius R_a adopted in this work has one of the largest values in literature for the general relativistic BHL accretion, it is still considerably far from a realistic condition. In the scenario of a kicked BBH post-merger remnant, the recoil velocity is $\lesssim 200\,\mathrm{km\,s^{-1}}$ for non-spinning binaries (Gonzalez, Sperhake, et al., 2007) where the spin effects can at most enhance the recoil up to $\approx 4000\,\mathrm{km\,s^{-1}}$ for 'superkick' configurations (Campanelli et al., 2007b; Gonzalez, Hannam, et al., 2007). Newtonian studies suggest that when a BBH is embedded in a gaseous environment, accretion makes their orbital and spin axes aligned (Bogdanovic, Reynolds, and Miller, 2007; Coleman Miller and Krolik, 2013), suppressing the superkick configuration. The maximum recoil for a spin-orbit aligned binary estimated from numerical relativity simulations is $\approx 500\,\mathrm{km\,s^{-1}}$ (Herrmann et al., 2007; Koppitz et al., 2007; Healy, Lousto, and Yosef Zlochower, 2014). Another physical system that can harbor a fast wind accreting onto a BH is an X-ray binary with a high-speed stellar wind; for example, Cygnus X-1 binary system features $v_\infty \gtrsim 1000\,\mathrm{km\,s^{-1}}$ (Davis and Hartmann, 1983; Gies et al., 2008; Grinberg et al., 2015). However, the orbital motion of the BH and a specific geometry of the wind present in these systems might require a deviation from the conventional BHL accretion setup.

Our present study opens up a number of different avenues for future work, with several questions still remaining to be answered. First, the energy outflow power can be affected by parameters other than those we have considered here: the magnitude of the BH spin, the inclination of the magnetic field relative to the wind velocity, the spin-wind orientation (Gracia-Linares and Guzmán, 2023), or hydrodynamic parameters such as the adiabatic index and the Mach number which are known to strongly influence the stability of the shock cone (Foglizzo, Galletti, and Ruffert, 2005). It would be also intriguing to investigate the inflow with a nonzero net angular momentum (Cruz-Osorio and Lora-Clavijo, 2016; Lora-Clavijo, Cruz-Osorio, and Méndez, 2015), which provides a more appropriate scenario for the common envelope phase. The inclusion of radiative effects (Zanotti, Roedig, et al., 2011) will also greatly change the dynamics for super-Eddington accretion flows. Future investigations would help constructing a more detailed physical picture of a black hole moving through a magnetized medium, with a better bridging of the scale gaps between currently available numerical models and realistic astrophysical scenarios.

Acknowledgements

We are grateful to James Stone, Jacob Fields, and Hengrui Zhu for technical support, and to Saavik Ford, James Fuller, Matthew Graham, Yuri Levin, Barry McKernan, Nicholas Rui, and Alexander Tchekhovskoy for insightful discussions. Simulations were performed on DOE OLCF Summit cluster under allocation AST198, and on DOE NERSC Perlmutter cluster under grant m4575. This research used resources of the Oak Ridge Leadership Computing Facility at the Oak Ridge National Laboratory, which is supported by the Office of Science of the U.S. Department of Energy under Contract No. DE-AC05-00OR22725, and resources of the National Energy Research Scientific Computing Center, which is supported by the Office of Science of the U.S. Department of Energy under Contract No. DE-AC02-05CH11231.

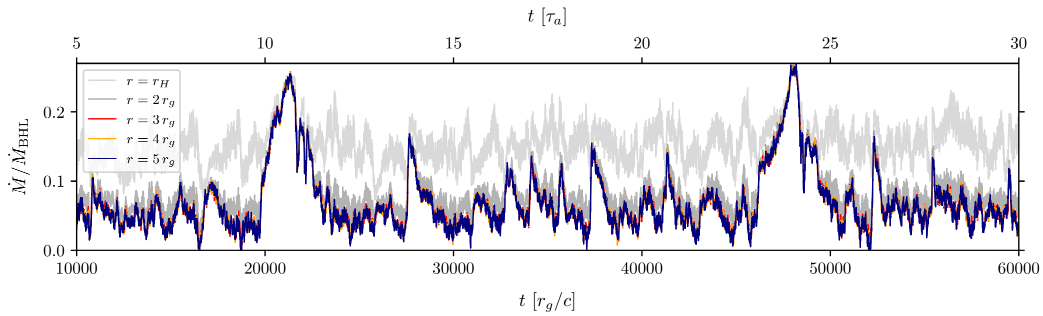

Figure 3.15: Mass accretion rate extracted at different radii for the β_{10}-θ_{90}-R_{200} model. All data points are displayed without smoothing.

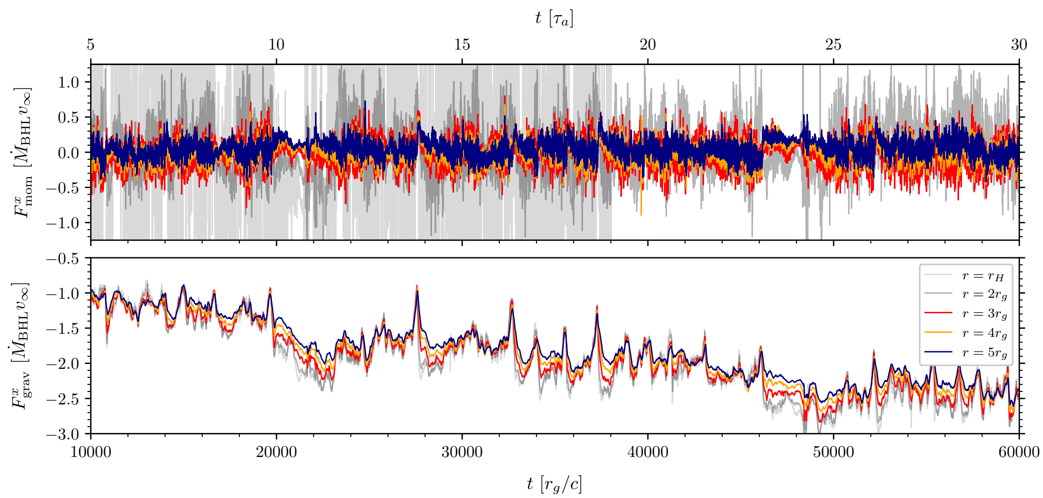

Figure 3.16: The $\hat{x}$ component of the momentum drag (top panel) and gravitational drag (lower panel) computed with different radii from the β_{10}-θ_{90}-R_{200} model. All data points are displayed without smoothing.

3.A Extraction radius of density-related integral quantities

As discussed in Sec. 3.2.4, the drift flooring algorithm artificially injects the mass density floor to maintain the comoving magnetization σ below an upper limit $\sigma_{\rm max}$. This often induces spurious increases in the fluid-related integral quantities when computed very close to the BH, where the magnetization is very high.

In Figure 3.15, we show the mass accretion rate $\dot{M}$ integrated at different radii $r_i = \{r_H, 2r_g, 3r_g, 4r_g, 5r_g\}$ from our representative model (β_{10}-θ_{90}-R_{200}) where $r_H = r_g(1 + \sqrt{1 - a^2/M^2})$ is the outer horizon radius. It can be clearly seen that the artificial effects from numerical flooring becomes almost absent in $r_i \geq 3r_g$.

Fig. 3.16 shows, for the same set of radii, the $\hat{x}$ component of the momentum drag $F^x_{\rm mom}$ computed at the spherical surface $r = r_i$ and the gravitational drag $F^x_{\rm grav}$

integrated over the whole computational domain except the spherical volume $r < r_i$. The momentum drag settles down to near zero for $r_i \geq 3r_g$. The magnitude of the gravitational drag monotonically decreases for a larger r_i since the region $r < r_i$ is simply excluded from the volume integral. The differences between them are not significant, indicating that the gravitational drag is mostly contributed from $r \geq 5r_g$.

Chapter 4

MAGNETOSPHERIC TRANSIENTS FROM BLACK HOLE–NEUTRON STAR MERGER

Kim, Yoonsoo et al. (2024). "Black Hole Pulsars and Monster Shocks as Outcomes of Black Hole–Neutron Star Mergers". In: *Astrophysical Journal Letters* 982.2, p. L54. DOI: 10.3847/2041-8213/adbff9. URL: https://iopscience.iop.org/article/10.3847/2041-8213/adbff9.

The merger of a black hole (BH) and a neutron star (NS) in most cases is expected to leave no material around the remnant BH; therefore, such events are often considered as sources of gravitational waves without electromagnetic counterparts. However, a bright counterpart can emerge if the NS is strongly magnetized, as its external magnetosphere can experience radiative shocks and magnetic reconnection during/after the merger.

We use magnetohydrodynamic simulations in the dynamical spacetime of a merging BH–NS binary to investigate its magnetospheric dynamics. We find that compressive waves excited in the magnetosphere develop into monster shocks as they propagate outward. After swallowing the NS, the BH acquires a magnetosphere that quickly evolves into a split monopole configuration and then undergoes an exponential decay (balding), enabled by magnetic reconnection and also assisted by the ring-down of the remnant BH. This spinning BH drags the split monopole into rotation, forming a transient pulsar-like state. It emits a striped wind if the swallowed magnetic dipole moment is inclined to the spin axis. We predict two types of transients from this scenario: (1) a fast radio burst emitted by the shocks as they expand to large radii and (2) an X/γ-ray burst emitted by the $e^{\pm}$ outflow heated by magnetic dissipation.

4.1 Introduction

Merging black hole (BH)–neutron star (NS) binaries are promising sources of gravitational waves (GWs) (see, e.g., R. Abbott et al., 2021b; R. Abbott et al., 2020; Abac et al., 2024, for recent detections). Depending on the mass ratio of the system and spin of the black hole, near-equal mass systems can feature tidal disruption of the neutron star during merger, leading to dynamical mass ejection and the formation of a massive disk (Foucart, 2012; Foucart, Hinderer, and Nissanke, 2018). These can power electromagnetic (EM) counterparts such as kilonova afterglows (Lattimer and Schramm, 1974; L.-X. Li and Paczynski, 1998; Tanaka et al., 2014; Kawaguchi, Kyutoku, et al., 2016; Fernández et al., 2017; Metzger, 2020; Gottlieb et al., 2023b; Kawaguchi, Domoto, et al., 2024) and gamma-ray bursts (GRBs) (Janka et al., 1999; Etienne, Liu, et al., 2012; Etienne, Paschalidis, and Shapiro, 2012; Paschalidis, Ruiz, and Shapiro, 2015; Shapiro, 2017; Ruiz, Shapiro, and Tsokaros, 2018; Hayashi, Fujibayashi, et al., 2022; Gottlieb et al., 2023a; Martineau et al., 2024). However, the high mass ratio typical of such systems (R. Abbott et al., 2021b; Abac et al., 2024) would likely result in a non-disruptive merger, leaving little or no matter surrounding the remnant BH (Foucart, 2012; Foucart, Hinderer, and Nissanke, 2018). Most BH–NS mergers are expected to fall in this latter category and be EM-quiet (Fragione, 2021; Biscoveanu, Landry, and Vitale, 2022), supported by the absence of EM counterparts to previous detections (e.g. Anand et al., 2021).

On the other hand, neutron stars can be equipped with strong exterior magnetic fields, leading to potential EM counterparts from magnetospheric interactions with their binary companion. Previously studied scenarios can be broadly split into two groups. Transients before merger (precursors) can be produced through magnetospheric interactions (McWilliams and J. Levin, 2011; Lai, 2012; Piro, 2012; Paschalidis, Etienne, and Shapiro, 2013; Carrasco, Viganò, et al., 2019; Carrasco, Shibata, and Reula, 2021) including flares (Most and Philippov, 2023a; Beloborodov, 2021), or through gravitationally driven resonances in the neutron star such as crustal shattering (Tsang et al., 2012; Penner et al., 2012; Most, Beloborodov, and Ripperda, 2024). Potential transients at merger (concurrent EM counterpart) have been attributed to either a net electric charge of the black hole (J. Levin, D'Orazio, and Garcia-Saenz, 2018; B. Zhang, 2019; Z.-G. Dai, 2019; Pan and Yang, 2019; Zhong, Z.-G. Dai, and Deng, 2019), or magnetic flux shedding during the merger process (D'Orazio and J. Levin, 2013; Mingarelli, J. Levin, and Lazio, 2015; D'Orazio, J. Levin, et al., 2016; East et al., 2021).

Predicting magnetospheric dynamics of the merger is intrinsically complicated by various competing processes, some of which can be inferred from previous numerical studies of a NS gravitationally collapsing into a BH. In this related scenario, part of the magnetic field is immediately shed during the collapse (Baumgarte and Shapiro, 2003; Lehner et al., 2012; Palenzuela, 2013; Most, Nathanail, and Rezzolla, 2018). In the absence of resistive dissipation, the resulting BH can in principle acquire a net electric charge (Nathanail, Most, and Rezzolla, 2017). However, pair-production in realistic environments will lead to an active magnetosphere supporting magnetic flux decay (balding) of the BH (Lyutikov and McKinney, 2011; Bransgrove, Ripperda, and Philippov, 2021; Selvi et al., 2024). On a technical level, most of the studies in numerical relativity have made use of the force-free electrodynamics or vacuum approaches to study magnetospheric dynamics. Compared to magnetohydrodynamic (MHD) approaches explicitly tracking matter dynamics, these crucially miss out the formation of monster radiative shocks from fast magnetosonic waves (Beloborodov, 2023) as was recently demonstrated by Most, Beloborodov, and Ripperda (2024), which could be responsible for some of the high-energy emission in this process.

Here, we present GRMHD simulations in full numerical relativity of a merging BH–NS binary, in which the NS is swallowed whole. While BH–NS merger simulations in GRMHD have become common recently (e.g., Chawla et al., 2010; Etienne, Liu, et al., 2012; Etienne, Paschalidis, and Shapiro, 2012; Kiuchi et al., 2015; Ruiz, Shapiro, and Tsokaros, 2018; Ruiz, Paschalidis, et al., 2020; Most, Papenfort, Tootle, et al., 2021; Hayashi, Fujibayashi, et al., 2022; Hayashi, Kiuchi, et al., 2023; Izquierdo et al., 2024), tracking the magnetospheric evolution requires special flooring techniques (Tchekhovskoy and Spitkovsky, 2013; Parfrey and Tchekhovskoy, 2017). We employ such a sophisticated MHD strategy to track the evolution of magnetosphere throughout inspiral and merger. Our simulations identify novel types of shock-powered and reconnection-driven transients from a BH–NS merger. Specifically, we show that monster shocks are formed during the final phase of the inspiral, which can primarily source X-ray and radio bursts. In the post-merger phase, we find that the magnetosphere of the remnant BH re-arranges into a short-lived black hole pulsar state (Selvi et al., 2024), capable of powering X-ray transients that may last for several milliseconds.

We describe the simulation setup and the configuration of the binary in Sec. 4.2. This is followed by detailed discussions of two new transients from non-disrupting BH–NS mergers. First, we present the formation of monster shocks in Sec. 4.3. Next, we provide a detailed analysis of the black hole pulsar state that our simulations reveal in Sec. 4.4. We discuss the properties of the expected EM emissions in Sec. 4.5. Finally, we conclude by summarizing our findings in Sec. 4.6.

Unless otherwise stated, we adopt Gaussian units with $c = G = 1$ throughout this chapter.

4.2 Methods

We track the time evolution of a BH–NS binary as well as the common binary magnetosphere using ideal GRMHD for dynamical spacetimes (Duez et al., 2005). To this end, we need to specify both initial conditions and evolution parameters.

We use the `Kadath/FUKA` (Papenfort et al., 2021; Grandclement, 2010) initial data framework to construct BH–NS initial data in extended conformal thin sandwich (XCTS) form (Grandclement, 2006; Taniguchi et al., 2007; Taniguchi et al., 2008; Foucart, Kidder, et al., 2008; Tacik et al., 2016). In order to ensure that the NS is fully swallowed at merger,[1] we adopt a non-spinning NS with mass $M_{\rm NS} = 1.4 M_\odot$ using the APR4 equation of state (Akmal, Pandharipande, and Ravenhall, 1998), and a BH with mass $M_{\rm BH} = 8.0 M_\odot$ and dimensionless spin $a = 0.3$ aligned with the orbital axis ($\hat{z}$). The initial orbital separation of the binary is 60 km, resulting in ~ 1.5 orbits before the merger. The neutron star is initially magnetized with a dipolar field with a strength $|B_*| = 1.9 \times 10^{16}$ G at the magnetic poles on the surface. The precise value of the magnetic field is unimportant for the magnetospheric dynamics we study, since we fix the properties of the magnetosphere in terms of dimensionless quantities such as magnetization $\sigma = b^2/\rho$, and plasma $\beta = 2P/b^2$, where b^2 is the magnetic energy density, ρ the rest-mass density and P the pressure. This allows us to rescale the resulting magnetospheric dynamics to arbitrary magnetic field strength. However, for purely numerical reasons we have found that using a stronger field strength eases the transition to a near force-free magnetosphere near the stellar surface in the inspiral computationally. Nevertheless, the chosen strength of the magnetic field hardly impacts the bulk dynamics of the NS (the plasma beta parameter is around $\beta \sim 10^3$ inside the NS during the inspiral). We simulate three models with an initial inclination between the magnetic dipole moment and the orbital axis $\theta_B = 0°, 30°$, and $60°$. The initial NS magnetic field is inclined toward the companion BH at $t = 0$.

Dynamical evolutions are performed with the `Einstein Toolkit` framework (Loffler et al., 2012), using the `Frankfurt/IllinoisGRMHD (FIL)` (Most, Papenfort, and Rezzolla, 2019; Etienne, Paschalidis, Haas, et al., 2015) code for solving the ideal GRMHD equations in a dynamical spacetime. The spacetime is evolved using `FIL`'s numerical relativity solver, which implements the Z4c equations (Bernuzzi and Hilditch, 2010; Hilditch, Bernuzzi, et al., 2013) in moving puncture gauge

[1] See Foucart (2012) and Foucart, Hinderer, and Nissanke (2018) for the allowed parameter space of a non-disrupting BH–NS merger.

(Alcubierre et al., 2003) using a fourth-order finite-difference discretization (Y. Zlochower et al., 2005). The ideal GRMHD equations are solved using the ECHO scheme (Del Zanna, Zanotti, et al., 2007) with upwind constraint transport (Londrillo and Del Zanna, 2004). Similar to our previous work (Most, Beloborodov, and Ripperda, 2024), the fourth-order derivative corrector in the ECHO scheme showed less robust behavior at strongly magnetized shockfronts, and we have disabled it in our runs. A key feature of our simulations is the ability to track the common magnetospheric dynamics in full MHD as opposed to vacuum or force-free electrodynamics. While several studies have evolved magnetic fields in the exterior region in the context of BH–NS mergers (Paschalidis, Ruiz, and Shapiro, 2015; Ruiz, Shapiro, and Tsokaros, 2018; Ruiz, Paschalidis, et al., 2020), reproducing correct (near-) force-free magnetospheric dynamics within the MHD formulation requires the use of robust primitive inversion schemes (Kastaun, Kalinani, and Ciolfi, 2021) and special flooring techniques (Tchekhovskoy and Spitkovsky, 2013; Parfrey and Tchekhovskoy, 2017), unlike floors commonly used in numerical relativity simulations (e.g. Poudel et al., 2020). A detailed prescription of the floors we use here is provided in Most, Beloborodov, and Ripperda (2024). It is precisely this flooring scheme that allows us to correctly capture and uncover the transients we present in this study. Similar to Most, Beloborodov, and Ripperda (2024), we have supplemented the high-density cold equation of state used in the initial data with a thermal equation of state, $P_{\rm th} = \rho\epsilon$, which primarily governs the magnetospheric dynamics. Here $P_{\rm th}$ is the thermal pressure, and ϵ the specific internal energy. We use a three-dimensional Cartesian grid with eight levels of nested moving mesh refinement (Schnetter, S. H. Hawley, and Hawke, 2004). The coarsest grid extends to $[-3025\ \mathrm{km}, 3025\ \mathrm{km}]^3$ and the finest resolution is 168 m. The finest grid level consists of two patches covering 2–3$\times$ the size of the NS as well as of the BH, being centered to and tracking each of them.

A detailed description of the initial evolution of non-disruptive BH–NS mergers can be found elsewhere (see e.g. Kyutoku, Shibata, and Taniguchi, 2021, for a recent review). Since the magnetospheric transients in our simulations are mainly driven during and after the merger, we briefly depict the merger process in Figure 4.1, which highlights the high degree of spatial asymmetry present in the process, and consequently, the need for full numerical relativity not only for the spacetime evolution but particularly to correctly determine the geometry of magnetic field in the post-merger phase.

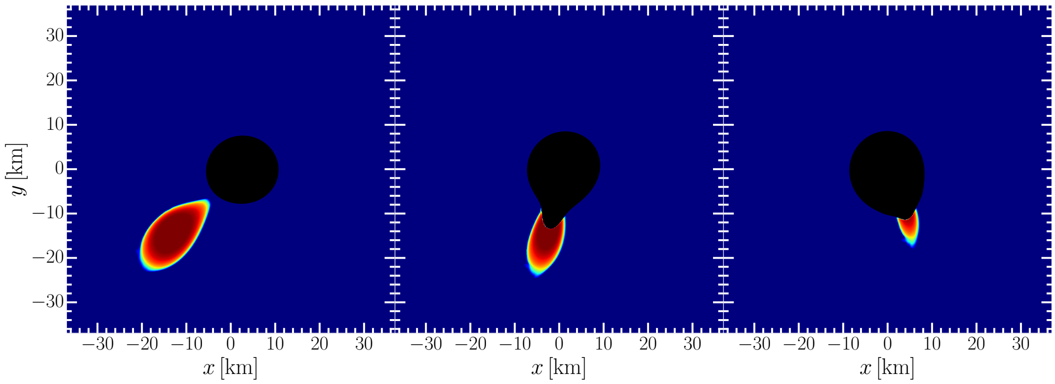

Figure 4.1: Merger of the BH–NS binary in our simulations, where the neutron star is swallowed whole. The entire process shown in this figure happens in less than one millisecond.

4.3 Monster shock

The initially dipolar magnetosphere of the NS is sheared in the vicinity of the BH before and during merger. This perturbation will launch waves into the magnetosphere, which will either be transverse (Alfvén) wave propagating along the magnetic field, or be a compressional (fast magnetosonic) wave. In a dipole background field, the compressional waves are expected from any non-toroidal perturbation in the magnetosphere, as happens during the merger.

Propagation of fast magnetosonic waves to larger radii r is not affected by the background field as long as their wave amplitude $E = \delta B \propto r^{-1}$ is much smaller than the background dipole field $B_{\rm bg} \propto r^{-3}$. With increasing r, this condition becomes broken, $B^2 - E^2$ approaches zero, and the plasma drift speed in the wave approaches the speed of light.[2] Recent analytical (Beloborodov, 2023) and numerical (A. Y. Chen, Yuan, X. Li, et al., 2022; Vanthieghem and Levinson, 2025) works have demonstrated that this leads to the formation of *monster shocks*.[3] In particular, in the equatorial plane of the magnetic dipole, the shock appears when $\delta B \approx B_{\rm bg}/2$, which implies $B^2 - E^2$ touching zero at the trough of the compressional wave. Near this point, the plasma develops a characteristic negative velocity $v^r < 0$, which leads to shock formation in front of the crest of the wave. In practice, searching for zones with $v_r < 0$ provides a simple way to identify regions of shock formation,

[2] Orbiting systems possess an orbital light cylinder, $r_{\rm LC} \sim 1/\Omega_{\rm orb}$, set by the orbital frequency $\Omega_{\rm orb}$. Steepening or distortion of the waves induced by a decreasing $B_{\rm bg}$ will only happen efficiently on closed field lines inside the light cylinder, in turn requiring a minimum amplitude of the perturbation (see, e.g., Most, Kim, et al., 2024 for a discussion in the context of non-linear steepening of Alfvén waves).

[3] See also Lyubarsky (2003) for an earlier work.

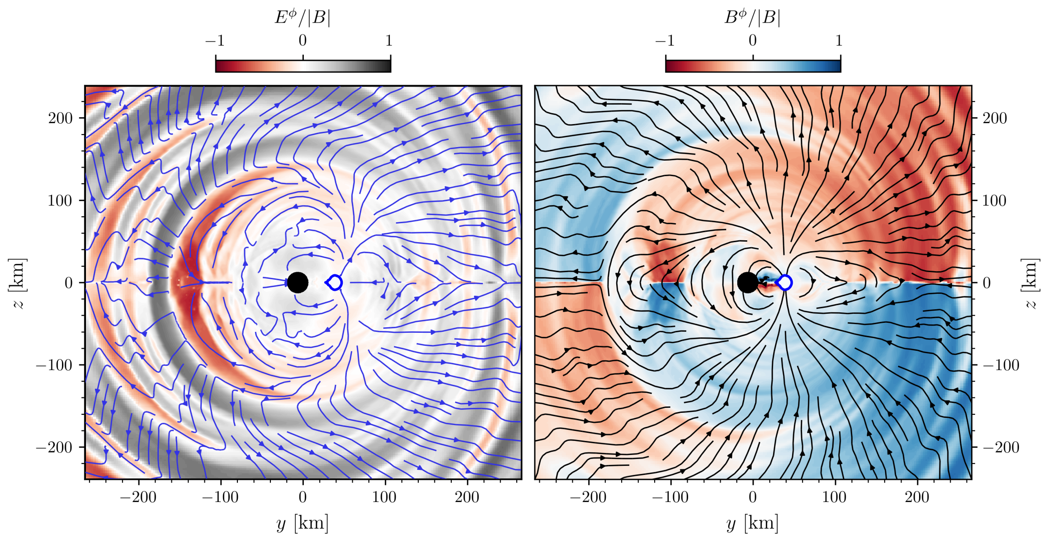

Figure 4.2: Poloidal structure (cut in the yz plane) of the perturbed magnetosphere of the BH–NS binary 0.9 ms before merger for the aligned ($\theta_B = 0°$) model. Fast magnetosonic waves have toroidal electric fields E^ϕ (left), and Alfvén waves have toroidal magnetic perturbations δB^ϕ (right). Streamlines show fluid velocity in the left panel and magnetic field lines in the right panel. The BH and NS are shown with a black and blue circle, respectively.

in addition to detection of velocity jumps and localized heating spikes. A similar analysis was performed in Most, Beloborodov, and Ripperda (2024) to demonstrate shock formation in the magnetosphere of a collapsing magnetar.

In our simulations, the inspiral of the magnetized NS drives a continuous excitation of magnetosonic waves in the magnetosphere, peaking around the plunge of the NS into the BH. The final plunge of the NS injects a strong rarefaction mode into the surrounding magnetosphere as the NS bulk velocity is maximally radially inward at the moment. In Fig. 4.2, we show the excited magnetosphere about half an orbit before the plunge for aligned ($\theta_B = 0°$) magnetic axis. We find that the wave emitted during the plunge leads to the development of a large $v^r < 0$ region characteristic of the monster shock, which we show in the top row of Fig. 4.3. This phenomenology of a leading shock with surrounding weaker shocks resembles the results for the collapsing magnetar (Most, Beloborodov, and Ripperda, 2024), and approximately agrees with the analytical prediction (Beloborodov, 2023, see Fig. 7 therein).

The profile of γv^r across the shock region is affected by deviations of $B_{\rm bg}$ from a pure dipole due to the orbital motion of the NS. As an additional validation, we have also confirmed that the regions with $v^r < 0$ develop $E^2 \approx B^2$ plateaus, corroborating

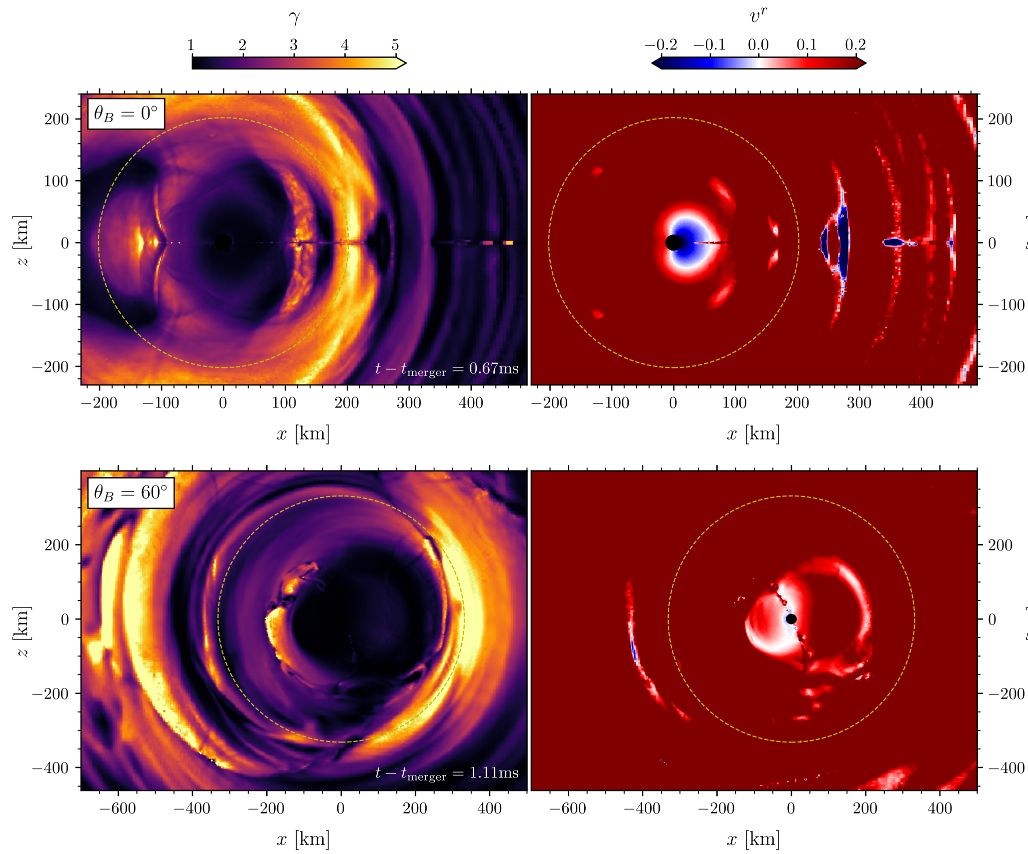

Figure 4.3: Monster shocks launched from BH–NS mergers. Shown here are the Lorentz factor (left panels) and the radial spatial velocity (right panels) on the meridional (xz) plane. Dashed orange circles are light spheres with the radius $r = c(t - t_{\rm merger})$. (Top) Simulation snapshot from the aligned model ($\theta_B = 0°$). A monster shock can be found near $x \simeq 250$ km, with its characteristic feature of a plasma moving radially inward ($v^r < 0$) preceding the shockfront. (Bottom) Inclined model $\theta_B = 60°$. A similar feature can be seen near $x \simeq -400$ km.

that the observed feature is the monster shock.

We have also identified monster shocks for the inclined models. One such model with $\theta_B = 60°$ is shown in in the bottom row of Fig. 4.3. We caution that due to the misalignment between magnetic equator and orbital plane, the strongest part of the shock will appear off the shown yz plane, and the trough of the wave preceding the monster shock might not strongly exhibit $v^r < 0$. Yet, we can clearly identify a similar leading shock structure as in the aligned case.

4.4 Transient black hole pulsar

In this section, we present a detailed analysis of the evolution of the post-merger magnetosphere, defined as the region within the light sphere ($r/c \leq t - t_{\rm merger}$), with a special emphasis on the near-horizon dynamics. The merger remnant settles down to a Kerr BH with the mass $M = 9.2M_\odot$ and the dimensionless spin $a = 0.57$. Relevant length and time scales are $r_g \equiv GM/c^2 = 13.6$ km and $r_g/c = 46\,\mu$s, or equivalently 1 millisecond amounts to $\sim 22r_g/c$. The angular velocity of the outer event horizon is $\Omega_H = ac/2r_+ = 3.43 \times 10^3 \mathrm{s}^{-1}$, where $r_+ = r_g(1 + \sqrt{1-a^2}) \approx 25$ km is the outer horizon radius. While we will quote values measured from our simulation data in the following discussions, we caution that it is nontrivial to map our results (especially time scales) in a coordinate-independent manner to those obtained from other studies that used a fixed Kerr background, since our merger simulations are performed using dynamically evolved coordinates.

4.4.1 Relaxation into a rotating split-monopole

The remnant BH is immersed in a dipole-like magnetic field shortly after the merger. Since black holes cannot support closed magnetic field lines (MacDonald and Thorne, 1982), the dipole gets stretched out, with the magnetic field lines opening up near the magnetic equator. In consequence, the BH magnetosphere transitions into a split-monopole topology (Komissarov, 2004b), and begins to dissipate the magnetic field energy at the current sheet. The inclination of the split-monopole configuration depends on the initial inclination of the NS magnetic field. For all simulations, the topology of magnetic field lines transitions into a split-monopole over a timescale of 1 ms,[4] which is consistent with multiple light crossing times across the horizon ($2r_+/c \approx 0.2$ ms).

The distribution of magnetic flux on the remnant BH is initially highly localized to the spot through which the NS plunged into (Fig. 4.1). Over the transition period to a split-monopole ($t - t_{\mathrm{merger}} \lesssim 1$ms), the magnetic flux density on the BH horizon is redistributed, relaxing into a relatively uniform distribution by $t - t_{\mathrm{merger}} \approx 2$ ms. The upper panels of Fig. 4.4 show the post-merger magnetosphere at $t - t_{\mathrm{merger}} = 3.3$ ms for the aligned model ($\theta_B = 0°$), displaying an axisymmetric split-monopole magnetosphere centered on the BH. Magnetic energy of the magnetosphere is partially dissipated via reconnection in the equatorial current sheet, heating the plasma, as can be seen from the plot of P_{th}/ρ in Fig. 4.4.

The frame dragging of the remnant BH induces co-rotation of magnetic field lines and forms a rotating split-monopole. The angular velocity of the magnetic field lines in an axisymmetric force-free split-monopole magnetosphere around a Kerr

[4] A similar reordering and collimation of the post-merger magnetic field may also have been observed in previous works (East et al., 2021).

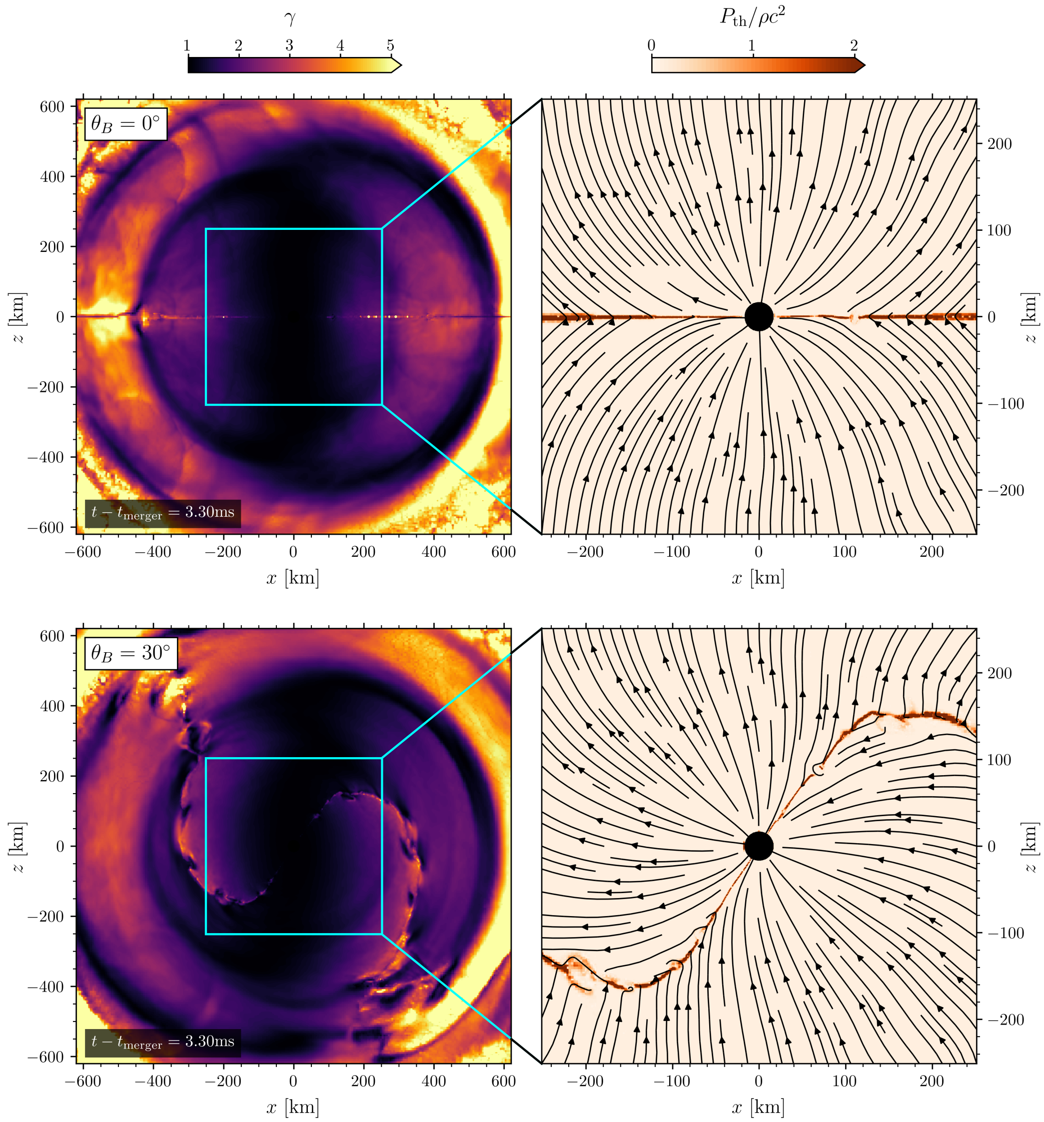

Figure 4.4: Post-merger magnetosphere of the remnant black hole having settled down to a rotating split monopole. The physical quantities are shown in the xz plane. Left: fluid Lorentz factor γ. Right: ratio of the thermal pressure $p_{\rm th}$ to the rest energy density ρc^2. Black solid lines show the in-plane magnetic field lines. An equatorial current sheet is formed at which the magnetic field lines in upper and lower hemispheres reconnect, dissipating magnetic energy and causing a flux decay (balding) of the BH. The inner magnetosphere is driven to co-rotate with the BH due to frame dragging. As a result, the post-merger magnetosphere of an inclined model (e.g. $\theta_B = 30°$, bottom panels) exhibits features similar to those of tilted pulsars (see also Fig. 4.10). The spin axis of the BH is along $\hat{z}$ in all models.

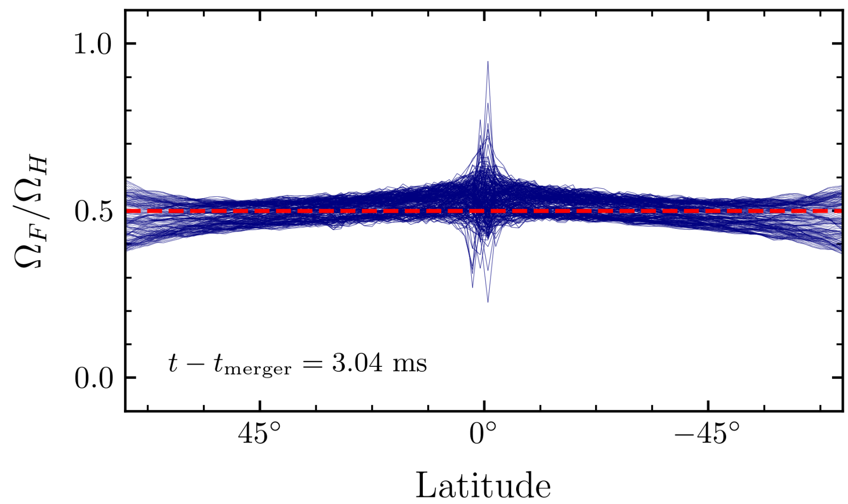

Figure 4.5: Angular velocity of magnetic field lines threading the apparent BH horizon for $\theta_B = 0°$ simulation. Shown are the distribution of Ω_F for each latitude and the stationary axisymmetric force-free solution $\Omega_F \simeq \Omega_H/2$ (red dashed line).

BH is given as $\Omega_F = a/8M$ to leading order in the spin (Komissarov, 2004a; Armas et al., 2020). For arbitrary high spins, Ω_F can be calculated either with a perturbative analytic expansion (e.g. Armas et al., 2020) or using an iterative numerical method (e.g. Contopoulos, Kazanas, and D. B. Papadopoulos, 2013; Nathanail and Contopoulos, 2014). The ratio Ω_F/Ω_H, which is $1/2$ in the limit $a \to 0$, remains $\lesssim 1\%$ different from $1/2$ for the spin $a \leq 0.7$ (e.g. see Figure 1 of Contopoulos, Kazanas, and D. B. Papadopoulos, 2013). Therefore, in the case of our merger remnant BH with $a = 0.57$, we can safely assume $\Omega_F/\Omega_H \simeq 0.5$.

For the aligned ($\theta_B = 0°$) model, we measure the rotation angular velocity of magnetic field lines as

$$\Omega_F = \frac{-y\,(u^x/u^0) + x\,(u^y/u^0)}{\varpi^2}, \tag{4.1}$$

where u^μ is the four-velocity of the plasma and $\varpi = \sqrt{r^2 - z^2}$ is the (coordinate) cylindrical radius. This description is appropriate for the ideal MHD limit we consider. Fig. 4.5 shows the measured Ω_F/Ω_H over a spherical surface $r = 2.4\,r_g$ encompassing the remnant BH.[5] We observe that the rotation angular velocity of magnetic field lines converges to $\Omega_H/2$ and the asymmetry present in its distribution is decayed out over time. In addition to the magnetic field morphology shown in

[5] When computing the horizon angular velocity Ω_H, we used the mean radius of the instantaneous apparent horizon of the BH.

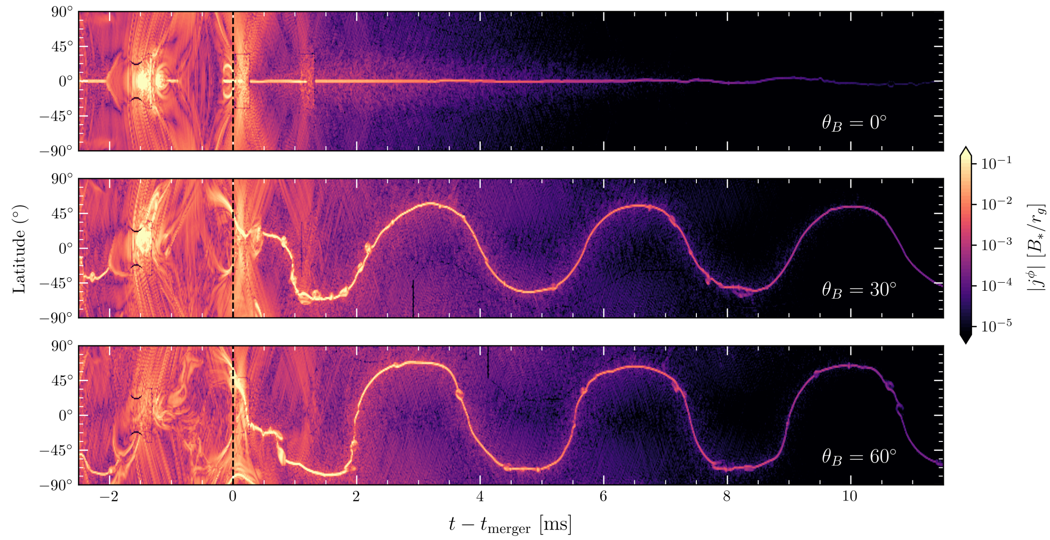

Figure 4.6: A spacetime diagram of the approximate electric current $\left|j^\phi\right|$ on a meridional arc $\phi = 0$ at $r = 2.4r_g$ in three simulations with different initial inclinations of the NS magnetic dipole moment ($\theta_B = 0°, 30°, 60°$), displaying the latitude of the post-merger magnetospheric BH current sheet. For the inclined models ($\theta_B = 30°, 60°$), the periodic oscillation in the latitude represents the rotation of the inclined current sheet. The orbital current sheet of the NS in the inspiral phase is also visible for $t - t_{\rm merger} \lesssim -2$ ms, where $t_{\rm merger}$ indicates the merger time.

Fig. 4.4, this provides solid evidence that the post-merger magnetosphere relaxes into a rotating split-monopole.

As naturally expected, for inclined magnetic field, the remnant BH settles down to a rotating, inclined split-monopole magnetosphere. The resulting global dynamics of the magnetosphere closely resembles that of a tilted pulsar, akin to a recently proposed *black hole pulsar* state (Selvi et al., 2024). We present detailed discussions on this transient BH pulsar in later sections.

4.4.2 Rotation and alignment of current sheets

The spinning remnant BH induces a rotation of the magnetic field lines and the current sheets via frame dragging with respect to its spin axis. In the following, we would like to track the motion of current sheets. These are easily identified with the (toroidal) electric current, j^ϕ, which we here approximate via its Newtonian expression,

$$j^\phi \approx \epsilon^{\phi ij} \partial_i B_j \,. \tag{4.2}$$

We then analyze the time evolution of the current on a fixed spherical surface of radius $r = 2.4r_g$. In Fig. 4.6, we show the distribution of $|j^\phi|$ on the meridional arc

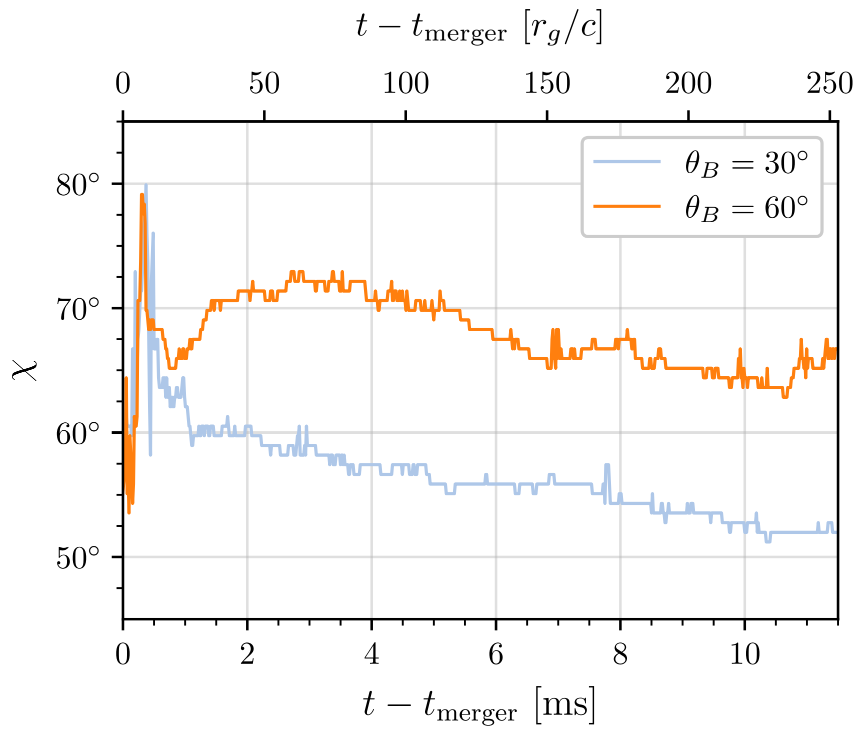

Figure 4.7: Time evolution of the current sheet inclination angle χ for the $\theta_B = 30°, 60°$ models.

$\phi = 0$ $(x > 0, y = 0)$ for all simulations. The equatorial current sheet in the aligned case ($\theta_B = 0°$) does not exhibit notable modulations in its latitude, where we have confirmed in Sec. 4.4.1 that the magnetosphere is in fact rotating with $\Omega_F = 0.5\Omega_H$. For the inclined cases, rotation of the current sheet is clearly seen in Fig. 4.6. The time interval between neighboring peaks is about 3.5 ms, revealing that the current sheet is rotating with about half of the horizon angular velocity.

Over each meridional lines (ϕ = const.) on the spherical surface $r = 2.4r_g$, we collect the latitude $\alpha_0(\phi)$ with the maximum value of $|j^\phi|$, which is effectively the latitude of the current sheet at that azimuthal angle. Then we define the current sheet inclination angle χ as[6]

$$\chi = \frac{\max[\alpha_0(\phi)] - \min[\alpha_0(\phi)]}{2}. \tag{4.3}$$

In Fig. 4.7, we show the measured $\chi(t)$ from $\theta_B = 30°, 60°$ simulations. A nonlinear deformation of the NS during the merger is found to greatly enhance the inclination angle of the magnetic field around the merger remnant, resulting in $\chi \approx 60°$ for

[6]See the section 3 of Selvi et al. (2024) for an alternative method to measure $\chi(t)$ in terms of the magnetic moment.

$\theta_B = 30°$. We observe a gradual decay in $\chi(t)$ for both models, indicating the alignment of the current sheet with respect to the BH spin axis over time, which is consistent with the result of Selvi et al. (2024). However, here we can only provide a crude estimate on the alignment timescale $\tau_\chi \approx 1000$–$2000\, r_g/c$, being limited by a short simulation time and a mild spin of the BH. We also caution that the observed alignment timescale could be affected by a high numerical dissipation (see Sec. 4.4.3).

4.4.3 Balding and ring-down of the remnant BH

In a split-monopole magnetosphere of a stationary BH, the total magnetic flux threading the horizon

$$\Phi_{\rm B} = \frac{1}{2}\oint |B^r| d\Omega, \tag{4.4}$$

exponentially decays as a result of magnetic reconnection in the current sheet (Lyutikov and McKinney, 2011; Bransgrove, Ripperda, and Philippov, 2021; Selvi et al., 2024). In the top panel of Fig. 4.8, we show the decay of the horizon magnetic flux $\Phi_{\rm B}$ for all simulations. Overall, the decay times shown in Fig. 4.8 are an order of magnitude shorter than those from the MHD simulations of Bransgrove, Ripperda, and Philippov (2021) and Selvi et al. (2024). This is likely due to artificially high numerical resistivity (i.e., low spatial grid resolution) compared to those studies. At higher resolution than we use, our MHD solution will equally not be able to recover the correct collisionless reconnection rate (Sironi and Spitkovsky, 2014; Bransgrove, Ripperda, and Philippov, 2021). We therefore treat our results mainly qualitatively, in that the BH pulsar forms and balds, and defer quantitative conclusions to an analytical model discussed in Sec. 4.4.4.

The magnetic flux decay timescale τ_Φ is almost identical for both of the inclined models, while the aligned model exhibits about 30% faster decay until $t - t_{\rm merger} \lesssim 6\,{\rm ms}$. However, in a split monopole magnetosphere of a stationary Kerr BH, the timescale τ_Φ may not notably depend on the current sheet inclination angle χ (Selvi et al., 2024). We investigate the origin of the accelerated magnetic flux decay by examining additional physical quantities, as follows.

Electromagnetic and gravitational perturbations around a BH can be analyzed by means of the Newman-Penrose (NP) scalars (Teukolsky, 1972; Teukolsky, 1973)

$$\psi_4 = -C_{abcd} n^a \bar{m}^b n^c \bar{m}^d, \tag{4.5}$$

$$\phi_2 = F_{ab} \bar{m}^a n^b, \tag{4.6}$$

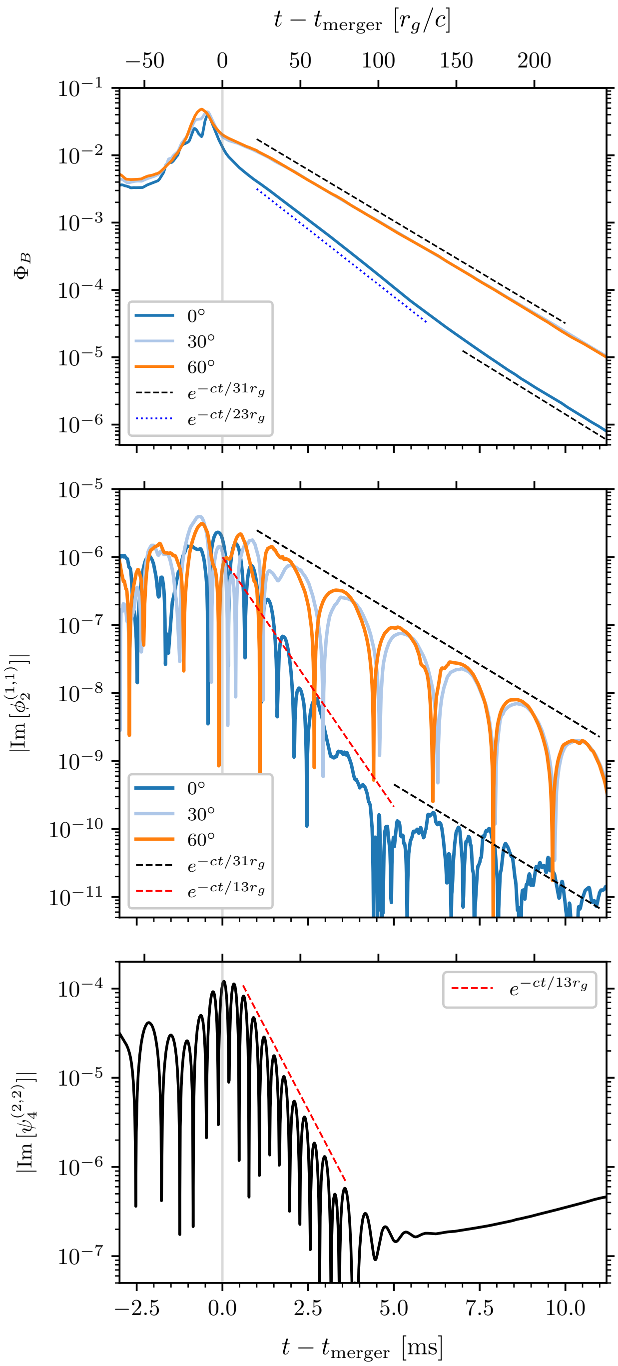

Figure 4.8: Top: total magnetic flux extracted on a spherical surface $r = 2.4r_g$ near the apparent horizon. The result from $\theta_B = 30°$ (cyan solid line) and $\theta_B = 60°$ (orange solid line) are lying almost on top of each other. Middle: imaginary part of $(l, m) = (1, 1)$ mode of the Maxwell Newman-Penrose (NP) scalar ϕ_2 extracted at $r = 4.3r_g$. Bottom: imaginary part of $(l, m) = (2, 2)$ mode of the NP scalar ψ_4 extracted at $r = 4.3r_g$. We only show the result from $\theta_B = 0°$ since the result is almost identical for all simulations. Exponential decays with timescales $31r_g/c$, $23r_g/c$ and $13r_g/c$ are indicated by the black dashed, blue dotted, and red dashed lines.

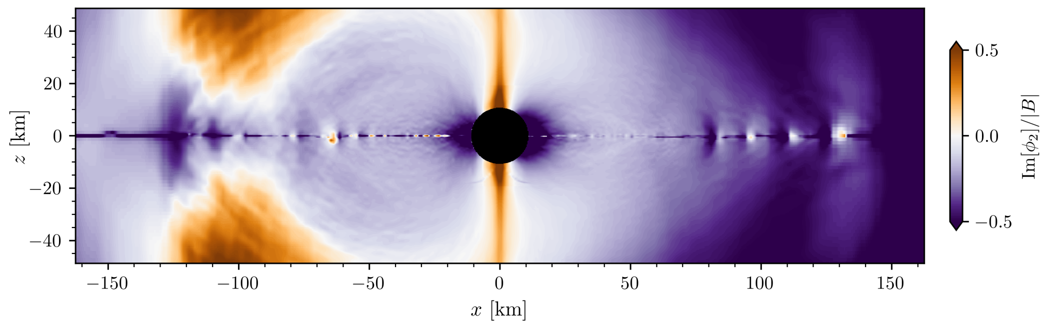

Figure 4.9: Imaginary part of the Maxwell Newman-Penrose scalar $\phi_2^{(l=1,m=1)}$, corresponding approximately to outgoing fast magnetosonic waves, on the vertical (xz) plane normalized with the magnitude of magnetic field for the aligned case $\theta_B = 0°$ at $t - t_{\rm merger} = 1.05\,$ms.

where C_{abcd} is the Weyl tensor, F_{ab} is the electromagnetic field tensor, and $(l^a, n^a, m^a, \bar{m}^a)$ are orthonormal null tetrads

$$l^a = (t^a + r^a)/\sqrt{2}, \tag{4.7}$$

$$n^a = (t^a - r^a)/\sqrt{2}, \tag{4.8}$$

$$m^a = (\theta^a + i\phi^a)/\sqrt{2}. \tag{4.9}$$

We use the dominant $(l, m) = (2, 2)$ quadrupole mode of ψ_4 to monitor the BH ringdown, and the $(l, m) = (1, 1)$ dipole mode of ϕ_2 to monitor the electromagnetic modulation in the magnetosphere.[7] We show the imaginary part of $\phi_2^{(l=1,m=1)}$ and $\psi_4^{(l=2,m=2)}$ (hereafter denoted simply as ϕ_2 and ψ_4 for brevity) in the middle and lower panels of Fig. 4.8. In the following discussions, we denote the exponential decay time scale of the NP scalar ϕ_2 (ψ_4) as $\tau_\phi^{\rm NP}$ ($\tau_\psi^{\rm NP}$).

We compute the quasi-normal mode (QNM) frequencies of the remnant BH for $(s, l, m) = (-2, 2, 2)$ and $(s, l, m) = (-1, 1, 1)$ fundamental modes using the `qnm` package (Stein, 2019). The imaginary parts of the two QNM frequencies are both around $12\, r_g/c$. From the real parts, we obtain the oscillation period 0.94 ms for ϕ_2 and 0.59 ms for ψ_4. The damped sinusoidal oscillation of ψ_4, shown in the bottom panel of Fig. 4.8, agrees well with both real and imaginary parts of the computed QNM frequency.

[7] The NP scalar ψ_4 corresponds to the outgoing gravitational radiation at null infinity. The Maxwell NP scalar ϕ_2 is proportional to the complex electric field $E_\theta + iE_\phi$. In an axisymmetric background magnetic field, E_θ corresponds to the Alfvénic modes and E_ϕ to the fast magnetosonic modes.

Inclined magnetic field ($\theta_B = 30°, 60°$) — Both simulations show $\tau_\phi^{\rm NP} = 31 r_g/c$, which is the same as their magnetic flux decaying timescale τ_Φ. Periodic oscillations of ϕ_2 for $t - t_{\rm merger} \gtrsim 1.5\,$ms are coming from the rotation of current sheets (see Fig. 4.6), which has a half-period of $2\pi/\Omega_H \approx 1.8\,$ms. From the fact that the measured decay timescales τ_Φ and $\tau_\phi^{\rm NP}$ not only agree with each other but also being disparate from the QNM frequency, we deduce that $\tau_\Phi = 31 r_g/c$ is the the flux decay timescale of the BH pulsar due to magnetic reconnection in our setup, and the time decay of ϕ_2 is simply a consequence of the declining magnetic field strength.

Aligned magnetic field ($\theta_B = 0°$) — In the early phase of the ringdown ($t - t_{\rm merger} \leq 5\,$ms), ϕ_2 exhibits a rapid decay with $\tau_\phi^{\rm NP} \approx \tau_\psi^{\rm NP}$. The period of the oscillations in ϕ_2, which lasts about 2.5 cycles, is measured to be 0.9ms and shows a good agreement with the QNM frequency (0.94ms). This indicates that the evolution of the post-merger magnetosphere is dominated by the ringdown of the BH, which rapidly sheds off magnetic fluxes from the horizon. We show ϕ_2 in the meridional (xz) plane in Fig. 4.9. The magnetic flux shedding driven by QNMs induces episodes of quasi-periodic modulations in the magnetosphere, which leads to a more rapid reconnection of the field lines on the equatorial plane. The same process has been also observed by Most, Beloborodov, and Ripperda (2024) for the gravitational collapse of a NS with its spin axis aligned with the magnetic moment. On the other hand, both τ_Φ and $\tau_\phi^{\rm NP}$ are slowed down to $\approx 31 r_g/c$ later in $t - t_{\rm merger} \geq 6\,$ms, implying that the balding process of the BH begins to be affected more by resistivity. The magnetic flux shedding by QNMs becomes subdominant as gravitational perturbations fade out, then the flux decay is governed by magnetic reconnection afterwards. We caution that this observed behavior may change at higher numerical resolutions, which will exhibit a better scale separation between plasma and gravitational effects.

4.4.4 Striped wind

The rotation of an inclined split-monopole magnetosphere on a BH leads to a striped wind (Selvi et al., 2024) which appears to be similar to those from oblique pulsars (e.g. Michel, 1982; Petri, 2012; Tchekhovskoy and Spitkovsky, 2013; Cerutti and Philippov, 2017), albeit without the presence of a closed zone. We illustrate this in Fig. 4.10 for the $\theta_B = 30°$ simulation, where the sign change in the toroidal magnetic field is clearly visible. Different from a stationary pulsar solution with $B^\phi \sim 1/r$ (Michel, 1982; Bogovalov, 1999), the magnetic field here decays over time. While this will not affect the geometry of the striped wind, its amplitude will naturally

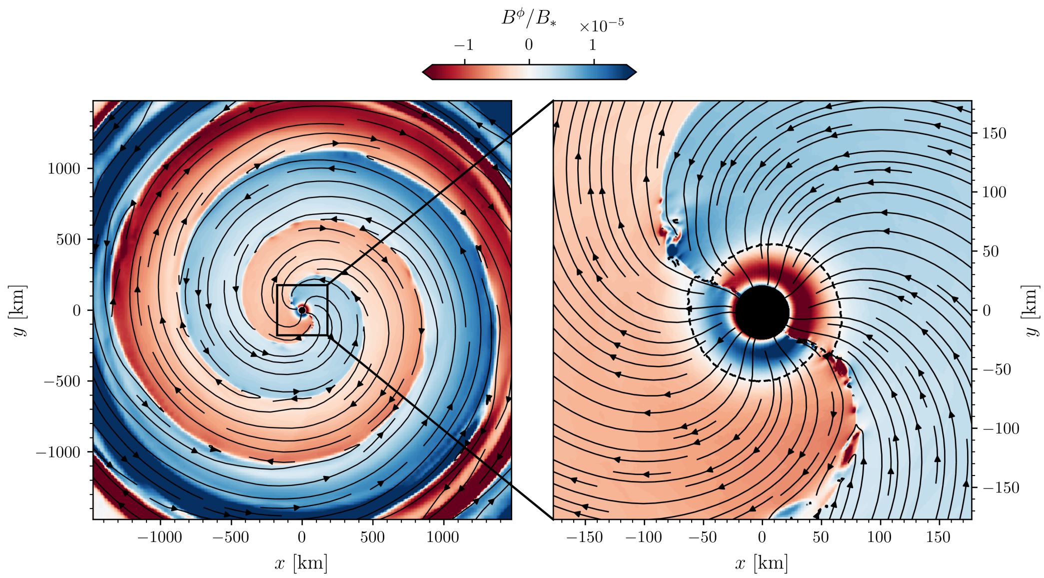

Figure 4.10: Pulsar-like striped wind from the remnant black hole at $t - t_{\rm merger}$ = 7.0 ms from $\theta_B = 30°$ simulation. We show the toroidal magnetic field B^ϕ with the magnetic field lines on the equatorial (xy) plane in both panels. The remnant black hole is shown with a black circle and spinning counter clockwise in this figure. In the right panel, we show the stagnation surface ($u^r = 0$) with a black dashed line.

become a function of retarded time, $B^\phi = B^\phi\,(r, \theta, t - r/c)$, as can be seen from the left panel of Fig. 4.10.

A stagnation surface at which $u^r = 0$, separating the inflow and outflow region of the plasma, appears in the vicinity of the BH (Bransgrove, Ripperda, and Philippov, 2021); we show it on the right panel of Fig. 4.10. Interestingly, the stagnation surface is discontinuous across the rotating current sheet, with its radius being greater at the upstream of the current sheet (trailing part of the striped wind), appearing as a half-split spheroid with an offset along the current sheet.

We also find that the rotation angular velocity of the magnetic field lines is slower (faster) at the upstream (downstream) of the rotating current sheet, exhibiting a symmetric deviation from $\Omega_F = \Omega_H/2$. We reserve a more detailed analysis of these near-horizon dynamics of oblique BH pulsars for future work.

An analytic model of the toroidal magnetic field B^ϕ in the wind can be developed as follows. For a nearly force-free wind from a rotating split-monopole, B^ϕ can be approximated as (Michel, 1982; Bogovalov, 1999; Tchekhovskoy, Philippov, and

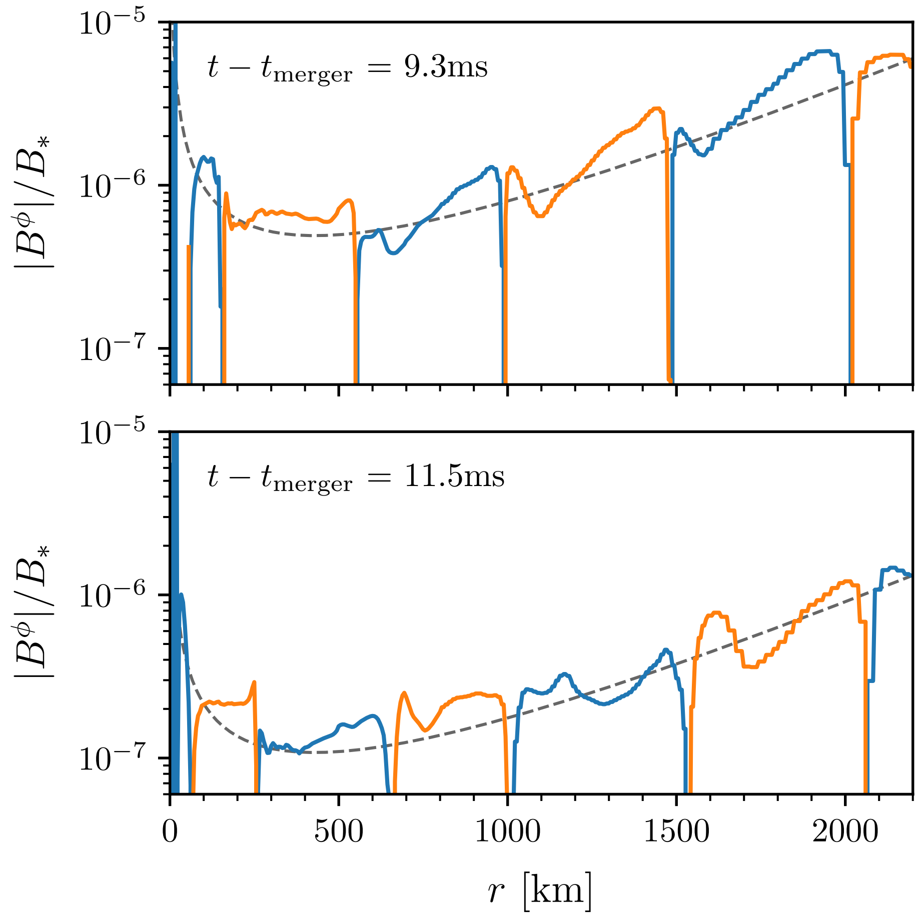

Figure 4.11: Toroidal magnetic field of the striped wind $|B^\phi(r)|$ on the equatorial plane along the $\hat{x}$ axis. Alternating signs (polaritires) of B^ϕ in each stripes are denoted with different colors. The dashed line shows the fit with Eq. (4.11).

Spitkovsky, 2016)

$$|B^\phi(r, \theta)| \approx \frac{\Omega r \sin\theta}{c}|B_r| = \frac{\Omega}{c}\frac{B_* r_*^2 \sin\theta}{r}, \tag{4.10}$$

where Ω is the rotation angular velocity, B_* is the surface magnetic field strength, and r_* is the radius of the rotator. For a BH pulsar, we can replace the angular velocity Ω with $\Omega_F = \Omega_H/2$, the radius r_* with r_H, and the surface magnetic field B_* with $B_H(t) = B_{H,0}e^{-t/\tau_\Phi}$. The resulting extension of Eq. (4.10) for a BH pulsar is

$$|B^\phi(r, \theta, t)| = \frac{\Omega_H}{2c}\frac{B_{H,0} r_H^2 e^{-(t-r/c)/\tau_\Phi} \sin\theta}{r}, \tag{4.11}$$

where $(t - r/c)$ accounts for a retarded time.

Fig. 4.11 compares the $\theta_B = 30°$ simulation data with Eq. (4.11) on the equatorial plane, using $\tau_\Phi = 31 r_g/c$ measured from the balding process (Sec. 4.4.3) and shifting $t \to t - t_{\rm merger}$. Our approximate analytic model shows a good agreement with the simulation result. The value of $B_{H,0}$ fitted from the simulation data is $1.5 \times 10^{-2} B_*$, revealing that the split-monopole BH pulsar inherits about 1% of the magnetic field strength from the companion NS. A separate estimate from the BH magnetic flux $\Phi_B = 2\pi r_H^2 B_{H,0}$ (top panel of Fig. 4.8) yields almost the same value of $B_{H,0}$, reassuring the validity of the analytic model Eq. (4.11) as well as the measured value of $B_{H,0}$.

4.4.5 Energetics

The wind from the BH pulsar is powered by the energy extracted from the remnant BH through the Blandford-Znajek (BZ) process (Blandford and Znajek, 1977), leading to a spin-down of the BH. The spin-down power of an aligned split-monopole magnetosphere, to a leading order of the BH spin,[8] is given as (Tchekhovskoy, Narayan, and McKinney, 2010)

$$P_{\rm BZ} = \frac{(\Phi_B^2/4\pi)\Omega_H^2}{6\pi c}. \tag{4.12}$$

The BZ power (4.12) can be written into a form more commonly used in the pulsar literature

$$L = \frac{2}{3c}\Omega_F^2 B_H^2 r_H^4, \tag{4.13}$$

with $\Omega_F = \Omega_H/2$ and $\Phi_B = 2\pi r_H^2 B_H$.

This spin-down power is carried by the electromagnetic Poynting flux, which is not a direct observable. It is the dissipation in the current sheets which converts the electromagnetic field energy of the wind into kinetic energy of particles and subsequent electromagnetic emissions (Philippov, Uzdensky, et al., 2019). In a steady pulsar magnetosphere, about 10–20 percent of the spin-down power can be dissipated within 10 light cylinder radii (e.g., Parfrey, Beloborodov, and Hui, 2012; A. Y. Chen and Beloborodov, 2014; Philippov, Spitkovsky, and Cerutti, 2015; see also Cerutti and Beloborodov, 2017 for a review).

Here we develop a toy model for the dissipation luminosity of a BH pulsar, closely following the approach by Cerutti, Philippov, and Dubus (2020). From here we will use t to denote the time after the formation of the split monopole i.e. $(t - t_{\rm merger}) \to t$.

[8]The relative correction from the next order term $\propto (\Omega_H)^4$ is less than 10^{-3} in our case. See Tchekhovskoy, Narayan, and McKinney (2010) for the expansion formula up to $(\Omega_H)^6$.

The total dissipation luminosity is given by a volume integral

$$\begin{aligned} L_D &= \int (\mathbf{J}\cdot\mathbf{E})\, r^2 \sin\theta dr d\theta d\phi \\ &= \frac{c\beta_{\rm rec}}{\pi} \int (B^\phi)^2\, r \sin\theta dr d\theta, \end{aligned} \tag{4.14}$$

where $\beta_{\rm rec}$ is the dimensionless reconnection rate (Uzdensky and Spitkovsky, 2014). A primary difference of our toy model from that of Cerutti, Philippov, and Dubus (2020) is the exponential damping term in the Eq. (4.11) associated with the flux decay of the BH. Substituting the expression (4.11) into (4.14) and performing angular integration,

$$L_D = \frac{2\beta_{\rm rec} L_0}{\pi} e^{-2t/\tau_\Phi} \int_{r_{\rm min}}^{r_{\rm max}} \frac{e^{2r/c\tau_\Phi}}{r} dr, \tag{4.15}$$

where $L_0 = (2/3c)\Omega_F^2 B_{H,0}^2 r_H^4$ is an instantaneous BZ power of the BH pulsar at $t = 0$. The upper and lower bounds of the integral in Eq. (4.15) correspond to the radial extent of the striped wind, $r_{\rm min} = r_H$ and $r_{\rm max} \approx ct$, which gives

$$L_D(t) = \frac{2\beta_{\rm rec} L_0}{\pi} e^{-2t/\tau_\Phi} \left[\mathrm{Ei}\left(\frac{2t}{\tau_\Phi}\right) - \mathrm{Ei}\left(\frac{2r_H}{c\tau_\Phi}\right)\right], \tag{4.16}$$

where $\mathrm{Ei}(x) = \int_{-\infty}^{x} (e^t/t)dt$ is the exponential intergral.

We apply our toy model to the $\theta_B = 30°$ simulation. The initial spin-down power L_0 can be computed from the mass and spin of the remnant BH, and using $B_{H,0}/B_* = 1.5\%$ fitted from the simulation result (see Sec. 4.4.4).[9] The flux decay timescale $\tau_\Phi = 31 r_g/c$ from our simulation is dominated by unphysical numerical resistivity, therefore we consider $\tau_\Phi = 100 r_g/c$ and $\tau_\Phi = 500 r_g/c$ motivated from the high-resolution (kinetic) simulations of Bransgrove, Ripperda, and Philippov (2021) as a more realistic input for assessing light curves. The reconnection rate is fixed to $\beta_{\rm rec} = 0.1$ from kinetic plasma simulations (Sironi and Spitkovsky, 2014).

In Fig. 4.12, we show the modelled dissipation luminosity $L_D(t)$ scaled with the initial NS magnetic field strength. The time curve of the dissipation luminosity exhibits a rapid rise to its peak value within a few milliseconds, followed by exponential then power-law decay over tens of milliseconds. A magnetar can power a burst with the luminosity $\sim 10^{47}\,\mathrm{erg\,s^{-1}}$, while a NS with $B_* \sim 10^{12}\,$G will emit a

[9] Note that this ratio $B_{H,0}/B_*$, namely the portion of the magnetic flux that a nascent BH pulsar inherits from the swallowed NS, can only be probed with a full numerical relativity merger simulation as performed here.

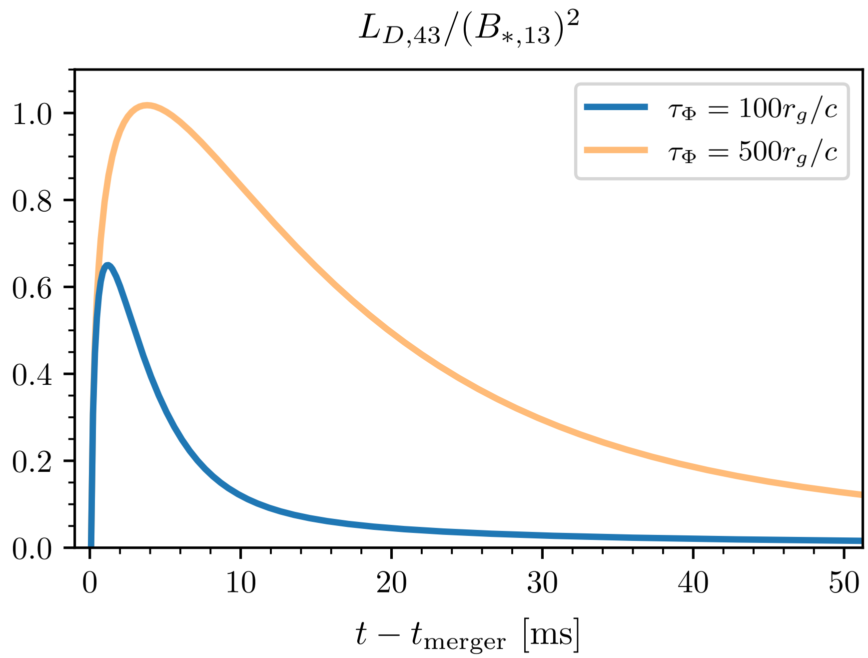

Figure 4.12: The dissipation luminosity from a BH pulsar $L_D(t)$ computed with an analytic model developed in Sec. 4.4.5, normalized with $L_{D,43} \equiv L_D/(10^{43}\,\mathrm{erg\,s^{-1}})$ and $B_{*,13} \equiv B_*/(10^{13}\,\mathrm{G})$. Due to a high (unphysical) numerical resistivity in our simulation, we construct the light curves using $\tau_\Phi = 100r_g/c$ (blue solid line) and $\tau_\Phi = 500r_g/c$ (orange solid line) consistent with bounds from high-resolution kinetic simulations of Bransgrove, Ripperda, and Philippov (2021).

relatively faint one with $\sim 10^{41}\,\mathrm{erg\,s^{-1}}$. The exponential factor $e^{2r/c\tau_\Phi}$ in Eq. (4.15) suggests that the region $r \approx r_{\rm max}$ is predominantly contributing to the total integral, implying the forefront of the expanding striped wind with a thickness $\Delta r \approx c\tau_\Phi$ is mainly powering the total dissipation luminosity.

The total dissipated energy $E = \int L_D(t)dt$ does not converge due to a t^{-1} asymptotic decay of $L_D(t)$. Realistically, dissipation in the current sheets would introduce a faster decrease of B^ϕ in radius, and the decay of $B_H(t)$ below a certain threshold can halt the pair production around the BH, turning off the BH pulsar. Naively setting the end time of the burst as when $L_D(t)$ drops down to $1/10$ of its peak value, the burst lasts about 15 ms (60 ms) for $\tau_\Phi = 100r_g/c$ ($500r_g/c$), with the average luminosity $2.6 \times 10^{43}\,\mathrm{erg\,s^{-1}}$ ($4.2 \times 10^{43}\,\mathrm{erg\,s^{-1}}$) for $B_* = 10^{13}\,\mathrm{G}$.

4.5 Electromagnetic transient

4.5.1 Radio burst

The power dissipated in monster shocks at small radii is immediately radiated in X-rays (Beloborodov, 2023). Later, when the shock expands to larger radii, it can become a bright source of radio emission and emit a powerful fast radio burst (FRB). Magnetized shocks emit a radio precursor by the synchrotron maser mechanism; it was initially proposed for termination shocks of pulsar winds (Hoshino et al., 1992; Lyubarsky, 2014) and then for internal shocks in magnetized $e^{\pm}$ outflows to explain repeating FRBs (Beloborodov, 2017).

Consider first the monster shock at small radii $r \sim 10^7$–10^8 cm. Kinetic plasma simulations of magnetized shocks (Sironi, Plotnikov, et al., 2021; Vanthieghem and Levinson, 2025) show precursor emission with frequency $\omega_{\rm pre} \sim 3\tilde{\omega}_B = 3e\tilde{B}/m_e c$, where $\tilde{B}$ is the upstream magnetic field measured in the plasma rest frame, e is the elementary charge, and m_e is the electron mass. $\tilde{B}$ is reduced from the background value $B_{\rm bg}$ by the strong expansion of the plasma ahead of the monster shock (Beloborodov, 2023):

$$\tilde{B} \approx \frac{\omega r}{2c\sigma_{\rm bg}} B_{\rm bg}, \tag{4.17}$$

where $\sigma_{\rm bg} = B_{\rm bg}^2/4\pi n_{\rm bg} m_e c^2$ is the background magnetization parameter, and ω is the frequency of the magnetospheric perturbation that led to shock formation (our simulation shows $\omega r/c \sim 10$). Density $n_{\rm bg}$ can be parameterized by multiplicity $\mathcal{M} \equiv n_{\rm bg}/n_0$, where $n_0 = \nabla \cdot \boldsymbol{E}/4\pi e \sim \Omega B_{\rm bg}/2\pi e c$ is the minimum density required to support the magnetospheric rotation with drift speed $\sim \Omega r$ (Goldreich and Julian, 1969). This gives $\omega_{\rm pre} \sim (r\omega/c)\mathcal{M}\Omega \sim 10^4 \mathcal{M}$ rad/s.

This simple estimate is, however, deficient because it neglects the deceleration of the upstream flow by strong radiative losses. Losses dramatically change the radio precursor from monster shocks at small radii by increasing its frequency and suppressing its power (Beloborodov, in preparation).

Powerful radio emission is expected from the relativistic shock when it expands far into the $e^{\pm}$ outflow, reaching $r \sim 10^{13}$–10^{14} cm (Beloborodov, 2017; Beloborodov, 2020). Then, a fraction $\sim 10^{-4}$ of the blast wave power is expected to convert to radio waves, whose frequency decreases with time (proportionally to the local B) and passes through the GHz band, best for radio observations. In this study, we do not follow the outflow dynamics with shocks at large radii; however, this may become possible for future MHD simulations. Our simulation shows that shocks launched from NS-BH mergers are asymmetric, but not strongly collimated. Therefore, they can produce FRBs observable for a broad range of line of sights. Note that no baryonic ejecta are expected from BH swallowing a NS, so nothing should block the FRB from observers.

4.5.2 Gamma-ray burst

The X-ray transient expected from the simulated merger is powered by dissipation of magnetospheric energy. Two dissipation mechanisms are observed in the simulation: shocks and magnetic reconnection in the split-monopole current sheet around the BH after the merger. Dissipation occurs at small radii, which correspond to a large compactness parameter $\ell = \sigma_{\rm T} L/r m_e c^3$, where L is the dissipation power and $\sigma_{\rm T}$ is the Thompson cross section. Note that L and ℓ scale as B^2. For a strongly magnetized NS, e.g. with $B \sim 10^{14}$ G, the huge ℓ implies that the dissipated energy becomes immediately thermalized. Thus, the merger ejects a hot "fireball" – a thermalized, magnetically dominated $e^{\pm}$ outflow. As the outflow expands to larger radii, it adiabatically cools, $e^{\pm}$ annihilate and release a burst of quasi-thermal radiation similar to the GRB from the magnetar collapse described in Most, Beloborodov, and Ripperda (2024).

An additional dissipation mechanism is expected to operate in the outflow at large radii, and can add a nonthermal tail to the GRB spectrum. It is caused by the striped structure of the outflow, similar to the striped winds from pulsars. The stripes develop current sheets where magnetic reconnection gradually dissipates the alternating magnetic flux (Lyubarsky and Kirk, 2001; Cerutti, Philippov, and Dubus, 2020). A similar mechanism was previously proposed to operate in canonical GRBs (Drenkhahn and Spruit, 2002). It will release energy after the outflow becomes optically thin (which happens quickly in the baryon-free outflow from BH–NS merger). Therefore, it can generate energetic particles, emitting a nonthermal component of the GRB.

4.6 Conclusions

We have presented a detailed numerical investigation into the magnetospheric dynamics of BH–NS mergers without tidal disruption. Using GRMHD simulations capable of probing the near force-free limit, we identify two mechanisms for generating an electromagnetic transient.

First, we observe that fast magnetosonic waves are launched into the magnetosphere of the NS before it plunges into the BH. These waves, as expanding outward with almost the speed of light, develop into monster shocks due to a more rapidly decaying ambient magnetic field (Beloborodov, 2023). The full MHD simulation is essential for tracking this effect, so it could not be captured by earlier vacuum or force-free simulations. The launched shocks are expected to emit a bright radio transient when they expand to large radii.

When the BH swallows the NS together with its magnetic dipole moment, its external magnetosphere quickly rearranges itself into a split-monopole configuration with a large-scale current sheet. Then, the BH gradually loses the acquired “magnetic hair.” This balding is assisted by magnetic reconnection and gravitational effects (QNMs). The relative importance of these two processes varies over time and depends on the misalignment between the magnetic dipole moment and the BH spin. The split monopole is dragged into rotation by the BH and forms a transient BH pulsar which can power a post-merger EM signal in the X-ray and γ-ray band.

The monster shocks and the balding BH pulsar were previously studied in symmetric setups with a single compact object (Bransgrove, Ripperda, and Philippov, 2021; Beloborodov, 2023; Most, Beloborodov, and Ripperda, 2024; Selvi et al., 2024). Our ab-initio simulations demonstrate how both phenomena naturally occur in the complex dynamical spacetime of the BH–NS merger.

The binary parameters considered in our work are representative of the BH–NS mergers detected to date (Abac et al., 2024), implying that shock formation from magnetosonic waves and the emergence of a BH pulsar could be a common outcome for the BH–NS populations observable with ground-based GW detectors such as the LIGO/Virgo/KAGRA network.

Acknowledgements

We are grateful to Ashley Bransgrove, Koushik Chatterjee, Alexander Chernoglazov, Amir Levinson, Keefe Mitman, Alexander Philippov, Eliot Quataert, Sebastiaan Selvi, Lorenzo Sironi, Anatoly Spitkovsky, Alexander Tchekhovskoy, Christopher Thompson, and Yici Zhong for insightful comments and discussions. Simulations were performed on the NSF Frontera cluster at the Texas Advanced Computing Center under grant AST21006, and on the Delta cluster at the National Center for Supercomputing Applications through allocation PHY210074.

BIBLIOGRAPHY

Abac, A. G. et al. (2024). "Observation of Gravitational Waves from the Coalescence of a 2.5–4.5 M $_\odot$ Compact Object and a Neutron Star". In: *Astrophysical Journal Letters* 970.2, p. L34. DOI: 10.3847/2041-8213/ad5beb. arXiv: 2404.04248.

Abbott, B. P. et al. (2016). "Observation of Gravitational Waves from a Binary Black Hole Merger". In: *Physical Review Letters* 116.6, p. 061102. DOI: 10.1103/PhysRevLett.116.061102. arXiv: 1602.03837.

– (2017). "Multi-messenger Observations of a Binary Neutron Star Merger". In: *Astrophysical Journal Letters* 848.2, p. L12. DOI: 10.3847/2041-8213/aa91c9. arXiv: 1710.05833.

– (2019). "GWTC-1: A Gravitational-Wave Transient Catalog of Compact Binary Mergers Observed by LIGO and Virgo during the First and Second Observing Runs". In: *Physical Review X* 9.3, p. 031040. DOI: 10.1103/PhysRevX.9.031040. arXiv: 1811.12907.

Abbott, R. et al. (2020). "GW190814: Gravitational Waves from the Coalescence of a 23 Solar Mass Black Hole with a 2.6 Solar Mass Compact Object". In: *Astrophysical Journal Letters* 896.2, p. L44. DOI: 10.3847/2041-8213/ab960f. arXiv: 2006.12611.

– (2021a). "GWTC-2: Compact Binary Coalescences Observed by LIGO and Virgo During the First Half of the Third Observing Run". In: *Physical Review X* 11, p. 021053. DOI: 10.1103/PhysRevX.11.021053. arXiv: 2010.14527.

– (2021b). "Observation of Gravitational Waves from Two Neutron Star–Black Hole Coalescences". In: *Astrophysical Journal Letters* 915.1, p. L5. DOI: 10.3847/2041-8213/ac082e. arXiv: 2106.15163.

– (2023). "GWTC-3: Compact Binary Coalescences Observed by LIGO and Virgo during the Second Part of the Third Observing Run". In: *Physical Review X* 13.4, p. 041039. DOI: 10.1103/PhysRevX.13.041039. arXiv: 2111.03606.

Afshordi, Niayesh et al. (2023). "Waveform Modelling for the Laser Interferometer Space Antenna". In: arXiv: 2311.01300.

Akiyama, Kazunori et al. (2019). "First M87 Event Horizon Telescope Results. I. The Shadow of the Supermassive Black Hole". In: *Astrophysical Journal Letters* 875, p. L1. DOI: 10.3847/2041-8213/ab0ec7. arXiv: 1906.11238.

Akmal, A., V. R. Pandharipande, and D. G. Ravenhall (1998). "The Equation of state of nucleon matter and neutron star structure". In: *Physical Review C* 58, pp. 1804–1828. DOI: 10.1103/PhysRevC.58.1804. arXiv: nucl-th/9804027.

Alcubierre, Miguel et al. (2003). "Gauge conditions for long term numerical black hole evolutions without excision". In: *Physical Review D* 67, p. 084023. DOI: 10.1103/PhysRevD.67.084023. arXiv: gr-qc/0206072.

Alic, Daniela et al. (2012). "Accurate Simulations of Binary Black-Hole Mergers in Force-Free Electrodynamics". In: *Astrophysical Journal* 754, p. 36. DOI: 10.1088/0004-637X/754/1/36. arXiv: 1204.2226.

Anand, Shreya et al. (2021). "Optical follow-up of the neutron star–black hole mergers S200105ae and S200115j". In: *Nature Astronomy* 5.1, pp. 46–53. DOI: 10.1038/s41550-020-1183-3. arXiv: 2009.07210.

Antonopoulou, Eleni, Argyrios Loules, and Antonios Nathanail (2025). "Magnetically arrested disk flux eruption events to describe SgrA* flares". In: arXiv: 2501.07521.

Appl, S., T. Lery, and H. Baty (2000). "Current-driven instabilities in astrophysical jets. Linear analysis". In: *Astronomy and Astrophysics* 355, pp. 818–828.

Archibald, R. F. et al. (2017). "Swift observations of two outbursts from the magnetar 4U 0142+61". In: *Astrophysical Journal* 834.2, p. 163. DOI: 10.3847/1538-4357/834/2/163. arXiv: 1611.09782.

Armas, Jay et al. (2020). "Consistent Blandford-Znajek Expansion". In: *Journal of Cosmology and Astroparticle Physics* 04, p. 009. DOI: 10.1088/1475-7516/2020/04/009. arXiv: 2002.01972.

Asano, Eiji, Toshio Uchida, and Ryoji Matsumoto (2005). "Time evolution of relativistic force-free fields connecting a neutron star and its disk". In: *Publications of the Astronomical Society of Japan* 57, p. 409. DOI: 10.1093/pasj/57.2.409. arXiv: astro-ph/0502371.

Baumgarte, Thomas W. and Stuart L. Shapiro (2003). "Collapse of a magnetized star to a black hole". In: *Astrophysical Journal* 585, pp. 930–947. DOI: 10.1086/346104. arXiv: astro-ph/0211339.

– (2010). *Numerical relativity: solving Einstein's equations on the computer*. OCLC: ocn496954929. Cambridge ; New York: Cambridge University Press. ISBN: 978-0-521-51407-1.

Beloborodov, Andrei M. (2013). "On the mechanism of hard X-ray emission from magnetars". In: *Astrophysical Journal* 762, p. 13. DOI: 10.1088/0004-637X/762/1/13. arXiv: 1201.0664.

– (2017). "A flaring magnetar in FRB 121102?" In: *Astrophysical Journal Letters* 843.2, p. L26. DOI: 10.3847/2041-8213/aa78f3. arXiv: 1702.08644.

– (2020). "Blast Waves from Magnetar Flares and Fast Radio Bursts". In: *Astrophysical Journal* 896.2, p. 142. DOI: 10.3847/1538-4357/ab83eb. arXiv: 1908.07743.

– (2021). "Emission of Magnetar Bursts and Precursors of Neutron Star Mergers". In: *Astrophysical Journal* 921.1, p. 92. DOI: 10.3847/1538-4357/ac17e7. arXiv: 2011.07310.

Beloborodov, Andrei M. (2023). "Monster Radiative Shocks in the Perturbed Magnetospheres of Neutron Stars". In: *Astrophysical Journal* 959.1, p. 34. DOI: 10.3847/1538-4357/acf659. arXiv: 2210.13509.

Bernuzzi, Sebastiano and David Hilditch (2010). "Constraint violation in free evolution schemes: Comparing BSSNOK with a conformal decomposition of Z4". In: *Physical Review D* 81, p. 084003. DOI: 10.1103/PhysRevD.81.084003. arXiv: 0912.2920.

Biscoveanu, Sylvia, Philippe Landry, and Salvatore Vitale (2022). "Population properties and multimessenger prospects of neutron star–black hole mergers following GWTC-3". In: *Monthly Notices of the Royal Astronomical Society* 518.4, pp. 5298–5312. DOI: 10.1093/mnras/stac3052. arXiv: 2207.01568.

Blakely, P. M. and N. Nikiforakis (2015). "Relativistic Bondi-Hoyle-Lyttleton accretion: A parametric study". In: *Astronomy and Astrophysics* 583, A90, A90. DOI: 10.1051/0004-6361/201525763.

Blandford, Roger D. and R. L. Znajek (1977). "Electromagnetic extractions of energy from Kerr black holes". In: *Monthly Notices of the Royal Astronomical Society* 179, pp. 433–456. DOI: 10.1093/mnras/179.3.433.

Bochenek, Christopher D. et al. (2020). "A fast radio burst associated with a Galactic magnetar". In: *Nature* 587.7832, pp. 59–62. DOI: 10.1038/s41586-020-2872-x. arXiv: 2005.10828.

Bogdanovic, Tamara, Christopher S. Reynolds, and M. Coleman Miller (2007). "Alignment of the spins of supermassive black holes prior to merger". In: *Astrophysical Journal Letters* 661, p. L147. DOI: 10.1086/518769. arXiv: astro-ph/0703054.

Bogovalov, S. V. (1999). "On the physics of cold mhd winds from oblique rotators". In: *Astronomy and Astrophysics* 349, pp. 1017–1026. arXiv: astro-ph/9907051.

Bondi, H. (1952). "On spherically symmetrical accretion". In: *Monthly Notices of the Royal Astronomical Society* 112, p. 195. DOI: 10.1093/mnras/112.2.195.

Borges, Rafael et al. (2008). "An improved weighted essentially non-oscillatory scheme for hyperbolic conservation laws". In: *Journal of Computational Physics* 227.6, pp. 3191–3211. ISSN: 0021-9991. DOI: https://doi.org/10.1016/j.jcp.2007.11.038.

Bransgrove, Ashley, Andrei M. Beloborodov, and Yuri Levin (2020). "A Quake Quenching the Vela Pulsar". In: DOI: 10.3847/1538-4357/ab93b7. arXiv: 2001.08658.

Bransgrove, Ashley, Bart Ripperda, and Alexander A. Philippov (2021). "Magnetic Hair and Reconnection in Black Hole Magnetospheres". In: *Physical Review Letters* 127.5, p. 055101. DOI: 10.1103/PhysRevLett.127.055101. arXiv: 2109.14620.

Bromberg, Omer and Alexander Tchekhovskoy (2016). “Relativistic MHD simulations of core-collapse GRB jets: 3D instabilities and magnetic dissipation”. In: *Monthly Notices of the Royal Astronomical Society* 456.2, pp. 1739–1760. DOI: 10.1093/mnras/stv2591. arXiv: 1508.02721.

Bugner, Marcus et al. (2016). “Solving 3D relativistic hydrodynamical problems with weighted essentially nonoscillatory discontinuous Galerkin methods”. In: *Physical Review D* 94.8, p. 084004. DOI: 10.1103/PhysRevD.94.084004. arXiv: 1508.07147.

Campanelli, Manuela et al. (2007a). “Large merger recoils and spin flips from generic black-hole binaries”. In: *Astrophysical Journal Letters* 659, pp. L5–L8. DOI: 10.1086/516712. arXiv: gr-qc/0701164.

– (2007b). “Maximum gravitational recoil”. In: *Physical Review Letters* 98, p. 231102. DOI: 10.1103/PhysRevLett.98.231102. arXiv: gr-qc/0702133.

Cao, Gang, Li Zhang, and Sineng Sun (2016). “Spectral simulations of an axisymmetric force-free pulsar magnetosphere”. In: *Monthly Notices of the Royal Astronomical Society* 455.4, pp. 4267–4273. DOI: 10.1093/mnras/stv2577. arXiv: 1511.07934.

Carrasco, Federico, Carlos Palenzuela, and Oscar Reula (2018). “Pulsar magnetospheres in General Relativity”. In: *Physical Review D* 98.2, p. 023010. DOI: 10.1103/PhysRevD.98.023010. arXiv: 1805.04123.

Carrasco, Federico and Oscar Reula (2017). “Novel scheme for simulating the force-free equations: Boundary conditions and the evolution of solutions towards stationarity”. In: *Physical Review D* 96.6, p. 063006. DOI: 10.1103/PhysRevD.96.063006. arXiv: 1703.10241.

Carrasco, Federico and Masaru Shibata (2020). “Magnetosphere of an orbiting neutron star”. In: *Physical Review D* 101.6, p. 063017. DOI: 10.1103/PhysRevD.101.063017. arXiv: 2001.04210.

Carrasco, Federico, Masaru Shibata, and Oscar Reula (2021). “Magnetospheres of black hole-neutron star binaries”. In: *Physical Review D* 104.6, p. 063004. DOI: 10.1103/PhysRevD.104.063004. arXiv: 2106.09081.

Carrasco, Federico, Daniele Viganò, et al. (2019). “Triggering magnetar outbursts in 3D force-free simulations”. In: *Monthly Notices of the Royal Astronomical Society* 484.1, pp. L124–L129. DOI: 10.1093/mnrasl/slz016. arXiv: 1901.08889.

Cashen, Benjamin, Adam Aker, and Michael Kesden (2017). “Gravitomagnetic dynamical friction”. In: *Physical Review D* 95.6, p. 064014. DOI: 10.1103/PhysRevD.95.064014. arXiv: 1610.01590.

Cernetic, Miha et al. (2024). “Supersonic turbulence simulations with GPU-based high-order Discontinuous Galerkin hydrodynamics”. In: *Monthly Notices of the Royal Astronomical Society* 534.3, pp. 1963–1984. DOI: 10.1093/mnras/stae2192. arXiv: 2401.06841.

Cerutti, Benoît and Andrei M. Beloborodov (2017). “Electrodynamics of pulsar magnetospheres”. In: *Space Science Reviews* 207.1-4, pp. 111–136. DOI: 10.1007/s11214-016-0315-7. arXiv: 1611.04331.

Cerutti, Benoît and Alexander A. Philippov (2017). “Dissipation of the striped pulsar wind”. In: *Astronomy and Astrophysics* 607, A134. DOI: 10.1051/0004-6361/201731680. arXiv: 1710.07320.

Cerutti, Benoît, Alexander A. Philippov, and Guillaume Dubus (2020). “Dissipation of the striped pulsar wind and non-thermal particle acceleration: 3D PIC simulations”. In: *Astronomy and Astrophysics* 642, A204. DOI: 10.1051/0004-6361/202038618. arXiv: 2008.11462.

Cerutti, Benoît, Alexander A. Philippov, Kyle Parfrey, et al. (2015). “Particle acceleration in axisymmetric pulsar current sheets”. In: *Monthly Notices of the Royal Astronomical Society* 448.1, pp. 606–619. DOI: 10.1093/mnras/stv042. arXiv: 1410.3757.

Chandrasekhar, S. (1943). “Dynamical Friction. I. General Considerations: the Coefficient of Dynamical Friction.” In: *Astrophysical Journal* 97, p. 255. DOI: 10.1086/144517.

Chatterjee, Koushik and Ramesh Narayan (2022). “Flux Eruption Events Drive Angular Momentum Transport in Magnetically Arrested Accretion Flows”. In: *Astrophysical Journal* 941.1, p. 30. DOI: 10.3847/1538-4357/ac9d97. arXiv: 2210.08045.

Chawla, Sarvnipun et al. (2010). “Mergers of Magnetized Neutron Stars with Spinning Black Holes: Disruption, Accretion and Fallback”. In: *Physical Review Letters* 105, p. 111101. DOI: 10.1103/PhysRevLett.105.111101. arXiv: 1006.2839.

Chen, Alexander Y. and Andrei M. Beloborodov (2014). “Electrodynamics of axisymmetric pulsar magnetosphere with electron-positron discharge: a numerical experiment”. In: *Astrophysical Journal Letters* 795.1, p. L22. DOI: 10.1088/2041-8205/795/1/L22. arXiv: 1406.7834.

– (2017). “Particle-in-cell simulations of the twisted magnetospheres of magnetars. I”. In: *Astrophysical Journal* 844.2, p. 133. DOI: 10.3847/1538-4357/aa7a57. arXiv: 1610.10036.

Chen, Alexander Y., Yajie Yuan, Xinyu Li, et al. (2022). “Propagation of a Strong Fast Magnetosonic Wave in the Magnetosphere of a Neutron Star”. In: arXiv: 2210.13506.

Chen, Alexander Y., Yajie Yuan, and Georgios Vasilopoulos (2020). “A Numerical Model for the Multiwavelength Lightcurves of PSR J0030+0451”. In: *Astrophysical Journal Letters* 893.2, p. L38. DOI: 10.3847/2041-8213/ab85c5. arXiv: 2002.06104.

Chen, Ken and Zi-Gao Dai (2024). "Electromagnetic Counterparts Powered by Kicked Remnants of Black Hole Binary Mergers in AGN Disks". In: *Astrophysical Journal* 961.2, p. 206. DOI: 10.3847/1538-4357/ad0dfd. arXiv: 2311.10518.

Chen, Yuxi, Gábor Tóth, and Tamas I. Gombosi (2016). "A fifth-order finite difference scheme for hyperbolic equations on block-adaptive curvilinear grids". In: *Journal of Computational Physics* 305, pp. 604–621. ISSN: 0021-9991. DOI: https://doi.org/10.1016/j.jcp.2015.11.003.

Cho, Jungyeon (2005). "Simulation of relativistic force-free magnetohydrodynamic turbulence". In: *Astrophysical Journal* 621, p. 324. DOI: 10.1086/427493. arXiv: astro-ph/0408318.

Cockburn, Bernardo and Chi-Wang Shu (2001). "Runge-Kutta discontinuous Galerkin methods for convection-dominated problems". In: *Journal of Scientific Computing* 16.3, pp. 173–261. ISSN: 1573-7691. DOI: 10.1023/A:1012873910884.

Colella, Phillip and Paul R. Woodward (1984). "The Piecewise Parabolic Method (PPM) for Gas Dynamical Simulations". In: *Journal of Computational Physics* 54, pp. 174–201. DOI: 10.1016/0021-9991(84)90143-8.

Coleman Miller, M. and Julian H. Krolik (2013). "Alignment of supermassive black hole binary orbits and spins". In: *Astrophysical Journal* 774, p. 43. DOI: 10.1088/0004-637X/774/1/43. arXiv: 1307.6569.

Contopoulos, Ioannis, Demosthenes Kazanas, and Christian Fendt (1999). "The axisymmetric pulsar magnetosphere". In: *Astrophysical Journal* 511, p. 351. DOI: 10.1086/306652. arXiv: astro-ph/9903049.

Contopoulos, Ioannis, Demosthenes Kazanas, and Demetrios B. Papadopoulos (2013). "The Force-Free Magnetosphere of a Rotating Black Hole". In: *Astrophysical Journal* 765, p. 113. DOI: 10.1088/0004-637X/765/2/113. arXiv: 1212.0320.

Costa, L. Filipe O., Rita Franco, and Vitor Cardoso (2018). "Gravitational Magnus effect". In: *Physical Review D* 98.2, p. 024026. DOI: 10.1103/PhysRevD.98.024026. arXiv: 1805.01097.

Cruz-Osorio, Alejandro and F. D. Lora-Clavijo (2016). "Non-axisymmetric relativistic wind accretion with velocity gradients on to a rotating black hole". In: *Monthly Notices of the Royal Astronomical Society* 460.3, pp. 3193–3201. DOI: 10.1093/mnras/stw1149. arXiv: 1605.04176.

Cruz-Osorio, Alejandro, F. D. Lora-Clavijo, and F. S. Guzman (2012). "Is the flip-flop behaviour of accretion shock cones on to black holes an effect of coordinates?" In: *Monthly Notices of the Royal Astronomical Society* 426, pp. 732–738. DOI: 10.1111/j.1365-2966.2012.21794.x. arXiv: 1210.6588.

Cruz-Osorio, Alejandro and Luciano Rezzolla (2020). “Common-envelope Dynamics of a Stellar-mass Black Hole: General Relativistic Simulations”. In: *Astrophysical Journal* 894.2, p. 147. DOI: 10.3847/1538-4357/ab89aa. arXiv: 2004.13782.

D’Orazio, Daniel J. and Janna Levin (2013). “Big Black Hole, Little Neutron Star: Magnetic Dipole Fields in the Rindler Spacetime”. In: *Physical Review D* 88.6, p. 064059. DOI: 10.1103/PhysRevD.88.064059. arXiv: 1302.3885.

D’Orazio, Daniel J., Janna Levin, et al. (2016). “Bright transients from strongly-magnetized neutron star-black hole mergers”. In: *Physical Review D* 94.2, p. 023001. DOI: 10.1103/PhysRevD.94.023001. arXiv: 1601.00017.

Dai, Zi-Gao (2019). “Inspiral of a Spinning Black Hole–Magnetized Neutron Star Binary: Increasing Charge and Electromagnetic Emission”. In: *Astrophysical Journal Letters* 873.2, p. L13. DOI: 10.3847/2041-8213/ab0b45. arXiv: 1902.07939.

Davis, R. and L. Hartmann (1983). “Constraints on the inclination and masses of the HDE 226868/Cygnus X-1 system from the observations.” In: *Astrophysical Journal* 270, pp. 671–677. DOI: 10.1086/161158.

Dedner, A. et al. (2002). “Hyperbolic divergence cleaning for the MHD equations”. In: *Journal of Computational Physics* 175.2, pp. 645–673. DOI: 10.1006/jcph.2001.6961.

Del Zanna, Luca, Simone Landi, et al. (2024). “A GPU-Accelerated Modern Fortran Version of the ECHO Code for Relativistic Magnetohydrodynamics”. In: *Fluids* 9.1. ISSN: 2311-5521. DOI: 10.3390/fluids9010016.

Del Zanna, Luca, Olindo Zanotti, et al. (2007). “ECHO: an Eulerian Conservative High Order scheme for general relativistic magnetohydrodynamics and magnetodynamics”. In: *Astronomy and Astrophysics* 473, pp. 11–30. DOI: 10.1051/0004-6361:20077093. arXiv: 0704.3206.

Deppe, Nils et al. (2022). “Simulating magnetized neutron stars with discontinuous Galerkin methods”. In: *Physical Review D* 105.12, p. 123031. DOI: 10.1103/PhysRevD.105.123031. arXiv: 2109.12033.

Deppe, Nils, François Hébert, et al. (2022). “A high-order shock capturing discontinuous Galerkin–finite difference hybrid method for GRMHD”. In: *Classical and Quantum Gravity* 39.19, p. 195001. DOI: 10.1088/1361-6382/ac8864. arXiv: 2109.11645.

Deppe, Nils, William Throwe, et al. (Mar. 2025). *SpECTRE v2025.03.17*. Version 2025.03.17. DOI: 10.5281/zenodo.15040490. URL: https://spectre-code.org.

Dexter, J. et al. (2020). “Sgr A* near-infrared flares from reconnection events in a magnetically arrested disc”. In: *Monthly Notices of the Royal Astronomical Society* 497.4, pp. 4999–5007. DOI: 10.1093/mnras/staa2288. arXiv: 2006.03657.

Dittmann, Alexander J., Adam M. Dempsey, and Hui Li (2024). “The Evolution of Inclined Binary Black Holes in the Disks of Active Galactic Nuclei”. In: *Astrophysical Journal* 964.1, p. 61. DOI: 10.3847/1538-4357/ad23ce. arXiv: 2310.03832.

Dönmez, Orhan (2012). “Relativistic simulation of flip-flop instabilities of Bondi–Hoyle accretion and quasi-periodic oscillations”. In: *Monthly Notices of the Royal Astronomical Society* 426.2, pp. 1533–1545. ISSN: 0035-8711. DOI: 10.1111/j.1365-2966.2012.21616.x.

Dönmez, Orhan, Olindo Zanotti, and Luciano Rezzolla (2011). “On the development of QPOs in Bondi-Hoyle accretion flows”. In: *Monthly Notices of the Royal Astronomical Society* 412, pp. 1659–1668. DOI: 10.1111/j.1365-2966.2010.18003.x. arXiv: 1010.1739.

Drenkhahn, G. and H. C. Spruit (2002). “Efficient acceleration and radiation in Poynting flux powered GRB outflows”. In: *Astronomy and Astrophysics* 391, p. 1141. DOI: 10.1051/0004-6361:20020839. arXiv: astro-ph/0202387.

Dubey, Anshu et al. (2014). “A survey of high level frameworks in block-structured adaptive mesh refinement packages”. In: *Journal of Parallel and Distributed Computing* 74, pp. 3217–3227. DOI: 10.1016/j.jpdc.2014.07.001. arXiv: 1610.08833.

Duez, Matthew D. et al. (2005). “Relativistic magnetohydrodynamics in dynamical spacetimes: Numerical methods and tests”. In: *Physical Review D* 72, p. 024028. DOI: 10.1103/PhysRevD.72.024028. arXiv: astro-ph/0503420.

Dumbser, Michael, Olindo Zanotti, Elena Gaburro, et al. (2024). “A well-balanced discontinuous Galerkin method for the first–order Z4 formulation of the Einstein–Euler system”. In: *Journal of Computational Physics* 504, p. 112875. DOI: 10.1016/j.jcp.2024.112875. arXiv: 2307.06629.

Dumbser, Michael, Olindo Zanotti, Raphaël Loubère, et al. (2014). “A posteriori subcell limiting of the discontinuous Galerkin finite element method for hyperbolic conservation laws”. In: *Journal of Computational Physics* 278, pp. 47–75. ISSN: 0021-9991. DOI: https://doi.org/10.1016/j.jcp.2014.08.009.

Dyson, Conor et al. (2024). “Relativistic aerodynamics of spinning black holes”. In: *Physical Review D* 109.10, p. 104038. DOI: 10.1103/PhysRevD.109.104038. arXiv: 2402.07981.

East, William E. et al. (2021). “Multimessenger Signals from Black Hole–Neutron Star Mergers without Significant Tidal Disruption”. In: *Astrophysical Journal Letters* 912.1, p. L18. DOI: 10.3847/2041-8213/abf566. arXiv: 2101.12214.

Edgar, Richard G. (2004). “A Review of Bondi-Hoyle-Lyttleton accretion”. In: *New Astronomy Reviews* 48, pp. 843–859. DOI: 10.1016/j.newar.2004.06.001. arXiv: astro-ph/0406166.

Einfeldt, B et al. (1991). “On Godunov-type methods near low densities”. In: *Journal of Computational Physics* 92.2, pp. 273–295. ISSN: 0021-9991. DOI: https://doi.org/10.1016/0021-9991(91)90211-3.

El Mellah, I., J. O. Sundqvist, and R. Keppens (2018). “Accretion from a clumpy massive-star wind in supergiant X-ray binaries”. In: *Monthly Notices of the Royal Astronomical Society* 475.3, pp. 3240–3252. DOI: 10.1093/mnras/stx3211. arXiv: 1711.08709.

Etienne, Zachariah B., Yuk Tung Liu, et al. (2012). “General relativistic simulations of black hole-neutron star mergers: Effects of magnetic fields”. In: *Physical Review D* 85, p. 064029. DOI: 10.1103/PhysRevD.85.064029. arXiv: 1112.0568.

Etienne, Zachariah B., Vasileios Paschalidis, Roland Haas, et al. (2015). “IllinoisGRMHD: An Open-Source, User-Friendly GRMHD Code for Dynamical Spacetimes”. In: *Classical and Quantum Gravity* 32, p. 175009. DOI: 10.1088/0264-9381/32/17/175009. arXiv: 1501.07276.

Etienne, Zachariah B., Vasileios Paschalidis, and Stuart L. Shapiro (2012). “General relativistic simulations of black hole-neutron star mergers: Effects of tilted magnetic fields”. In: *Physical Review D* 86, p. 084026. DOI: 10.1103/PhysRevD.86.084026. arXiv: 1209.1632.

Etienne, Zachariah B., Mew-Bing Wan, et al. (2017). “GiRaFFE: An Open-Source General Relativistic Force-Free Electrodynamics Code”. In: *Classical and Quantum Gravity* 34.21, p. 215001. DOI: 10.1088/1361-6382/aa8ab3. arXiv: 1704.00599.

Evans, Charles R. and John F. Hawley (1988). “Simulation of magnetohydrodynamic flows: A Constrained transport method”. In: *Astrophysical Journal* 332, pp. 659–677. DOI: 10.1086/166684.

Fambri, Francesco et al. (2018). “ADER discontinuous Galerkin schemes for general-relativistic ideal magnetohydrodynamics”. In: *Monthly Notices of the Royal Astronomical Society* 477.4, pp. 4543–4564. DOI: 10.1093/mnras/sty734. arXiv: 1801.02839.

Fernández, Rodrigo et al. (2017). “Dynamics, nucleosynthesis, and kilonova signature of black hole—neutron star merger ejecta”. In: *Classical and Quantum Gravity* 34.15, p. 154001. DOI: 10.1088/1361-6382/aa7a77. arXiv: 1612.04829.

Fishbone, L. G. and V. Moncrief (1976). “Relativistic fluid disks in orbit around Kerr black holes.” In: *Astrophysical Journal* 207, pp. 962–976. DOI: 10.1086/154565.

Foglizzo, Thierry, P. Galletti, and M. Ruffert (2005). “A Fresh look at the unstable simulations of Bondi-Hoyle-Lyttleton accretion”. In: *Astronomy and Astrophysics* 435, p. 397. DOI: 10.1051/0004-6361:20042201. arXiv: astro-ph/0502168.

Font, Jose A. and Jose M. Ibanez (1998a). "A Numerical Study of Relativistic Bondi-Hoyle Accretion onto a Moving Black Hole: Axisymmetric Computations in a Schwarzschild Background". In: *Astrophysical Journal* 494.1, pp. 297–316. DOI: 10.1086/305205.

– (1998b). "Nonaxisymmetric relativistic Bondi-Hoyle accretion onto a Schwarzschild black hole". In: *Monthly Notices of the Royal Astronomical Society* 298, p. 835. DOI: 10.1046/j.1365-8711.1998.01664.x. arXiv: astro-ph/9804254.

Font, Jose A., Jose M. Ibanez, and Philippos Papadopoulos (1999). "Nonaxisymmetric relativistic Bondi-Hoyle accretion onto a Kerr black hole". In: *Monthly Notices of the Royal Astronomical Society* 305, p. 920. DOI: 10.1046/j.1365-8711.1999.02459.x. arXiv: astro-ph/9810344.

Ford, K. E. S. and B. McKernan (2022). "Binary black hole merger rates in AGN discs versus nuclear star clusters: loud beats quiet". In: *Monthly Notices of the Royal Astronomical Society* 517.4, pp. 5827–5834. DOI: 10.1093/mnras/stac2861. arXiv: 2109.03212.

Foucart, Francois (2012). "Black Hole-Neutron Star Mergers: Disk Mass Predictions". In: *Physical Review D* 86, p. 124007. DOI: 10.1103/PhysRevD.86.124007. arXiv: 1207.6304.

Foucart, Francois, Tanja Hinderer, and Samaya Nissanke (2018). "Remnant baryon mass in neutron star-black hole mergers: Predictions for binary neutron star mimickers and rapidly spinning black holes". In: *Physical Review D* 98.8, p. 081501. DOI: 10.1103/PhysRevD.98.081501. arXiv: 1807.00011.

Foucart, Francois, Lawrence E. Kidder, et al. (2008). "Initial data for black hole-neutron star binaries: A Flexible, high-accuracy spectral method". In: *Physical Review D* 77, p. 124051. DOI: 10.1103/PhysRevD.77.124051. arXiv: 0804.3787.

Fragione, Giacomo (2021). "Black-hole–Neutron-star Mergers Are Unlikely Multimessenger Sources". In: *Astrophysical Journal Letters* 923.1, p. L2. DOI: 10.3847/2041-8213/ac3bcd. arXiv: 2110.09604.

Gaburov, Evghenii, Anders Johansen, and Yuri Levin (2012). "Magnetically-levitating disks around supermassive black holes". In: *Astrophysical Journal* 758, p. 103. DOI: 10.1088/0004-637X/758/2/103. arXiv: 1201.4873.

Galishnikova, Alisa et al. (2025). "Strongly Magnetized Accretion with Low Angular Momentum Produces a Weak Jet". In: *Astrophysical Journal* 978.2, p. 148. DOI: 10.3847/1538-4357/ad9926. arXiv: 2409.11486.

Gardiner, Thomas A. and James M. Stone (2008). "An Unsplit Godunov Method for Ideal MHD via Constrained Transport in Three Dimensions". In: *Journal of Computational Physics* 227, pp. 4123–4141. DOI: 10.1016/j.jcp.2007.12.017. arXiv: 0712.2634.

Giacintucci, S. and T. Venturi (2009). "Tailed radio galaxies as tracers of galaxy clusters. Serendipitous discoveries with the GMRT". In: *Astronomy and Astrophysics* 505, p. 55. DOI: `10.1051/0004-6361/200912609`. arXiv: `0907.2306`.

Gies, D. R. et al. (2008). "Stellar Wind Variations During the X-ray High and Low States of Cygnus X-1". In: *Astrophysical Journal* 678, p. 1237. DOI: `10.1086/586690`. arXiv: `0801.4286`.

Goldreich, Peter and William H. Julian (1969). "Pulsar electrodynamics". In: *Astrophysical Journal* 157, p. 869. DOI: `10.1086/150119`.

Gonzalez, J. A., M. D. Hannam, et al. (2007). "Supermassive recoil velocities for binary black-hole mergers with antialigned spins". In: *Physical Review Letters* 98, p. 231101. DOI: `10.1103/PhysRevLett.98.231101`. arXiv: `gr-qc/0702052`.

Gonzalez, J. A., Ulrich Sperhake, et al. (2007). "Total recoil: The Maximum kick from nonspinning black-hole binary inspiral". In: *Physical Review Letters* 98, p. 091101. DOI: `10.1103/PhysRevLett.98.091101`. arXiv: `gr-qc/0610154`.

Gottlieb, Ore et al. (2023a). "Large-scale Evolution of Seconds-long Relativistic Jets from Black Hole–Neutron Star Mergers". In: *Astrophysical Journal Letters* 954.1, p. L21. DOI: `10.3847/2041-8213/aceeff`. arXiv: `2306.14947`.

Gottlieb, Ore et al. (2023b). "Hours-long Near-UV/Optical Emission from Mildly Relativistic Outflows in Black Hole–Neutron Star Mergers". In: *Astrophysical Journal Letters* 953.1, p. L11. DOI: `10.3847/2041-8213/acec4a`. arXiv: `2306.14946`.

Gracia-Linares, Miguel and Francisco S. Guzmán (2015). "Accretion of supersonic winds onto black holes in 3D: stability of the shock cone". In: *Astrophysical Journal* 812, p. 23. DOI: `10.1088/0004-637X/812/1/23`. arXiv: `1510.05947`.

– (2023). "Accretion of supersonic magnetized winds onto black holes". In: *Monthly Notices of the Royal Astronomical Society* 519.4, pp. 6020–6027. DOI: `10.1093/mnras/stad084`. arXiv: `2301.04307`.

Graham, M. J. et al. (2020). "Candidate Electromagnetic Counterpart to the Binary Black Hole Merger Gravitational Wave Event S190521g". In: *Physical Review Letters* 124.25, p. 251102. DOI: `10.1103/PhysRevLett.124.251102`. arXiv: `2006.14122`.

Grandclement, Philippe (2006). "Accurate and realistic initial data for black hole-neutron star binaries". In: *Physical Review D* 74. [Erratum: Phys.Rev.D 75, 129903 (2007)], p. 124002. DOI: `10.1103/PhysRevD.74.124002`. arXiv: `gr-qc/0609044`.

– (2010). "Kadath: A Spectral solver for theoretical physics". In: *Journal of Computational Physics* 229, pp. 3334–3357. DOI: `10.1016/j.jcp.2010.01.005`. arXiv: `0909.1228`.

Grete, Philipp, Forrest W. Glines, and Brian W. O'Shea (2021). "K-Athena: a performance portable structured grid finite volume magnetohydrodynamics code". In: *IEEE Transactions on Parallel and Distributed Systems* 32.1, pp. 85–907. DOI: 10.1109/TPDS.2020.3010016. arXiv: 1905.04341.

Grinberg, V. et al. (2015). "Long term variability of Cygnus X-1 - VII. Orbital variability of the focussed wind in Cyg X-1/HDE 226868 system". In: *Astronomy and Astrophysics* 576, A117. DOI: 10.1051/0004-6361/201425418. arXiv: 1502.07343.

Gröbner, Matthias et al. (2020). "Binary black hole mergers in AGN accretion discs: gravitational wave rate density estimates". In: *Astronomy and Astrophysics* 638, A119. DOI: 10.1051/0004-6361/202037681. arXiv: 2005.03571.

Gruzinov, Andrei (1999). *Stability in Force-Free Electrodynamics*. arXiv: astro-ph/9902288.

Hairer, E., S.P. Nørsett, and G. Wanner (1993). *Solving Ordinary Differential Equations II: Stiff and Differential-Algebraic Problems*. Springer. ISBN: 9783540604525.

Hakobyan, Hayk, Bart Ripperda, and Alexander A. Philippov (2023). "Radiative Reconnection-powered TeV Flares from the Black Hole Magnetosphere in M87". In: *Astrophysical Journal Letters* 943.2, p. L29. DOI: 10.3847/2041-8213/acb264. arXiv: 2209.02105.

Hardcastle, Martin J. and I. Sakelliou (2004). "Jet termination in wide- angle tailed radio sources". In: *Monthly Notices of the Royal Astronomical Society* 349, p. 560. DOI: 10.1111/j.1365-2966.2004.07522.x. arXiv: astro-ph/0312245.

Harris, Charles R. et al. (Sept. 2020). "Array programming with NumPy". In: *Nature* 585.7825, pp. 357–362. DOI: 10.1038/s41586-020-2649-2.

Harten, Amiram, Peter D. Lax, and Bram van Leer (1983). "On Upstream Differencing and Godunov-Type Schemes for Hyperbolic Conservation Laws". In: *SIAM Review* 25.1, pp. 35–61. DOI: 10.1137/1025002.

Hayashi, Kota, Sho Fujibayashi, et al. (2022). "General-relativistic neutrino-radiation magnetohydrodynamic simulation of seconds-long black hole-neutron star mergers". In: *Physical Review D* 106.2, p. 023008. DOI: 10.1103/PhysRevD.106.023008. arXiv: 2111.04621.

Hayashi, Kota, Kenta Kiuchi, et al. (2023). "General-relativistic neutrino-radiation magnetohydrodynamics simulation of seconds-long black hole-neutron star mergers: Dependence on the initial magnetic field strength, configuration, and neutron-star equation of state". In: *Physical Review D* 107.12, p. 123001. DOI: 10.1103/PhysRevD.107.123001. arXiv: 2211.07158.

Healy, James, Carlos O. Lousto, and Yosef Zlochower (2014). "Remnant mass, spin, and recoil from spin aligned black-hole binaries". In: *Physical Review D* 90.10, p. 104004. DOI: 10.1103/PhysRevD.90.104004. arXiv: 1406.7295.

Herrmann, Frank et al. (2007). "Gravitational recoil from spinning binary black hole mergers". In: *Astrophysical Journal* 661, pp. 430–436. DOI: 10.1086/513603. arXiv: gr-qc/0701143.

Hesthaven, J. S. and T. Warburton (2007). *Nodal Discontinuous Galerkin Methods: Algorithms, Analysis, and Applications*. Texts in Applied Mathematics. Springer New York. ISBN: 9780387720654.

Hilditch, David, Sebastiano Bernuzzi, et al. (2013). "Compact binary evolutions with the Z4c formulation". In: *Physical Review D* 88, p. 084057. DOI: 10.1103/PhysRevD.88.084057. arXiv: 1212.2901.

Hilditch, David and Andreas Schoepe (2019). "Hyperbolicity of divergence cleaning and vector potential formulations of general relativistic magnetohydrodynamics". In: *Physical Review D* 99.10, p. 104034. DOI: 10.1103/PhysRevD.99.104034. arXiv: 1812.03485.

Hopkins, Philip F., Michael Y. Grudic, et al. (2024). "FORGE'd in FIRE: Resolving the End of Star Formation and Structure of AGN Accretion Disks from Cosmological Initial Conditions". In: *The Open Journal of Astrophysics* 7, 18, p. 18. DOI: 10.21105/astro.2309.13115. arXiv: 2309.13115.

Hopkins, Philip F., Jonathan Squire, et al. (2024). "FORGE'd in FIRE II: The Formation of Magnetically-Dominated Quasar Accretion Disks from Cosmological Initial Conditions". In: *The Open Journal of Astrophysics* 7, 19, p. 19. DOI: 10.21105/astro.2310.04506. arXiv: 2310.04506.

Hoshino, Masahiro et al. (1992). "Relativistic magnetosonic shock waves in synchrotron sources - Shock structure and nonthermal acceleration of positrons". In: *Astrophysical Journal* 390, pp. 454–479. DOI: 10.1086/171296.

Hoyle, F. and R. A. Lyttleton (1939). "The effect of interstellar matter on climatic variation". In: *Proceedings of the Cambridge Philosophical Society* 35.3, p. 405. DOI: 10.1017/S0305004100021150.

Igumenshchev, Igor V. (2008). "Magnetically Arrested Disks and Origin of Poynting Jets: Numerical Study". In: *Astrophysical Journal* 677, p. 317. DOI: 10.1086/529025. arXiv: 0711.4391.

Igumenshchev, Igor V., Ramesh Narayan, and Marek A. Abramowicz (2003). "Three-dimensional mhd simulations of radiatively inefficient accretion flows". In: *Astrophysical Journal* 592, pp. 1042–1059. DOI: 10.1086/375769. arXiv: astro-ph/0301402.

Ishibashi, Wako and Matthias Gröbner (2020). "Evolution of binary black holes in AGN accretion discs: Disc-binary interaction and gravitational wave emission". In: *Astronomy and Astrophysics* 639, A108. DOI: 10.1051/0004-6361/202037799. arXiv: 2006.07407.

Ivanova, N. et al. (2013). "Common Envelope Evolution: Where we stand and how we can move forward". In: *Astronomy and Astrophysics Review* 21, p. 59. DOI: 10.1007/s00159-013-0059-2. arXiv: 1209.4302.

Izquierdo, Manuel R. et al. (2024). "Large eddy simulations of magnetized mergers of black holes and neutron stars". In: *Physical Review D* 110.8, p. 083017. DOI: 10.1103/PhysRevD.110.083017. arXiv: 2403.09770.

Janka, H. -T. et al. (1999). "Black hole: Neutron star mergers as central engines of gamma-ray bursts". In: *Astrophysical Journal Letters* 527, p. L39. DOI: 10.1086/312397. arXiv: astro-ph/9908290.

Kaaz, Nicholas, Andrea Antoni, and Enrico Ramirez-Ruiz (2019). "Bondi–Hoyle–Lyttleton Accretion onto Star Clusters". In: *Astrophysical Journal* 876.2, p. 142. DOI: 10.3847/1538-4357/ab158b. arXiv: 1901.03649.

Kaaz, Nicholas, Ariadna Murguia-Berthier, et al. (2023). "Jet Formation in 3D GRMHD Simulations of Bondi–Hoyle–Lyttleton Accretion". In: *Astrophysical Journal* 950.1, p. 31. DOI: 10.3847/1538-4357/acc7a1. arXiv: 2201.11753.

Kaaz, Nicholas, Sophie Lund Schrøder, et al. (2023). "The Hydrodynamic Evolution of Binary Black Holes Embedded within the Vertically Stratified Disks of Active Galactic Nuclei". In: *Astrophysical Journal* 944.1, p. 44. DOI: 10.3847/1538-4357/aca967. arXiv: 2103.12088.

Kalapotharakos, Constantinos and Ioannis Contopoulos (2009). "Three-dimensional numerical simulations of the pulsar magnetosphere: Preliminary results". In: *Astronomy and Astrophysics* 496, pp. 495–502. DOI: 10.1051/0004-6361:200810281. arXiv: 0811.2863.

Kaspi, V. M. et al. (2003). "A Major Soft Gamma Repeater-like Outburst and Rotation Glitch in the No-longer-so-anomalous X-Ray Pulsar 1E 2259+586". In: *Astrophysical Journal Letters* 588, pp. L93–L96. DOI: 10.1086/375683. arXiv: astro-ph/0304205.

Kastaun, Wolfgang, Jay Vijay Kalinani, and Riccardo Ciolfi (2021). "Robust Recovery of Primitive Variables in Relativistic Ideal Magnetohydrodynamics". In: *Physical Review D* 103.2, p. 023018. DOI: 10.1103/PhysRevD.103.023018. arXiv: 2005.01821.

Kawaguchi, Kyohei, Nanae Domoto, et al. (2024). "Three dimensional end-to-end simulation for kilonova emission from a black-hole neutron-star merger". In: arXiv: 2404.15027.

Kawaguchi, Kyohei, Koutarou Kyutoku, et al. (2016). "Models of Kilonova/macronova Emission From Black Hole–neutron Star Mergers". In: *Astrophysical Journal* 825.1, p. 52. DOI: 10.3847/0004-637X/825/1/52. arXiv: 1601.07711.

King, A. R., J. P. Lasota, and Wolfgang Kundt (1975). "Black Holes and Magnetic Fields". In: *Physical Review D* 12, pp. 3037–3042. DOI: 10.1103/PhysRevD.12.3037.

Kiuchi, Kenta et al. (2015). “High resolution magnetohydrodynamic simulation of black hole-neutron star merger: Mass ejection and short gamma ray bursts”. In: *Physical Review D* 92.6, p. 064034. DOI: 10.1103/PhysRevD.92.064034. arXiv: 1506.06811.

Komissarov, S. S. (2002). “On the properties of time dependent, force-free, degenerate electrodynamics”. In: *Monthly Notices of the Royal Astronomical Society* 336, p. 759. DOI: 10.1046/j.1365-8711.2002.05313.x. arXiv: astro-ph/0202447.

– (2004a). “Electrodynamics of black hole magnetospheres”. In: *Monthly Notices of the Royal Astronomical Society* 350, p. 407. DOI: 10.1111/j.1365-2966.2004.07446.x. arXiv: astro-ph/0402403.

– (2004b). “General relativistic MHD simulations of monopole magnetospheres of black holes”. In: *Monthly Notices of the Royal Astronomical Society* 350, p. 1431. DOI: 10.1111/j.1365-2966.2004.07738.x. arXiv: astro-ph/0402430.

– (2006). “Simulations of axisymmetric magnetospheres of neutron stars”. In: *Monthly Notices of the Royal Astronomical Society* 367, pp. 19–31. DOI: 10.1111/j.1365-2966.2005.09932.x. arXiv: astro-ph/0510310.

– (2007). “Multi-dimensional Numerical Scheme for Resistive Relativistic MHD”. In: *Monthly Notices of the Royal Astronomical Society* 382, p. 995. DOI: 10.1111/j.1365-2966.2007.12448.x. arXiv: 0708.0323.

Komissarov, S. S. and Jonathan C. McKinney (2007). “Meissner effect and Blandford-Znajek mechanism in conductive black hole magnetospheres”. In: *Monthly Notices of the Royal Astronomical Society* 377, pp. L49–L53. DOI: 10.1111/j.1745-3933.2007.00301.x. arXiv: astro-ph/0702269.

Koppitz, Michael et al. (2007). “Recoil Velocities from Equal-Mass Binary-Black-Hole Mergers”. In: *Physical Review Letters* 99, p. 041102. DOI: 10.1103/PhysRevLett.99.041102. arXiv: gr-qc/0701163.

Kopriva, David A. (2009). *Implementing Spectral Methods for Partial Differential Equations*. Springer Dordrecht. DOI: 10.1007/978-90-481-2261-5.

Koyuncu, Fahrettin and Orhan Dönmez (2014). “Numerical simulation of the disk dynamics around the black hole: Bondi Hoyle accretion”. In: *Modern Physics Letters A* 29, p. 1450115. DOI: 10.1142/S0217732314501156.

Kulkarni, Akshay K. and Marina M. Romanova (2008). “Accretion to Magnetized Stars through the Rayleigh-Taylor Instability: Global Three-Dimensional Simulations”. In: *Monthly Notices of the Royal Astronomical Society* 386, p. 673. DOI: 10.1111/j.1365-2966.2008.13094.x. arXiv: 0802.1759.

Kwan, Tom M., Lixin Dai, and Alexander Tchekhovskoy (2023). “The Effects of Gas Angular Momentum on the Formation of Magnetically Arrested Disks and the Launching of Powerful Jets”. In: *Astrophysical Journal Letters* 946.2, p. L42. DOI: 10.3847/2041-8213/acc334. arXiv: 2211.12726.

Kyutoku, Koutarou, Masaru Shibata, and Keisuke Taniguchi (2021). “Coalescence of black hole–neutron star binaries”. In: *Living Reviews in Relativity* 24.1, p. 5. DOI: 10.1007/s41114-021-00033-4. arXiv: 2110.06218.

Lai, Dong (2012). “DC Circuit Powered by Orbital Motion: Magnetic Interactions in Compact Object Binaries and Exoplanetary Systems”. In: *Astrophysical Journal Letters* 757, p. L3. DOI: 10.1088/2041-8205/757/1/L3. arXiv: 1206.3723.

Lalakos, Aretaios et al. (2024). “Jets with a Twist: The Emergence of FR0 Jets in a 3D GRMHD Simulation of Zero-angular-momentum Black Hole Accretion”. In: *Astrophysical Journal* 964.1, p. 79. DOI: 10.3847/1538-4357/ad0974. arXiv: 2310.11487.

Lattimer, J. M. and D. N. Schramm (1974). “Black-hole-neutron-star collisions”. In: *Astrophysical Journal Letters* 192, p. L145. DOI: 10.1086/181612.

Legred, Isaac et al. (2023). “Simulating neutron stars with a flexible enthalpy-based equation of state parametrization in spectre”. In: *Physical Review D* 107.12, p. 123017. DOI: 10.1103/PhysRevD.107.123017. arXiv: 2301.13818.

Lehner, Luis et al. (2012). “Intense Electromagnetic Outbursts from Collapsing Hypermassive Neutron Stars”. In: *Physical Review D* 86, p. 104035. DOI: 10.1103/PhysRevD.86.104035. arXiv: 1112.2622.

Levin, Janna, Daniel J. D’Orazio, and Sebastian Garcia-Saenz (2018). “Black Hole Pulsar”. In: *Physical Review D* 98.12, p. 123002. DOI: 10.1103/PhysRevD.98.123002. arXiv: 1808.07887.

Li, Li-Xin (2000). “Screw instability and blandford-znajek mechanism”. In: *Astrophysical Journal Letters* 531, p. L111. DOI: 10.1086/312538. arXiv: astro-ph/0001420.

Li, Li-Xin and Bohdan Paczynski (1998). “Transient events from neutron star mergers”. In: *Astrophysical Journal Letters* 507, p. L59. DOI: 10.1086/311680. arXiv: astro-ph/9807272.

Li, Xinyu et al. (2020). “Simulation of a compact object with outflows moving through a gaseous background”. In: *Monthly Notices of the Royal Astronomical Society* 494.2. [Erratum: Mon.Not.Roy.Astron.Soc. 504, 3166–3167 (2021)], pp. 2327–2336. DOI: 10.1093/mnras/stab1180. arXiv: 1912.06864.

Liska, Matthew et al. (2018). “Formation of Precessing Jets by Tilted Black-hole Discs in 3D General Relativistic MHD Simulations”. In: *Monthly Notices of the Royal Astronomical Society* 474.1, pp. L81–L85. DOI: 10.1093/mnrasl/slx174. arXiv: 1707.06619.

– (2021). “Disc tearing and Bardeen–Petterson alignment in GRMHD simulations of highly tilted thin accretion discs”. In: *Monthly Notices of the Royal Astronomical Society* 507.1, pp. 983–990. DOI: 10.1093/mnras/staa099. arXiv: 1904.08428.

Liska, Matthew et al. (2022). “H-AMR: A New GPU-accelerated GRMHD Code for Exascale Computing with 3D Adaptive Mesh Refinement and Local Adaptive Time Stepping”. In: *Astrophysical Journal Supplement Series* 263.2, p. 26. DOI: 10.3847/1538-4365/ac9966. arXiv: 1912.10192.

Livio, Mario and Noam Soker (1988). “The Common Envelope Phase in the Evolution of Binary Stars”. In: *Astrophysical Journal* 329, p. 764. DOI: 10.1086/166419.

Loffler, Frank et al. (2012). “The Einstein Toolkit: A Community Computational Infrastructure for Relativistic Astrophysics”. In: *Classical and Quantum Gravity* 29, p. 115001. DOI: 10.1088/0264-9381/29/11/115001. arXiv: 1111.3344.

Londrillo, P. and Luca Del Zanna (2004). “On the divergence-free condition in godunov-type schemes for ideal magnetohydrodynamics: the upwind constrained transport method”. In: *Journal of Computational Physics* 195, pp. 17–48. DOI: 10.1016/j.jcp.2003.09.016. arXiv: astro-ph/0310183.

López-Cámara, Diego, Enrique Moreno Méndez, and Fabio De Colle (2020). “Disc formation and jet inclination effects in common envelopes”. In: *Monthly Notices of the Royal Astronomical Society* 497.2, pp. 2057–2065. DOI: 10.1093/mnras/staa1983. arXiv: 2004.04158.

Lora-Clavijo, F. D., Alejandro Cruz-Osorio, and Enrique Moreno Méndez (2015). “Relativistic Bondi–Hoyle–Lyttleton Accretion Onto a Rotating Black Hole: Density Gradients”. In: *The Astrophysical Journal Supplement Series* 219.2, p. 30. DOI: 10.1088/0067-0049/219/2/30.

Lora-Clavijo, F. D. and F. S. Guzman (2013). “Axisymmetric Bondi–Hoyle accretion on to a Schwarzschild black hole: shock cone vibrations”. In: *Monthly Notices of the Royal Astronomical Society* 429.4, pp. 3144–3154. DOI: 10.1093/mnras/sts573. arXiv: 1212.2139.

Lowell, Beverly et al. (2024). “Rapid Black Hole Spin-down by Thick Magnetically Arrested Disks”. In: *Astrophysical Journal* 960.1, p. 82. DOI: 10.3847/1538-4357/ad09af. arXiv: 2302.01351.

Lyubarsky, Yuri (2003). “Fast magnetosonic waves in pulsar winds”. In: *Monthly Notices of the Royal Astronomical Society* 339, p. 765. DOI: 10.1046/j.1365-8711.2003.06221.x. arXiv: astro-ph/0211046.

– (2014). “A model for fast extragalactic radio bursts”. In: *Monthly Notices of the Royal Astronomical Society* 442, p. 9. DOI: 10.1093/mnrasl/slu046. arXiv: 1401.6674.

– (2020). “Fast Radio Bursts from Reconnection in a Magnetar Magnetosphere”. In: *Astrophysical Journal* 897.1, p. 1. DOI: 10.3847/1538-4357/ab97b5. arXiv: 2001.02007.

Lyubarsky, Yuri and J. G. Kirk (2001). “Reconnection in a striped pulsar wind”. In: *Astrophysical Journal* 547, p. 437. DOI: 10.1086/318354. arXiv: astro-ph/0009270.

Lyutikov, Maxim and Jonathan C. McKinney (2011). “Slowly balding black holes”. In: *Physical Review D* 84, p. 084019. DOI: 10.1103/PhysRevD.84.084019. arXiv: 1109.0584.

MacDonald, D. and Kip S. Thorne (1982). “Black-hole electrodynamics - an absolute-space/universal-time formulation”. In: *Monthly Notices of the Royal Astronomical Society* 198, pp. 345–383.

MacLeod, Morgan, Andrea Antoni, et al. (2017). “Common Envelope Wind Tunnel: Coefficients of Drag and Accretion in a Simplified Context for Studying Flows around Objects Embedded within Stellar Envelopes”. In: *Astrophysical Journal* 838.1, 56, p. 56. DOI: 10.3847/1538-4357/aa6117. arXiv: 1704.02372.

MacLeod, Morgan and Enrico Ramirez-Ruiz (2015). “Asymmetric Accretion Flows within a Common Envelope”. In: *Astrophysical Journal* 803.1, 41, p. 41. DOI: 10.1088/0004-637X/803/1/41. arXiv: 1410.3823.

Mahlmann, J. F., T. Akgün, et al. (2019). “Instability of twisted magnetar magnetospheres”. In: *Monthly Notices of the Royal Astronomical Society* 490.4, pp. 4858–4876. DOI: 10.1093/mnras/stz2729. arXiv: 1908.00010.

Mahlmann, J. F., M. A. Aloy, et al. (2021a). “Computational General Relativistic Force-Free Electrodynamics: I. Multi-Coordinate Implementation and Testing”. In: *Astronomy and Astrophysics* 647, A57. DOI: 10.1051/0004-6361/202038907. arXiv: 2007.06580.

– (2021b). “Computational General Relativistic Force-Free Electrodynamics: II. Characterization of Numerical Diffusivity”. In: *Astronomy and Astrophysics* 647, A58. DOI: 10.1051/0004-6361/202038908. arXiv: 2007.06599.

Mahlmann, J. F., Alexander A. Philippov, Amir Levinson, et al. (2022). “Electromagnetic fireworks: Fast radio bursts from rapid reconnection in the compressed magnetar wind”. In: *Astrophysical Journal Letters* 932, p. L20. DOI: 10.3847/2041-8213/ac7156. arXiv: 2203.04320.

Mahlmann, J. F., Alexander A. Philippov, V. Mewes, et al. (2023). “Three-dimensional Dynamics of Strongly Twisted Magnetar Magnetospheres: Kinking Flux Tubes and Global Eruptions”. In: *Astrophysical Journal Letters* 947.2, p. L34. DOI: 10.3847/2041-8213/accada. arXiv: 2302.07273.

Maltsev, Vadim et al. (2023). “Hybrid discontinuous Galerkin-finite volume techniques for compressible flows on unstructured meshes”. In: *Journal of Computational Physics* 473, 111755, p. 111755. DOI: 10.1016/j.jcp.2022.111755.

Martineau, Tia et al. (2024). “Black Hole-Neutron Star Binaries near Neutron Star Disruption Limit in the Mass Regime of Event GW230529”. In: arXiv: 2405.06819.

McKernan, B. et al. (2022). "LIGO–Virgo correlations between mass ratio and effective inspiral spin: testing the active galactic nuclei channel". In: *Monthly Notices of the Royal Astronomical Society* 514.3, pp. 3886–3893. DOI: 10.1093/mnras/stac1570. arXiv: 2107.07551.

McKinney, Jonathan C. (2006a). "General relativistic force-free electrodynamics: a new code and applications to black hole magnetospheres". In: *Monthly Notices of the Royal Astronomical Society* 367, pp. 1797–1807. DOI: 10.1111/j.1365-2966.2006.10087.x. arXiv: astro-ph/0601410.

– (2006b). "Relativistic force-free electrodynamic simulations of neutron star magnetospheres". In: *Monthly Notices of the Royal Astronomical Society* 368, pp. L30–L34. DOI: 10.1111/j.1745-3933.2006.00150.x. arXiv: astro-ph/0601411.

McKinney, Jonathan C., Alexander Tchekhovskoy, and Roger D. Blandford (2012). "General Relativistic Magnetohydrodynamic Simulations of Magnetically Choked Accretion Flows around Black Holes". In: *Monthly Notices of the Royal Astronomical Society* 423, p. 3083. DOI: 10.1111/j.1365-2966.2012.21074.x. arXiv: 1201.4163.

McWilliams, Sean T. and Janna Levin (2011). "Electromagnetic extraction of energy from black hole-neutron star binaries". In: *Astrophysical Journal* 742, p. 90. DOI: 10.1088/0004-637X/742/2/90. arXiv: 1101.1969.

Metzger, Brian D. (2020). "Kilonovae". In: *Living Reviews in Relativity* 23.1, p. 1. DOI: 10.1007/s41114-019-0024-0. arXiv: 1910.01617.

Michel, F. Curtis (1982). "Theory of pulsar magnetospheres". In: *Reviews of Modern Physics* 54, pp. 1–66. DOI: 10.1103/RevModPhys.54.1.

Miley, G. K., K. J. Wellington, and H. van der Laan (1975). "The structure of the radio galaxy NGC 1265." In: *Astronomy and Astrophysics* 38.3, pp. 381–390.

Mingarelli, Chiara M. F., Janna Levin, and T. Joseph W. Lazio (2015). "Fast Radio Bursts and Radio Transients from Black Hole Batteries". In: *Astrophysical Journal Letters* 814.2, p. L20. DOI: 10.1088/2041-8205/814/2/L20. arXiv: 1511.02870.

Misner, Charles W., Kip S. Thorne, and John Archibald Wheeler (1973). *Gravitation*. W. H. Freeman.

Moeckel, Nickolas and Henry B. Throop (2009). "Bondi-Hoyle-Lyttleton Accretion onto a Protoplanetary Disk". In: *Astrophysical Journal* 707, pp. 268–277. DOI: 10.1088/0004-637X/707/1/268. arXiv: 0910.3539.

Moesta, Philipp et al. (2012). "On the detectability of dual jets from binary black holes". In: *Astrophysical Journal Letters* 749, p. L32. DOI: 10.1088/2041-8205/749/2/L32. arXiv: 1109.1177.

Most, Elias R., Andrei M. Beloborodov, and Bart Ripperda (2024). "Monster Shocks, Gamma-Ray Bursts, and Black Hole Quasi-normal Modes from Neutron-star Collapse". In: *Astrophysical Journal Letters* 974.1, p. L12. DOI: 10.3847/2041-8213/ad7e1f. arXiv: 2404.01456.

Most, Elias R., Yoonsoo Kim, et al. (2024). "Nonlinear Alfvén-wave Dynamics and Premerger Emission from Crustal Oscillations in Neutron Star Mergers". In: *Astrophysical Journal Letters* 973.2, p. L37. DOI: 10.3847/2041-8213/ad785c. arXiv: 2407.17026.

Most, Elias R., Antonios Nathanail, and Luciano Rezzolla (2018). "Electromagnetic emission from blitzars and its impact on non-repeating fast radio bursts". In: *Astrophysical Journal* 864.2, p. 117. DOI: 10.3847/1538-4357/aad6ef. arXiv: 1801.05705.

Most, Elias R., L. Jens Papenfort, and Luciano Rezzolla (2019). "Beyond second-order convergence in simulations of magnetized binary neutron stars with realistic microphysics". In: *Monthly Notices of the Royal Astronomical Society* 490.3, pp. 3588–3600. DOI: 10.1093/mnras/stz2809. arXiv: 1907.10328.

Most, Elias R., L. Jens Papenfort, Samuel D. Tootle, et al. (2021). "On accretion discs formed in MHD simulations of black hole–neutron star mergers with accurate microphysics". In: *Monthly Notices of the Royal Astronomical Society* 506.3, pp. 3511–3526. DOI: 10.1093/mnras/stab1824. arXiv: 2106.06391.

Most, Elias R. and Alexander A. Philippov (2020). "Electromagnetic precursors to gravitational wave events: Numerical simulations of flaring in pre-merger binary neutron star magnetospheres". In: *Astrophysical Journal Letters* 893.1, p. L6. DOI: 10.3847/2041-8213/ab8196. arXiv: 2001.06037.

– (2022). "Electromagnetic precursor flares from the late inspiral of neutron star binaries". In: *Monthly Notices of the Royal Astronomical Society* 515.2, pp. 2710–2724. DOI: 10.1093/mnras/stac1909. arXiv: 2205.09643.

– (2023a). "Electromagnetic Precursors to Black Hole–Neutron Star Gravitational Wave Events: Flares and Reconnection-powered Fast Radio Transients from the Late Inspiral". In: *Astrophysical Journal Letters* 956.2, p. L33. DOI: 10.3847/2041-8213/acfdae. arXiv: 2309.04271.

– (2023b). "Reconnection-Powered Fast Radio Transients from Coalescing Neutron Star Binaries". In: *Physical Review Letters* 130.24, p. 245201. DOI: 10.1103/PhysRevLett.130.245201. arXiv: 2207.14435.

Most, Elias R. and Hai-Yang Wang (2024a). "Decoupling of a supermassive black hole binary from its magnetically arrested circumbinary accretion disk". In: arXiv: 2410.23264.

– (2024b). "Magnetically Arrested Circumbinary Accretion Flows". In: *Astrophysical Journal Letters* 973.1, p. L19. DOI: 10.3847/2041-8213/ad7713. arXiv: 2408.00757.

Murguia-Berthier, Ariadna et al. (2017). "Accretion Disk Assembly During Common Envelope Evolution: Implications for Feedback and LIGO Binary Black Hole Formation". In: *Astrophysical Journal* 845.2, p. 173. DOI: 10.3847/1538-4357/aa8140. arXiv: 1705.04698.

Narayan, Ramesh, Igor V. Igumenshchev, and Marek A. Abramowicz (2003). "Magnetically arrested disk: an energetically efficient accretion flow". In: *Publications of the Astronomical Society of Japan* 55, p. L69. DOI: 10.1093/pasj/55.6.L69. arXiv: astro-ph/0305029.

Narayan, Ramesh, Jason Li, and Alexander Tchekhovskoy (2009). "Stability of Relativistic Force-Free Jets". In: *Astrophysical Journal* 697, pp. 1681–1694. DOI: 10.1088/0004-637X/697/2/1681. arXiv: 0901.4775.

Narayan, Ramesh, Aleksander Sadowski, et al. (2012). "GRMHD Simulations of Magnetized Advection-Dominated Accretion on a Non-Spinning Black Hole: Role of Outflows". In: *Monthly Notices of the Royal Astronomical Society* 426, p. 3241. DOI: 10.1111/j.1365-2966.2012.22002.x. arXiv: 1206.1213.

Nathanail, Antonios and Ioannis Contopoulos (2014). "Black Hole Magnetospheres". In: *Astrophysical Journal* 788.2, p. 186. DOI: 10.1088/0004-637X/788/2/186. arXiv: 1404.0549.

Nathanail, Antonios, Elias R. Most, and Luciano Rezzolla (2017). "Gravitational collapse to a Kerr–Newman black hole". In: *Monthly Notices of the Royal Astronomical Society* 469.1, pp. L31–L35. DOI: 10.1093/mnrasl/slx035. arXiv: 1703.03223.

Nonomura, Taku and Kozo Fujii (2013). "Robust explicit formulation of weighted compact nonlinear scheme". In: *Computers & Fluids* 85. International Workshop on Future of CFD and Aerospace Sciences, pp. 8–18. ISSN: 0045-7930. DOI: https://doi.org/10.1016/j.compfluid.2012.09.001.

Núñez-de la Rosa, Jonatan and Claus-Dieter Munz (2018). "Hybrid DG/FV schemes for magnetohydrodynamics and relativistic hydrodynamics". In: *Computer Physics Communications* 222, pp. 113–135. ISSN: 0010-4655. DOI: https://doi.org/10.1016/j.cpc.2017.09.026.

O'Dea, C. P. and F. N. Owen (1986). "Multifrequency VLA Observations of the Prototypical Narrow-Angle Tail Radio Source, NGC 1265". In: *Astrophysical Journal* 301, p. 841. DOI: 10.1086/163948.

Okawa, Hirotada and Vitor Cardoso (2014). "Black holes and fundamental fields: Hair, kicks, and a gravitational Magnus effect". In: *Physical Review D* 90.10, p. 104040. DOI: 10.1103/PhysRevD.90.104040. arXiv: 1405.4861.

Palenzuela, Carlos (2013). "Modeling magnetized neutron stars using resistive MHD". In: *Monthly Notices of the Royal Astronomical Society* 431, pp. 1853–1865. DOI: 10.1093/mnras/stt311. arXiv: 1212.0130.

Palenzuela, Carlos, Travis Garrett, et al. (2010). "Magnetospheres of Black Hole Systems in Force-Free Plasma". In: *Physical Review D* 82, p. 044045. DOI: 10.1103/PhysRevD.82.044045. arXiv: 1007.1198.

Palenzuela, Carlos, Luis Lehner, and Steven L. Liebling (2010). "Dual Jets from Binary Black Holes". In: *Science* 329, p. 927. DOI: 10.1126/science.1191766. arXiv: 1005.1067.

Palenzuela, Carlos, Luis Lehner, and Shin'ichirou Yoshida (2010). "Understanding possible electromagnetic counterparts to loud gravitational wave events: Binary black hole effects on electromagnetic fields". In: *Physical Review D* 81, p. 084007. DOI: 10.1103/PhysRevD.81.084007. arXiv: 0911.3889.

Pan, Zhen and Huan Yang (2019). "Black Hole Discharge: very-high-energy gamma rays from black hole-neutron star mergers". In: *Physical Review D* 100.4, p. 043025. DOI: 10.1103/PhysRevD.100.043025. arXiv: 1905.04775.

Papenfort, L. Jens et al. (2021). "New public code for initial data of unequal-mass, spinning compact-object binaries". In: *Physical Review D* 104.2, p. 024057. DOI: 10.1103/PhysRevD.104.024057. arXiv: 2103.09911.

Pareschi, Lorenzo and Giovanni Russo (2005). "Implicit–Explicit Runge–Kutta schemes and applications to hyperbolic systems with relaxation". In: *Journal of Scientific Computing* 25.1, pp. 129–155. DOI: 10.1007/s10915-004-4636-4.

Parfrey, Kyle, Andrei M. Beloborodov, and Lam Hui (2012). "Introducing PHAEDRA: a new spectral code for simulations of relativistic magnetospheres". In: *Monthly Notices of the Royal Astronomical Society* 423, pp. 1416–1436. DOI: 10.1111/j.1365-2966.2012.20969.x. arXiv: 1110.6669.

– (2013). "Dynamics of Strongly Twisted Relativistic Magnetospheres". In: *Astrophysical Journal* 774, p. 92. DOI: 10.1088/0004-637X/774/2/92. arXiv: 1306.4335.

Parfrey, Kyle, Alexander A. Philippov, and Benoît Cerutti (2019). "First-Principles Plasma Simulations of Black-Hole Jet Launching". In: *Physical Review Letters* 122.3, p. 035101. DOI: 10.1103/PhysRevLett.122.035101. arXiv: 1810.03613.

Parfrey, Kyle and Alexander Tchekhovskoy (2017). "General-Relativistic Simulations of Four States of Accretion onto Millisecond Pulsars". In: *Astrophysical Journal Letters* 851.2, p. L34. DOI: 10.3847/2041-8213/aa9c85. arXiv: 1708.06362.

Paschalidis, Vasileios, Zachariah B. Etienne, and Stuart L. Shapiro (2013). "General relativistic simulations of binary black hole-neutron stars: Precursor electromagnetic signals". In: *Physical Review D* 88.2, p. 021504. DOI: 10.1103/PhysRevD.88.021504. arXiv: 1304.1805.

Paschalidis, Vasileios, Milton Ruiz, and Stuart L. Shapiro (2015). "Relativistic Simulations of Black Hole–neutron Star Coalescence: the jet Emerges". In: *Astrophysical Journal Letters* 806.1, p. L14. DOI: 10.1088/2041-8205/806/1/L14. arXiv: 1410.7392.

Paschalidis, Vasileios and Stuart L. Shapiro (2013). "A new scheme for matching general relativistic ideal magnetohydrodynamics to its force-free limit". In: *Physical Review D* 88.10, p. 104031. DOI: 10.1103/PhysRevD.88.104031. arXiv: 1310.3274.

Penner, Andrew J. (2011). "General Relativistic Magnetohydrodynamic Bondi–Hoyle Accretion". In: *Monthly Notices of the Royal Astronomical Society* 414, p. 1467. DOI: 10.1111/j.1365-2966.2011.18480.x. arXiv: 1011.2976.

– (2013). "Ultrarelativistic Bondi–Hoyle Accretion I: Axisymmetry". In: *Monthly Notices of the Royal Astronomical Society* 428, pp. 2171–2184. DOI: 10.1093/mnras/sts176. arXiv: 1205.4957.

Penner, Andrew J. et al. (2012). "Crustal failure during binary inspiral". In: *Astrophysical Journal Letters* 749, p. L36. DOI: 10.1088/2041-8205/749/2/L36. arXiv: 1109.5041.

Persson, Per-Olof and Jaime Peraire (2006). "Sub-Cell Shock Capturing for Discontinuous Galerkin Methods". In: *44th AIAA Aerospace Sciences Meeting and Exhibit*. DOI: 10.2514/6.2006-112. eprint: https://arc.aiaa.org/doi/pdf/10.2514/6.2006-112.

Petri, J. (2012). "The pulsar force-free magnetosphere linked to its striped wind: time-dependent pseudo-spectral simulations". In: *Monthly Notices of the Royal Astronomical Society* 424, p. 605. DOI: 10.1111/j.1365-2966.2012.21238.x. arXiv: 1205.0889.

– (2015). "General-relativistic monopole magnetosphere of neutron stars: a pseudo-spectral discontinuous Galerkin approach". In: *Monthly Notices of the Royal Astronomical Society* 447, p. 3170. DOI: 10.1093/mnras/stu2626. arXiv: 1412.3601.

– (2016). "General-relativistic force-free pulsar magnetospheres". In: *Monthly Notices of the Royal Astronomical Society* 455.4, pp. 3779–3805. DOI: 10.1093/mnras/stv2613. arXiv: 1511.01337.

Petrich, Loren I., Stuart L. Shapiro, Richard F. Stark, et al. (1989). "Accretion onto a Moving Black Hole: A Fully Relativistic Treatment". In: *Astrophysical Journal* 336, p. 313. DOI: 10.1086/167013.

Petrich, Loren I., Stuart L. Shapiro, and Saul A. Teukolsky (1988). "Accretion onto a moving black hole: An exact solution". In: *Physical Review Letters* 60, pp. 1781–1784. DOI: 10.1103/PhysRevLett.60.1781.

Pfeiffer, Harald P. and Andrew I. MacFadyen (2013). "Hyperbolicity of Force-Free Electrodynamics". In: arXiv: 1307.7782.

Philippov, Alexander A., Benoît Cerutti, et al. (2015). "Ab-initio pulsar magnetosphere: the role of general relativity". In: *Astrophysical Journal Letters* 815.2, p. L19. DOI: 10.1088/2041-8205/815/2/L19. arXiv: 1510.01734.

Philippov, Alexander A., Anatoly Spitkovsky, and Benoît Cerutti (2015). "Ab-initio pulsar magnetosphere: three-dimensional particle-in-cell simulations of oblique pulsars". In: *Astrophysical Journal Letters* 801.1, p. L19. DOI: 10.1088/2041-8205/801/1/L19. arXiv: 1412.0673.

Philippov, Alexander A., Dmitri A. Uzdensky, et al. (2019). "Pulsar Radio Emission Mechanism: Radio Nanoshots as a Low Frequency Afterglow of Relativistic Magnetic Reconnection". In: *Astrophysical Journal Letters* 876.1, p. L6. DOI: 10.3847/2041-8213/ab1590. arXiv: 1902.07730.

Piro, Anthony L. (2012). "Magnetic Interactions in Coalescing Neutron Star Binaries". In: *Astrophysical Journal* 755, p. 80. DOI: 10.1088/0004-637X/755/1/80. arXiv: 1205.6482.

Porth, O. et al. (2021). "Flares in the Galactic Centre – I. Orbiting flux tubes in magnetically arrested black hole accretion discs". In: *Monthly Notices of the Royal Astronomical Society* 502.2, pp. 2023–2032. DOI: 10.1093/mnras/stab163. arXiv: 2006.03658.

Poudel, Amit et al. (2020). "Increasing the Accuracy of Binary Neutron Star Simulations with an improved Vacuum Treatment". In: *Physical Review D* 102.10, p. 104014. DOI: 10.1103/PhysRevD.102.104014. arXiv: 2009.06617.

Reinarz, Anne et al. (2020). "ExaHyPE: An engine for parallel dynamically adaptive simulations of wave problems". In: *Computer Physics Communications* 254, p. 107251. ISSN: 0010-4655. DOI: 10.1016/j.cpc.2020.107251.

Rembiasz, Tomasz et al. (2017). "On the Measurements of Numerical Viscosity and Resistivity in Eulerian MHD Codes". In: *The Astrophysical Journal Supplement Series* 230.2, 18, p. 18. DOI: 10.3847/1538-4365/aa6254. arXiv: 1611.05858.

Ressler, Sean M., Eliot Quataert, et al. (2021). "Magnetically modified spherical accretion in GRMHD: reconnection-driven convection and jet propagation". In: *Monthly Notices of the Royal Astronomical Society* 504.4, pp. 6076–6095. DOI: 10.1093/mnras/stab311. arXiv: 2102.01694.

Ressler, Sean M., Alexander Tchekhovskoy, et al. (2017). "The disc-jet symbiosis emerges: modelling the emission of Sagittarius A* with electron thermodynamics". In: *Monthly Notices of the Royal Astronomical Society* 467.3, pp. 3604–3619. DOI: 10.1093/mnras/stx364. arXiv: 1611.09365.

Ripperda, Bart, Fabio Bacchini, and Alexander A. Philippov (2020). "Magnetic Reconnection and Hot Spot Formation in Black Hole Accretion Disks". In: *Astrophysical Journal* 900.2, p. 100. DOI: 10.3847/1538-4357/ababab. arXiv: 2003.04330.

Ripperda, Bart, Matthew Liska, et al. (2022). "Black Hole Flares: Ejection of Accreted Magnetic Flux through 3D Plasmoid-mediated Reconnection". In: *Astrophysical Journal Letters* 924.2, p. L32. DOI: 10.3847/2041-8213/ac46a1. arXiv: 2109.15115.

Rueda-Ramírez, Andrés M., Will Pazner, and Gregor J. Gassner (2022). "Subcell limiting strategies for discontinuous Galerkin spectral element methods". In: *Computers & Fluids* 247, p. 105627. ISSN: 0045-7930. DOI: https://doi.org/10.1016/j.compfluid.2022.105627.

Ruiz, Milton, Vasileios Paschalidis, et al. (2020). "Black hole-neutron star coalescence: effects of the neutron star spin on jet launching and dynamical ejecta mass". In: *Physical Review D* 102.12, p. 124077. DOI: 10.1103/PhysRevD.102.124077. arXiv: 2011.08863.

Ruiz, Milton, Stuart L. Shapiro, and Antonios Tsokaros (2018). "Jet launching from binary black hole-neutron star mergers: Dependence on black hole spin, binary mass ratio and magnetic field orientation". In: *Physical Review D* 98.12, p. 123017. DOI: 10.1103/PhysRevD.98.123017. arXiv: 1810.08618.

Rusanov, V.V (1962). "The calculation of the interaction of non-stationary shock waves and obstacles". In: *USSR Computational Mathematics and Mathematical Physics* 1.2, pp. 304–320. ISSN: 0041-5553. DOI: https://doi.org/10.1016/0041-5553(62)90062-9.

Schnetter, Erik, Scott H. Hawley, and Ian Hawke (2004). "Evolutions in 3-D numerical relativity using fixed mesh refinement". In: *Classical and Quantum Gravity* 21, pp. 1465–1488. DOI: 10.1088/0264-9381/21/6/014. arXiv: gr-qc/0310042.

Schoepe, Andreas, David Hilditch, and Marcus Bugner (2018). "Revisiting Hyperbolicity of Relativistic Fluids". In: *Physical Review D* 97.12, p. 123009. DOI: 10.1103/PhysRevD.97.123009. arXiv: 1712.09837.

Selvi, Sebastiaan et al. (2024). "Current Sheet Alignment in Oblique Black Hole Magnetospheres: A Black Hole Pulsar?" In: *Astrophysical Journal Letters* 968.1, p. L10. DOI: 10.3847/2041-8213/ad4a5b. arXiv: 2402.16055.

Shapiro, Stuart L. (2017). "Black holes, disks, and jets following binary mergers and stellar collapse: The narrow range of electromagnetic luminosities and accretion rates". In: *Physical Review D* 95.10, p. 101303. DOI: 10.1103/PhysRevD.95.101303. arXiv: 1705.04695.

Shima, E. et al. (1985). "Hydrodynamic calculations of axisymmetric accretion flow". In: *Monthly Notices of the Royal Astronomical Society* 217, pp. 367–386. DOI: 10.1093/mnras/217.2.367.

Shu, Chi-Wang and Stanley Osher (1988). "Efficient implementation of essentially non-oscillatory shock-capturing schemes". In: *Journal of Computational Physics* 77.2, pp. 439–471. ISSN: 0021-9991. DOI: https://doi.org/10.1016/0021-9991(88)90177-5.

Shu, Chi-Wang and Stanley Osher (1989). “Efficient implementation of essentially non-oscillatory shock-capturing schemes, II”. In: *Journal of Computational Physics* 83.1, pp. 32–78. ISSN: 0021-9991. DOI: https://doi.org/10.1016/0021-9991(89)90222-2.

Sironi, Lorenzo, Illya Plotnikov, et al. (2021). “Coherent Electromagnetic Emission from Relativistic Magnetized Shocks”. In: *Physical Review Letters* 127, p. 035101. DOI: 10.1103/PhysRevLett.127.035101. arXiv: 2107.01211.

Sironi, Lorenzo and Anatoly Spitkovsky (2014). “Relativistic Reconnection: an Efficient Source of Non-Thermal Particles”. In: *Astrophysical Journal Letters* 783, p. L21. DOI: 10.1088/2041-8205/783/1/L21. arXiv: 1401.5471.

Spitkovsky, Anatoly (2006). “Time-dependent force-free pulsar magnetospheres: axisymmetric and oblique rotators”. In: *Astrophysical Journal Letters* 648, pp. L51–L54. DOI: 10.1086/507518. arXiv: astro-ph/0603147.

Stein, Leo C. (2019). “qnm: A Python package for calculating Kerr quasinormal modes, separation constants, and spherical-spheroidal mixing coefficients”. In: *Journal of Open Source Software* 4.42, p. 1683. DOI: 10.21105/joss.01683. arXiv: 1908.10377.

Stone, James M., Patrick D. Mullen, et al. (2024). “AthenaK: A Performance-Portable Version of the Athena++ AMR Framework”. In: *arXiv e-prints*, arXiv:2409.16053, arXiv:2409.16053. DOI: 10.48550/arXiv.2409.16053. arXiv: 2409.16053.

Stone, James M., Kengo Tomida, et al. (2020). “The Athena++ Adaptive Mesh Refinement Framework: Design and Magnetohydrodynamic Solvers”. In: *The Astrophysical Journal Supplement Series* 249.1, p. 4. DOI: 10.3847/1538-4365/ab929b.

Stone, Nicholas C., Brian D. Metzger, and Zoltan Haiman (2017). “Assisted inspirals of stellar mass black holes embedded in AGN discs: solving the ‘final au problem’”. In: *Monthly Notices of the Royal Astronomical Society* 464.1, pp. 946–954. DOI: 10.1093/mnras/stw2260. arXiv: 1602.04226.

Szilágyi, Béla (2014). “Key Elements of Robustness in Binary Black Hole Evolutions using Spectral Methods”. In: *Int. J. Mod. Phys. D* 23.7, p. 1430014. DOI: 10.1142/S0218271814300146. arXiv: 1405.3693.

Taam, Ronald E. and Eric L. Sandquist (2000). “Common envelope evolution of massive binary stars”. In: *Annual Review of Astronomy and Astrophysics* 38, pp. 113–141. DOI: 10.1146/annurev.astro.38.1.113.

Tacik, Nick et al. (2016). “Initial data for black hole–neutron star binaries, with rotating stars”. In: *Classical and Quantum Gravity* 33.22, p. 225012. DOI: 10.1088/0264-9381/33/22/225012. arXiv: 1607.07962.

Tagawa, Hiromichi, Zoltan Haiman, and Bence Kocsis (2020). “Formation and Evolution of Compact Object Binaries in AGN Disks”. In: *Astrophysical Journal* 898.1, p. 25. DOI: 10.3847/1538-4357/ab9b8c. arXiv: 1912.08218.

Tanaka, Masaomi et al. (2014). “Radioactively Powered Emission from Black Hole-Neutron Star Mergers”. In: *Astrophysical Journal* 780, p. 31. DOI: 10.1088/0004-637X/780/1/31. arXiv: 1310.2774.

Taniguchi, Keisuke et al. (2007). “Quasiequilibrium black hole-neutron star binaries in general relativity”. In: *Physical Review D* 75, p. 084005. DOI: 10.1103/PhysRevD.75.084005. arXiv: gr-qc/0701110.

– (2008). “Relativistic black hole-neutron star binaries in quasiequilibrium: Effects of the black hole excision boundary condition”. In: *Physical Review D* 77, p. 044003. DOI: 10.1103/PhysRevD.77.044003. arXiv: 0710.5169.

Tavani, M. et al. (2021). “An X-ray burst from a magnetar enlightening the mechanism of fast radio bursts”. In: *Nature Astronomy* 5.4, pp. 401–407. DOI: 10.1038/s41550-020-01276-x. arXiv: 2005.12164.

Tchekhovskoy, Alexander, Ramesh Narayan, and Jonathan C. McKinney (2010). “Black Hole Spin and the Radio Loud/Quiet Dichotomy of Active Galactic Nuclei”. In: *Astrophysical Journal* 711, pp. 50–63. DOI: 10.1088/0004-637X/711/1/50. arXiv: 0911.2228.

– (2011). “Efficient Generation of Jets from Magnetically Arrested Accretion on a Rapidly Spinning Black Hole”. In: *Monthly Notices of the Royal Astronomical Society* 418, pp. L79–L83. DOI: 10.1111/j.1745-3933.2011.01147.x. arXiv: 1108.0412.

Tchekhovskoy, Alexander, Alexander A. Philippov, and Anatoly Spitkovsky (2016). “Three-dimensional analytical description of magnetized winds from oblique pulsars”. In: *Monthly Notices of the Royal Astronomical Society* 457.3, pp. 3384–3395. DOI: 10.1093/mnras/stv2869. arXiv: 1503.01467.

Tchekhovskoy, Alexander and Anatoly Spitkovsky (2013). “Time-Dependent 3D Magnetohydrodynamic Pulsar Magnetospheres: Oblique Rotators”. In: *Monthly Notices of the Royal Astronomical Society* 435, p. 1. DOI: 10.1093/mnrasl/slt076. arXiv: 1211.2803.

Tejeda, Emilio and Alejandro Aguayo-Ortiz (2019). “Relativistic wind accretion on to a Schwarzschild black hole”. In: *Monthly Notices of the Royal Astronomical Society* 487.3, pp. 3607–3617. DOI: 10.1093/mnras/stz1513. arXiv: 1906.04923.

Teukolsky, Saul A. (1972). “Rotating black holes - separable wave equations for gravitational and electromagnetic perturbations”. In: *Physical Review Letters* 29, pp. 1114–1118. DOI: 10.1103/PhysRevLett.29.1114.

– (1973). “Perturbations of a rotating black hole. 1. Fundamental equations for gravitational electromagnetic and neutrino field perturbations”. In: *Astrophysical Journal* 185, pp. 635–647. DOI: 10.1086/152444.

Teukolsky, Saul A. (2015a). "Short note on the mass matrix for Gauss–Lobatto grid points". In: *Journal of Computational Physics* 283, pp. 408–413. ISSN: 0021-9991. DOI: https://doi.org/10.1016/j.jcp.2014.12.012.

– (2015b). "The Kerr Metric". In: *Classical and Quantum Gravity* 32.12, p. 124006. DOI: 10.1088/0264-9381/32/12/124006. arXiv: 1410.2130.

– (2016). "Formulation of discontinuous Galerkin methods for relativistic astrophysics". In: *Journal of Computational Physics* 312, pp. 333–356. DOI: 10.1016/j.jcp.2016.02.031. arXiv: 1510.01190.

The Matplotlib Development Team (Feb. 2025). *Matplotlib: Visualization with Python*. Version v3.10.1. DOI: 10.5281/zenodo.14940554.

Thompson, Christopher and Robert C. Duncan (1995). "The Soft gamma repeaters as very strongly magnetized neutron stars - 1. Radiative mechanism for outbursts". In: *Monthly Notices of the Royal Astronomical Society* 275, pp. 255–300. DOI: 10.1093/mnras/275.2.255.

Tichy, Wolfgang et al. (2023). "The new discontinuous Galerkin methods based numerical relativity program Nmesh". In: *Classical and Quantum Gravity* 40.2, p. 025004. DOI: 10.1088/1361-6382/acaae7. arXiv: 2212.06340.

Trott, Christian R. et al. (2022). "Kokkos 3: Programming Model Extensions for the Exascale Era". In: *IEEE Transactions on Parallel and Distributed Systems* 33.4, pp. 805–817. DOI: 10.1109/TPDS.2021.3097283.

Tsang, David et al. (2012). "Resonant Shattering of Neutron Star Crusts". In: *Physical Review Letters* 108, p. 011102. DOI: 10.1103/PhysRevLett.108.011102. arXiv: 1110.0467.

Uchida, Toshio (1997). "Theory of force-free electromagnetic fields. I. General theory". In: *Phys. Rev. E* 56 (2), pp. 2181–2197. DOI: 10.1103/PhysRevE.56.2181.

Uzdensky, Dmitri A. and Anatoly Spitkovsky (2014). "Physical Conditions in the Reconnection Layer in Pulsar Magnetospheres". In: *Astrophysical Journal* 780, p. 3. DOI: 10.1088/0004-637X/780/1/3. arXiv: 1210.3346.

Vanthieghem, Arno and Amir Levinson (2025). "Fast Radio Bursts as Precursor Radio Emission from Monster Shocks". In: *Physical Review Letters* 134.3, p. 035201. DOI: 10.1103/PhysRevLett.134.035201. arXiv: 2407.15076.

Vilar, François (2019). "A posteriori correction of high-order discontinuous Galerkin scheme through subcell finite volume formulation and flux reconstruction". In: *Journal of Computational Physics* 387, pp. 245–279. DOI: 10.1016/j.jcp.2018.10.050.

Virtanen, Pauli et al. (2020). "SciPy 1.0: Fundamental Algorithms for Scientific Computing in Python". In: *Nature Methods* 17, pp. 261–272. DOI: 10.1038/s41592-019-0686-2.

Wald, Robert M. (1974). “Black hole in a uniform magnetic field”. In: *Physical Review D* 10, pp. 1680–1685. DOI: 10.1103/PhysRevD.10.1680.

Wang, Zipeng et al. (2024). “Gravitational Magnus effect from scalar dark matter”. In: *Physical Review D* 110.2, p. 024009. DOI: 10.1103/PhysRevD.110.024009. arXiv: 2402.07977.

White, Christopher J., James M. Stone, and Eliot Quataert (2019). “A Resolution Study of Magnetically Arrested Disks”. In: *Astrophysical Journal* 874.2, p. 168. DOI: 10.3847/1538-4357/ab0c0c. arXiv: 1903.01509.

Yu, Cong (2011). “A High-Order WENO-based Staggered Godunov-type Scheme with Constrained Transport for Force-free Electrodynamics”. In: *Monthly Notices of the Royal Astronomical Society* 411, pp. 2461–2470. DOI: 10.1111/j.1365-2966.2010.17859.x. arXiv: 1010.3592.

Yuan, Yajie, Andrei M. Beloborodov, Alexander Y. Chen, and Yuri Levin (2020). “Plasmoid Ejection by Alfvén Waves and the Fast Radio Bursts from SGR 1935+2154”. In: *Astrophysical Journal Letters* 900.2, p. L21. DOI: 10.3847/2041-8213/abafa8. arXiv: 2006.04649.

Yuan, Yajie, Andrei M. Beloborodov, Alexander Y. Chen, Yuri Levin, et al. (2022). “Magnetar Bursts Due to Alfvén Wave Nonlinear Breakout”. In: *Astrophysical Journal* 933.2, p. 174. DOI: 10.3847/1538-4357/ac7529. arXiv: 2204.08513.

Yuan, Yajie, Yuri Levin, et al. (2021). “Alfvén Wave Mode Conversion in Pulsar Magnetospheres”. In: *Astrophysical Journal* 908.2, p. 176. DOI: 10.3847/1538-4357/abd405. arXiv: 2007.11504.

Yuan, Yajie, Anatoly Spitkovsky, et al. (2019). “Black hole magnetosphere with small-scale flux tubes – II. Stability and dynamics”. In: *Monthly Notices of the Royal Astronomical Society* 487.3, pp. 4114–4127. DOI: 10.1093/mnras/stz1599. arXiv: 1901.02834.

Zanotti, Olindo, Francesco Fambri, and Michael Dumbser (2015). “Solving the relativistic magnetohydrodynamics equations with ADER discontinuous Galerkin methods, a posteriori subcell limiting and adaptive mesh refinement”. In: *Monthly Notices of the Royal Astronomical Society* 452.3, pp. 3010–3029. DOI: 10.1093/mnras/stv1510. arXiv: 1504.07458.

Zanotti, Olindo, Francesco Fambri, Michael Dumbser, and Arturo Hidalgo (2015). “Space-time adaptive ADER discontinuous Galerkin finite element schemes with a posteriori sub-cell finite volume limiting”. In: *Computers & Fluids* 118, pp. 204–224. ISSN: 0045-7930. DOI: https://doi.org/10.1016/j.compfluid.2015.06.020.

Zanotti, Olindo, Constanze Roedig, et al. (2011). “General relativistic radiation hydrodynamics of accretion flows. I: Bondi-Hoyle accretion”. In: *Monthly Notices of the Royal Astronomical Society* 417, pp. 2899–2915. DOI: 10.1111/j.1365-2966.2011.19451.x. arXiv: 1105.5615.

Zhang, Bing (2019). “Charged Compact Binary Coalescence Signal and Electromagnetic Counterpart of Plunging Black Hole–Neutron Star Mergers”. In: *Astrophysical Journal Letters* 873.2, p. L9. DOI: 10.3847/2041-8213/ab0ae8. arXiv: 1901.11177.

Zhdankin, Vladimir, Bart Ripperda, and Alexander A. Philippov (2023). “Particle acceleration by magnetic Rayleigh-Taylor instability: Mechanism for flares in black hole accretion flows”. In: *Physical Review Research* 5.4, p. 043023. DOI: 10.1103/PhysRevResearch.5.043023. arXiv: 2302.05276.

Zhong, Shu-Qing, Zi-Gao Dai, and Can-Min Deng (2019). “Electromagnetic Emission post Spinning Black Hole-Magnetized Neutron Star Mergers”. In: *Astrophysical Journal Letters* 883.1, p. L19. DOI: 10.3847/2041-8213/ab40c5. arXiv: 1909.00494.

Zlochower, Y. et al. (2005). “Accurate black hole evolutions by fourth-order numerical relativity”. In: *Physical Review D* 72, p. 024021. DOI: 10.1103/PhysRevD.72.024021. arXiv: gr-qc/0505055.

Appendix A

SPHERICAL KERR-SCHILD COORDINATES

The line element of the Kerr spacetime (see e.g., Teukolsky, 2015b for a review) in the Kerr-Schild coordinates is given as

$$g_{ab} = \eta_{ab} + 2Hl_a l_b, \tag{A.1}$$

with

$$H = \frac{Mr^3}{r^4 + a^2 z^2}, \quad l_a = \left(1, \frac{rx + ay}{r^2 + a^2}, \frac{ry - ax}{r^2 + a^2}, \frac{z}{r}\right).$$

Here, M is the mass and $a \equiv J/M$ is the rotational parameter of the black hole, where J is its angular momentum.[1] The coordinate variable r is defined via

$$\frac{x^2 + y^2}{r^2 + a^2} + \frac{z^2}{r^2} = 1. \tag{A.2}$$

For $a = 0$, we see that $r^2 = x^2 + y^2 + z^2$ is the usual radial coordinate.

Explicitly writing out the metric, we have

$$\begin{aligned} ds^2 = & -dt^2 + dx^2 + dy^2 + dz^2 \\ & + \frac{2Mr^3}{r^4 + a^2 z^2}\left[dt + \frac{r(xdx + ydy) + a(ydx - xdy)}{r^2 + a^2} + \frac{zdz}{r}\right]^2, \end{aligned} \tag{A.3}$$

which is often called 'Cartesian' Kerr-Schild coordinates. A nice feature of the Kerr-Schild form (A.3) is that the determinant of the spacetime metric is unity, i.e. $\sqrt{-g} = 1$, often greatly simplifying algebra for some calculations.

The singularity is at $r = 0$, which is a ring $x^2 + y^2 = a^2$, $z = 0$. Inner and outer horizon radii are

$$r_\pm = M \pm \sqrt{M^2 - a^2} \tag{A.4}$$

In the *spherical* Kerr-Schild coordinates, the Kerr metric has a form

$$\begin{aligned} ds^2 = & -(1 - B)\, dt^2 + (1 + B)\, dr^2 + \Sigma\, d\theta^2 \\ & + (r^2 + a^2 + Ba^2 \sin^2\theta) \sin^2\theta\, d\phi^2 \\ & + 2B\, dtdr - 2aB \sin^2\theta\, dtd\phi - 2a(1 + B)\sin^2\theta dr d\phi \end{aligned} \tag{A.5}$$

[1]The dimensionless spin $a = J/M^2$ is also frequently used in literature.

where $\Sigma = r^2 + a^2 \cos^2\theta$ and $B = 2Mr/\Sigma$. The locations of inner and outer horizon are given same as (A.4). Horizons appear as exact spheres in the spherical Kerr-Schild coordinates, which is often helpful for implementing a computational domain for numerical simulations.

The coordinate transformation between the Kerr-Schild (A.3) and the spherical Kerr-Schild coordinates (A.5) is

$$x = (r\cos\phi - a\sin\phi)\sin\theta, \tag{A.6a}$$

$$y = (r\sin\phi + a\cos\phi)\sin\theta, \tag{A.6b}$$

$$z = r\cos\theta. \tag{A.6c}$$

Appendix B

THE WALD MAGNETOSPHERE SOLUTION

Wald (1974) derived an exact axisymmetric solution of Maxwell equations in the Kerr spacetime, describing a magnetosphere with an asymptotically uniform magnetic field B_0 aligned with the spin axis of the black hole. The original solution given in terms of the vector potential is

$$A_b = \frac{B_0}{2}[(\partial_\phi)_b + 2a(\partial_t)_b], \tag{B.1}$$

where ∂_ϕ and ∂_t are Killing vector fields of the Kerr spacetime in ϕ and t directions, and $a = J/M$ is the rotational parameter of the black hole.

In the spherical Kerr-Schild coordinates (see Appendix A), each components of the Wald solution (B.1) are

$$A_t = \frac{B_0}{2}(g_{t\phi} + 2ag_{tt}), \tag{B.2a}$$

$$A_r = \frac{B_0}{2}(g_{r\phi} + 2ag_{tr}), \tag{B.2b}$$

$$A_\theta = 0, \tag{B.2c}$$

$$A_\phi = \frac{B_0}{2}(g_{\phi\phi} + 2ag_{t\phi}). \tag{B.2d}$$

Computing magnetic fields from the vector potential (B.2), we get

$$\tilde{B}^r = B_0 r^2 \sin\theta\cos\theta\left[1 + \frac{a^2}{r^2} + \frac{2M}{r}\left(\frac{r^4 - a^4}{(r^2 + a^2\cos^2\theta)^2} - 1\right)\right] \tag{B.3a}$$

$$\tilde{B}^\theta = -B_0 r\sin^2\theta - \frac{a^2 M B_0 \sin^2\theta}{(r^2 + a^2\cos^2\theta)^2}(r^2 - a^2\cos^2\theta)(2 - \sin^2\theta) \tag{B.3b}$$

$$\tilde{B}^\phi = aB_0\sin\theta\cos\theta\left[1 + \frac{2Mr(r^2 - a^2)}{(r^2 + a^2\cos^2\theta)^2}\right]. \tag{B.3c}$$

Here $\tilde{B}^i = \sqrt{\gamma}B^i$ where $\sqrt{\gamma} = \sqrt{1 + B}\,\Sigma\sin\theta$ is the square root of the determinant of the spatial metric in the spherical Kerr-Schild coordinates.

We also write out $\tilde{B}^i$ in the Cartesian *representation*

$$\bar{x} = r\sin\theta\cos\phi, \tag{B.4a}$$

$$\bar{y} = r\sin\theta\sin\phi, \tag{B.4b}$$

$$\bar{z} = r\cos\theta, \tag{B.4c}$$

which are often used for representing tensor quantities in the code (e.g. in SpECTRE). Resulting expressions are:

$$\begin{aligned}\tilde{B}^{\bar{x}} = aB_0\bar{z}\Bigg[&(a\bar{x} - r\bar{y})\left\{\frac{1}{r^4} + \frac{2Mr(r^2 - a^2)}{(r^4 + a^2z^2)^2}\right\} \\ &+ aMr\bar{x}\left\{\frac{r^2 - z^2}{r^4(r^4 + a^2z^2)} - \frac{4(r^2 + z^2)}{(r^4 + a^2z^2)^2}\right\}\Bigg]\end{aligned} \tag{B.5a}$$

$$\begin{aligned}\tilde{B}^{\bar{y}} = aB_0\bar{z}\Bigg[&(r\bar{x} + a\bar{y})\left\{\frac{1}{r^4} + \frac{2Mr(r^2 - a^2)}{(r^4 + a^2z^2)^2}\right\} \\ &+ aMr\bar{y}\left\{\frac{r^2 - z^2}{r^4(r^4 + a^2z^2)} - \frac{4(r^2 + z^2)}{(r^4 + a^2z^2)^2}\right\}\Bigg]\end{aligned} \tag{B.5b}$$

$$\tilde{B}^{z} = B_0\left[1 + \frac{a^2z^2}{r^4} + \frac{Ma^2}{r^3}\left\{1 - \frac{z^2(a^2 + z^2)(5r^4 + a^2z^2)}{(r^4 + a^2z^2)^2}\right\}\right]. \tag{B.5c}$$

from which one can check that $\tilde{B}^i \to (0, 0, B_0)$ for $a \to 0$. We use the expressions (B.5) for initializing the densitized magnetic fields $\tilde{B}^i$ in Chapter 2.

Note that the barred coordinates $\bar{x}, \bar{y}$ are *not equal* to the x, y coordinates appearing in the original Kerr-Schild form (A.3), whereas $\bar{z} = z$. Barred coordinates $\bar{x}, \bar{y}, \bar{z}$ are simply Cartesian projections of the spherical Kerr-Schild coordinates (A.5), where they are related with the Kerr-Schild coordinates by

$$\frac{\bar{x}}{r} = \frac{x}{\sqrt{r^2 + a^2}}, \tag{B.6a}$$

$$\frac{\bar{y}}{r} = \frac{y}{\sqrt{r^2 + a^2}}, \tag{B.6b}$$

$$\bar{z} = z, \tag{B.6c}$$

$$r^2 = \bar{x}^2 + \bar{y}^2 + \bar{z}^2. \tag{B.6d}$$